

---

# Handbook of Laser-Induced Breakdown Spectroscopy

---

---

# Handbook of Laser-Induced Breakdown Spectroscopy

---

**David A. Cremers**

*Applied Research Associates, Inc.  
Albuquerque, NM*

and

**Leon J. Radziemski**

*Research Corporation  
Tucson, AZ*



John Wiley & Sons, Ltd

Copyright © 2006 John Wiley & Sons Ltd, The Atrium, Southern Gate, Chichester,  
West Sussex PO19 8SQ, England  
Telephone (+44) 1243 779777

Email (for orders and customer service enquiries): cs-books@wiley.co.uk  
Visit our Home Page on [www.wiley.com](http://www.wiley.com)

All Rights Reserved. No part of this publication may be reproduced, stored in a retrieval system or transmitted in any form or by any means, electronic, mechanical, photocopying, recording, scanning or otherwise, except under the terms of the Copyright, Designs and Patents Act 1988 or under the terms of a licence issued by the Copyright Licensing Agency Ltd, 90 Tottenham Court Road, London W1T 4LP, UK, without the permission in writing of the Publisher. Requests to the Publisher should be addressed to the Permissions Department, John Wiley & Sons Ltd, The Atrium, Southern Gate, Chichester, West Sussex PO19 8SQ, England, or emailed to [permreq@wiley.co.uk](mailto:permreq@wiley.co.uk), or faxed to (+44) 1243 770620.

Designations used by companies to distinguish their products are often claimed as trademarks. All brand names and product names used in this book are trade names, service marks, trademarks or registered trademarks of their respective owners. The Publisher is not associated with any product or vendor mentioned in this book.

This publication is designed to provide accurate and authoritative information in regard to the subject matter covered. It is sold on the understanding that the Publisher is not engaged in rendering professional services. If professional advice or other expert assistance is required, the services of a competent professional should be sought.

#### ***Other Wiley Editorial Offices***

John Wiley & Sons Inc., 111 River Street, Hoboken, NJ 07030, USA

Jossey-Bass, 989 Market Street, San Francisco, CA 94103-1741, USA

Wiley-VCH Verlag GmbH, Boschstr. 12, D-69469 Weinheim, Germany

John Wiley & Sons Australia Ltd, 42 McDougall Street, Milton, Queensland 4064, Australia

John Wiley & Sons (Asia) Pte Ltd, 2 Clementi Loop #02-01, Jin Xing Distripark, Singapore 129809

John Wiley & Sons Canada Ltd, 22 Worcester Road, Etobicoke, Ontario, Canada M9W 1L1

Wiley also publishes its books in a variety of electronic formats. Some content that appears in print may not be available in electronic books.

#### ***Library of Congress Cataloging in Publication Data***

Cremers, David A.

Handbook of laser-induced breakdown spectroscopy / David A. Cremers and Leon J. Radziemski.  
p. cm.

Includes bibliographical references and index.

ISBN-13: 978-0-470-09299-6 (cloth : alk. paper)

ISBN-10: 0-470-09299-8 (cloth : alk. paper)

1. Atomic emission spectroscopy. 2. Laser spectroscopy. I. Radziemski, Leon J., 1937–  
II. Title.

QD96.A8C74 2006

543'.52—dc22

2006006408

#### ***British Library Cataloguing in Publication Data***

A catalogue record for this book is available from the British Library

ISBN-13 978-0-470-09299-6 (HB)

ISBN-10 0-470-09299-8 (HB)

Typeset in 10/12pt Times by Integra Software Services Pvt. Ltd, Pondicherry, India

Printed and bound in Great Britain by TJ International Ltd, Padstow, Cornwall

This book is printed on acid-free paper responsibly manufactured from sustainable forestry  
in which at least two trees are planted for each one used for paper production.

*To Tom Loree, scientist and colleague, who started the LIBS project at  
Los Alamos National Laboratory in the late 1970s*

---

# Contents

---

<b>Foreword</b>	<b>xi</b>
<b>Preface</b>	<b>xiii</b>
<b>Acronyms, Constants and Symbols</b>	<b>xvii</b>
<b>1 History</b>	<b>1</b>
1.1 Atomic Optical Emission Spectrochemistry (OES)	1
1.1.1 Conventional OES	1
1.1.2 Laser OES	1
1.2 Laser-Induced Breakdown Spectroscopy (LIBS)	2
1.3 LIBS History 1960–1980	6
1.4 LIBS History 1980–1990	9
1.5 LIBS History 1990–2000	11
1.6 Active Areas of Investigation, 2000–2002	15
References	16
<b>2 Basics of the LIBS Plasma</b>	<b>23</b>
2.1 LIBS Plasma Fundamentals	23
2.1.1 Spectral Lines and Line Profiles	25
2.1.2 Determining Electron Densities from Spectral Line Widths	27
2.1.3 Plasma Opacity	30
2.1.4 Temperature and Thermodynamic Equilibrium	31
2.2 Laser-Induced Breakdown	36
2.2.1 Breakdown in Gases	36
2.2.2 Post-Breakdown Phenomena in Gases	39
2.2.3 Breakdown In and On Solids, Aerosols and Liquids	39
2.2.4 Post-Breakdown Phenomena on Solid Surfaces	41
2.3 Laser Ablation	43
2.4 Double or Multiple Pulse LIBS	47
2.5 Summary	49
References	50
<b>3 Apparatus Fundamentals</b>	<b>53</b>
3.1 Basic LIBS Apparatus	53
3.2 Lasers	54

3.2.1 Laser Fundamentals	54
3.2.2 Types of Lasers	55
3.2.3 Properties of Laser Light Important for LIBS	58
3.2.4 Generation of Additional Wavelengths	60
3.2.5 Double Pulse Operation	61
3.3 Optical Systems	62
3.3.1 Focusing and Light Collection	62
3.3.2 Lenses	63
3.3.3 Fiber Optic Cables	65
3.4 Methods of Spectral Resolution	69
3.4.1 Introduction	69
3.4.2 Spectral Resolution Devices	70
3.5 Detectors	83
3.6 Detection System Calibrations	88
3.6.1 Wavelength Calibration	88
3.6.2 Spectral Response Calibration	90
3.7 Timing Considerations	93
3.8 Methods of LIBS Deployment	94
References	96
<b>4 Determining LIBS Analytical Figures-of-Merit</b>	<b>99</b>
4.1 Introduction	99
4.2 Basics of LIBS Measurements	99
4.3 Precision	105
4.4 Calibration	107
4.4.1 Calibration Curves	107
4.4.2 Calibration Standards	113
4.5 Detection Limit	115
4.6 Accuracy	115
References	116
<b>5 Qualitative LIBS Analysis</b>	<b>119</b>
5.1 Introduction	119
5.2 Identifying Elements	119
5.3 Material Identification	122
5.4 Process Monitoring	125
5.4.1 Experimental	126
5.4.2 Results	127
5.4.3 Conclusions	133
5.5 Material Sorting/Distinguishing	133
5.5.1 Surface Condition	134
5.5.2 Type of Analysis	134
5.5.3 Sorting Materials of Close Composition	136
5.6 Site Screening Using LIBS	137
References	141

<b>6 Quantitative LIBS Analysis</b>	<b>143</b>
6.1 Introduction	143
6.2 Effects of Sampling Geometry	143
6.3 Other Sampling Considerations	147
6.4 Particle Size and Incomplete Vaporization	151
6.5 Use of Internal Standardization	152
6.6 Chemical Matrix Effects	153
6.7 Example of LIBS Measurement: Impurities in Lithium Solutions	155
6.7.1 Objective	155
6.7.2 Experimental	156
6.7.3 Results	158
6.7.4 Discussion of Results	163
6.8 Reported Figures-of-Merit for LIBS Measurements	164
6.9 Conclusions	168
References	168
<b>7 Remote LIBS Measurements</b>	<b>171</b>
7.1 Introduction	171
7.2 Conventional Open Path LIBS	173
7.2.1 Apparatus	173
7.2.2 Focusing the Laser Pulse	174
7.2.3 Collecting the Plasma Light	178
7.2.4 Results Using Conventional LIBS	179
7.3 Stand-off LIBS Using Femtosecond Pulses	182
7.3.1 Conventional Remote LIBS Using Femtosecond Laser Pulses	182
7.3.2 Remote Analysis by Femtosecond Pulse Produced Filamentation	184
7.3.3 Teramobile	185
7.3.4 Remote LIBS Using Femtosecond Pulses	186
7.4 Fiber Optic LIBS	187
7.4.1 Fiber Optics for Light Collection	187
7.4.2 Fibers for Laser Pulse Delivery	189
7.4.3 Applications of Fiber Optics	192
References	195
<b>8 Examples of Recent LIBS Fundamental Research, Instruments and Novel Applications</b>	<b>197</b>
8.1 Introduction	197
8.2 Fundamentals	197
8.3 Calibration-Free LIBS (CF-LIBS)	201
8.4 Laser and Spectrometer Advances	203
8.5 Surface Analysis	205

8.6 Double Pulse Studies and Applications	208
8.7 Steel Applications	210
8.8 LIBS for Biological Materials	211
8.9 Nuclear Reactor Applications	212
8.10 LIBS for Space Applications	214
References	223
<b>9 The Future of LIBS</b>	<b>227</b>
9.1 Introduction	227
9.2 Expanding the Understanding and Capability of the LIBS Process	227
9.3 Widening the Universe of LIBS Applications	229
9.4 Factors that will Speed the Commercialization of LIBS	230
9.4.1 LIBS Standardization and Quantification	230
9.4.2 Routine LIBS use in Industrial Applications	230
9.4.3 Availability of Components and Systems	231
9.5 Conclusion	232
References	233
<b>Appendix A Safety Considerations in LIBS</b>	<b>237</b>
A.1 Safety Plans	237
A.2 Laser Safety	237
A.3 Generation of Aerosols	238
A.4 Laser Pulse Induced Ignition	239
References	239
<b>Appendix B Recommended Methods for Commencing LIBS Research on a Variety of Samples</b>	<b>241</b>
References	243
<b>Appendix C Representative LIBS Detection Limits</b>	<b>245</b>
C.1 Detection Limits from the Literature	245
C.2 Uniform Detection Limits	263
References	265
<b>Appendix D Major LIBS References</b>	<b>271</b>
<b>Index</b>	<b>275</b>

---

# Foreword

---

The most significant series of events occurring in the past four decades in the field of analytical atomic spectroscopy have been the invention of the laser and the development of array detectors. These events have led in the past 25 years to the emergence of laser-induced breakdown spectroscopy (LIBS), also called laser-induced plasma spectroscopy (LIPS), laser spark spectroscopy (LSS), and laser optical emission spectroscopy (LOES). This technique has dominated the analytical atomic spectroscopy scene in the last decade much like atomic absorption spectroscopy dominated in the 1960–1970s, ICP atomic emission spectroscopy in the 1970–1980s, and ICP mass spectrometry in the 1980–1990s. Certainly much of the growth of LIBS as an analytical technique is directly attributed to the pioneering research of Cremers and Radziemski. The 1981 papers by Radziemski and Loree certainly began the revolution involving LIBS. The extreme interest in LIBS is apparent when one looks at the rapid increase in publications since 1965, namely fewer than 50/year from 1965 to about 1995 and since then the increase has been nearly exponential with more than 100 in 1997, more than 200 in 1999, more than 300 in 2003, and about 400 in 2004. In addition, the interest in LIBS is obvious when one looks at the number of LIBS sessions at PITTCOR and FACSS and the conferences devoted exclusively to LIBS.

Few analytical techniques other than LIBS have ever resulted in such a general interest in the analytical community. Fundamental papers involving the measurement of electron number densities and plasma temperatures; determination of the approach to local thermodynamic equilibrium; the experimental and theoretical aspects of laser breakdown in gases, liquids, solids and aerosols; the modeling of laser-induced breakdown and ablation on solids; the modeling of post-breakdown of solids; and the use of multiple laser pulses in LIBS have all occurred in the physics and chemistry literature. The great attention to theoretical aspects of LIBS has been fueled by numerous and far-reaching applications of LIBS. Applications have involved solids, liquids, gases, and aerosols and specifically metals, environmental particles, including aerosols, water contamination, archaeological studies, artwork dating and cleaning, sampling of biological materials including bacteria and spores, analyses during machining, and homeland security involving analysis of explosives and biological and chemical warfare agents. The analytical interest has resulted primarily because of the multi-element capability, the applicability to virtually all sample types, the low sample requirements (almost non-destructive), the speed of measurements, and the lack of sample preparation. The major difficulty with LIBS involving calibration is a major current research area where calibration-free and absolute analysis are active areas of research activity.

I look forward to the further development of LIBS during the next decade. This book will certainly be useful to all researchers and will be useful to me in a field that has captivated my interest in the past few decades.

Professor J.D. Winefordner  
V.T. and Louise Jackson Professor of Chemistry  
Graduate Research Professor  
Head, Analytical Division  
Department of Chemistry  
University of Florida, Gainesville, Florida USA

---

# Preface

---



DC on the left and LR on the right

The invention of the laser has resulted in many technological spin-offs. One that has emerged as a field-deployable, analytical technique is laser-induced breakdown spectroscopy (LIBS), also sometimes called laser-induced plasma spectroscopy (LIPS) or laser spark spectroscopy (LSS). LIBS uses a low-energy pulsed laser (typically tens to hundreds of millijoules per pulse) to generate a plasma which vaporizes a small amount of the sample. Spectra emitted by the excited species, mostly atoms, are used to develop quantitative and qualitative analytical information. Targets have included gases, liquids, and aerosols, with an emphasis on solids. Applications have been many and range from sampling iron and steel, soil for contamination, metals used in nuclear reactors for degradation, artwork for dating,

teeth of mummies for evidence of water contamination in the past, and detection of aerosols emitted from smokestacks or during machining operations. In the past five years, new applications have sprung up around sampling of biological materials, planetary exploration, and homeland security. Improved techniques are being developed, and LIBS instrumentation is now available commercially. Experiments have driven improved theoretical and computational models of plasma initiation and expansion.

In the early 1980s there were few groups working on LIBS. In the past decade, however, the field has expanded greatly with many international groups now investigating and developing the method for a variety of applications. The first international conference solely on LIBS was held in Pisa, Italy in 2000. Subsequently, international meetings have been held every 2 years, and meetings focused on work in the European and Mediterranean areas on the odd years.

Several edited books and book chapters published in the last decade and a half provided snapshots of the status of LIBS at the time of their publication. Our goals are somewhat different. In addition to a comprehensive update of the forefront of LIBS development and applications, we review and summarize, for the novice, the principles of plasma spectroscopy and analytical spectrochemistry as it applies to LIBS. Included are new data and archival material to assist experienced as well as new users. Embedded are comments on the many advantages of the method along with its limitations, to provide the reader a balanced overview of LIBS capabilities.

In the first chapter we present a historical review of LIBS development through to the year 2002, based on the peer-reviewed literature. We focus on the earliest time an innovation or application appeared on the scene, rather than tracing every development through to the present day. Of course, continuous improvements in apparatus, techniques, and fundamental understanding drive the reexamination of old applications, and the emergence of new applications spurs improvements in a recurring spiral of progress. Chapter 2 contains a review of the basic principles of plasma atomic emission spectroscopy. A plasma is a local assembly of atoms, ions and free electrons, overall electrically neutral, in which the charged species often act collectively. Natural light emitting plasmas, like the sun, have been known forever. Electrically-induced plasmas have been generated in the laboratory since the 1800s, and laser-induced plasmas have been investigated since the 1960s. In this chapter we deal with the intricacies of LIBS plasma formation, lifetime and decay, in and on a variety of media, focusing on spectral information as the primary diagnostic technique. The use of spectral line properties for determining plasma properties such as temperature and electron density is discussed. Laser ablation and the effect of multiple laser pulses on plasma properties are also reviewed here.

LIBS uses instrumentation similar to that employed by other atomic spectroscopic methods, and each important element of a LIBS apparatus is discussed in turn in Chapter 3. The unique characteristics of LIBS originate from the use of a powerful laser pulse to both ‘prepare’ the target sample and then ‘excite’ the constituent atoms to emit light. To generate and capture those signals, a combination of modern laser, detector, timing, and data-gathering instrumentation, with traditional spectroscopic

apparatus including spectrometers and their optics is needed. New developments in fiber optics and detector technology are highlighted. The calibration of wavelength and spectral response is treated, along with methods of LIBS deployment from basic set-ups to more advanced configurations.

The next three chapters deal with fundamental concepts in spectroscopic chemical analysis and how they apply to and are modified by the conditions under which LIBS operates. Analytical figures-of-merit are used to benchmark the capabilities of an analysis method and to compare the performance of distinct analytical techniques using a common set of parameters. These include limits of detection, precision, accuracy, sensitivity and selectivity. In Chapter 4 we present a discussion of the more important figures-of-merit and how they are used to characterize LIBS. The basic element of any LIBS measurement is the emission spectrum recorded from a single plasma. Each firing of the laser atomizes a portion of the sample in the focal volume and produces a plasma that excites and re-excites the atoms to emit light. This is then applied either to qualitative analysis as discussed in Chapter 5, or quantitative measurements as presented extensively in Chapter 6. In the former, some basic and practical methods of element and material identification are presented. In the latter, we discuss the ultimate goal, to provide a highly quantitative analysis, hence to determine with high precision and accuracy the concentration of a species in a sample or the absolute mass of a species. We treat how LIBS interacts with different forms of samples, internal standardization and matrix effects. A detailed example of measuring impurities in a lithium solution is presented.

The ability to make remote measurement in field environments is one of the principal advantages of LIBS. This application and three basic techniques for its use are treated in Chapter 7. In the first method, the laser beam is directed over an open path (through air, gas or vacuum) to the target on which a plasma is formed, and then the plasma light is collected at a distance. In the second method, the laser pulses are injected into a fiber optic and transported to the remotely located target sample, while in the third method, a compact probe containing a small laser is positioned next to the remotely located sample and the plasma light is sent back to the detection system over a fiber optic cable. We discuss subjects such as conventional stand-off analysis, the development of very long distance analysis, and details of the physics and engineering of fiber optics.

In Chapter 8 we consider the recent history from 2003 on, emphasizing the latest trends in LIBS research and applications, and focusing on what a new applier of LIBS needs to know to perform state-of-the-art LIBS experiments. Subjects reviewed include fundamentals enhanced by modeling and experiments, double pulse studies and applications to nuclear reactors and detection of biological agents. The chapter ends with a detailed review of the progress towards sending LIBS on a mission to Mars. A book on LIBS would not be complete without some speculations on the most promising directions for the future, methods of expanding LIBS applications, and factors that will speed its commercialization. These are the subjects of Chapter 9.

The appendices contain fundamental information that will be useful to the LIBS community. They include: (A) a discussion of the essentials of basic safety

considerations for LIBS operations; (B) a guide for getting a quick start in LIBS development; (C) published detection limits, as well as a unique list of element detection limits using a uniform method of analysis developed for this text, and (D) a list of major LIBS references.

Starting from fundamentals and moving through a thorough discussion of equipment, methods, and applications, we believe that the *Handbook of Laser-Induced Breakdown Spectroscopy* will provide a unique reference source that will be of value for many years for this important new analytical technique.

David Cremers  
Leon Radziemski

---

# Acronyms, Constants and Symbols

---

Item	Definition	Value, units, or comments
$\alpha(\lambda)$	absorption coefficient as a function of wavelength	/cm
AOTF	acousto-optic tunable filter	Chapter 3
APD	avalanche photodiode	a sensitive photodiode type detector
$c$	speed of light in vacuum	299 792 458 m/s
CCD	charge coupled device	two dimensional array of photodiodes, Chapter 3
COD	continuous optical discharge	
CF-LIBS	calibration-free LIBS	Chapter 8
CW	continuous wave	
CRM	certified reference material	used to calibrate LIBS, Chapter 4
$e$	electron charge	$1.60217653 \times 10^{-19}$ C
$eV$	electron volt	$1.60217653 \times 10^{-19}$ J
$\varepsilon(\lambda)$	emissivity as a function of wavelength	
$\varepsilon_0$	electric constant	$8.854187817 \times 10^{-12}$ Farads/m
f#	f-number of an optical system (e.g. lens or spectrograph)	e.g. $f\# = f/d = (\text{lens focal length}) / (\text{lens diameter})$
FOC	fiber optic cable	Chapter 3
FOM	figures-of-merit	a set of parameters to benchmark the performance of an analytical method, Chapter 4
FWHM	full-width at half maximum	width of a spectral line at the points of half maximum intensity
$\Gamma$	full-width at half maximum intensity of a spectral line	units of wavelength, wavenumber or frequency
HWHM	half-width at half maximum	half width of a spectral line at the points of half maximum intensity
$h$	Planck constant	$6.6260693 \times 10^{-34}$ J/s
$\hbar$	Planck constant/ $2\pi$	$1.0545717 \times 10^{-34}$ J/s
ICCD	intensified CCD array	Chapter 3
ICP	inductively coupled plasma	
IPDA	intensified PDA	Chapter 3
IR	infra-red	refers to a spectral region, $\lambda > 700$ nm
$k$	Boltzmann constant	$1.3806505 \times 10^{-23}$ J/K
LIBS	laser-induced breakdown spectroscopy	
LIDAR	Light detection and ranging	optical methods of remote sensing of materials in the atmosphere
LIPS	laser-induced plasma spectroscopy	
LIF	laser-induced fluorescence	alternate name for the LIBS method

---

(Continued)

Item	Definition	Value, units, or comments
LOD	limit of detection	Chapter 4
LOQ	limit of quantification	Chapter 4, LOQ = 3.3LOD, usually
LSC	laser-supported combustion	type of plasma wave, Chapter 2
LSD	laser-supported detonation	type of plasma wave, Chapter 2
LSR	laser-supported radiation	type of plasma wave, Chapter 2
LSS	laser spark spectroscopy	alternate name for the LIBS method
LTE	local thermodynamic equilibrium	Chapter 2
LTSD	lens-to-sample distance	
$\lambda$	wavelength	nm, angstroms ( $\text{\AA}$ ); 1 $\text{\AA}$ = 0.1 nm
m	electron mass	$9.1093826 \times 10^{-31}$ kg
MCP	multichannel plate	intensifier for a CCD and PDA, Chapter 3
NA	numerical aperture	
Nd:YAG	neodymium YAG laser	type of solid state laser typically used for LIBS
NIR	near IR	refers to a spectral region, $700 < \lambda < 3000$ nm
OES	optical emission spectroscopy	
PCA	principal component analysis	
PD	photodiode	solid state optical detector, Chapter 3
PDA	photodiode array	one-dimensional array of photodiodes
PMT	photomultiplier tube	optical detector
ppm	parts-per-million	concentration unit, usually stated as w/w
$\nu$	frequency	Hz
$n_e$	electron density	/cm <sup>3</sup>
R-FIBS	remote filament induced breakdown spectroscopy	Chapter 7
RSD	relative standard deviation	Chapter 4
RM	reference material	used to calibrate LIBS, Chapter 4
$\sigma$	wavenumber	/cm
s	standard deviation	Chapter 4
T	Absolute temperature	degrees Kelvin (K)
$t_b$	gate width	time period over which the plasma light is recorded
$t_d$	delay time	time period between arrival of the laser pulse at the sample to form the plasma and the start of recording of the plasma light signal
Torr	unit of pressure	
UV	ultraviolet	refers to a spectral region, $180 < \lambda < 400$ nm
VIS	visible	refers to a spectral region, $400 < \lambda < 700$ nm
VUV	vacuum ultraviolet	refers to a spectral region, $\lambda < 180$ nm
XRF	x-ray fluorescence	method of element detection

Values from P.J. Mohr and B.N. Taylor (2005). CODATA recommended values of the fundamental constants: 2002. Rev. Mod. Phys. 77: 1–108.

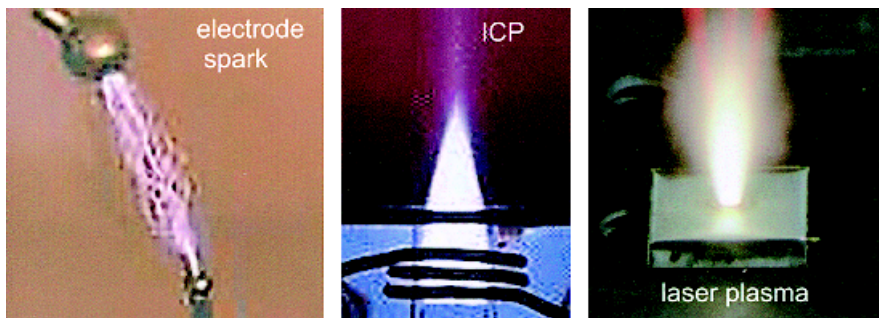


**Plate 1** Photographs of a conventional electrode spark, an inductively coupled plasma, and a laser-induced spark. The size scales are different (see Figure 1.1)

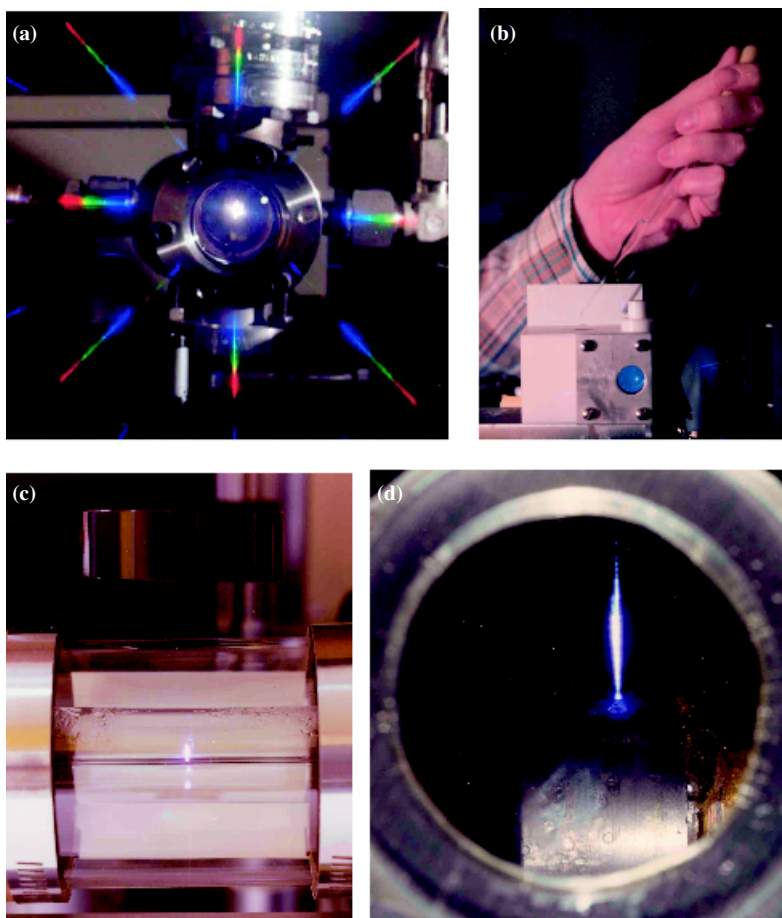


**Plate 2** The laser spark (a) in a gas, (b) in a liquid, (c) on the surface of a liquid, and (d) on a beryllium (see Figure 1.3)

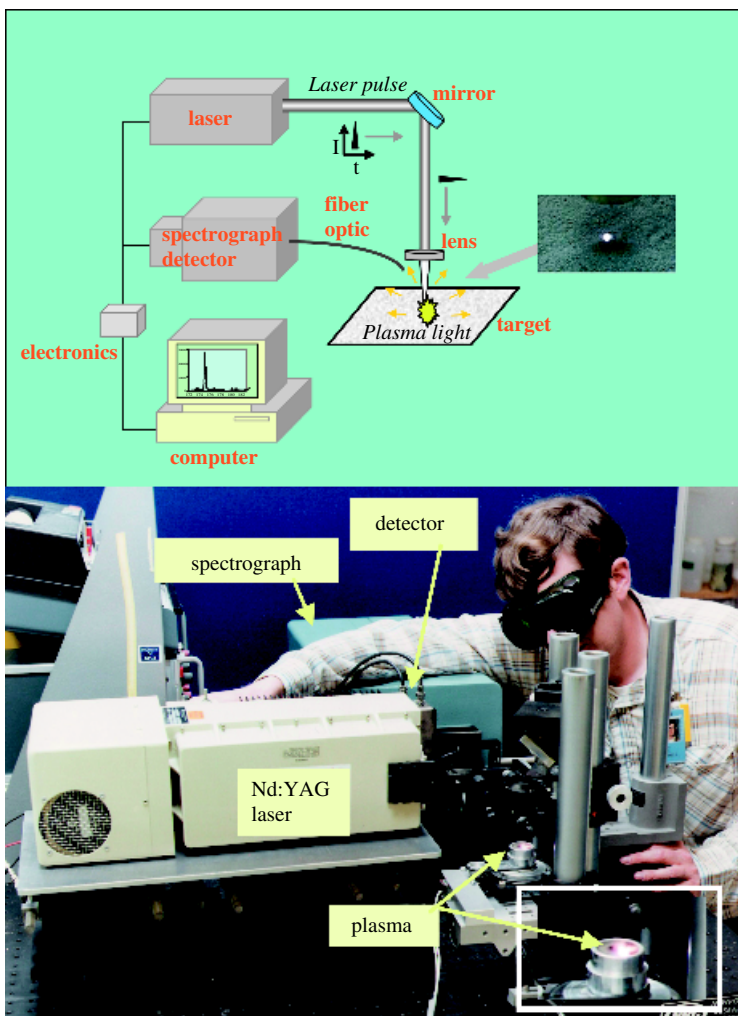


**Plate 3** Diagram of a typical LIBS set-up. The photo shows a simple LIBS set-up used to analyze material on a filter (see Figure 3.1)

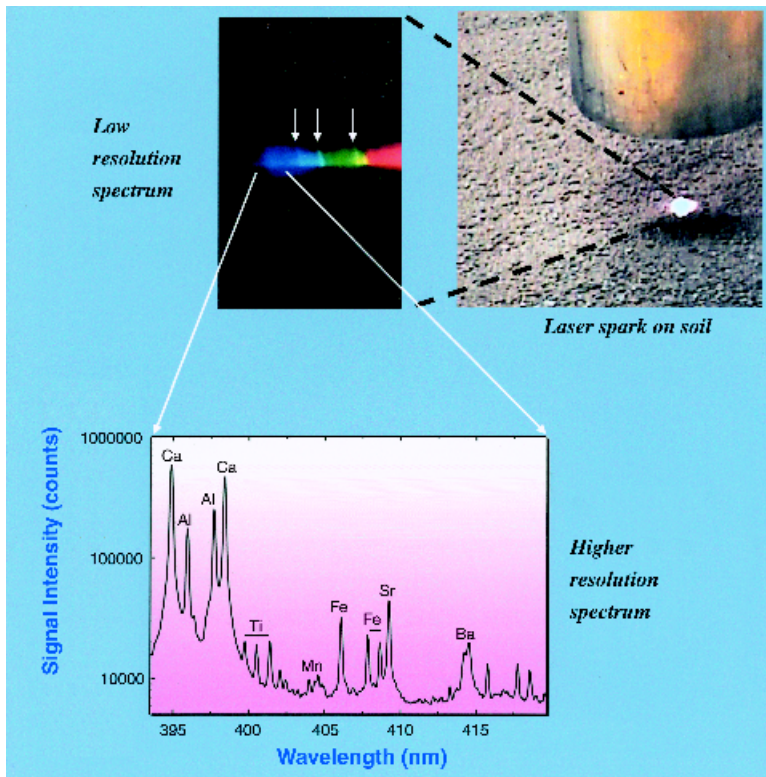


**Plate 4** LIBS spectrum produced by a simple transmission diffraction grating from the plasma formed at the right on soil. Here only strong lines of nitrogen from air are observed. Higher resolution of the spectrum shows emissions from major, minor and trace elements in the soil (see Figure 3.16)

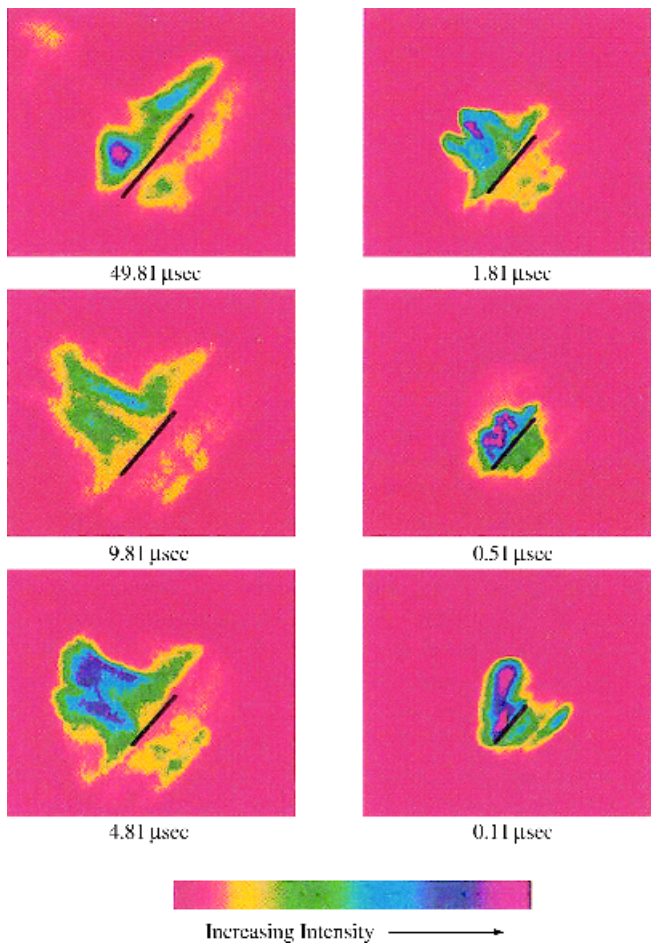


**Plate 5** Cr emission observed using the AOTF with an ICCD. (Reproduced from Multari and Cremers, Copyright 1996 IEEE) (see Figure 3.20)

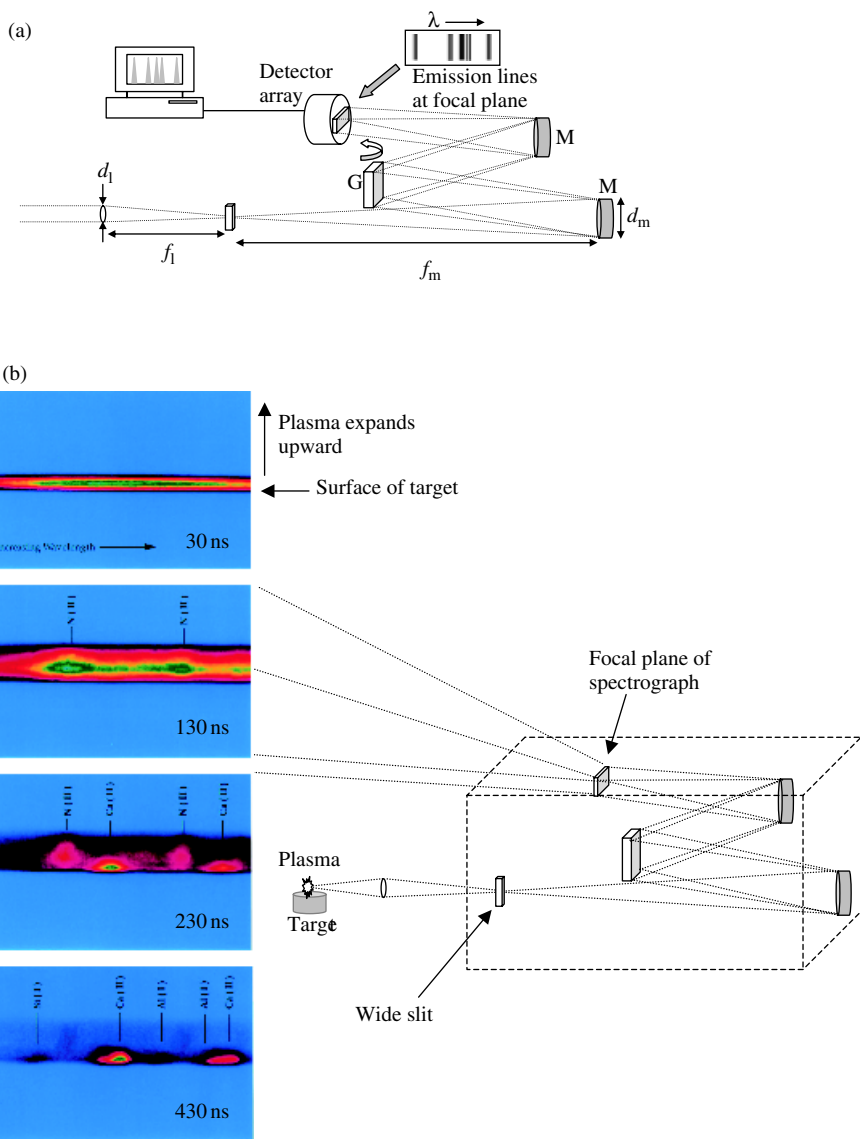


**Plate 6** (a) Detection of LIBS spectrum using a Czerny-Turner spectrograph and array detector. (b) Examples of LIBS spectra recorded at the focal plane of a spectrograph. (Multari *et al.*, 1996, with permission from Society for Applied Spectroscopy) (see Figure 3.21)

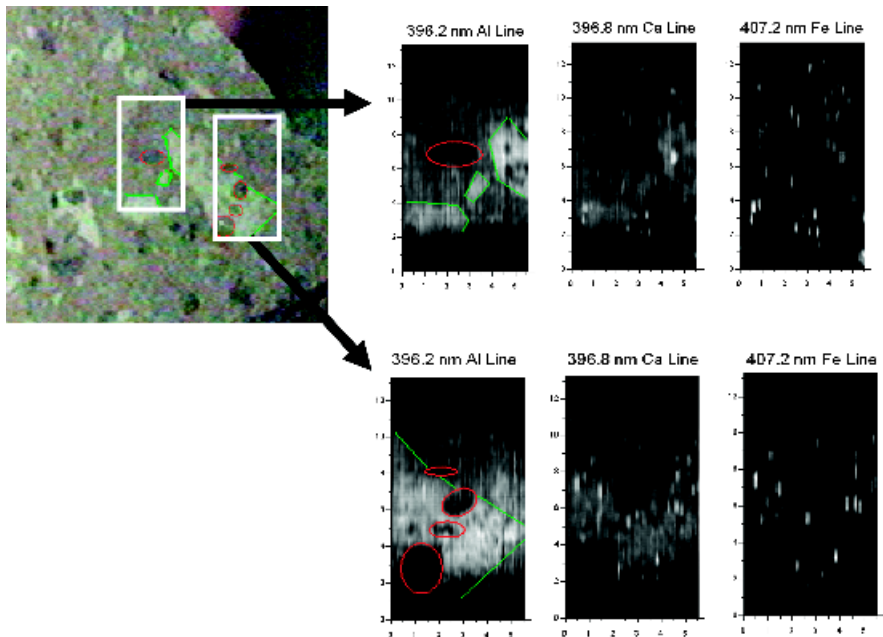


**Plate 7** Map of element emissions along a rock sample obtained by scanning a series of long sparks along the surface (see Figure 3.30)

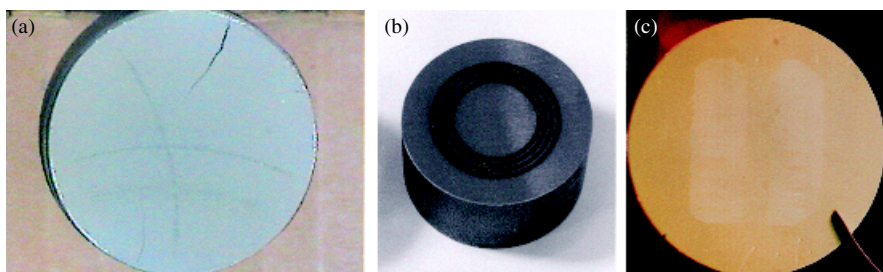


**Plate 8** Examples of some calibration samples. (a) Pressed basalt certified reference material showing the tracks produced by translating the sample under repetitive laser sparks. (b) Steel certified reference material showing concentric tracks produced by a high repetition rate laser. (Yamamoto *et al.*, 2005, with permission from Society for Applied Spectroscopy.) (c) Calibration filter containing an analyte at a certain surface concentration (e.g.  $\text{ng}/\text{cm}^2$ ). The tracks produced on the sample by scanning the filter under a series of long sparks formed on the surface are visible (see Figure 4.16)

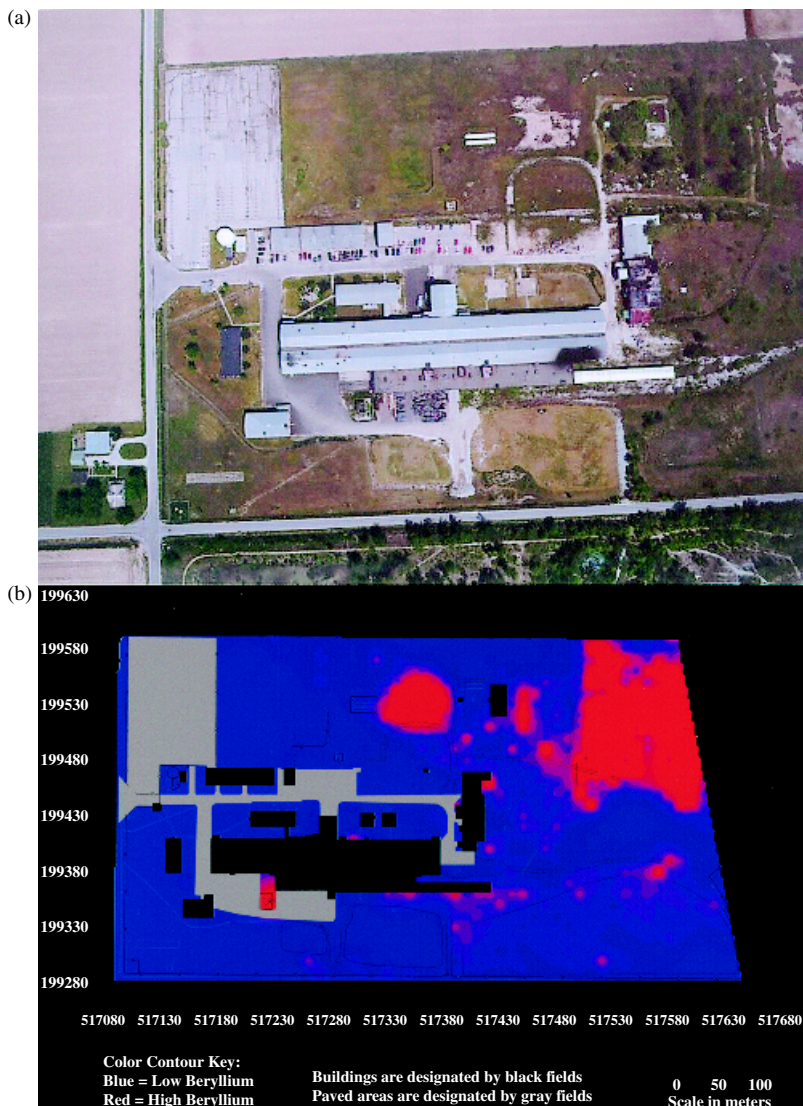


**Plate 9** (a) Aerial photo of a former beryllium facility at Luckey, Ohio, USA. (b) Map of main features and locations of high and low beryllium concentrations. (Photo and figure courtesy of Science and Engineering Associates, Inc.) (see Figure 5.23)

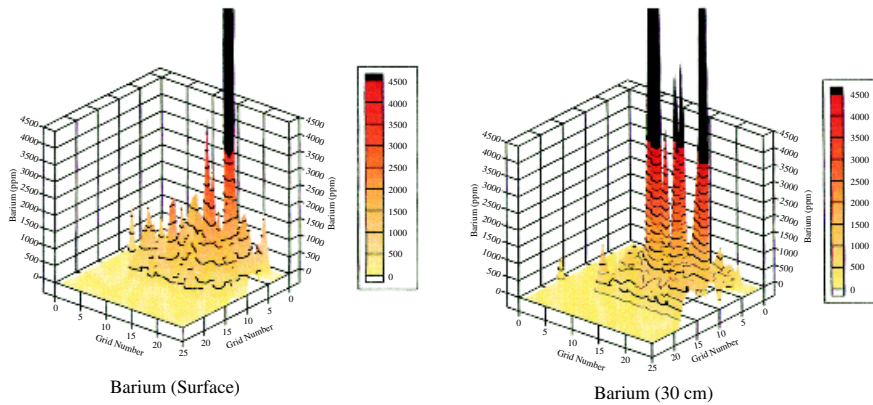


**Plate 10** Barium concentrations in soil determined using the field portable LIBS instrument of Figure 5.21(b). The grid refers to spatial position along the area of contamination with the determined concentrations plotted on the vertical axis. Each measurement required about 2 min, including sample exchange in the instrument (see Figure 5.24)

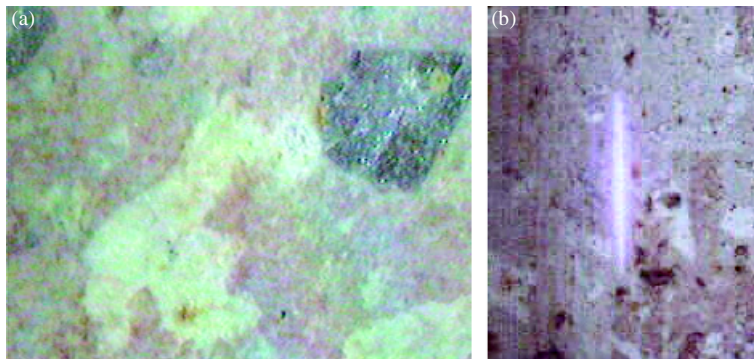


**Plate 11** (a) Close-up photo of a ground surface of a rhyolite rock sample. Distinct features are 1–2 mm in size. (b) Analysis of the same rock using a long spark (1 cm) to average over inhomogeneities (see Figure 6.7)



**Plate 12** Demonstration of stand-off LIBS using a laboratory instrument to interrogate a cliff bank. The spark is shown in the inset. The distance was 24 m between the spark and the optical system (focusing and light collection) (see Figure 7.2)

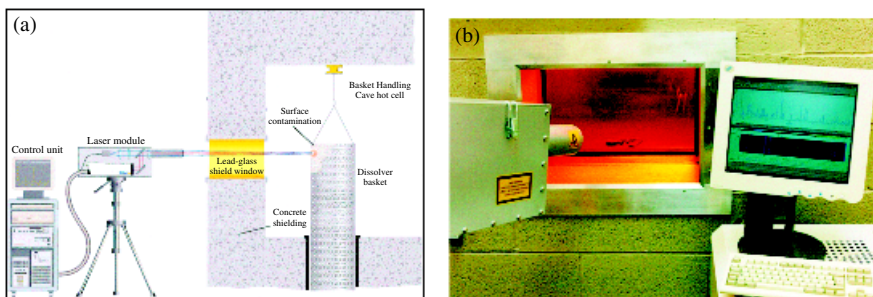


**Plate 13** (a) Schematic showing the deployment of the remote LIBS instrument to monitor surface contamination. (b) Laser beam of the instrument being directed through the lead glass shield window (Applied Photonics, 2004a. Courtesy of Applied Photonics, Ltd) (see Figure 7.7)

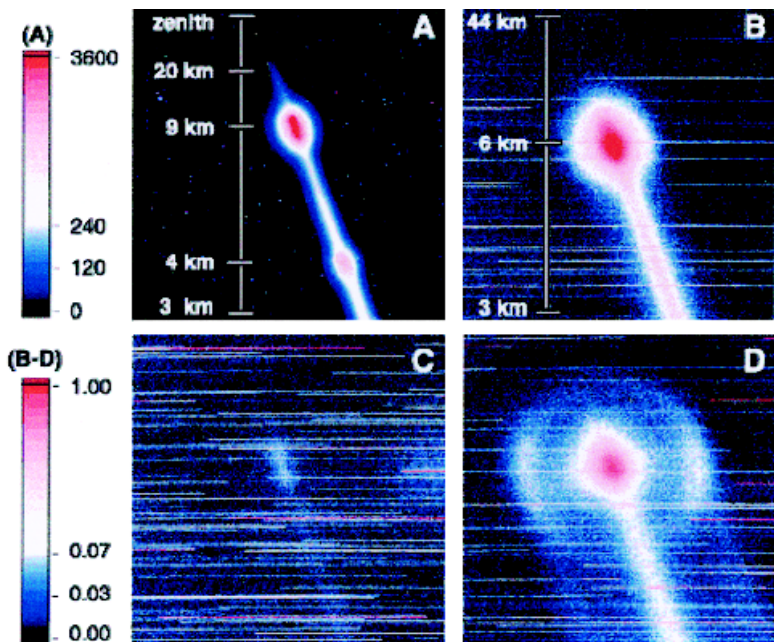


**Plate 14** CCD camera images of filaments produced by a femtosecond laser beam propagating vertically through the atmosphere. The femtosecond pulses were produced by the Teramobile. (A) Fundamental wavelength, exhibiting signals from more than 20 km and multiple-scattering halos on haze layers at 4- and 9-km altitudes. (B–D) White light (385 to 485 nm) emitted by the femtosecond laser beam. These images have the same altitude range, and their common color scale is normalized to allow direct comparison with that of (A). (Reprinted with permission from Kasparian *et al.*, 2003) (see Figure 7.10)

---

# 1 History

---

## 1.1 ATOMIC OPTICAL EMISSION SPECTROCHEMISTRY (OES)

### 1.1.1 CONVENTIONAL OES

Since the early 1800s, scientists realized that elements emitted specific colors of light. As atomic theory developed, spectroscopists learned that those colors, wavelengths or frequencies were a unique signature for each atom and ion. Hence spectra became fingerprints of the emitting atomic species. This is the basis for spectrochemical analysis using atoms.

Early sources of spectra were the sun, flames and gas discharges, such as the old Geissler tube. These were plasma sources, with varying degrees of ionization depending on the source conditions. Against the 5000 K photosphere of the sun, we see the Fraunhofer absorption lines due to neutral and once ionized species. In the solar corona highly ionized spectra are observed because of temperatures that reach into the hundreds of thousands of degrees.

Many sources have been developed for spectrochemistry, but two workhorses have been the conventional electrode spark and, more recently, the inductively coupled plasma (ICP). These are illustrated in Figure 1.1 (Plate 1), which also contains a photograph of the laser spark. The electrode spark has excitation temperatures up to 50 000 K, while the argon ICP temperature is more typically about 10 000 K. Typically they are used for laboratory analyses but occasionally are pressed into service for situations requiring more rapid data acquisition. For example, the conventional spark has been used for decades to monitor the steel making process by withdrawing a molten sample which is then solidified and transported to a laboratory located in the plant for rapid analysis. Decisions on additives are made based on these spectroscopic data.

### 1.1.2 LASER OES

As soon as the laser was developed in the early 1960s, spectrochemists began investigating its potential uses (Radziemski, 2002). An early observation was that a pulsed laser could produce a small plasma in air. The emission from that plasma

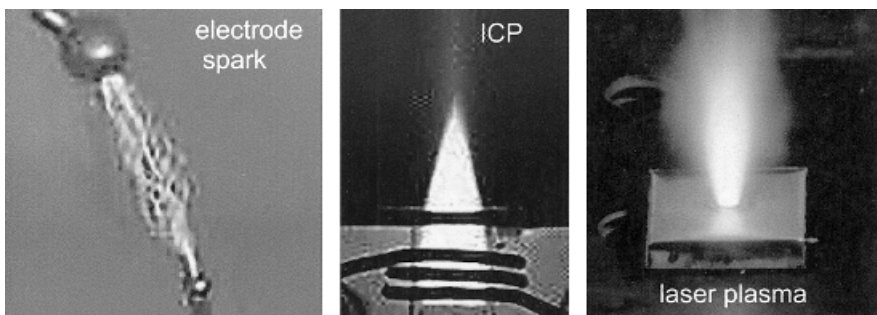


**Figure 1.1** Photographs of a conventional electrode spark, an inductively coupled plasma, and a laser-induced spark. The size scales are different (see Plate 1)

showed the potential for spectrochemical analysis. However, from 1960 to 1980 the analytical capability was so inferior to that of the conventional spark and laser technology was in its infancy, so that the technique was less favored than a related one – laser ablation into a conventional plasma source. Here the laser was used to vaporize a small amount of sample for analysis by, for example, the conventional electrode spark (Moenke and Moenke-Blankenburg, 1973). However, that was not the only way the laser could be used in spectrochemistry.

The development of tunable dye lasers meant that one could illuminate a prepared source of atoms with radiation resonant with a transition in one of the atomic species. Then either the absorption of the laser beam or the laser-induced fluorescence could be used as an analytical signal. These techniques discriminated against background and increased the signal to noise considerably by recycling the same atoms many times. Sometimes the atoms were placed in the laser cavity itself. The intra-cavity absorption technique was a very sensitive spectrochemical method, if difficult to employ generally.

Both absorption and fluorescence are used in many applications. However, because the laser needs to be tuned to a specific transition in a specific species, it is not as broadly useful as a hot plasma in which a variety of species can be excited and monitored simultaneously.

## 1.2 LASER-INDUCED BREAKDOWN SPECTROSCOPY (LIBS)

Laser-induced breakdown spectroscopy (LIBS), also sometimes called laser-induced plasma spectroscopy (LIPS) or laser spark spectroscopy (LSS) has developed rapidly as an analytical technique over the past two decades. As most commonly used and shown schematically in Figure 1.2, the technique employs a low-energy pulsed laser (typically tens to hundreds of mJ per pulse) and a focusing lens to generate a plasma that vaporizes a small amount of a sample. A portion of the plasma light is collected and a spectrometer disperses the light emitted by excited atomic and ionic species

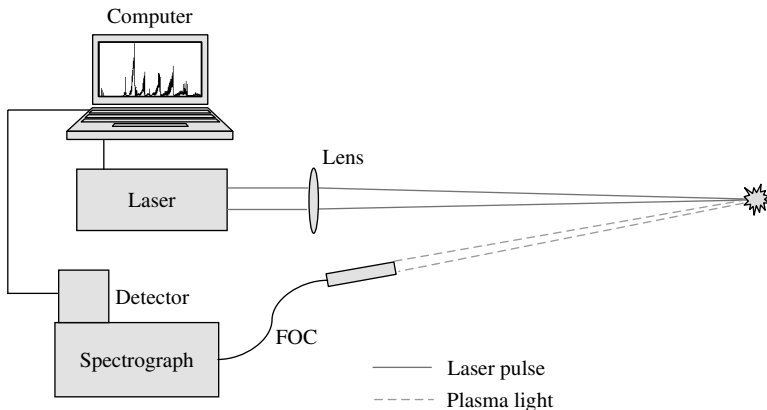


**Figure 1.2** A schematic of a simple apparatus for laser-induced breakdown spectroscopy illustrating the principal components

in the plasma, a detector records the emission signals, and electronics take over to digitize and display the results. The **book cover** shows a LIBS spectrum with certain strong spectral features standing out from the continuous background plasma light.

LIBS is an appealing technique compared with many other types of elemental analysis, because setting up an apparatus to perform a LIBS measurement is very simple. One merely focuses a laser pulse in or on a sample, which can be a gas, liquid, aerosol or solid, to form a microplasma, examples of which are shown in Figure 1.3. The spectra emitted are used to determine the sample's elemental constituents. However, the basic physical and chemical processes involved are not so simple. The initiation, formation and decay of the plasma are complex processes. Absorption of the incident laser radiation occurs through the mechanism of inverse bremsstrahlung, involving three-body collisions between photons, electrons, and atoms or molecules. In gases and liquids the plasma creates a shock wave in the surrounding medium transferring energy by means of conduction, radiation and the shock wave. When the experiment deals with a sample surface in a vacuum, the plasma and ejecta expand freely away from the surface at different speeds. Excitation of specific energy levels in different atoms is likewise complex, and depends on factors such as thermodynamic equilibrium and interactions with other atoms and molecules generally lumped under the category of matrix effects. After the laser pulse has terminated (typically within 10 ns), the plasma decays over an interval of one to several microseconds, depending on the laser energy deposited. In vacuum that temporal process is shortened. Most LIBS experiments involve repetitive plasmas with frequencies of 10 Hz or greater.

The spectra observed change as the plasma evolves temporally as shown in Figure 1.4. Soon after initiation, continuum and ionic spectra are seen. The continuum

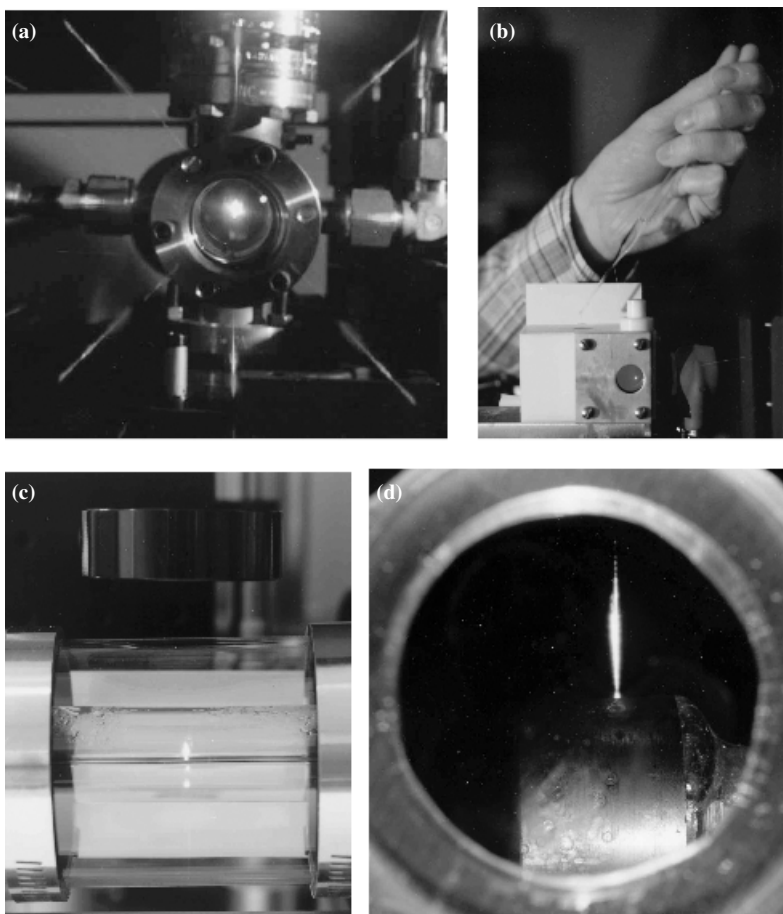


**Figure 1.3** The laser spark (a) in a gas, (b) in a liquid, (c) on the surface of a liquid, and (d) on a beryllium (see Plate 2)

is the ‘white light’ from the plasma that contains little spectroscopic information and the ions result from electrons ejected by neutral atoms. As the plasma decays, these are followed by spectra from neutral atoms and eventually simple molecules formed from the recombination of atoms. Throughout the temporal history, one observes a diminishing continuum spectral background due to recombination of free electrons with ions. Inspection of the LIBS spectrum reveals immediate qualitative information about sample composition. After calibration, quantitative information can be obtained. These issues will be treated in greater depth in subsequent chapters.

During the past 10 years, the LIBS technique has made significant progress towards becoming a viable commercial technology. Over the years many useful reviews have been published (Adrain and Watson, 1984; Cremers and Radziemski, 1987; Radziemski and Cremers, 1989; Radziemski, 1994; Lee *et al.*, 1997;

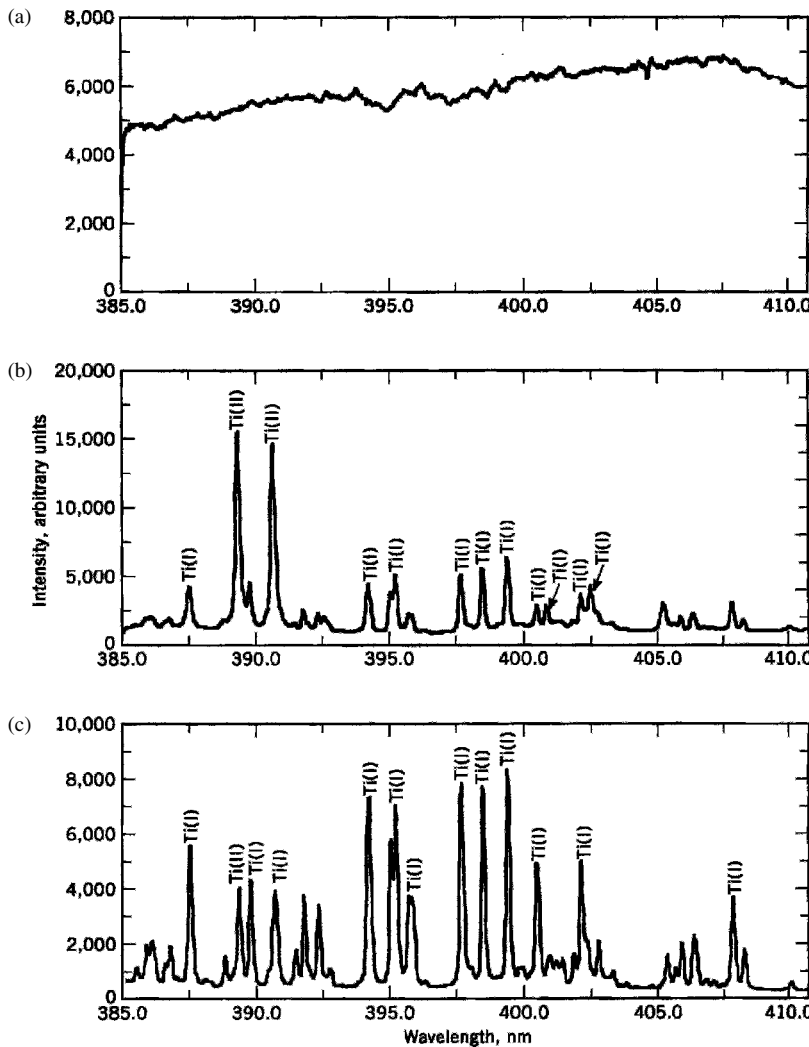


**Figure 1.4** Gated titanium spectra of a LIBS plasma illustrating the development of the spectra as a function of the time after plasma initiation. The time intervals are: (a) 0–0.5  $\mu$ s; (b) 0.5–5  $\mu$ s; and (c) 10–110  $\mu$ s

Rusak *et al.*, 1997; Tognoni *et al.*, 2002; Lee *et al.*, 2004). In this chapter we consider the history of the technique and some applications that have spurred its development. We focus on the first time an innovation or application appeared on the scene, rather than tracing every innovation through to the present day. Note however, that contemporary improvements in apparatus, techniques and fundamental understanding are driving reexaminations of old applications. Conversely, the emergence of new applications drives improvements in a recurring spiral of progress.

**Table 1.1** Significant milestones in the development of LIBS as an analytical technique applicable to a variety of samples and circumstances

---

1960	Ted Maiman develops the first pulsed laser
1963	First analytical use of a laser-plasma on surfaces, hence the birth of laser-induced breakdown spectroscopy
1963	First report of a laser plasma in a gas
1963	Laser micro-spectral analysis demonstrated, primarily with cross-excitation
1963	Laser plasmas in liquids were initially investigated
1964	Time-resolved laser plasma spectroscopy introduced
1966	Characteristics of laser-induced air sparks studied
1966	Molten metal directly analyzed with the laser spark
1970	Continuous optical discharge reported
1970	Q-switched laser use reported, results compared with normal laser pulses
1971	Biological materials investigated with LIBS
1972	Steel analysis carried out with a Q-switched laser
1978	Laser spectrochemical analysis of aerosols reported
1980	LIBS used for corrosion diagnostics in nuclear reactors
1982	Initial use of the acoustic properties of the laser-induced spark
1984	Analysis of liquid samples and hazardous aerosols demonstrated
1988	Attempts made to enhance intensities through electric and magnetic fields
1989	Metals detected in soils using laser plasma method
1992	Portable LIBS unit for monitoring surface contaminants developed
1992	Stand-off LIBS for space applications demonstrated
1993	Underwater solid analysis via dual-pulse LIBS demonstrated
1995	Demonstration of fiber optic delivery of laser pulses
1995	Multiple-pulse LIBS reported for use on steel samples
1997	LIBS use in applications in painted works of art and illuminated manuscripts
1998	Subsurface soil analysis by LIBS-based cone penetrometers shown
1998	Reports on the use of echelle spectrometers coupled with CCD detectors
1999	Trace metal accumulation in teeth observed with LIBS
1999	Pulses from different lasers used to enhance LIBS performance
1999	Calibration-free LIBS introduced
2000	Report on commercial instrument for coal analysis
2000	Demonstration of LIBS on a NASA Mars rover
2000	First International conference on LIBS – Pisa, Italy
2002	Second International Conference on LIBS – Orlando, FL
2004	Third International Conference on LIBS – Malaga, Spain
2004	LIBS approved for 2009 Mars mission

---

Table 1.1 illustrates some significant milestones in LIBS development. These will be addressed individually in the following sections.

### 1.3 LIBS HISTORY 1960–1980

Shortly after the pulsed ruby laser was invented in 1960 the laser-induced plasma was observed. The first published report mentioning the plasma was a meeting abstract by Brech and Cross in 1962 (Brech and Cross, 1962). Early on, the laser was used primarily as an ablation source with cross-excitation to provide the spectrum. In 1963, Debras-Guédon and Liodec published the first analytical

use for spectrochemical analysis of surfaces (Debras-Guédon and Liodec, 1963). Maker *et al.* in 1964 reported the first observation of optically induced breakdown in a gas (Maker *et al.*, 1964). Runge *et al.* in the same year discussed the use of a pulsed Q-switched ruby laser for direct spark excitation on metals (Runge *et al.*, 1964). Linear calibration curves were obtained for nickel and chromium in iron, with precisions of 5.3 % and 3.8 %, respectively. They also analyzed molten metal. In 1966, Evtushenko looked at the effect of sparks from two lasers (Evtushenko *et al.*, 1966). About the same time, Young *et al.* described the characteristics of laser-induced air sparks (Young *et al.*, 1966).

In the period from 1964 to 1967 the first instruments based primarily on laser-ablation with cross-excitation were developed by Zeiss (Germany), Jarrell-Ash (USA) and JEOL Ltd (Japan). Although they could be operated with the laser plasma generating the spectral emissions, most often the laser was used only for ablation followed by cross-excitation with a conventional spark. Because the auxiliary spark could contaminate and complicate the analysis through the introduction of electrode material, auxiliary excitation by electrodeless methods was also developed. The instruments could not typically compete in accuracy and precision with conventional spark spectroscopy, although they could handle nonconducting samples. Some instruments continued in use through the 1990s. An excellent discussion of those devices and the associated techniques is contained in the book entitled *Laser Micro Analysis* (Moenke-Blankenburg, 1989).

Time resolution of the decaying plasma helps to monitor the plasma evolution, to discriminate against the continuum light, and to sort out spectral features. It is especially valuable in reducing interferences between spectral features that appear at the same or adjacent wavelengths but in different temporal windows as illustrated in Figure 1.4. Different detection systems to obtain temporally resolved spectra were used in the 1960s, including a streak camera and rotating mirrors. A method more suited to modern detectors, electronically gating and averaging the signals from many plasmas, was developed by Schroeder *et al.* (Schroeder *et al.*, 1971). As detectors have developed, the preferred methods of time resolution have moved from boxcar averagers, for example, to gated, intensified charge coupled detectors. Fast photodetectors are used to record the temporal profile of plasma emissions from single pulses. An early review of the field was published by Scott and Strasheim in 1970 (Scott and Strasheim, 1970).

During this period, much of the research on the laser plasma and its uses appeared in the Russian literature. For example, Afanas'ev and Krokhin published on the vaporization of matter exposed to laser emission (Afanas'ev and Krokhin, 1967). In 1966, Raizer reported on breakdown and heating of gases under the influence of a laser beam, which was a summary of original work and a review of the state of the art (Raizer, 1966). Biberman and Norman did a thorough analysis of the origins of the continuous spectrum from the laser plasma which underlies the discrete spectral lines (Biberman and Norman, 1967). In 1974, Buravlev *et al.* commented on using a laser in spectral analysis of metals and alloys (Buravlev *et al.*, 1974). Much of the physics covered in the Russian literature was summarized in the classic book by

Raizer, *Laser-induced Discharge Phenomena*, published in English in 1977 (Raizer, 1977). Underlying that is the classic book on the physics of shock waves and high-temperature hydrodynamic phenomena, a text originally published in Russian in 1964, translated into English in 1966, and recently reprinted (Zel'dovich and Raizer, 2002).

Early on it was recognized that physical and chemical matrix effects would have to be dealt with if LIBS was to develop as a quantitative method. Cerrai and Trucco discussed matrix effects in laser-sampled spectrochemical analysis (Cerrai and Trucco, 1968). They focused on the dependence of spectral line intensities on physical conditions such as grain sizes and boundaries. This was followed by a paper by Marich *et al.* concluding that physical effects were more important than chemical ones (Marich *et al.*, 1970). However others, like Scott and Strasheim, found signal suppression due to various effects linked to the components of the matrix (Scott and Strasheim, 1970). It is now accepted that a variety of physical and chemical effects play important roles in signal strength, and repeatability.

Biological media with metallic contamination were investigated by the laser plasma as reported in papers by Marich *et al.* and Treytl *et al.* (Marich *et al.*, 1970; Treytl *et al.*, 1972). The former deals with the effect of the matrix on the spectral emission from a variety of samples, including human serum and liver. The latter provides detection limits for the analysis of metals in biological materials. Metals in the form of reagent grade salts were incorporated into gelatin or albumin matrices. Limits of detection ranged from  $2 \times 10^{-15}$  gm for magnesium and copper to  $3 \times 10^{-13}$  gm for mercury and iron.

A novel variation of the pulsed plasma is the continuous optical discharge (COD). In this case a continuous wave (CW) laser beam is focused to sustain a plasma as long as the laser remains on. The laser is usually of the continuous CO<sub>2</sub> variety. Initiation requires another pulsed laser or a conventional spark. Early papers on this subject were published by Generalov, and Keefer (Generalov *et al.*, 1970; Keefer, 1974). Spectrochemical analysis by the COD was investigated by Cremers *et al.* (Cremers *et al.*, 1985).

Materials processes such as welding were obvious applications of high powered lasers. The plasma literature in that field overlapped with that of spectrochemical applications. In the first of a series of books, Ready (Ready, 1971) provided an overview of the variety of phenomena induced by high power laser pulses. Some of the subjects discussed were: optical damage of materials; the interaction between laser radiation and surfaces resulting in ablation, melting, and crater formation; the effect of laser light on biological systems; and optically induced gas breakdown. The most recent version edited by Ready is a compendium of 30 years of research, the *LIA Handbook of Laser Materials Processing* (Ready, 2001).

Generating a plasma in water was considered first by Buzukov *et al.* (Buzukov *et al.*, 1969). Lauterborn (Lauterborn, 1972) conducted high-speed photography of plasmas in liquids. This was followed by measurements of shock waves and cavities caused by laser-induced breakdown in water, glycerin, and benzene by Teslenko (Teslenko, 1977). These mechanistic studies focusing on the shock wave formation and propagation continued throughout the 1970s.

In the mid to late 1970s aerosols became a subject of research. The effects of dust and particles in the beam as they influenced breakdown were studied by Lencioni (Lencioni, 1973). He found that when long focal-length lenses were used, dust in the beam initiated strings of mini-plasmas. Belyaev *et al.* discussed laser spectrochemical analysis of aerosols in a 1978 publication (Belyaev *et al.*, 1978). In 1979 Edwards and Fleck Jr published on the two-dimensional modeling of aerosol breakdown in air (Edwards and Fleck Jr, 1979). This was followed by a study in 1982 by Ivanov and Kopytin on selective interaction of a train of laser pulses with an aerosol medium (Ivanov and Kopytin, 1982).

A spin-off method of LIBS called TABLASER was described by Measures and Kwong starting in 1979 (Measures and Kwong, 1979). That technique uses an ablation laser pulse followed by a laser pulse through the plume. The second pulse from a dye laser is tuned to a transition in the element of interest and results in laser-induced fluorescence. Interest in this type of arrangement surfaced again in the 1990s.

## 1.4 LIBS HISTORY 1980–1990

As lasers and other LIBS components became smaller and the *in situ* advantages of the laser plasma became more obvious, additional applications appeared. Interest at Los Alamos National Laboratory was kindled by two 1981 papers on the time-integrated (Loree and Radziemski, 1981) and time-resolved (Radziemski and Loree, 1981) forms of the technique in gases. The term LIBS was originally used in the former 1981 paper, and TRELIBS, identified with the time-resolved version, in the latter. Currently LIBS is the term used for either method.

Los Alamos then funded an internal study of the use of this technique for detection of toxic beryllium dust, resulting in papers on detecting beryllium in air (Radziemski *et al.*, 1983a) and on filters (Cremers and Radziemski, 1985). Figure 1.5 shows a long spark created by using a cylindrical lens, on a rotating stage on which a blackened piece of filter paper has been set for contrast. During that period, Los Alamos scientists studied the detection of hazardous gases (Cremers and Radziemski, 1983), aerosols (Radziemski *et al.*, 1983b), and liquids (Cremers *et al.*, 1984; Wachter and Cremers, 1987). Sensing of steels and other metals in molten or solid forms were also investigated (Cremers, 1987).

Some research focused on diagnostics and enhancements. The plasma generates shock waves that can be heard and recorded as acoustic signals, whose strengths are related to the energy deposited in the medium. The acoustic properties of the spark were first studied by Belyaev *et al.* (Belyaev *et al.*, 1982). Kitamori (Kitamori *et al.*, 1988) started an interesting line of research in particle counting in liquids by using the acoustic effect produced by the plasma. He also made observations of the optical emission. Beginning with the early 1990s, more quantitative uses of acoustic signals were reported, for example by Diaci and Mozina (Diaci and Mozina, 1992), who studied the blast waveforms detected simultaneously by a microphone and a



**Figure 1.5** A long spark created by using a cylindrical lens, on a filter set on a rotating stage

laser probe. Starting in 1988, there were several reports of attempts to enhance the plasma by the use of auxiliary magnetic or electric fields. None have reported dramatic success.

Much interest was shown in the initiation of the spark on single microspheres or droplets. Results included a paper by Chylek *et al.* (1986), on the effect of size and material of liquid spherical particles on laser-induced breakdown. This line of research was continued in a paper by Biswas *et al.* (1988) detailing the irradiance and laser wavelength dependence of plasma spectra from single levitated aerosol droplets. Chang *et al.* (1988) discussed laser-induced breakdown in large transparent water droplets.

In the late 1980s interest increased in making LIBS more quantitative by addressing the factors such as differential excitation. These included many works from the Niemax group in Dortmund (Ko *et al.*, 1989; Leis *et al.*, 1989). In the study by Ko *et al.* the stability of internal standardization was investigated. They found that the chromium to iron intensities in binary mixtures were not a function of time after plasma initiation, hence temperature, or completeness of vaporization. This was in contrast to zinc to copper ratios in brass. The conclusion was that internal standardization was not a given in all cases, but the conditions for its use needed to be established for each situation. In the study by Leis *et al.*, the atomization and propagation properties of the plasma plume were investigated.

Studies of toxic and superconducting materials were made. These included analysis of beryllium in beryllium-copper alloys (Millard *et al.*, 1986) and detection of cadmium, lead and zinc (Essien *et al.*, 1988). The superconducting materials community published many papers on laser ablation for deposition of superconducting thin films, and sometimes addressed the optical emission as a diagnostic

technique for process monitoring. A method of monitoring corrosion in the core regions of nuclear reactors was detailed by Adrain (Adrain, 1982) and a working system was described.

At the close of the decade, a book edited by Radziemski and Cremers, *Laser-induced Plasmas and Applications*, summarized the relevant physics, chemistry and applications at that time (Radziemski and Cremers, 1989). It contained detailed chapters updating the physics of breakdown and post-breakdown phenomena, and an updated review of the technique.

## 1.5 LIBS HISTORY 1990–2000

As the field proceeded into the 1990s, applications and fundamental studies developed rapidly. There were several useful reviews during this decade (Radziemski, 1994; Song *et al.*, 1997; Rusak *et al.*, 1998). Hou and Jones (Hou and Jones, 2000) reviewed several techniques with field capability and presented the advantages and disadvantages of each.

More research groups surfaced in the US and in other countries. In Australia, Grant *et al.* provided detection limits for minor components in iron ore (Grant *et al.*, 1991). This was done with a view to developing a field-based technique. Later Chadwick's group in Australia analyzed lignite and produced a commercial instrument for coal analysis (Wallis *et al.*, 2000). Sabsabi and Cielo (Canada) started publishing their work on aluminum alloy targets with papers in 1992 and 1995 (Sabsabi and Cielo, 1992, 1995). Palleschi's group in Pisa, Italy began addressing applications with respect to pollutant detection such as the paper by Lazzari *et al.* on the detection of mercury in air (Lazzari *et al.*, 1994).

The application of LIBS to remote analysis, begun in the 1980s, developed rapidly in the 1990s. It was an important area of investigation by Cremers' group at Los Alamos. Cremers *et al.* (Cremers *et al.*, 1995) discussed remote elemental analysis by laser-induced breakdown spectroscopy using a fiber optic cable. Angel's group also published on the use of a fiber optic probe to determine lead in paint (Marquardt *et al.*, 1996). LIBS for the analysis of lunar surfaces was first mentioned in papers by Blacic *et al.* and Kane *et al.* (Blacic *et al.*, 1992; Kane *et al.*, 1992). This was followed by a seminal paper by Knight *et al.* (Knight *et al.*, 2000) on characterization of LIBS for planetary exploration, and a report on the use of LIBS on a prototype Martian rover (Wiens *et al.*, 2002). Figure 1.6 shows a K9 rover with the LIBS sensor unit on the mast.

Efforts to make LIBS more quantitative continued. Davies *et al.* (Davies *et al.*, 1996) reported on relevant factors for *in situ* analytical spectroscopy in the nuclear industry. Russo's group at Lawrence Berkeley Laboratory undertook detailed studies of the ablation process as reported by Mao *et al.* (Mao *et al.*, 1995). Winefordner's group at the University of Florida initiated studies of the variables influencing the precision of LIBS measurements. Their first publication in this area was by Castle *et al.* (Castle *et al.*, 1998) where a variety of factors were considered and inter- and



**Figure 1.6** The K9 rover in the field with the LIBS sensor mounted on the right side of the mast head instrument suite. (Photo courtesy of NASA Ames Research Center)

intra-shot measurement precisions were calculated. The best precision obtained was 0.03 %. Gornushkin *et al.* reported on a curve of growth methodology applied to laser-induced plasma emission spectroscopy (Gornushkin *et al.*, 1999). A procedure called ‘calibration-free LIBS’ (CF-LIBS) was developed in Palleschi’s group, as explained in a paper by Ciucci *et al.* (Ciucci *et al.*, 1999). In effect, one assumes thermodynamic equilibrium, and uses spectral lines representing the bulk of the vaporized material, to deduce the concentration of the element of interest. Matrix effects continued to be studied. For example, the effects of water content and grain size were reported by Wisbrun *et al.* (Wisbrun *et al.*, 1994). These works and others have sharpened the focus on factors that can enhance or hinder the ability to obtain quantitative results.

Throughout the decade unique applications continued to emerge. Harith *et al.* studied the hydrodynamic evolution of laser driven diverging shock waves (Harith *et al.*, 1990). Quantitative simultaneous elemental determinations in alloys, using LIBS in an ultra-high-vacuum, was reported by Theim *et al.* (Theim *et al.*, 1994). The US Army Aberdeen Proving Ground laboratory under Mizolek began its investigations of LIBS with two publications by Simeonsson and Mizolek (Simeonsson and Mizolek, 1993, 1994). They studied LIBS in carbon monoxide, carbon dioxide, methanol and chloroform, and used a variety of laser wavelengths

from 193 to 1064 nm. The group of Aragón, Aguilera and Campos (Aragón *et al.*, 1993) applied LIBS to determining carbon content in molten steel. Poulain and Alexander (Poulain and Alexander, 1995) used LIBS to measure the salt concentration in seawater aerosol droplets. Singh's group published on quantification of metal hydrides (Singh *et al.*, 1996) and LIBS spectra from a coal-fired MHD facility (Zhang *et al.*, 1995).

Art analysis has received much attention, for example as described by Anglos *et al.* (Anglos *et al.*, 1997), who worked on diagnostics of painted artworks using LIBS for pigment identification, and Georgiou *et al.* (Georgiou *et al.*, 1998), who described excimer laser restoration of painted artworks. Vadillo and Laserna published work on depth-resolved analysis of multilayered samples, a technique that is used in forensic archeometry (Vadillo and Laserna, 1997). Applications to biological materials were developed. Samek *et al.* studied trace metal accumulation in teeth (Samek *et al.*, 1999). Pallikaris *et al.* (Pallikaris *et al.*, 1998) reported on the use of LIBS for monitoring corneal hydration, while Sattmann *et al.* started work on polymer identification that resulted in an apparatus to sort plastics (Sattmann *et al.*, 1998).

Determination of the composition of soils and contaminants received considerable attention. Eppler *et al.* (Eppler *et al.*, 1996) reported on matrix effects in the detection of Pb and Ba in soil. Detection limits of 57 and 42 ppm (w/w) for Pb and Ba, respectively, were achieved. A cylindrical focusing lens yielded higher experimental precision than a spherical lens. Miles and Cortes performed subsurface heavy-metal detection with the use of a cone penetrometer system (Miles and Cortes, 1998). A real-time fiber-optic LIBS probe for the *in situ* detection of metals in soils was used by Theriault *et al.* (Theriault *et al.*, 1998).

Much work was directed to improvement in instrumentation and techniques. Undoubtedly the greatest impact was achieved by the introduction of the compact echelle spectrometer mated with the ever-more capable CCD detectors, intensified or not. A good introduction to these subjects can be found in Vadillo *et al.* (Vadillo *et al.*, 1996), who reported on space and time-resolved LIBS using CCD detection. Also Barnard *et al.* (Barnard *et al.*, 1993) commented on the design and evaluation of echelle grating optic systems for ICP-OES, and Harnley and Fields (Harnley and Fields, 1997) wrote on solid-state array detectors for analytical spectrometry. Bauer *et al.* described an echelle spectrometer and intensified CCD combination (Bauer *et al.*, 1998).

Diode lasers may be sources of the future because of their small size and simplicity of operation. An introduction to the subject for laser spectrochemistry was given by Lawrenz and Niemax (Lawrenz and Niemax, 1989). A passively Q-switched Nd:YAG microchip laser was described by Zayhowski (Zayhowski, 2000). The laser was 1 to 2 mm on a side and was diode pumped. Peak powers approaching 0.5 MW were reported.

As lasers with new parameters became available they were put to use on LIBS applications. The result of 60 ps Nd:YAG 532 nm pulses was reported by Davis *et al.* (Davis *et al.*, 1993). Kagawa *et al.* (Kagawa *et al.*, 1994) wrote on XeCl excimer laser-induced shock wave plasmas and applications to emission

spectrochemical analysis. Sattman *et al.* (Sattman *et al.*, 1995) discussed analysis of steel samples using multiple Q-switched Nd:YAG laser pulses. Lasers with pulses of different lengths were used and their results compared. Femtosecond, picosecond, and nanosecond laser ablation of solids was discussed by Chikov *et al.* (Chikov *et al.*, 1996). Fedosejevs' femtosecond LIBS group has focused on laser pulses of hundreds of microjoules, dubbed ‘microlibs,’ as reported by Rieger *et al.* (Rieger *et al.*, 2000). Microline imaging was discussed by Mateo *et al.* in Laserna’s group (Mateo *et al.*, 2000). Angel *et al.* reported on using dual pulses and pulses of 1.3 ps and 140 fs (Angel *et al.*, 2001). Both show very low background signals, so time resolution is not necessary; however the low signal levels dictate a higher repetition rate and adequate summing of spectra.

Later in the 1990s the applications turned to very practical problems, such as monitoring environmental contamination, control of materials processing, sorting of materials to put them in proper scrap bins, and slurry monitoring. Barrette and Turmel (Barrette and Turmel, 2000) used LIBS for on-line iron-ore slurry monitoring for real-time process control. Buckley *et al.* (Buckley *et al.*, 2000) implemented LIBS as a continuous emissions monitor for toxic metals. Palanco and Laserna (Palanco and Laserna 2000) studied the full automation of a laser-induced breakdown spectrometer for quality assessment in the steel industry with sample handling, surface preparation, and quantitative analysis capabilities. St-Onge and Sabsabi (St-Onge and Sabsabi, 2000) published on quantitative depth-profile analysis using LIPS on galvannealed coatings on steel. Laser ablation continues as an active area, and is well summarized in a review by Russo *et al.* (Russo *et al.*, 2002).

An emphasis on developing rugged, moveable instrumentation emerged at this time. Optical fibers were built into LIBS systems, primarily for carrying the spark light to the spectrometer, but also for the delivery of the laser pulse as well. More compact echelle spectrographs have been developed. An instrument the size of a small suitcase, used for analysis of contaminants in soils and lead in paint, was made



**Figure 1.7** A portable LIBS surface analyzer, circa 1998

in Cremers' Los Alamos laboratory as reported by Yamamoto *et al.* (Yamamoto *et al.*, 1996). A later version of this unit is shown in Figure 1.7. Capability and compactness have improved since that time. The maturity of LIBS was demonstrated by its recent adoption for use in planetary geology on a 2009 mission to Mars.

## 1.6 ACTIVE AREAS OF INVESTIGATION, 2000–2002

As we entered the new millennium, international meetings in Pisa, Italy (Corsi *et al.*, 2001), Cairo, Egypt (Harith *et al.*, 2002), Orlando, FL, USA (Hahn *et al.*, 2003), Crete (Anglos and Harith, 2004) and Spain (Laserna, 2005) provided excellent summaries of the current status of LIBS applications. New areas of study include increasing exploration of the vacuum ultraviolet region of the spectrum. Biological applications on human teeth, bones and tissue are becoming more common. Pollen, spores and bacteria are being studied to see if unique signatures can be determined. Homeland security applications are proliferating. Surface mapping and imaging modes using line sparks are proving useful to determine surface compositional variations. Sophisticated statistical techniques are being applied to extract signals and reliability factors. New papers are appearing in relevant journals every month. The growth of publications involving LIBS through 2002 is illustrated in Figure 1.8. LIBS instruments are being marketed, especially for materials analysis and toxic materials identification. Because LIBS is the most versatile analytical method yet developed, many applications studied in the earlier LIBS periods have resurfaced because of increased needs or improved instrumental capabilities. Likewise patents

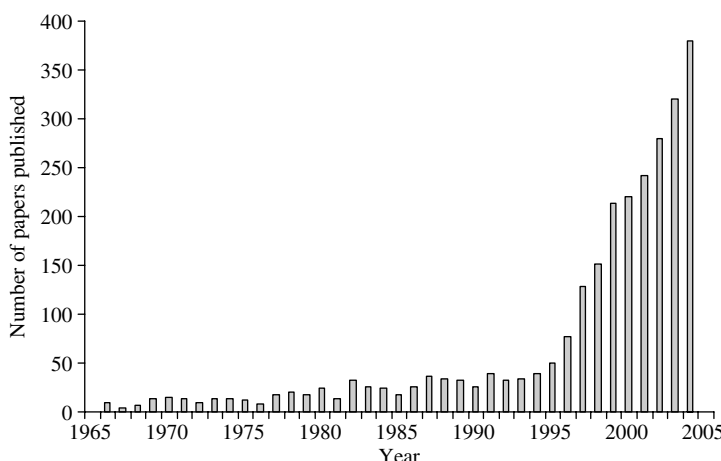


**Figure 1.8** LIBS papers per year, 1966–2005. In the last 5 years, about 1140 papers have been published relating to LIBS. (Courtesy of M. Sabsabi)

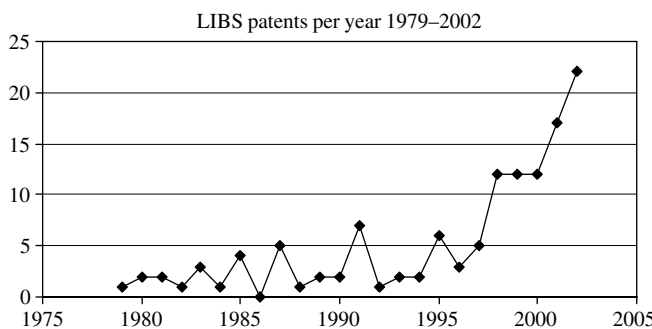


**Figure 1.9** LIBS patents per year, 1979–2002. (Courtesy of M. Sabsabi)

involving LIBS are proliferating rapidly, as illustrated in Figure 1.9. All this points to the fact that interest in LIBS as an analytical technique is increasing, a trend which we believe will continue in the coming years.

## REFERENCES

- Adrain, R.S. (1982). Some industrial uses of laser induced plasmas. Ch. 7 in *Industrial Applications of Lasers*, ed. H. Koebner, John Wiley & Sons, Inc., New York: 135–176.
- Adrain, R.S. and J. Watson (1984). Laser microspectral analysis: a review of principles and applications. *J. Appl. Phys.* 51: 1915–1940.
- Afanas'ev, V. Yu and O.N. Krokhin (1967). Vaporization of matter exposed to laser emission. *Soviet Physics JETP* 25: 639–645.
- Angel, S.M., D.N. Stratidis, K.L. Eland, T. Lai, M.A. Berg and D.M. Gold (2001). LIBS using dual- and ultra-short laser pulses. *Fresenius J. Anal. Chem.* 369: 320–327.
- Anglos, D., S. Couris and C. Fotakis (1997). Artworks: laser-induced breakdown spectroscopy in pigment identification. *Appl. Spectrosc.* 51: 1025–1030.
- Anglos, D. and M.A. Harith (2004). 2nd Euro-Mediterranean symposium on laser induced breakdown spectroscopy (EMSLIBS-II). *J. Anal. At. Spectrom.* 19: 10N–11N.
- Aragón, C., J.A. Aguilera and J. Campos (1993). Determination of carbon content in molten steel using laser-induced breakdown spectroscopy. *Appl. Spectrosc.* 47: 606–608.
- Barnard, T.W., M.J. Crockett, J.C. Ivaldi and P.L. Lundberg (1993). Design and evaluation of an echelle grating optical system for ICP-OES. *Anal. Chem.* 65: 1225–1230.
- Barrette, L. and S. Turmel (2000). On-line iron-ore slurry monitoring for real-time process control of pellet making processes using laser-induced breakdown spectroscopy: graphite vs total carbon detection. *Spectrochim. Acta Part B* 56: 715–724.
- Bauer, H.E., F. Leis and K. Niemax (1998). Laser induced breakdown spectrometry with an echelle spectrometer and intensified charge coupled device detection. *Spectrochim. Acta Part B* 53: 1815–1825.
- Belyaev, E.B., A.P. Godlevskii and Y.D. Kopytin (1978). Laser spectrochemical analysis of aerosols. *Sov. J. Quant. Electro.* 8: 1459–1463.
- Belyaev, E. B., *et al.* (1982). Nature of the acoustic emission during laser breakdown of gaseous disperse systems. *Sov. Tech. Phys. Lett.* 8: 144–147.
- Biberman, L.M. and G.E. Norman (1967). Continuous spectra of atomic gases and plasma. *Sov. Phys. Uspekhi* 10: 52–54.

- Biswas, A., H. Latifi, L.J. Radziemski and R.L. Armstrong (1988). Irradiance and laser wavelength dependence of plasma spectra from single levitated aerosol droplets. *Appl. Opt.* 27: 2386–2391.
- Blacic, J.D., D.R. Pettit and D.A. Cremers (1992). Laser-induced breakdown spectroscopy for remote elemental analysis of planetary surfaces. Proceedings of the International Symposium on Spectral Sensing Research, Maui, HI.
- Brech, F. and L. Cross (1962). Optical microemission stimulated by a ruby laser. *Appl. Spectrosc.* 16: 59.
- Buckley, S.G., H.A. Johnsen, K.K.R. Hencken and D.W. Hahn (2000). Implementation of laser-induced breakdown spectroscopy as a continuous emissions monitor for toxic metals. *Waste Manage.* 20: 455–462.
- Buravlev, Yu. M., B.P. Nadezhda and L.N. Babanskaya (1974). Use of a laser in spectral analysis of metals and alloys. *Zavodskaya劳ratoriya* 40: 165–171.
- Buzukov, A.A., Y.A. Popov and V.S. Teslenko (1969). Experimental study of explosion caused by focusing monopulse laser radiation in water. *Zhurnal Prikladnoi Mekhaniki i Tekhnicheskoi Fiziki* 10: 17–22.
- Castle, B.C., K. Talabardon, B.W. Smith and J.D. Winefordner (1998). Variables influencing the precision of laser-induced breakdown spectroscopy measurements. *Appl. Spectrosc.* 52: 649–657.
- Cerrai, E. and R. Trucco (1968). On the matrix effect in laser sampled spectrochemical analysis. *Energia Nucleare* 15: 581–585.
- Chang, R.K., J.H. Eickmans, W.-F. Hsieh, C.F. Wood, J.-Z. Zhang and J.-B. Zheng (1988). Laser-induced breakdown in large transparent water droplets. *Appl. Opt.* 27: 2377–2385.
- Chikov, B.N., C. Momma, S. Nolte, F. von Alvensleben and A. Tünnerman (1996). Femtosecond, picosecond, and nanosecond laser ablation of solids. *Appl. Phys. A* 63: 109–115.
- Chylek, P., M.A. Jarzembski, N.Y. Chou and R.G. Pinnick (1986). Effect of size and material of liquid spherical particles on laser-induced breakdown. *Appl. Phys. Lett.* 49: 1475–1477.
- Cucci, A., M. Corsi, V. Palleschi, S. Ratelli, A. Salvetti and E. Tognoni (1999). New procedure for quantitative elemental analysis by laser-induced plasma spectroscopy. *Appl. Spectrosc.* 53: 960–964.
- Corsi, M., V. Palleschi and E. Tognoni (Eds) (2001). Special Issue, 1st International Conference on Laser Induced Plasma Spectroscopy. *Spectrochim. Acta Part B* 50: 565–1034.
- Cremers, D.A. and L.J. Radziemski (1983). Detection of chlorine and fluorine in air by laser-induced breakdown spectrometry. *Anal. Chem.* 55: 1252–1256.
- Cremers, D.A., L.J. Radziemski and T.R. Loree (1984). Spectrochemical analysis of liquids using the laser spark. *Appl. Spectrosc.* 38: 721–726.
- Cremers, D.A. and L.J. Radziemski (1985). Direct detection of beryllium on filters using the laser spark. *Appl. Spectrosc.* 39: 57–60.
- Cremers, D.A., F.L. Archuleta and R.J. Martinez (1985). Evaluation of the continuous optical discharge for spectrochemical analysis. *Spectrochim. Acta Part B* 40: 665–679.
- Cremers, D.A. (1987). The analysis of metals at a distance using laser-induced breakdown spectroscopy. *Appl. Spectrosc.* 41: 572–578.
- Cremers, D.A. and L.J. Radziemski (1987). Laser plasmas for chemical analysis. Ch. 5 in *Laser Spectroscopy and its Applications*, eds L.J. Radziemski, R.W. Solarz and J.A. Paisner, Marcel Dekker, New York: 351–415.
- Cremers, D.A., J.E. Barefield and A.C. Koskelo (1995). Remote elemental analysis by laser-induced breakdown spectroscopy using a fiberoptic cable. *Appl. Spectrosc.* 49: 857–860.
- Davies, C.M., H.H. Telle and A.W. Williams (1996). Remote in situ analytical spectroscopy and its applications in the nuclear industry. *Fresenius J. Anal. Chem.* 355: 895–899.

- Davis, L.M., L.-Q. Li and D.R. Keefer (1993). Picosecond resolved evolution of laser breakdown in gases. *J. Phys. D: Appl. Phys.* 26: 222–230.
- Debras-Guédon, J. and N. Liodec (1963). De l'utilisation du faisceau d'un amplificateur à ondes lumineuses par émission induite de rayonnement (laser à rubis), comme source énergétique pour l'excitation des spectres d'émission des éléments. *C.R. Acad. Sci.* 257: 3336–3339.
- Diaci, J. and J. Mozina (1992). A study of blast waveforms detected simultaneously by a microphone and a laser probe during laser ablation. *Appl. Phys. A* 55: 352–358.
- Edwards, A.L. and J.A. Fleck Jr (1979). Two-dimensional modeling of aerosol-induced breakdown in air. *J. Appl. Phys.* 50: 4307–4313.
- Eppler, A.S., D.A. Cremers, D.D. Hickmott, M.J. Ferris and A.C. Koskelo (1996). Matrix effects in the detection of Pb and Ba in soils using laser-induced breakdown spectroscopy. *Appl. Spectrosc.* 50: 1175–1181.
- Essien, M., L.J. Radziemski and J. Sneddon (1988). Detection of cadmium, lead and zinc in aerosols by laser-induced breakdown spectroscopy. *J. Anal. At. Spectrom.* 3: 985–988.
- Evtushenko, T.P., *et al.* (1966). Investigation of air sparks by two synchronized lasers. *Sov. Phys.-Tech. Phys.* 11: 818–822.
- Generalov, N.A., V.P. Zimakov, G.I. Kozlov, V.A. Masyukov and Y.P. Raiser (1970). Continuous optical discharge. *JETP Lett.* 11: 302–306.
- Georgiou, S., V. Zafiropoulos, D. Anglos, C. Balas, V. Tornari and C. Fotakis (1998). Excimer laser restoration of painted artworks: procedures, mechanisms and effects. *Appl. Surf. Sci.* 129: 738–745.
- Gornushkin, I.B., J.M. Anzano, L.A. King, B.W. Smith, N. Omenetto and J.D. Winefordner (1999). Curve of growth methodology applied to laser-induced plasma emission spectroscopy. *Spectrochim. Acta Part B* 54: 491–503.
- Grant, K.J., G.L. Paul and J.A. O'Neill (1991). Quantitative elemental analysis of iron ore by laser-induced breakdown spectroscopy. *Appl. Spectrosc.* 45: 701–705.
- Hahn, D.W., A.W. Mizolek and V. Palleschi (Eds) (2003). Special Issue, LIBS 2002. *Appl. Opt.* 42: 5933–6225.
- Harith, M.A., V. Palleschi, A. Salvetti, D.P. Singh, G. Tropiano and M. Vaselli (1990). Hydrodynamic evolution of laser driven diverging shock waves. *Laser Part. Beams* 8: 247–252.
- Harith, M.A., V. Palleschi and L.J. Radziemski (Eds) (2002). Special Issue, 1st Euro-Mediterranean Symposium on Laser-induced Breakdown Spectroscopy. *Spectrochim. Acta Part B* 57: 1107–1249.
- Harnley, J.M. and R.E. Fields (1997). Solid-state array detectors for analytical spectrometry. *Appl. Spectrosc.* 51: 334A–351A.
- Hou, X.D. and B.T. Jones (2000). Field instrumentation in atomic spectroscopy. *Microchem. J.* 66: 115–145.
- Ivanov, Y.V. and Y.D. Kopytin (1982). Selective interaction of a train of laser pulses with an aerosol medium. *Sov. J. Quant. Electro.* 12: 355–357.
- Kagawa, K., K. Kawai, M. Tani and T. Kobayashi (1994). XeCl excimer laser-induced shock wave plasma and its application to emission spectrochemical analysis. *Appl. Spectrosc.* 48: 198–205.
- Kane, K.Y., D.A. Cremers, R.C. Elphic and D.S. McKay (1992). An in situ technique for elemental analysis of lunar surfaces. Joint Workshop on New Technologies for Lunar Resource Assessment (6 April 1992), Santa Fe, NM. NASA-CR-191918.
- Keefer, D.R. (1974). Experimental study of a stationary laser-sustained air plasma. *J. Appl. Phys.* 46: 1080–1083.
- Kitamori, T., K. Yokose, K. Suzuki, T. Sawada and Y. Gohshi (1988). Laser breakdown acoustic effect of ultrafine particle in liquids and its application to particle counting. *Jpn. J. Appl. Phys.* 27: L983–L985.

- Knight, A.K., N.L. Scherbarth, D.A. Cremers and M.J. Ferris (2000). Characterization of laser-induced breakdown spectroscopy (LIBS) for application to space exploration. *Appl. Spectrosc.* 54: 331–340.
- Ko, J.B., W. Sdorra and K. Niemax (1989). On the internal standardization in optical spectrometry of microplasmas produced by laser ablation of solid samples. *Fresenius Z. Anal. Chem.* 335: 648–651.
- Laserna, J.J. (2005). Third international conference on laser induced plasma spectroscopy and applications. *Spectrochim. Acta Part B* 60: 877–878.
- Lauterborn, W. (1972). High-speed photography of laser-induced breakdown in liquids. *Appl. Phys. Lett.* 21: 27–29.
- Lawrenz, J. and K. Niemax (1989). A semiconductor diode laser spectrometer for laser spectrochemistry. *Spectrochim. Acta Part B* 44: 155–164.
- Lazzari, C., M. de Rosa, S. Rastelli, A. Ciucci, V. Palleschi and A. Savetti (1994). Detection of mercury in air by time resolved laser-induced breakdown spectroscopy technique. *Laser Part. Beams* 12: 525–530.
- Lee, W.B., J. Wu, Y.-I. Lee and J. Sneddon (2004). Recent applications of laser-induced breakdown spectrometry: a review of material approaches. *Appl. Spectrosc. Rev.* 39: 27–97.
- Lee, Y.-I., K. Song and J. Sneddon (1997). Laser induced plasmas for analytical atomic spectroscopy. Ch. 5 in *Lasers in Analytical Atomic Spectroscopy*, eds J. Sneddon, T.L. Thiem and Y.-I. Lee, VCH, New York: 197–235.
- Leis, F., W. Sdorra, J.B. Ko and K. Niemax (1989). Basic investigations for laser microanalysis: I. Optical emission spectrometry of laser-produced sample plumes. *Mikrochim. Acta (Wein)* 11: 185–199.
- Lencioni, D.E. (1973). The effect of dust on 10.6- $\mu\text{m}$  laser-induced air breakdown. *Appl. Phys. Lett.* 23: 12–14.
- Loree, T.R. and L.J. Radziemski (1981). Laser-induced breakdown spectroscopy: time-integrated applications. *Plasma Chem. Plasma Proc.* 1: 271–280.
- Maker, P.D., R.W. Terhune and C.M. Savage (1964). Optical third harmonic generation. Proceedings of the 3rd International Conference on Quantum Electronics, Paris, Columbia University Press, New York, Vol. 2: 1559.
- Mao, X.L., M.A. Shannon, A.J. Fernandez and R.E. Russo (1995). Temperature and emission spatial profiles of laser-induced plasmas during ablation using time-integrated emission spectroscopy. *Appl. Spectrosc.* 49: 1054–1062.
- Marich, K.W., P.W. Carr, W.J. Treytl and D. Glick (1970). Effect of matrix material on laser-induced elemental spectral emission. *Anal. Chem.* 42: 1775–1779.
- Marquardt, B.J., S.R. Goode and S.M. Angel (1996). In situ determination of lead in paint by laser-induced breakdown spectroscopy using a fiber-optic probe. *Anal. Chem.* 68: 977–981.
- Mateo, M.P., S. Palanco, J.M. Vadillo and J.J. Laserna (2000). Fast atomic mapping of heterogeneous surfaces using microline-imaging laser-induced breakdown spectrometry. *Appl. Spectrosc.* 54: 1429–1434.
- Measures, R.M. and H.S. Kwong (1979). TABLASER:trace (element) analyzer based on laser ablation and selectively excited radiation. *Appl. Opt.* 18: 281–286.
- Miles, B. and J. Cortes (1998). Subsurface heavy-metal detection with the use of a laser-induced breakdown spectroscopy (LIBS) penetrometer system. *Field Anal. Chem. Technol.* 2: 75–87.
- Millard, J.A., R.D. Dalling and L.J. Radziemski (1986). Time resolved laser-induced breakdown spectrometry for the rapid determination of beryllium in beryllium-copper alloys. *Appl. Spectrosc.* 40: 491–494.
- Moenke, H. and L. Moenke-Blankenburg (1973). *Laser Microspectrochemical Analysis*, A. Hilger, London and Crane, Russak and Co., Inc., New York.
- Moenke-Blankenburg, L. (1989). *Laser Micro Analysis*, John Wiley & Sons, Inc., New York.

- Palanco, S. and J.J. Laserna (2000). Full automation of a laser-induced breakdown spectrometer for quality assessment in the steel industry with sample handling, surface preparation and quantitative analysis capabilities. *J. Anal. At. Spectrom.* 15: 1321–1327.
- Pallikaris, I.G., H.S. Ginis, G.A. Kounis, D. Anglos, T.G. Papazoglou and L.P. Naoumidis (1998). Corneal hydration monitored by laser-induced breakdown spectroscopy. *J. Refr. Surgery* 14: 655–660.
- Poulain, D.E. and D.R. Alexander (1995). Influences on concentration measurements of liquid aerosols by laser-induced breakdown spectroscopy. *Appl. Spectrosc.* 49: 569–579.
- Radziemski, L.J. and T.R. Loree (1981). Laser-induced breakdown spectroscopy: time-resolved spectrochemical applications. *Plasma Chem. Plasma Proc.* 1: 281–293.
- Radziemski, L.J., D.A. Cremers and T.R. Loree (1983a). Detection of beryllium by laser-induced breakdown spectroscopy. *Spectrochim. Acta Part B* 38: 349–353.
- Radziemski, L.J., T.R. Loree, D.A. Cremers and N.M. Hoffman (1983b). Time-resolved laser-induced breakdown spectrometry of aerosols. *Anal. Chem.* 55: 1246–1251.
- Radziemski, L.J. and D.A. Cremers (1989). Spectrochemical analysis using laser plasma excitation. Ch. 7 in *Laser-induced Plasmas and Applications*, eds L.J. Radziemski and D.A. Cremers, Marcel Dekker, New York: 303–325.
- Radziemski, L.J. and D.A. Cremers (Eds) (1989). *Laser-induced Plasmas and Applications*, Marcel Dekker, New York.
- Radziemski, L.J. (1994). Review of selected analytical applications of laser plasmas and laser ablation, 1987–1994. *Microchem. J.* 50: 218–234.
- Radziemski, L.J. (2002). From LASER to LIBS, the path of technology development. *Spectrochim. Acta Part B* 57: 1109–1114.
- Raizer, Y.P. (1966). Breakdown and heating of gases under the influence of a laser beam. *Sov. Phys. Uspekhi* 8: 650–673.
- Raizer, Y.P. (1977). *Laser-induced Discharge Phenomena*, Consultants Bureau, New York, NY.
- Ready, J.F. (1971). *Effects of High-power Laser Radiation*, Academic Press, New York, NY.
- Ready, J.F. (2001). *LIA Handbook of Laser Materials Processing*, Laser Institute of America, Orlando, FL.
- Rieger, G.W., M. Taschuk, Y.Y. Tsui and R. Fedosejevs (2000). Laser-induced breakdown spectroscopy with low-energy laser pulses. *Proc. SPIE* 4087: 1127–1136.
- Runge, E.F., R.W. Minck and F.R. Bryan (1964). Spectrochemical analysis using a pulsed laser source. *Spectrochim. Acta* 20: 733–735.
- Rusak, D.A., B.C. Castle, B.W. Smith and J.D. Winefordner (1997). Fundamentals and applications of laser-induced breakdown spectroscopy. *Crit. Rev. Anal. Chem.* 27: 257–290.
- Rusak, D.A., B.C. Castle, B.W. Smith and J.D. Winefordner (1998). Recent trends and the future of laser-induced breakdown spectroscopy. *Trends Anal. Chem.* 17: 453–461.
- Russo, R.E., X. Mao and S.S. Mao (2002). Physics of laser ablation in microchemical analysis. *Anal. Chem.* 74: 70A–77A.
- Sabsabi, M. and P. Cielo (1992). Laser-induced breakdown spectroscopy on aluminum alloy targets. *SPIE* 2069: 191–201.
- Sabsabi, M. and P. Cielo (1995). Quantitative analysis of aluminum alloys by laser-induced breakdown spectroscopy and plasma characterization. *Appl. Spectrosc.* 49: 499–507.
- Samek, O., D.C.S. Beddows, H.H. Telle, G.W. Morris, M. Liska and J. Kaiser (1999). Quantitative analysis of trace metal accumulation in teeth using laser-induced breakdown spectroscopy. *Appl. Phys. A* 69: 179–182.
- Sattman, R., V. Sturm and R. Noll (1995). Laser-induced breakdown spectroscopy of steel samples using multiple Q-switch Nd:YAG laser pulses. *J. Phys. D: Appl. Phys.* 28: 2181–2187.
- Sattman, R., I. Moench, H. Krause, R. Noll, S. Couris, A. Hatziapostolou, A. Mavromanolakis, C. Fotakis, E. Larrauri and R. Miguel (1998). Laser-induced breakdown spectroscopy for polymer identification. *Appl. Spectrosc.* 52: 456–461.

- Schroeder, W.W., J.J. van Niekerk, L. Dicks, A. Strasheim and H.V.D. Piepen (1971). A new electronic time resolution system for direct reading spectrometers and some applications in the diagnosis of spark and laser radiations. *Spectrochim. Acta Part B* 26: 331–340.
- Scott, R.H. and A. Strasheim (1970). Laser induced plasmas for analytical spectroscopy. *Spectrochim. Acta Part B* 25: 311–332.
- Simeonsson, J.B. and A.W. Mizolek (1993). Time-resolved emission studies of ArF laser produced microplasmas. *Appl. Opt.* 32: 939–947.
- Simeonsson, J.B. and A.W. Mizolek (1994). Spectroscopic studies of laser-produced plasmas formed in CO and CO<sub>2</sub> using 193, 266, 355, 532, and 1064 nm laser radiation. *Appl. Phys. B* 59: 1–9.
- Singh, J.P., H. Zhang, F.-Y. Yueh and K.P. Carney (1996). Investigation of the effects of atmospheric conditions on the quantification of metal hydrides using laser-induced breakdown spectroscopy. *Appl. Spectrosc.* 50: 764–773.
- Song, K., Y.-I. Lee and J. Sneddon (1997). Applications of laser-induced breakdown spectrometry (LIBS). *Appl. Spectrosc. Rev.* 32: 183–235.
- St-Onge, L. and M. Sabsabi (2000). Towards quantitative depth-profile analysis using laser-induced plasma spectroscopy: investigation of galvannealed coatings on steel. *Spectrochim. Acta Part B* 55: 299–308.
- Teslenko, V.S. (1977). Investigation of photoacoustic and photohydrodynamic parameters of laser breakdown in liquids. *Sov. J. Quant. Electro.* 7: 981–984.
- Theriault, G.A., S. Bodensteiner and S.H. Lieberman (1998). A real-time fiber-optic LIBS probe for the in situ delineation of metals in soils. *Field Anal. Chem. Technol.* 2: 117–125.
- Thiem, T.L., R.H. Salter, J.A. Gardner, Y.I. Lee and J. Sneddon (1994). Quantitative simultaneous elemental determinations in alloys using LIBS in an ultra-high-vacuum. *Appl. Spectrosc.* 48: 58–64.
- Tognoni, E., V. Palleschi, M. Corsi and G. Christoforetti (2002). Quantitative micro-analysis by laser-induced breakdown spectroscopy: a review of the experimental approaches. *Spectrochim. Acta Part B* 57: 1115–1130.
- Treytl, W.J., J.B. Orenberg, K.W. Marich, A.J. Saffir and D. Glick (1972). Detection limits in analysis of metals in biological materials by laser microprobe optical emission spectrometry. *Anal. Chem.* 44: 1903–1904.
- Vadillo, J.M., M. Milan and J.J. Laserna (1996). Space and time-resolved laser-induced breakdown spectroscopy using charge-coupled device detection. *Fresenius J. Anal. Chem.* 355: 10–15.
- Vadillo, J.M. and J.J. Laserna (1997). Depth-resolved analysis of multilayered samples by laser-induced breakdown spectrometry. *J. Anal. At. Spectrom.* 12: 859–862.
- Wachter, J.R. and D.A. Cremers (1987). Determination of uranium in solution using laser-induced breakdown spectroscopy. *Appl. Spectrosc.* 41: 1042–1048.
- Wallis, F.J., B.L. Chadwick and R.J.S. Morrison (2000). Analysis of lignite using laser-induced breakdown spectroscopy. *Appl. Spectrosc.* 54: 1231–1235.
- Wiens, R.C., R.E. Arvidson, D.A. Cremers, M.J. Ferris, J.D. Blacic, F.P. Seelos IV and K.S. Deal (2002). Combined remote mineralogical and elemental identification from rovers: field and laboratory tests using reflectance and laser-induced breakdown spectroscopy. *J. Geophys. Res.* 107: 10.1029/2000JE001439.
- Wisbrun, R., I. Schechter, R. Niessner, H. Schroeder and K.L. Kompa (1994). Detector for trace elemental analysis of solid environmental samples by laser plasma spectroscopy. *Anal. Chem.* 66: 2964–2975.
- Yamamoto, K.Y., D.A. Cremers, M.J. Ferris and L.E. Foster (1996). Detection of metals in the environment using a portable laser-induced breakdown spectroscopy instrument. *Appl. Spectrosc.* 50: 222–233.
- Young, M., M. Hercher and C.-Y. Yu (1966). Some characteristics of laser-induced air sparks. *J. Appl. Phys.* 37: 4938–4940.

- Zayhowski, J.J. (2000). Passively Q-switched Nd:YAG microchip lasers and applications. *J. Alloys Compd.* 303: 393–400.
- Zel'dovich, Ya.B. and Yu.P. Raizer (2002). *Physics of Shock Waves and High-temperature Hydrodynamic Phenomena*, eds W.D. Hayes and R.F. Probstein, Dover, Mineola NY.
- Zhang, H., J.P. Singh, F.-Y. Yueh and R.L. Cook (1995). Laser-induced breakdown spectra in a coal-fired MHD facility. *Appl. Spectrosc.* 49: 1617–1623.

---

## 2 Basics of the LIBS Plasma

---

### 2.1 LIBS PLASMA FUNDAMENTALS

Light emitting plasmas have been studied in earnest since the 1920s, and laser-induced plasmas since the 1960s. In this chapter we will deal with the intricacies of LIBS plasma formation, lifetime, and decay in and on a variety of media. Good references to plasmas and relevant spectroscopic diagnostics are books by Griem (Griem, 1964, 1974, 1997), Lochte-Holtgreven (Lochte-Holtgreven, 1968) and Bekefi (Bekefi, 1976), and chapters by Weyl (Weyl, 1989), Root (Root, 1989), Radziemski and Cremers (Radziemski and Cremers, 1989b), and Kim (Kim, 1989) in *Laser-induced Plasmas and Applications* (Radziemski and Cremers, 1989a).

A plasma is a local assembly of atoms, ions and free electrons, overall electrically neutral, in which the charged species often act collectively. Plasmas are characterized by a variety of parameters, the most basic being the degree of ionization. A weakly ionized plasma is one in which the ratio of electrons to other species is less than 10%. At the other extreme, highly ionized plasmas may have atoms stripped of many of their electrons, resulting in very high electron to atom/ion ratios. LIBS plasmas typically fall in the category of weakly ionized plasmas. A schematic overview of the temporal history of a LIBS plasma initiated by a single laser pulse is shown in Figure 2.1. At early times, ionization is high. As electron-ion recombination proceeds, neutral atoms, and then molecules form. Throughout there is a background continuum that decays with time more quickly than the spectral lines. The continuum is primarily due to bremsstrahlung (free-free) and recombination (free-bound) events. In the bremsstrahlung process photons are emitted by electrons accelerated or decelerated in collisions. A recombination occurs when a free electron is captured into an ionic or atomic energy level and gives up its excess kinetic energy in the form of a photon. Time resolution of the plasma light in LIBS allows for discrimination in favor of the region where the signals of interest predominate. The symbol  $t_d$  represents the delay from the initiation of the laser to the opening of the window during which signal will be accepted;  $t_b$  represents the length of that window. LIBS has also been performed in a double-pulse mode, where two laser pulses from the same or different lasers are incident on the target. The first application of this variation was to liquids by Cremers *et al.* (Cremers *et al.*, 1984). We will discuss its more recent use in ablation of solids at the end of this chapter.

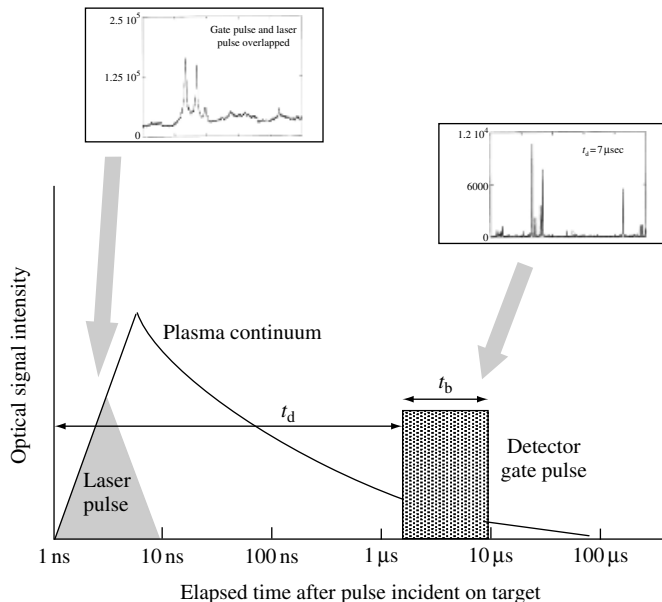


**Figure 2.1** A schematic overview of the temporal history of a LIBS plasma. The delay and window are shown. Inserts illustrate the kind of spectra one might observe at the different times

The timescales shown in Figure 2.1 are appropriate for a plasma initiated in air at 1 atm by a 5 to 10 ns 1064-nm laser pulse from a Nd:YAG laser. For much longer (e.g. CO<sub>2</sub> laser) or much shorter pulses (e.g. pico- or femtosecond lasers) the timescale will expand or contract accordingly. As ambient pressure decreases, the plasma lifetime decreases because there is less trapping and recycling of the absorbed energy in the plasma volume. Plasmas formed by the modest laser energies used for LIBS are typically less than 10% ionized at the earliest observable time.

Typical plasma radiation processes are shown in Figure 2.2. When  $E$  is given in joules, the frequency, wave number and wavelength of a transition are given by:

$$\nu = \Delta E / h \quad \sigma = \nu / c \quad \lambda = 1 / \sigma, \quad (2.1)$$

where  $\Delta E$  is an energy level difference. [Note: The table of Acronyms, Constants and Symbols contains the definition of characters often used in equations, like  $h$  (Planck's constant) or  $c$  (speed of light). Symbols used only once are defined under the equation where they are introduced. Occasionally the same symbol is used differently in different equations. In that case it is defined for the particular occasion.] Energy levels are conventionally listed with the ground state as zero, and in pseudo energy units of wavenumber,  $E/hc$ , commonly /cm. In that case, the wavenumber of the transition can be read directly from the difference of two energy level values.

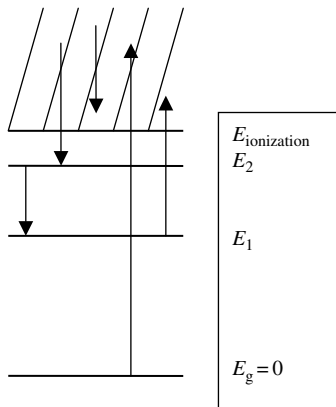


**Figure 2.2** Typical transitions in an atom or ion. From left to right: bound–bound; free–bound; free–free; ionization from the ground state; ionization from an excited state

The goal of the LIBS technique is to create an optically thin plasma which is in thermodynamic equilibrium and whose elemental composition is the same as that of the sample. When those conditions are fulfilled, relationships discussed below connect observed spectral line intensities with relative concentrations of elements. Typically these conditions are only met approximately. We will consider each of them in more detail. Given these and other complexities it is somewhat amazing that analytical results can be obtained. But with care they can, so usually these problems are no more than annoyances.

### 2.1.1 SPECTRAL LINES AND LINE PROFILES

The main diagnostic technique for plasmas involves the relationship between plasma properties and spectral line characteristics. Line widths are related to plasma temperature and electron density. Line shapes and shifts can be a diagnostic for the principal broadening mechanism. There are other diagnostic techniques. Langmuir probes and Thompson scattering can be used to measure electron densities, Schlieren or other interferometric techniques can reveal refractive index changes, and Abel inversion can assist in unfolding properties in the plasma by layer. Even the plasma acoustic emission can be employed for diagnosis. Optical techniques other than the passive observations of emission lines, such as laser-induced fluorescence, can cast light on critical plasma parameters. For an overview of diagnostic techniques see Lochte-Holtgreven (Lochte-Holtgreven, 1968) or Hauer and Baldis (Hauer and Baldis, 1989), and for some recent uses see Section 8.2.

Spectral line profiles are determined by the dominant broadening mechanisms. Pure Doppler broadening results in a Gaussian line profile, shown here in

wavenumber units, but which can be converted easily to frequency or wavelength units:

$$I(\sigma) = (4 \ln 2 / \pi \Gamma^2)^{1/2} \exp[-4 \ln 2 (\sigma - \sigma_0)^2 / \Gamma^2] \quad (2.2)$$

where  $\Gamma$  is the full-width at half-maximum (FWHM),

$$\Gamma = (8kT \ln 2 / Mc^2)^{1/2} \sigma_0 \quad (2.3)$$

where  $M$  is the species mass and  $\sigma_0$  the central wave number of the transition. Other common effects such as natural line broadening and collision broadening due to collisions with neutrals lead to a symmetric Lorentz profile:

$$I(\sigma) = (\Gamma / 2\pi) / [(\sigma - \sigma_0)^2 + (\Gamma/2)^2]. \quad (2.4)$$

Often the two are of comparable magnitudes, and the resulting profile obtained by convolution of the two is called the Voigt profile. Figure 2.3 compares the characteristics of Gauss and Lorentz profiles of equal full-width at half-maximum (FWHM), and the resulting Voigt profile. The Gaussian will dominate close to the line center, the Lorentz in the line wings. Voigt profiles will depend on the relative strength of the two effects. For detailed analysis of Voigt profiles see Hummer and Rybicki (Hummer and Rybicki, 1971) or Whiting (Whiting, 1968).

The term collision broadening is often used to describe the effect of collisions of neutral atoms or molecules. It exists even in the absence of a plasma, and is seen, for example, in absorption lines that start on low lying energy levels. Collisions with ions and electrons result in Stark broadening. An energy level in an electric field is split into sublevels according to the absolute value of the quantum number  $m_J$  representing the  $z$  component of the total angular momentum  $J$ . Hence, in the

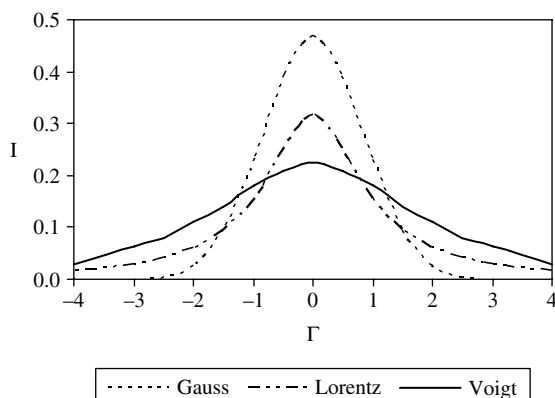


**Figure 2.3** Gauss and Lorentz profiles of equal half widths. The Voigt profile is the result of the convolution of the other two

Stark effect in most atoms, the fine structure transitions between levels of different  $m_J$  are not symmetric about the unperturbed level position, and an asymmetric, shifted line can be the result. If the splitting of the levels is not too large, the resulting broadening may appear to be symmetric. This is different than for atoms in a magnetic field (the Zeeman effect), where at low fields, isolated sublevels split symmetrically around the parent level.

### 2.1.2 DETERMINING ELECTRON DENSITIES FROM SPECTRAL LINE WIDTHS

Under normal LIBS conditions, the most important contributions to the line width are the Doppler width and the Stark effect. It is easy to see why the natural line width can be neglected. Natural line widths are related to energy level widths by  $\sim \Delta E \Delta t > \hbar$ , where  $\Delta E$  is the width of the level, and  $\Delta t$  its lifetime. For a transition between two energy levels with natural lifetimes of 10 ns, the natural spectral line width is about  $\sqrt{2}$  times the level width or  $7 \times 10^{-4}$ /cm. At 500 nm the line width in the example above amounts to 0.002 nm. These are unobservable at the spectrometer resolutions used in LIBS experiments.

The Doppler width depends only on the absolute temperature and the atomic mass of the emitting species. Starting from Equation (2.3) and converting to wavelength units for FWHM, we obtain:

$$\Delta\lambda_D = 7.2 \times 10^{-7} (T/M)^{1/2} \lambda_o \quad (2.5)$$

where  $M$  is the atomic mass of the element and  $\lambda_o$  the central wavelength of the spectral line. Calculated Doppler and Stark widths (discussed below) for some lines commonly observed in LIBS experiments are shown in Table 2.1. Some observations and comparisons will be made after the discussion of Stark width that follows.

As mentioned above, in Stark effect degenerate sublevels identified by the quantum number  $m_J$  are partially or completely split, leading either to (1) an unresolved, broadened, and often shifted level center-of-gravity, or (2) a resolved series of sublevels. Selection rules on the transitions between the sublevels allow one to predict the intensity of the resulting line (Cowan, 1981, pp. 498–504). The electric field that causes Stark effect in LIBS plasmas results primarily from collisions with electrons, with small contributions due to collisions with ions. The calculation of the effect of nearby perturbers upon emitting species has historically taken two directions. The quasi-static Holtzman theory assumes that the relative motion between perturber and emitter is small, so that the perturbation is constant over times on the order of a level lifetime. At the opposite extreme, the impact theory assumes that the emitter is unperturbed except for isolated instantaneous interactions. Griem's books mentioned above contain good detail on the theory behind these calculations and how they lead to expressions for Stark widths.

**Table 2.1** Doppler and Stark widths for lines of some elements of interest in LIBS experiments. Widths are calculated full-width at half maximum intensity (FWHM), for a plasma temperature of 10 000 K and an electron density of  $10^{17}/\text{cm}^3$ , except where noted

Element	$\lambda$ (nm)	Atomic mass	Temperature (K)	Doppler FWHM (nm)	Stark width coefficient <sup>a</sup> (FWHM in Å at $10^{16}/\text{cm}^3$ )	Stark width (FWHM in nm at $10^{17}/\text{cm}^3$ )
Hydrogen	656.3	1	11 000	0.047		0.4440 <sup>b</sup>
Hydrogen	656.3	1	20 000	0.067		
Hydrogen	656.3	1	50 000	0.106		
Hydrogen	486.1	1		0.035		0.8300 <sup>c</sup>
Deuterium	656.0	2	10 000	0.033		
He	587.5	4	10 000	0.021	0.1700	0.3400
Li	670.7	6.9	10 000	0.018	0.0138	0.0276
Li	610.3	6.9	10 000	0.017	0.2140	0.4280
Li	460.2	6.9	10 000	0.013	1.2700	2.5400
Li	413.2	6.9	10 000	0.011	3.4100	6.8200
Be	234.9	9	10 000	0.006	0.0009	0.0018
Be (II)	313.1	9	10 000	0.008	0.0537	0.1074
C	193.1	12	10 000	0.004	0.0022	0.0044
C	247.9	12	10 000	0.005	0.0036	0.0072
O	777.3	16	10 000	0.014	0.0315	0.0630
Na	589.2	23	10 000	0.009	0.0157	0.0314
Mg	285.2	24	10 000	0.004	0.0041	0.0082
Al	309.2	27	10 000	0.004	0.0260	0.0520
Si	288.1	28	10 000	0.004	0.0064	0.0128
Si	390.5	28	10 000	0.005	0.0117	0.0234
S	181.4	32.1	10 000	0.002	0.0022	0.0044
K	766.5	39.1	10 000	0.009	0.0415	0.0830
Ca	422.6	40	10 000	0.005	0.0063	0.0126

<sup>a</sup> Coefficients from Appendix 4 ( neutrals) or 5 ( ions) of Griem (Griem, 1974).

<sup>b</sup> Experimental, at  $T \sim 11 000$  K and  $n_e = 2 \times 10^{16}/\text{cm}^3$  (Parigger *et al.*, 2003). If this scales linearly with electron density, the approximate value at  $n_e = 10^{17}/\text{cm}^3$  would be 2.2 nm.

<sup>c</sup> Experimental, at  $T \sim 11 000$  K and  $n_e = 9.2 \times 10^{15}/\text{cm}^3$  (Parigger *et al.*, 2003). If this scales linearly with electron density, the approximate value at  $n_e = 10^{17}/\text{cm}^3$  would be 10 nm.

Stark broadened line widths can be used to calculate the electron density in plasmas. For example, the following expressions relate the line width and shift to electron and ion densities (Equations 226 and 227 in Griem, 1974):

$$w_{\text{total}} \sim [1 + 1.75 A(1 - 0.75r)](n_e/10^{16})w \quad (2.6)$$

$$d_{\text{total}} \sim [1 \pm 2.00 A(1 - 0.75r)](n_e/10^{16})d \quad (2.7)$$

where  $w_{\text{total}}$  is the measured half-width at half maximum (HWHM),  $A$  in this case is a parameter giving the ion contribution [ $A$  scales as  $(n_e)^{1/4}$ ],  $r$  is the ratio of the mean distance between ions to the Debye radius, and  $w$  is the HWHM Stark width caused by the electron density (scaling as  $n_e$  as indicated). If  $A$  is 0 (no ionic contribution) and the electron density is  $10^{16}/\text{cm}^3$ , the Stark widths can be read from Appendices 4 and 5 of Griem (Griem, 1974). Limitations on these expressions

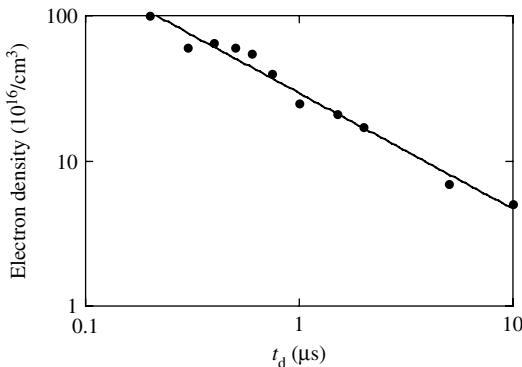
and scaling to other densities are discussed in his 1964 and 1974 books. Expressions (2.6) and (2.7) can be used to determine electron density. There have been other effects added to Stark theories by Oks (Oks, 1999). Detailed recent studies of  $H_\alpha$  and  $H_\beta$  broadening, including a more accurate treatment of ion dynamics, have been described by Parigger *et al.* (Parigger *et al.*, 2003) and Gigosos *et al.* (Gigosos *et al.*, 2003).

Table 2.1 contains the predictions of Stark widths and compares them with Doppler widths. The second, third and fourth columns are the parameters needed to apply Equation (2.5), and the resulting Doppler widths are in the fifth column. Stark broadening coefficients, from Appendices 4 (neutral) or 5 (ions) of Griem (Griem, 1974), are given in the sixth column. Stark broadening widths calculated from Equation (2.6) are found in the seventh column. The ionic contribution was neglected, so  $A$  was set equal to zero in Equation (2.6). The Stark widths are calculated for an electron density of  $10^{17}/\text{cm}^3$ .

Let us now consider some of the results in Table 2.1. Regarding hydrogen, the Stark widths have recently been re-determined by Oks and Parigger as mentioned above. Published values from the latter work are given in column seven, but these were made at different electron densities. Footnotes *b* and *c* contain the values adjusted to  $n_e = 10^{17}/\text{cm}^3$ . For hydrogen, the Stark widths are considerably larger than the Doppler widths for the temperatures given in the table. Moving on to lithium, values are given for several lines to illustrate the variation of Stark width as the upper energy level gets closer to the ionization potential. Lithium has an ionization potential of 5.4 eV. The upper levels for the four lines listed are: 1.8 eV for the 2p-2s resonance lines at 670.7 nm, 3.9 eV for 3d-2p at 610.3 nm, 4.5 eV for 4d-2p at 460.2 nm and 4.8 eV for 5d-2p at 413.2 nm. While the Doppler FWHM values for these lines vary from 0.01 to 0.02 nm, the Stark widths increase from 0.03 to almost 7 nm. In general, Stark widths and shifts will be largest for the upper levels closer to the ionization limit, and for upper levels that originate in electron configurations that have optical electrons with high angular momentum. Hence f levels are affected more than d levels and so on.

As one goes higher in atomic mass, the Doppler widths get smaller. Hence, even for many strong lines that originate from upper levels that are still far from the ionization limit, the Stark broadening can dominate. Regarding shifts in wavelengths, except for high f levels, these are typically less than 0.1 nm. Whether the Stark widths and shifts of lines from LIBS plasmas are observable depends on the optical and spectral resolving powers of the spectrometer-detector system.

When using LIBS at atmospheric pressure, ambient background species densities of molecular oxygen and nitrogen are on the order of  $2 \times 10^{19}/\text{cm}^3$ . Electron densities measured by Stark broadening are often  $10^{18}/\text{cm}^3$  at less than a microsecond into the plasma, and  $10^{16}/\text{cm}^3$  at 5 to 10  $\mu\text{s}$  after the laser pulse. Figure 2.4 contains examples of LIBS electron densities obtained from specific experiments. Of course, if LIBS is performed in different atmospheres, such as 7 Torr of CO<sub>2</sub> on Mars or 90 atm on Venus, these densities will be orders of magnitude different.



**Figure 2.4** Electron densities measured in some LIBS experiments. Data abstracted from Stark widths of F, Ar, N and Cl lines

### 2.1.3 PLASMA OPACITY

Having introduced the concepts of line profile and line width, we can now discuss the opacity of a plasma. Fundamentally, a plasma is optically thin when the emitted radiation traverses and escapes from the plasma without significant absorption or scattering. The intensity of radiation emitted from a plasma is given by:

$$I(\lambda) = [\varepsilon(\lambda)/\alpha(\lambda)] \{1 - \exp[-\alpha(\lambda)L]\} \quad (2.8)$$

where  $\varepsilon(\lambda)$  is the emissivity,  $\alpha(\lambda)$  is the absorption coefficient (/cm), and  $L$  is the plasma length along the line of sight to the observer. Note that when  $\alpha$  is small:

$$I(\lambda) = [\varepsilon(\lambda)/\alpha(\lambda)][\alpha(\lambda)L] \sim \varepsilon(\lambda)L \quad (2.9)$$

which is the condition for the plasma to be optically thin.

There are two relatively easy ways of checking for the optical thickness of a plasma. Strong spectral lines of elements have well known relative intensities, sometimes determined from atomic physics coupling theory (LJ, jj, etc.), sometimes determined experimentally. When re-absorption becomes noticeable, the observed intensities will depart from the expected values, the stronger lines effectively saturating. Starting with the most intense lines, they approach a flat-topped profile, evidence of self-absorption (see Figure 8.3 for calculated profiles). In more extreme cases, a single line will appear to have a dip at the central frequency. In such a case the line is said to be self-reversed. The subtle onset of self-absorption poses a problem for converting line intensities to concentrations, as discussed in Chapter 4. Self-absorption is also a major problem for calibration-free LIBS (CF-LIBS) as discussed in Chapter 8.

There are other experimental methods to detect self-absorption. One is to use a spherical mirror behind the plasma and compare the intensity of a given line with and without the mirror in place. When using this method care must be taken to illuminate the spectrograph properly, as discussed in Bekefi (Bekefi, 1976).

### 2.1.4 TEMPERATURE AND THERMODYNAMIC EQUILIBRIUM

Plasma descriptions start by trying to characterize properties of the assembly of atoms, molecules, electrons and ions rather than the individual species. If thermodynamic equilibrium exists, then plasma properties, such as the relative populations of energy levels, and the distribution of the speed of the particles, can be described through the concept of temperature. In fact, thermodynamic equilibrium is rarely complete, so physicists have settled for a useful approximation, local thermodynamic equilibrium (LTE). All one demands is that equilibration occurs in small regions of space, although it may be somewhat different from region to region. A useful approximation usually exists after a sufficient number of collisions have occurred to thermalize the plasma, which means to spread the energy in the plasma across volume and species. Even then, not all species may be in thermodynamic equilibrium. It is common for heavy species (atoms and ions) and light species (electrons) to equilibrate separately more quickly, and later in time with each other. The fundamental physical reason is that energy between collision partners is shared more equally the closer the masses of the colliding particles. Note that there may be more than one ‘temperature.’ An example of the direct observation of the equilibration of electron and atom temperatures in a LIBS plasma was given in a paper describing a study of an oxygen plasma induced by CO<sub>2</sub> laser radiation (Radziemski *et al.*, 1985). Figure 2.5 illustrates the convergence of electron temperature, measured by a Langmuir probe, with excitation temperatures measured by the Boltzmann method, where the plasma was initiated by a 10.6 μm CO<sub>2</sub> laser pulse. The probe measurements are represented by the black circles (500 mJ/pulse)

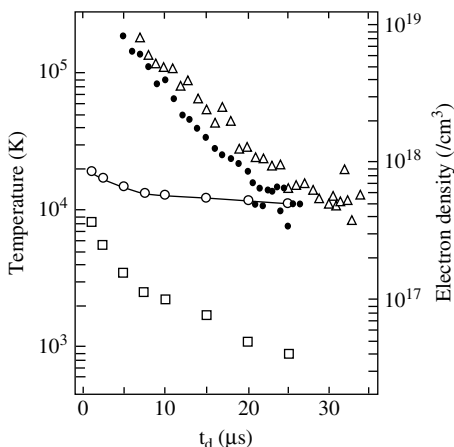


**Figure 2.5** Illustration of the convergence of electron temperature measured by a Langmuir probe (black circles, 500 mJ pulse; open triangles, 800 mJ pulse), with excitation temperature measured by the Boltzmann method (open circles). (Reproduced from Radziemski *et al.*, 1985, with permission from Elsevier)

and open triangles (800 mJ/pulse), and the Boltzmann temperatures by the open circles (500 mJ/pulse). The open squares are the electron densities measured using Stark effect line widths. Convergence of temperatures over a period of 25  $\mu$ s is clearly seen.

A variety of tests have been developed to ascertain whether thermodynamic equilibrium exists. Probably the simplest is that the relative intensities of atomic spectral lines from closely upper spaced levels in the same multiplet agree with predictions from basic theory (White, 1934; Kuhn, 1963). Of course, self absorption and interferences from nearby lines can limit the usefulness of this approach. Another test has to do with the electron density being high enough for collisions to dominate the population of levels. Griem (Griem, 1997, p. 219) discusses various criteria for the hydrogen atom, which depend on the energy difference between the levels involved. The larger that difference, the more difficult it is to establish equilibrium. The worst case in neutral atoms (except for the ground to first excited states of monatomic gases) is the 10.2 eV difference between the ground and first excited state of hydrogen. Griem's analysis suggests that for a temperature of 1 eV ( $\sim$ 11 000 K) and atmospheric pressure, an electron density of  $10^{17}/\text{cm}^3$  would ensure LTE. The approximations imply that LIBS plasmas generated by an irradiance of  $>10^8 \text{ W/cm}^2$ , at atmospheric pressure, would be sufficiently thermalized several hundred nanoseconds after initiation. The situation could be different for plasmas formed with femtosecond pulses, or at low pressure. Recent studies referred to in Chapter 8 point to the possibility of multicomponent plasmas.

If experiment determines that LTE exists, the distribution of several quantities, including electron speeds and populations of energy levels or ion stages are dependent on a single quantity, temperature. The Maxwellian velocity distribution function  $f_M$  is:

$$f_M = (m/2\pi kT)^{3/2} \exp(-mv^2/2kT) \quad (2.10)$$

where  $m$  is the electron mass and  $v$  the electron speed. Relative populations of energy levels, whether atomic or molecular in origin, are given by the Boltzmann distribution:

$$N_j/N_o = (g_j/Z) \exp(-E_j/kT) \text{ with respect to the ground state or} \quad (2.11)$$

$$N_j/N_i = (g_j/g_i) \exp[-(E_j - E_i)/kT] \text{ for relative population,} \quad (2.12)$$

where  $i$  and  $j$  refer to two levels,  $N_o$  is the total species population,  $N_{i,j}$  are the populations of levels  $E_{i,j}$ ,  $g_{i,j}$  are the statistical weights of the levels ( $2J_{i,j} + 1$ ),  $J$  is the total angular momentum quantum number of the term, and  $Z$  is the partition function usually taken as the statistical weight of the ground state. The spectral line radiant intensity is given by:

$$I = h\nu gA N/4\pi = (hcN_o gA/4\pi \lambda Z) \exp(-E/kT). \quad (2.13)$$

$I$  is in units of W/sr,  $\nu$  is the line frequency, and  $A$  is the transition probability (Einstein  $A$  coefficient).  $N$  may be the absolute number or the number density. If the

latter is the case, then Equation (2.13) gives the radiant intensity per unit volume of source. The ratio of the intensities of two lines is:

$$I'/I = (\lambda' g' A' / \lambda' g A) \exp[-(E' - E)/kT]. \quad (2.14)$$

Choosing lines for which the  $g$ ,  $A$  and  $E$  values and the wavelengths are known, and measuring the relative intensities, enables one to calculate  $T$  by the two-line method. If the lines have significantly different line widths, then integrated intensities are the measurement of choice. Figure 2.6 illustrates the parameters useful for determining temperature from the two-line method.

Relative intensities are not easy to measure precisely. A way to improve temperature values is to use many lines simultaneously and perform a graphical analysis. We rearrange Equation (2.13) into the form:

$$\begin{aligned} \ln(4\pi Z/hcN_o) + \ln(I\lambda/gA) &= -E/kT \quad \text{or} \\ \ln(I\lambda/gA) &= -E/kT - \ln(4\pi Z/hcN_o). \end{aligned} \quad (2.15)$$

This is the equation of a straight line with slope of  $-1/kT$ . Hence if one plots the quantity on the left against  $E$  (of the upper state for emission), and if there is a Boltzmann distribution, a straight line is obtained. Some of the crucial factors in obtaining a good Boltzmann plot are accurate line intensities, accurate transition probabilities, and well spaced upper levels. The further apart the extremes of the upper level values, the easier it will be to define the slope of the line. To illustrate, Figure 2.7 shows a LIBS spectrum of basalt, with iron lines used for a multi-line Boltzmann plot indicated by stars. The fundamental data for these lines are contained in Table 2.2 and the resulting plot is shown in Figure 2.8.

From the slope of the line in Figure 2.8, the temperature is determined to be 7500 K.

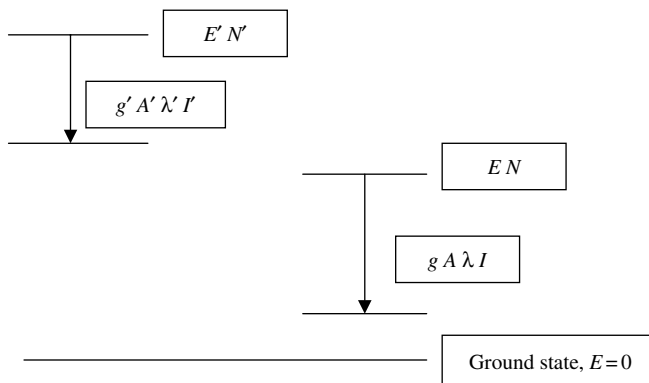


**Figure 2.6** Illustration of parameters and energy levels for the two-line method of determining plasma temperature

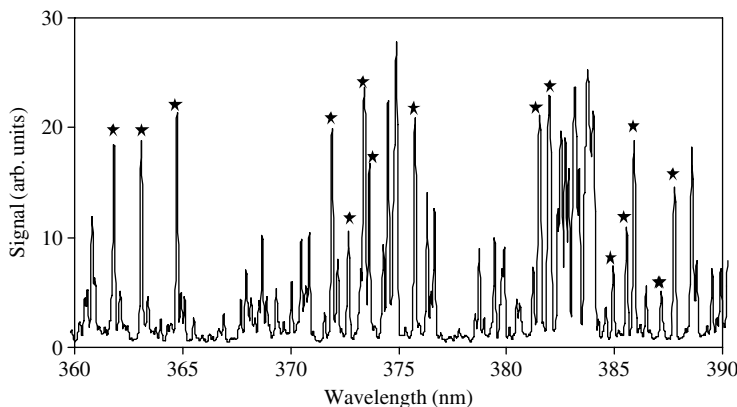


**Figure 2.7** LIBS spectrum of basalt and iron lines used in the Boltzmann plot of Figure 2.8

**Table 2.2** Neutral Fe [Fe(I)] parameters for a Boltzmann temperature determination (see Figure 2.8)<sup>a</sup>

Wavelength (nm)	$E_u$ (eV)	$gA^b$	Wavelength (nm)	$E_u$ (eV)	$gA^b$
361.877	4.42	5.1	382.043	4.10	6.01
363.146	4.37	4.65	384.044	4.22	1.41
364.784	4.31	3.21	384.997	4.23	0.61
371.994	3.33	1.78	385.637	3.27	0.23
372.762	4.28	1.12	385.991	3.21	0.87
373.487	4.18	9.92	387.250	4.19	0.53
373.713	3.37	1.28	387.857	3.28	0.2
381.584	4.73	9.1			

<sup>a</sup> Data from: <http://physics.nist.gov/PhysRefData/ASD/index.html>

<sup>b</sup> In units of  $10^8$ /s.

The relative populations among ion stages in LTE are given by the Saha (or Saha–Eggert) equation. To use this expression to obtain temperature, called the temperature of the ionization equilibrium, relative intensities of lines from different ion stages of the same atom (occasionally different atoms) are measured. The electron density must be known from other experiments. Figure 2.9 illustrates the quantities involved in Equation (2.16):

$$N(Z,0)n_e/N(Z-1,0) = 2g(Z,0)/g(Z-1,0)(mkT/2\pi\hbar^2)^{3/2} \exp(-\Delta E/kT) \quad (2.16)$$

where  $N(Z,0)$  is the population of the ground state of ion stage  $Z$ ,  $N(Z-1,0)$  is the population of the ground state of ion stage  $Z-1$ ,  $m$  is the electron mass,  $n_e$  is the electron density, and  $\Delta E$  is the ionization energy of stage  $Z$  relative to stage  $Z-1$ . In terms of relative intensities:

$$I'/I = \lambda' g' A' N(Z) / \lambda g A N(Z-1). \quad (2.17)$$

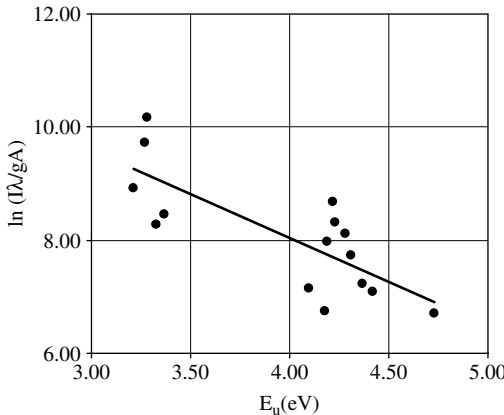


Figure 2.8 Multiline Boltzmann plot based on the data of Table 2.2

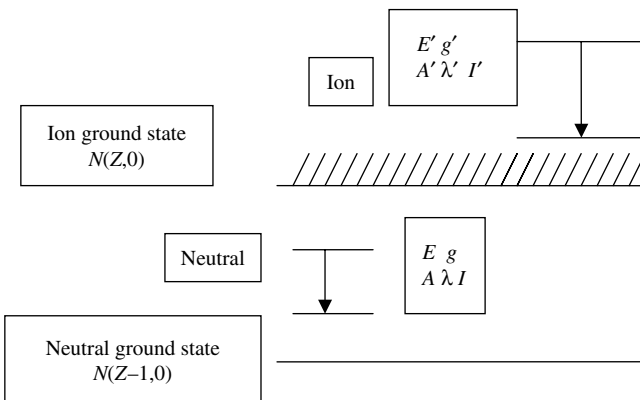
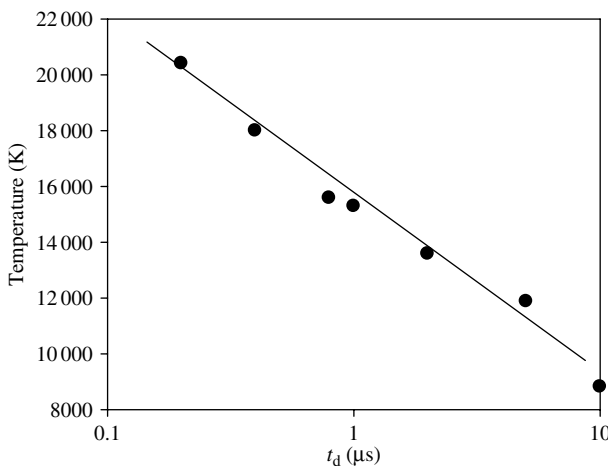


Figure 2.9 Illustration of parameters and energy levels for the Saha method of determining plasma temperature

For a specific application of the methods see Aguilera and Aragón (Aguilera and Aragón, 2004).

In addition to temperatures from atom, ions and the ionization equilibrium, it is possible to measure vibrational and rotational temperatures. Sometimes more than one of these temperatures can be measured simultaneously. If the results do not agree, doubt is cast upon the completeness of LTE.

Temperatures achieved in LIBS plasmas are of course dependent on the energy deposition, hence the fluence and irradiance. For irradiance values of  $\sim 10^{10} \text{ W/cm}^2$ , the temperature is typically 8000–12 000 K at 1–2  $\mu\text{s}$  into the plasma lifetime ( $t_d$ ). Figure 2.10 contains an example of LIBS temperatures obtained from Boltzmann and Saha analyses.



**Figure 2.10** Air plasma temperature as a function of time after plasma formation using Saha and Boltzmann data from C and Be lines

## 2.2 LASER-INDUCED BREAKDOWN

### 2.2.1 BREAKDOWN IN GASES

There are two key steps that lead to breakdown in a gas. First, there must be some free electrons in the focal volume of the laser beam. Sometimes these are transient electrons liberated by cosmic rays or the natural radioactivity of the earth. At other times they are generated by the first few photons of the pulse itself, being liberated from dust, negative ions such as  $O_2^-$ , organic vapors, or through multiphoton ionization of atoms or molecules in the atmosphere. Multiphoton effects are necessary for direct ionization of species like  $N_2$  and  $O_2$  because their ionization energies are much greater than energies of photons normally used. For example, the ionization potential of  $O_2$  is 12.2 eV and of  $N_2$  is 15.6 eV, while Nd:YAG 1064, 532 and 266 nm photons have energies of 1.25, 2.33 and 4.7 eV, respectively. Despite the very small cross-sections for the multiphoton process, irradiances of  $10^{10} \text{ W/cm}^2$  are sufficient for weak multiphoton ionization to occur.

The second step in the process of breakdown is generating sufficient electron and ion densities. For the irradiance values typically used in LIBS ( $10^8\text{--}10^{10} \text{ W/cm}^2$ ), this occurs through avalanche or cascade ionization. At higher irradiance values, significant multiphoton production of electrons can occur through:



where  $m$  is the number of photons. In the classical picture, free electrons are accelerated by the electric field in the optical pulse during the time period between collisions with neutral species. The collisions thermalize the electrons quickly.

A small number of electrons in the tail of the Maxwellian distribution will have enough energy to ionize an atom or molecule through the reaction



This starts to produce other free electrons that gain energy from the field and produce more ionization. The process of electron multiplication continues during the laser pulse and results in the ionization of the gas and breakdown. Alternately, electrons can acquire energy from photons in three-body collisions with atoms or molecules (inverse Bremsstrahlung). As the number of ions increases the electron–photon–ion collisions increase yielding a higher probability of further electron multiplication.

The change in electron density can be represented by the following equation which contains growth and loss terms:

$$dn_e/dt = n_e(\nu_i - \nu_a - \nu_r) + W_m I^m n - \nabla(D \nabla n_e) \quad (2.20)$$

where  $\nu_i$ ,  $\nu_a$  and  $\nu_r$  are the impact ionization, attachment and recombination rates, respectively,  $W_m$  is the multiphoton ionization rate coefficient,  $I^m$  is the irradiance ( $\text{W}/\text{cm}^2$ ) necessary for an  $m$ -photon process to occur,  $n$  is the number density of the species being irradiated,  $\nabla$  is the gradient operator and  $D$  is the diffusion coefficient for electrons. Values for these coefficients are discussed in depth by Weyl (Weyl, 1989).

The breakdown threshold is difficult to pin down with accuracy because of the many variables involved. These include the characteristics of the medium (dust, ionization thresholds), the laser pulse characteristics (temporal pulse length, wavelength), and the irradiance (related to the focal properties of the optics). The latter also affects the balance between cascade and multiphoton ionization. In general, a pressure independent value for breakdown threshold indicates a dominance of multiphoton ionization.

A thorough investigation of the breakdown thresholds in molecular oxygen and nitrogen using 10 ns, 1064 nm Nd:YAG photons was done by Stricker and Parker (Stricker and Parker, 1982), over pressure ranges from 1 to 50 atm. In this range of pressures, the process was avalanche, not multiphoton ionization. Their value of the breakdown threshold in laboratory air was  $8.2 \times 10^{10} \text{ W}/\text{cm}^2$ . The slope of the curve implied that an order of magnitude increase in the pressure resulted in an order of magnitude increase in the breakdown threshold. For a 7–8 ns Nd:YAG pulse in air, at the frequency fundamental, doubled, tripled and quadrupled wavelengths of 1064, 532, 355 and 266 nm, respectively, breakdown thresholds were measured, and values from others' experiments summarized (Simeonsson and Mizolek, 1994). These and other representative results for breakdown thresholds in atmospheric pressure gases for several lasers and wavelengths are listed in Table 2.3.

Measurements have been made using pulses in the pico- and femtosecond regimes. In 1983, Williams *et al.* published the results of a study of the breakdown threshold in laboratory air using the Nd:YAG frequency doubled to 532 nm, with pulse lengths in the 30–140 ps regime (Williams *et al.*, 1983). Their

**Table 2.3** Measured breakdown thresholds for several lasers and gases

Laser, wavelength, pulse length, other	Gas and pressure	Breakdown threshold irradiance (W/cm <sup>2</sup> )	Reference
Nd:YAG, 1064 nm, 10 ns	Laboratory air, 1 atm	$8.2 \times 10^{10}$	Stricker and Parker, 1982
Nd:YAG, 1064 nm, 8 ns	Laboratory air, 1 atm	$2.0 \times 10^{10}$	Simeonsson and Mizolek, 1994
Nd:YAG, 1064 nm, 8 ns, spot diameter $5 \times 10^{-3}$ cm	Laboratory air, 1 atm	$5.0 \times 10^{11}$	Tambay and Thareja, 1991
Nd:YAG, 1064 nm, 7 ps	Nitrogen, 760 Torr	$8 \times 10^{14}$	Dewhurst, 1978
Nd:YAG, 532 nm, 7 ns	Laboratory air, 1 atm	$1.5 \times 10^{10}$	Simeonsson and Mizolek, 1994
Nd:YAG, 532 nm, 6 ns, spot diameter $5 \times 10^{-3}$ cm	Laboratory air, 1 atm	$1.0 \times 10^{11}$	Tambay and Thareja, 1991
Nd:YAG, 532 nm, 8 ns	Laboratory air, 1 atm	$2.5 \times 10^{12}$	Bindhu <i>et al.</i> , 2004
Nd:YAG, 532 nm, 80 ps	Laboratory air, 1 atm	$1.8 \times 10^{13}$	Williams <i>et al.</i> , 1983
Nd:YAG, 532 nm, 25 ps	Nitrogen, 760 Torr	$4 \times 10^{13}$	Dewhurst, 1978
Nd:YAG, 355 nm, 7 ns	Laboratory air, 1 atm	$2.7 \times 10^{10}$	Simeonsson and Mizolek, 1994
Nd:YAG, 355 nm, 4 ns, spot diameter $5 \times 10^{-3}$ cm	Laboratory air, 1 atm	$1.05 \times 10^{11}$	Tambay and Thareja, 1991
Nd:YAG, 266 nm, 7 ns	Laboratory air, 1 atm	$1.7 \times 10^{10}$	Simeonsson and Mizolek, 1994
Nd:YAG, 266 nm, 4 ns, spot diameter $5 \times 10^{-3}$ cm	Laboratory air, 1 atm	$1.06 \times 10^{11}$	Tambay and Thareja, 1991
ArF, 193 nm, 10 ns	Laboratory air, 1 atm	$9.7 \times 10^9$	Simeonsson and Mizolek, 1994

threshold values ranged from 1 to  $4 \times 10^{13}$  W/cm<sup>2</sup>. Other results from Dewhurst (Dewhurst, 1978) are included in Table 2.3. More information on breakdown will be found in Weyl (Weyl, 1989). Given variations in experimental conditions and changes in laser technology, values indicated here should be used only as a guide to likely results. If the breakdown threshold is a critical parameter, the researcher should do the measurements on the actual system.

Often breakdown thresholds are reported in terms of the corresponding classical electric field. The expression for converting between irradiance and electric field is (Hecht, 1987, p. 44):

$$I = c\epsilon_0 \langle E^2 \rangle = 2.6 \times 10^{-3} E^2 \quad (2.21)$$

where  $I$  is the irradiance in W/cm<sup>2</sup>,  $\langle E^2 \rangle$  the time averaged value of the square of the electric field amplitude, with  $E$  in V/cm. Hence an irradiance of  $10^{10}$  W/cm<sup>2</sup> corresponds to an electric field of 2 MV/cm.

## 2.2.2 POST-BREAKDOWN PHENOMENA IN GASES

After breakdown in a gas, absent a surface, the luminous plasma expands outward in all directions from the point at which breakdown initiated. Depending on the irradiance, some of the laser energy may be transmitted through the plasma volume, some scattered, and the rest absorbed. The plasma advances up the beam towards the laser during the laser pulse, because the absorption of the photons is asymmetric in that direction. Hence the plasma has a slight conical shape with the blunt end towards the lens. In the case of gases more transparent to the incident wavelength, more of the energy would be absorbed at the site of the plasma being formed, resulting in spherical expansion.

With the development of continuous, high power CO<sub>2</sub> lasers in the 1960s, continuous laser-induced plasmas in gases became possible. These also are called continuous optical discharges (CODs). The first observation was published by Generalov *et al.* (Generalov *et al.*, 1970). CODs have been achieved in a variety of gases at pressures ranging from 1 to over 200 atm with 10.6 μm CO<sub>2</sub> lasers employing powers of at least 25 W. The Russian literature often refers to this device operated in a flowing atmosphere as an optical plasmatron. Plasma temperatures are typically below 15 000 K. Keefer (Keefer, 1974) also reported early experimentation on laser-sustained plasmas, and later provided a good review of the field (Keefer, 1989). The use of the COD for spectrochemical analysis was studied by Cremers *et al.* (Cremers *et al.*, 1985), where a 45 W CO<sub>2</sub> laser was used to generate a plasma in xenon.

## 2.2.3 BREAKDOWN IN AND ON SOLIDS, AEROSOLS AND LIQUIDS

The majority of problems to which LIBS is applied involve solids in air, to a lesser extent liquids and aerosols. In addition, there can be unwanted breakdown on the surfaces of optical components that will shorten their life and scatter the incoming laser radiation. As a result, breakdown and post breakdown phenomena on or in transparent and opaque dielectrics, metals and liquids is of interest. Optical damage studies are one area of interest. To a great extent the subject is empirical. Thresholds are quite sensitive to the purity of the material, the surface preparation, smoothness and particles that have adhered to the surface. If the laser beam is multimode it may have hot spots that initiate plasma formation below the average threshold values. Typical reported values for LIBS type plasmas on solids are in the range of 10<sup>8</sup>–10<sup>10</sup> W/cm<sup>2</sup>.

The availability of pico- and femtosecond lasers has illuminated some of the processes of ablation. Through observations of the onset of ablation, one can obtain an estimate of breakdown thresholds. Papers by Hashida *et al.* and Semerok *et al.* discuss both thresholds and ablation rates for 532 nm, 6 ns Nd:YAG and 800 nm Ti:sapphire at 70 fs and 5 ps on copper substrates (Hashida *et al.*, 2002; Semerok *et al.*, 2002). Their results and others are contained in Table 2.4 and follow expected

**Table 2.4** Recent measured breakdown thresholds for some laser pulses on solids

Laser, wavelength, pulse length	Surface, gas and pressure	Breakdown threshold irradiance (W/cm <sup>2</sup> )	Reference
Nd:YAG, 532 nm, 6 ns	Cu, atm air	$1.67 \times 10^9$	Semerok <i>et al.</i> , 2002
Ti:sapphire, 800 nm, 5 ps	Cu, atm air	$9 \times 10^{10}$	Hashida <i>et al.</i> , 2002
Ti:sapphire, 800 nm, 70 fs	Cu, atm air	$2.5 \times 10^{11}$	Hashida <i>et al.</i> , 2002
Colliding-pulse laser, 620 nm, 90 fs	BaTiO <sub>3</sub> , vacuum	$5 \times 10^{11}$	Millon <i>et al.</i> , 2003
Colliding-pulse laser, 620 nm, 120 fs	Fused silica, atm air	$1 \times 10^{13}$	von der Linde and Schüller, 1996 (also investigated were glass, sapphire and magnesium fluoride)
Nd:YAG, 1064 nm, 6.4 ns	Fused silica, argon	$5.5 \times 10^{10}$	Galt <i>et al.</i> , 2003

progressions. If breakdown threshold is an important factor, it should be measured with the samples and laser being used in the experiment.

For transparent materials such as those from which lenses and windows are made, breakdown can occur at the surface or within the material. Thresholds have been measured for four transparent dielectrics (glass, magnesium fluoride, sapphire and fused silica) by von der Linde and Schüller (von der Linde and Schüller, 1996). The results for fused silica are typical and contained in Table 2.4. In general one expects the surface thresholds to be lower because of surface defects such as scratches, pits or dust particles. The most common type of damage in LIBS experiments arises when a laser beam has passed through the focusing lens and is incident on a window as it is proceeding to a focus. If one is not careful, a plasma can be initiated on the window, or on the exit side of the focusing lens by retro reflection.

Aerosol induced breakdown is a complex subject because of the many parameters involved. These include the composition of composite particles, shapes, density, materials, atmosphere and water content. Suffice it to say, that these factors, in general, lower the breakdown threshold. Particles ejected a sufficient distance from surfaces under irradiation may cause single or multiple plasma formation detached from the surface, thereby screening the surface, partially or totally, from absorbing incoming laser radiation. Laser beam blooming, focusing and distortion can also occur.

Breakdown thresholds in water and other liquids have been measured as well. There is great interest in this area in the community performing laser surgery in the eye. Culminating an extensive study, Kennedy *et al.* published the results of experiments and calculations of breakdown thresholds in a variety of aqueous media (Kennedy *et al.*, 1995). Their goal was to gain an understanding of the role of laser-induced breakdown as a possible ocular damage mechanism. Samples included ocular media, saline, tap and distilled water. Some of their results are listed in Table 2.5. The variations for different types of samples are also presented in the

**Table 2.5** Recent measured breakdown thresholds for some laser pulses in liquids

Laser, wavelength, pulse length	Medium	Breakdown threshold irradiance ( $\text{W}/\text{cm}^2$ )	Reference
Nd:YAG, 1064 nm, 7 ns	Tap water	$5.6 \times 10^9$	Kennedy <i>et al.</i> , 1995
	Ultra pure water	$1.82 \times 10^{10}$	
	Vitreous	$1.27 \times 10^{10}$	
	Saline	$8.31 \times 10^9$	
Nd:YAG, 532 nm, 3 ns	Tap water	$9.35 \times 10^9$	Kennedy <i>et al.</i> , 1995
Nd:YAG, 1064 nm, 80 ps	Tap water	$1.91 \times 10^{11}$	Kennedy <i>et al.</i> , 1995
Dye laser, 580 nm, 100 fs	Tap water	$5.6 \times 10^{12}$	Kennedy <i>et al.</i> , 1995
Nd:YAG, 1064 nm, 6 ns	Distilled water	$7.6 \times 10^{10}$	Vogel <i>et al.</i> , 1996
Nd:YAG, 1064 nm, 30 ps	Distilled water	$4.5 \times 10^{11}$	Vogel <i>et al.</i> , 1996

table for the 1064 nm, 7 ns experiments. The results of Vogel *et al.* are included for comparison (Vogel *et al.*, 1996).

## 2.2.4 POST-BREAKDOWN PHENOMENA ON SOLID SURFACES

When the laser irradiance is high enough to cause a plasma plume, the leading edge of the pulse rapidly heats, melts and vaporizes material into a layer just above the surface. Some of the laser energy then heats the evaporated material. While the plasma is weakly ionized, part of the laser energy continues through to the surface and part is absorbed in the plasma or material behind it. At high enough energy, the plasma can become opaque to the laser beam and the surface is shielded, while the plasma front grows towards the laser as described above. This occurs when the plasma frequency becomes greater than the laser frequency, or in terms of the critical electron density  $n_c$ , at:

$$n_c \sim (10^{21}/\lambda^2)/\text{cm}^3 \quad (2.22)$$

where  $\lambda$  is the laser wavelength in microns. The cutoff near 10  $\mu\text{m}$  occurs at an electron density of  $10^{19}/\text{cm}^3$ . At 1000 nm that value is  $10^{21}/\text{cm}^3$ , and at 250 nm it is  $1.6 \times 10^{22}/\text{cm}^3$ . The latter large values can be reached in the first few picoseconds of plasma formation, leading to absorption of the rising edge of a nanosecond pulse. Later in a nanosecond pulse, absorption by the plasma and heated gas can affect the trailing edge.

Consider the formation of a plasma on a plane surface and expanding up the laser beam, as illustrated in Figure 2.11.

There are three important zones, the plasma front, the shock front and the absorption front. At the lowest intensities the shock front precedes the absorption front which is coupled to the plasma front. In this model, both the energy of the shock deposited in the atmosphere behind it, plus the radiation from the plasma,

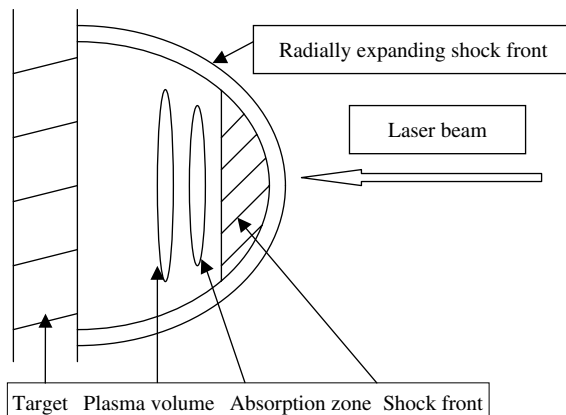


**Figure 2.11** Schematic diagram of the development of a laser plasma initiated on a solid surface

are required to move the absorption front towards the laser beam. This is called a laser-supported combustion (LSC) wave. At higher laser intensities, the shock front is strong enough to heat the gas, leading to absorption of the laser beam. Hence the absorption zone comes up just behind the shock front, and both are ahead of the plasma front. This is called the laser-supported detonation (LSD) wave by analogy to what happens in chemical detonations. At the highest intensities, the radiation from the plasma itself is sufficient to heat the atmosphere in front of it to the point at which it becomes absorbing. Hence the absorption zone is coupled to the plasma front. This is called a laser-supported radiation (LSR) wave.

When the incident irradiance is not much larger than the breakdown threshold, the LIBS plasma is typically in the LSD regime when expanding into atmospheric pressure air. Figure 2.12 illustrates schematically the relative positions of the expanding plasma, absorption zone and shock front. At higher irradiances it is better described by an LSR wave, where those three zones have effectively merged. Root (Root, 1989) provided qualitative indications of the variation of velocity, pressure, temperature and density for the three types of plasmas, LSC, LSD and LSR in a one-dimensional approximation. A recent work that models this regime, and then goes on to ablation mechanisms and rates as well as analytical considerations, is given in the significant modeling effort reported by Bogaerts *et al.* (Bogaerts *et al.*, 2003). Their results will be discussed in Chapter 8. After the termination of the laser pulse, the plasma loses energy and decays. Mechanisms include recombination, radiation and conduction.

The effect of a cover gas in certain regimes of pressure is to slow down and confine the plume. Also, the plasma size goes through various regimes as pressure is reduced. At very low pressures the luminous part of the plasma can be very small. Figure 2.13 illustrates the difference in size of plasmas at two pressures, 0.00012 and 7 Torr of CO<sub>2</sub>.

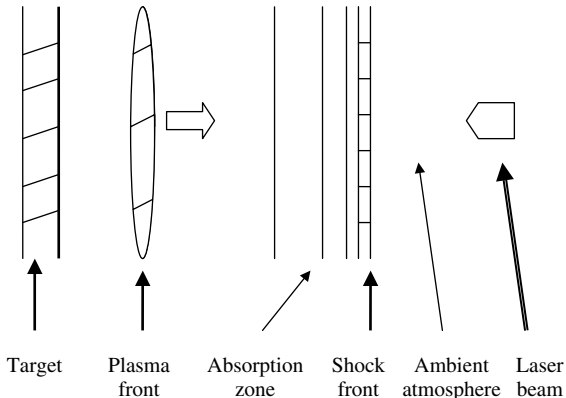


**Figure 2.12** Schematic elements of a laser detonation wave (LDW) expanding into an ambient atmospheric pressure gas

### 2.3 LASER ABLATION

Ablation scenarios are dependent on a multidimensional matrix of parameters including material properties and laser properties. Laser fluences of microjoules to millijoules per square centimeter can cause desorption of atoms and ions with no obvious physical change to the surface. At higher fluences, different mechanisms come into play because, for subsequent pulses, the laser energy is incident upon melted and recondensed matter. The surface reflectivity changes and an ablation crater, with or without elevated walls, forms. The elements of the original sample may have been selectively evaporated so that the redeposited material no longer exhibits the original composition. Important issues in ablation are: the minimum power density to initiate vaporization; the effects of longer or shorter laser pulse lengths; the rate at which ablation proceeds; and the goal of retaining the composition of the sample after ablation into the plasma. We discuss each of these in turn.

An estimate of the minimum power density within a laser pulse required to produce vaporization was given in Moenke-Blankenburg (Moenke-Blankenburg, 1989):

$$I_{\min} = \rho L_v \kappa^{1/2} / \Delta t^{1/2} (\text{W/cm}^2) \quad (2.23)$$

where  $\rho$  is the density of the target material,  $L_v$  is the latent heat of vaporization,  $\kappa$  is the thermal diffusivity of the target, and  $\Delta t$  is the laser pulse length. For pure aluminum,  $I_{\min}$  is about  $1.75 \times 10^8 \text{ W/cm}^2$  (Cremers and Knight, 2000).

The effect of laser wavelength is partly through the plasma frequency is described partly through the critical electron density given by Equation (2.22). However this must be coupled with the temporal length of the laser pulse to provide a full picture

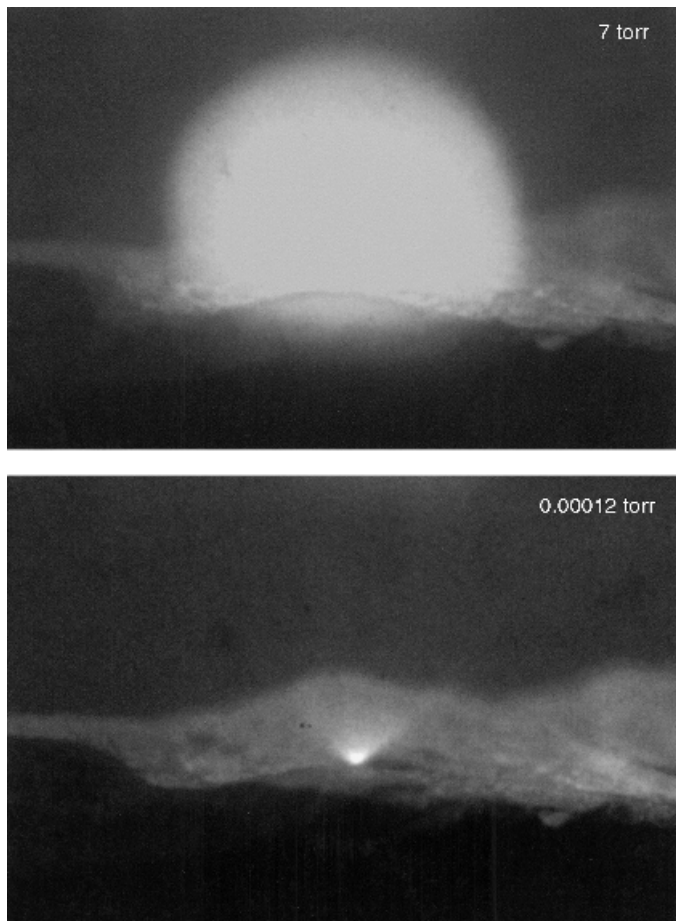


**Figure 2.13** Size variation of a LIBS plasma at 7 Torr and 0.00012 Torr of CO<sub>2</sub>. (Reproduced from Radziemski *et al.*, 2005, with permission from Elsevier)

of effects. Figure 2.14 illustrates the types of surface interactions that can dominate with lasers of different pulse lengths. The potential advantage of picosecond and femtosecond pulses is that absorption and interaction with the surface could be finished before a plasma or plume could form to absorb the laser energy. At terawatt powers the surface material could be rapidly ionized and ejected from the surface by Coulomb repulsion, rather than through thermal effects, as discussed by Russo *et al.* (Russo *et al.*, 2002a).

The maximum mass of material M that can be evaporated by a laser pulse of energy E is estimated to be:

$$M = E(1 - R)/[C_p(T_b - T_0) + L_v] \quad (2.24)$$

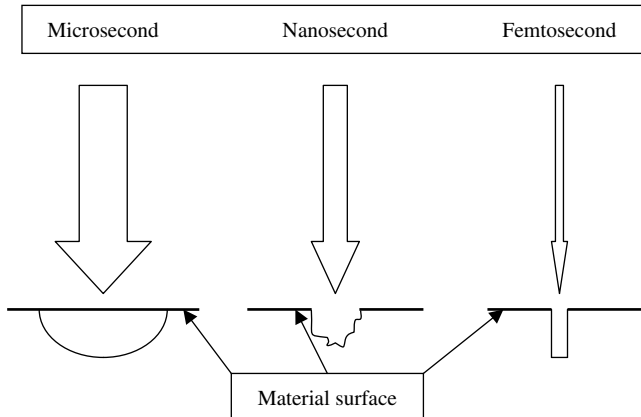


**Figure 2.14** Schematics of the interactions of lasers with different pulse lengths on solid surfaces. The microsecond and nanosecond interactions proceed through heating, melting and vaporization. Pulses shorter than the plasma initiation time lead to direct vaporization and the ability, for example, to drill holes with precision

where  $R$  is the surface reflectivity,  $C_p$  is the specific heat,  $T_b$  the boiling point (K),  $T_0$  room temperature (K) and  $L_v$  the latent heat of vaporization. This expression can be converted to ablated depth per pulse by using fluence  $F$  instead of  $E$ , and dividing by the density of the material.

In a study published in 1999, Vadillo *et al.* investigated the effect of plasma shielding on the ablation rate of pure metals as a function of many parameters: cover gas, pressure, fluence, and sample composition (Vadillo *et al.*, 1999). The metals were Zn, Al, Cu, Ni, Fe, Mo, W and Ti. A table of relevant physical constants was provided. Because the samples were drilled through completely, the parameter of  $\mu\text{m}$  per pulse was used as the figure of merit for ablation. The laser was an excimer pumped dye laser operating at 581 nm. Ablation rates in air ranged from  $0.04 \mu\text{m}/\text{pulse}$  for tungsten at  $1.3 \text{ J/cm}^2$  to  $5 \mu\text{m}/\text{pulse}$  for aluminum at  $16.7 \text{ J/cm}^2$ . Table 2.6 reproduces some of the results contained in Table 2 of Vadillo *et al.* (Vadillo *et al.*, 1999). Note the leveling off of depth per pulse with increasing fluence, which is caused by increasing plasma shielding with higher fluence. They also observed a significant increase in average ablation rate with decrease in air pressure from 1000 to 250 mbar, but a leveling off below that value.

Finally, they calculated theoretical ablation rates from Equation (2.24) modified to provide ablation depth as described above. They found that, for several metals, the theoretical and observed rates matched within 20% for a fluence of  $5.3 \text{ J/cm}^2$ , but deviated for lower and higher fluences. In a different experiment, Semerok *et al.* (Semerok *et al.*, 2002) used Ti:sapphire laser pulses on copper at pulse durations between 70 fs and 10 ps. At  $20 \text{ J/cm}^2$  per pulse, they found ablation rates from 0.24 to  $0.15 \mu\text{m}$  per pulse. Multari *et al.* performed a thorough study of some of the geometric factors related to ablation, such as lens-to-surface distance (LTSD)

**Table 2.6** Averaged ablation rate values in  $\mu\text{m}/\text{pulse}$  for some pure metals, at atmospheric pressure in air, as a function of fluence

Fluence ( $\text{J}/\text{cm}^2$ )	1.3	5.3	7.7	16.7
	Depth/pulse ( $\mu\text{m}$ )			
Aluminum	1.3	2.5	4.2	5.0
Copper	0.11	0.50	0.38	0.50
Tungsten	0.04	0.20	0.23	0.15

Data from Vadillo *et al.* (1999), with permission from John Wiley & Sons, Ltd

and angle of incidence on the surface (Multari *et al.*, 1996). They observed, for a Nd:YAG 10 ns pulse at  $1.06 \mu\text{m}$  and 185 mJ per pulse, that solid aluminum was ablated at between 10 and 100 ng per pulse, depending on the lens used and the LTSD.

Material ablated into the plasma can have the form of particles (either fresh, or melted and cooled) as well as atoms and/or molecules. Because of the different volatilities of elements and their compounds, the vaporization of elements into the plasma does not necessarily mirror the sample's composition. The result is shown in Figure 2.15 (Yamamoto *et al.*, 2005). Spectroscopic data plotted in the figure illustrate the large departure from stoichiometry possible, in this case for particles ablated from a steel sample. The black circles represent calibrated measurements, the other symbols a variety of LIBS measurements.

It is apparent that minimizing selective vaporization in order to retain stoichiometry is critical. Two phenomena appear to make this minimization more likely. When the energy deposited into the sample is much larger than the latent heat of vaporization for all of the constituents, it is likely that all constituents can be completely vaporized and removed. This is because target thermal properties and constants no longer play a major role. The same effect can be induced by desorbing atoms through nonthermal processes, such as bond breaking and photochemistry on a rapid time scale, faster than energy relaxation can occur at the surface. Ready (Ready, 1971) and Chan and Russo (Chan and Russo, 1991) have commented on the general nature of several regimes. For longer microsecond laser pulses and lower irradiances  $<10^6 \text{ W}/\text{cm}^2$ , the thermal nature of the process allows differential vaporization. At  $>10^9 \text{ W}/\text{cm}^2$  and nanosecond pulses, the pressure over the surface inhibits further vaporization until the substrate reaches a critical temperature. Because of the more uniform heating and a more explosive release, the melt ejected should be closer to the sample composition.

The literature is replete with models of the ablation process for a variety of laser and sample parameters. The recent review article by Bogaerts *et al.* (Bogaerts *et al.*, 2003) provides a good summary and list of references for these models, as well as references to the experimental literature. Most of the models start with pulses of at least a few nanoseconds in length, and assume that the interaction with the surface is through heating of the solid, followed by melting and vaporization. Especially

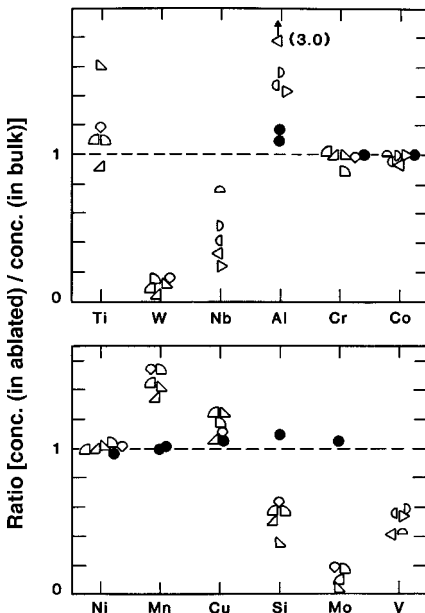


**Figure 2.15** Relative concentrations of elements in ablated material and bulk material. This illustrates the large departure from stoichiometry that is possible for ejected material. The case shown is for particles ablated from a steel sample by an acousto-optically Q-switched laser (Yamamoto *et al.*, 2005, with permission from Society for Applied Spectroscopy). The solid black circles represent calibrated concentrations to verify the method

for metals, where the relaxation of photon-excited electrons to the lattice is very rapid, this is a good starting point. For shorter laser pulses, the energy deposition by photons competes with the relaxation time, and a more sophisticated model of the coupling of electron temperature to lattice temperature is needed.

Laser ablation is of interest for many applications other than LIBS, for example for laser-ablation-ICP or ICP-MS. See for example a review by Russo *et al.* (Russo *et al.*, 2002b). Also, extensive use is made of laser ablation and desorption for material deposition in developing thin films and new superconducting materials, as discussed in Miller and Haglund (Miller and Haglund, 1998).

## 2.4 DOUBLE OR MULTIPLE PULSE LIBS

As mentioned earlier, researchers have used double or multiple pulses for LIBS, in various configurations, because it can result in very large enhancements in signal intensities. Figure 2.16 illustrates the timing between two pulses, where  $\Delta t$  represents the temporal difference between the arrival of the two pulses at the target. Here  $t_d$  stands for the delay from the initiation of the *second* laser pulse to the opening

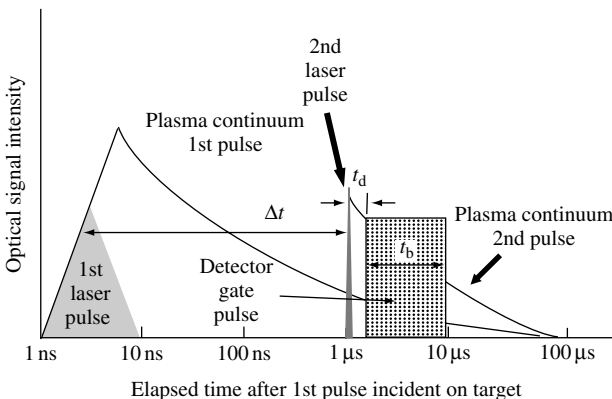


**Figure 2.16** The temporal history of a LIBS plasma when two laser pulses are used. The delay between the pulses is  $\Delta t$ , the delay to the opening of the window  $t_d$ , and window length is  $t_b$

of the window during which signal will be accepted. Several methods of generating the pulses and arranging them geometrically have been tried. These include:

- (1) multiple pulses within the same flashlamp pulse;
- (2) collinear beams from two lasers focused on the same spot on the target;
- (3) orthogonal beams, typically with one beam perpendicular and one parallel to the surface:
  - (a) where the pulse for the beam parallel to the surface is first in time forming an air spark (pre-ablative);
  - (b) where the pulse for the beam parallel to the surface is second, and reheats the material ablated by the first pulse (reheating).

Figure 2.17 illustrates these configurations schematically.

Proceeding historically, Uebbing *et al.* (Uebbing *et al.*, 1991) used the orthogonal reheating scheme and found enhanced intensities, less dependence on the matrix in which the element was found, but higher (poorer) detection limits. Sattman *et al.* (Sattman *et al.*, 1995), with method (1) above, used bursts of one to six laser pulses within a single flashlamp pulse. The multiple Q-switched pulses were generated by a Nd:YAG laser with one oscillator and two amplifiers. Pulse intervals ranged from 2 to 100  $\mu$ s. With a goal of improving the performance of LIBS in steel analysis, they found increased material ablation for multiple pulses, compared with a single pulse of energy equal to the sum of that of the individual pulses. For example a  $2 \times 40$  mJ double pulse removed about 1.4  $\mu$ g while two single noninteracting 40 mJ pulses only removed 1.0  $\mu$ g. Similarly, line intensities were greater and analytical performance improved. The improvement was ascribed to higher plasma temperatures and electron densities. They continued this work by investigating multiple-pulse steel analysis in the vacuum ultraviolet, finding detection limits of less than 10  $\mu$ g/g for phosphorus, sulfur and carbon (Sturm *et al.*, 2000).

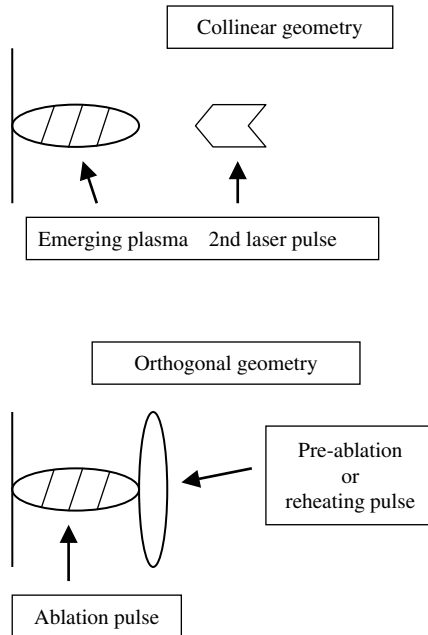


**Figure 2.17** Alternative geometries for double-pulse experiments: collinear and orthogonal. In the collinear case, the second laser pulse is incident both on the surface and the plasma formed by the first pulse. In the orthogonal case, the pulse parallel to the surface can come before (air plasma) or after (reheat) the pulse perpendicular to the surface

St-Onge *et al.* reported using two different wavelengths in double-pulse LIBS, 266 nm and 1064 nm from a Nd:YAG laser (St-Onge *et al.*, 2002). They found enhancements of 5 to 10 times using the two pulses over either of the single pulses, almost independent of which pulse came first.

Several papers from Angel's group dealt with the utility of method (3a), enhancing signals from metals and glasses from 10 to 30 times, as summarized in Stratis *et al.* (Stratis *et al.*, 2001). The mechanism by which the pre-ablation pulse caused enhanced ablation was not clear. Possibilities included sample heating, lowering the pressure above the sample surface, increasing electron density above the surface, and the interaction of the expanding shock on the surface.

## 2.5 SUMMARY

We have just touched the surface of a rich sub-field of physics and physical chemistry regarding laser plasmas. New data are emerging to clarify complex issues, and some of these will be discussed in Chapter 8. The principles discussed in this chapter will be useful in subsequent discussions that will focus on their application to spectrochemical analysis.

## REFERENCES

- Aguilera, J.A. and C. Aragón (2004). Characterization of a laser-induced plasma by spatially resolved spectroscopy of neutral atom and ion emissions. Comparison of local and spatially integrated measurements. *Spectrochim. Acta Part B* 59: 1861–1876.
- Bekeli, G. (Ed.) (1976). *Principles of Laser Plasmas*, John Wiley & Sons, Inc., New York.
- Bindhu, C.V., S.S. Harilal, M.S. Tillack, F. Najmabadi and A.C. Gaeris (2004). Energy absorption and propagation in laser-created sparks. *Appl. Spectrosc.* 58: 719–726.
- Bogaerts, A., Z. Chen, R. Gijbels and A. Vertes (2003). Laser ablation for analytical sampling: what can we learn from modeling? *Spectrochim. Acta Part B* 58: 1867–1893.
- Chan, W.T. and R.E. Russo (1991). Study of laser–material interactions using inductively coupled plasma–atomic emission spectrometry. *Spectrochim. Acta Part B* 46: 1471–1486.
- Cowan, R.D. (1981). *The Theory of Atomic Structure and Spectra*, University of California Press, Berkeley.
- Cremers, D.A., L.J. Radziemski and T.R. Loree (1984). Spectrochemical analysis of liquids using the laser spark. *Appl. Spectrosc.* 38: 721–726.
- Cremers, D.A., F.L. Archuleta and R.J. Martinez (1985). Evaluation of the continuous optical discharge for spectrochemical analysis. *Spectrochim. Acta Part B* 40: 665–679.
- Cremers, D.A. and A.K. Knight (2000). Laser-induced breakdown spectroscopy. In *Encyclopedia of Analytical Chemistry*, ed. R.A. Meyers, John Wiley & Sons, Ltd, Chichester: 9595–9613.
- Dewhurst, R. (1978). Comparative data on molecular gas breakdown thresholds in high-laser radiation fields. *J. Phys. D. Appl. Phys.* 11: 191–195.
- Galt, S., M. Sjoberg, M. Lopez Quiroga-Teixeiro and S. Hard (2003). Optical breakdown in fused silica and argon gas: application to Nd:YAG laser limiter. *Appl. Opt.* 42: 579–584.
- Generalov, N.A., V.P. Zimakov, G.I. Kozlov, V.A. Masyukov and Yu.P. Raiser (1970). Continuous optical discharge. *JETP Lett.* 11: 302–304.
- Gigosos, M.A., M.A. González and V. Cardenoso (2003). Computer simulated Balmer-alpha, -beta, and -gamma Stark line profiles for non-equilibrium plasmas diagnostics. *Spectrochim. Acta Part B* 58: 1489–1504.
- Griem, H.R. (1964). *Plasma Spectroscopy*, McGraw-Hill, New York.
- Griem, H.R. (1974). *Spectral Line Broadening by Plasmas*, Academic Press, New York.
- Griem, H.R. (1997). *Principles of Plasma Spectroscopy*, Cambridge University Press, New York.
- Hashida, M., A.F. Semerok, O. Godbert, G. Petite, Y. Izawa and J.-F. Wagner (2002). Ablation threshold dependence on pulse duration for copper. *Appl. Surf. Sci.* 197–198: 862–867.
- Hauer, A.A. and H.A. Baldis (1989). Introduction to laser plasma diagnostics. Ch. 3 in *Laser-induced Plasmas and Applications*, eds L.J. Radziemski and D.A. Cremers, Marcel Dekker, New York.
- Hecht, E. (1987). *Optics*, 2nd edn, Addison-Wesley, Reading, MA.
- Hummer, D.G. and G. Rybicki (1971). The formation of spectral lines. *Ann. Rev. Astron. Astrophys.* 9: 237–270.
- Keefer, D.R. (1974). Experimental study of a stationary laser-sustained air plasma. *J. Appl. Phys.* 46: 1080–1083.
- Keefer, D.R. (1989). Laser-sustained plasmas. Ch. 4 in *Laser-induced Plasmas and Applications*, eds L.J. Radziemski and D.A. Cremers, Marcel Dekker, New York.
- Kennedy, P.K., S.A. Boppart, D.X. Hammer, B.A. Rockwell, G.D. Noojin and W.P. Roach (1995). A first-order model for computation of laser-induced breakdown thresholds in ocular and aqueous media: Part II – comparison to experiment. *IEEE J. Quant. Elec.* 31: 2250–2257.
- Kim, Y.W. (1989). Fundamentals of analysis of solids by laser-produced plasmas. Ch. 8 in *Laser-induced Plasmas and Applications*, eds L.J. Radziemski and D.A. Cremers, Marcel Dekker, New York.

- Kuhn, H.G. (1963). *Atomic Spectra*, 2nd edn, Academic Press, New York.
- Lochte-Holtgreven, W. (1968). *Plasma Diagnostics*, John Wiley & Sons, Inc., New York.
- Miller, J.C. and R.F. Haglund (Eds) (1998). *Laser Ablation and Desorption*, Academic Press, New York.
- Millon, E., J. Perrière, R.M. Défourneau, D. Défourneau, O. Albert and J. Etchepare (2003). Femtosecond pulsed-laser deposition of BaTiO<sub>3</sub>. *Appl. Phys. A* 77: 73–80.
- Moenke-Blankenburg, L. (1989). *Laser Micro Analysis*, John Wiley & Sons, Inc., New York, p. 25.
- Multari, R.A., L.E. Foster, D.A. Cremers and M.J. Ferris (1996). The effects of sampling geometry on elemental emissions in laser-induced breakdown spectroscopy. *Appl. Spectrosc.* 50: 1483–1499.
- Oks, E. (1999). Advance in diagnostics for high-temperature plasmas based on the analytical result for the ion dynamical broadening of hydrogen lines. *Phys. Rev. E* 60: R2480–R2483.
- Parigger, C.G., D.H. Plemmons and E. Oks (2003). Balmer series H $\beta$  measurements in a laser-induced hydrogen plasma. *Appl. Opt.* 42: 5992–6000.
- Radziemski, L.J., D.A. Cremers and T.M. Niemczyk (1985). Measurement of the properties of a CO<sub>2</sub> laser-induced air-plasma by double floating probe and spectroscopic techniques. *Spectrochim. Acta Part B* 40: 517–525.
- Radziemski, L.J. and D.A. Cremers (Eds) (1989a). *Laser-induced Plasmas and Applications*, Marcel Dekker, New York.
- Radziemski, L.J. and D.A. Cremers (1989b). Spectrochemical analysis using laser plasma excitation. Ch. 7 in *Laser-induced Plasmas and Applications*, eds L.J. Radziemski and D.A. Cremers, Marcel Dekker, New York.
- Radziemski, L.J., D.A. Cremers, K. Benelli, C. Khoo and R.D. Harris (2005). Use of the vacuum ultraviolet spectral region for laser-induced breakdown spectroscopy-based Martian geology and exploration. *Spectrochim. Acta Part B* 60: 237–248.
- Ready, J.F. (1971). *Effects of High-power Laser Radiation*, Academic Press, New York.
- Root, R.G. (1989). Modeling of post-breakdown phenomena. Ch. 2 in *Laser-induced Plasmas and Applications*, eds L.J. Radziemski and D.A. Cremers, Marcel Dekker, New York.
- Russo, R.E., X. Mao and S.S. Mao (2002a). The physics of laser ablation in microchemical analysis. *Anal. Chem.* 74: 70A–77A.
- Russo, R.E., X.L. Mao, H.C. Liu, J. Gonzalez and S.S. Mao (2002b). Laser ablation in analytical chemistry – a review. *Talanta* 57: 425–451.
- Sattman, R., V. Sturm and R. Noll (1995). Laser-induced breakdown spectroscopy of steel samples using multiple Q-switch Nd:YAG laser pulses. *J. Phys. D: Appl. Phys.* 28: 2181–2187.
- Semerok, A., B. Sallé, J.-F. Wagner and G. Petite (2002). Femtosecond, picosecond, and nanosecond laser microablation: laser plasma and crater investigation. *Laser Part. Beams* 20: 67–72.
- Simeonsson, J.B. and A.W. Miziolek (1994). Spectroscopic studies of laser-produced plasmas formed in CO and CO<sub>2</sub> using 193, 266, 355, 532, and 1064 nm laser radiation. *Appl. Phys. B* 59: 1–9.
- St-Onge, L., V. Detalle and M. Sabsabi (2002). Enhanced laser-induced breakdown spectroscopy using the combination of fourth-harmonic and fundamental Nd:YAG laser pulses. *Spectrochim. Acta Part B* 57: 121–135.
- Stricker, J. and J.G. Parker (1982). Experimental investigation of electrical breakdown in nitrogen and oxygen induced by focused laser radiation at 1.064  $\mu\text{m}$ . *J. Appl. Phys.* 53: 851–855.
- Stratis, D.N., K.L. Eland and S.M. Angel (2001). Effect of pulse delay time on a pre-ablation dual-pulse LIBS plasma. *Appl. Spectrosc.* 55: 1297–1303.
- Sturm, V., L. Peter and R. Noll (2000). Steel analysis with laser-induced breakdown spectrometry in the vacuum ultraviolet. *Appl. Spectrosc.* 54: 1275–1278.
- Tambay, R. and R.K. Thareja (1991). Laser-induced breakdown studies of laboratory air at 0.266, 0.355, 0.532, and 1.06  $\mu\text{m}$ . *J. Appl. Phys.* 70: 2890–2892.

- Uebbing, J., J. Brust, W. Sdorra, F. Leis and K. Niemax (1991). Reheating of a laser-produced plasma by a second laser pulse. *Appl. Spectrosc.* 45: 1419–1423.
- Vadillo, J.M., J.M. Fernandez-Romero, C. Rodriguez and J.J. Laserna (1999). Effect of plasma shielding on laser ablation rate of pure metals at reduced pressure. *Surf. Interface Anal.* 27: 1009–1015.
- Vogel, A., K. Nahen, D. Theisen and J. Noack (1996). Plasma formation in water by picosecond and nanosecond Nd:YAG laser pulses. I. Optical breakdown at threshold and superthreshold irradiance. *IEEE J. Sel. Topics Electr.* 2: 847–860.
- von der Linde, D. and H. Schüller (1996). Breakdown threshold and plasma formation in femtosecond laser–solid interaction. *J. Opt. Soc. Am. B* 13: 216–222.
- Weyl, G.M. (1989). Physics of laser-induced breakdown. Ch. 1 in *Laser-induced Plasmas and Applications*, eds L.J. Radziemski and D.A. Cremers, Marcel Dekker, New York.
- White, H.E. (1934). *Introduction to Atomic Spectra*, McGraw-Hill, New York.
- Whiting, E.E. (1968). An empirical approximation to the Voigt profile. *J. Quant. Spectrosc. Radiat. Transfer* 8: 1379–1384.
- Williams, W.E., M.J. Soileau and E.W. Van Stryland (1983). Picosecond air breakdown studies at 0.53 μm. *Appl. Phys. Lett.* 43: 352–354.
- Yamamoto, K.Y., D.A. Cremers, L.E. Foster, M.P. Davies and R.D. Harris (2005). Laser-induced breakdown spectroscopy analysis of solids using a long pulse (150 ns) Q-switched Nd:YAG laser. *Appl. Spectrosc.* 59: 1082–1097.

---

# 3 Apparatus Fundamentals

---

## 3.1 BASIC LIBS APPARATUS

LIBS is a plasma-based method of atomic emission spectroscopy (AES) that uses instrumentation similar to that used by other AES methods. The unique characteristics of LIBS originate from the use of a powerful laser pulse to both ‘prepare’ the target sample and then ‘excite’ the constituent atoms to emit light. Sample preparation results from the action of the focused laser pulse on the target that removes a small mass of the target in the form of atoms and small particles (Chapter 2). Coincident with ablation is the formation of a microplasma in the focal volume of the laser pulse that excites the ablated atoms. The plasma continues this excitation after the laser pulse. In addition, small ablated particles are vaporized in the hot plasma and the resulting atoms excited.

A typical LIBS apparatus is shown diagrammatically in Figure 3.1 (Plate 3) along with a photo of a simple LIBS apparatus. The main components are:

- (1) the pulsed laser that generates the powerful optical pulses used to form the microplasma;
- (2) the focusing system of mirror and lens that directs and focuses the laser pulse on the target sample;
- (3) target holder or container (if needed);
- (4) the light collection system (lens, mirrors or fiber optic) that collects the spark light and transports the light to the detection system;
- (5) detection system consisting of a method to spectrally filter or disperse the light such as a spectrograph and a detector to record the light;
- (6) computer and electronics to gate the detector, fire the laser, and store the spectrum.

The basic components of any LIBS system are similar but the component specifications are tailored to the particular application. These specifications include physical parameters such as size, weight, packaging, power and utilities required for operation as well as technical specifications pertaining to operational performance. These will be discussed in detail below, but examples include the energy of the laser pulse and the spectral resolution of the spectrograph.

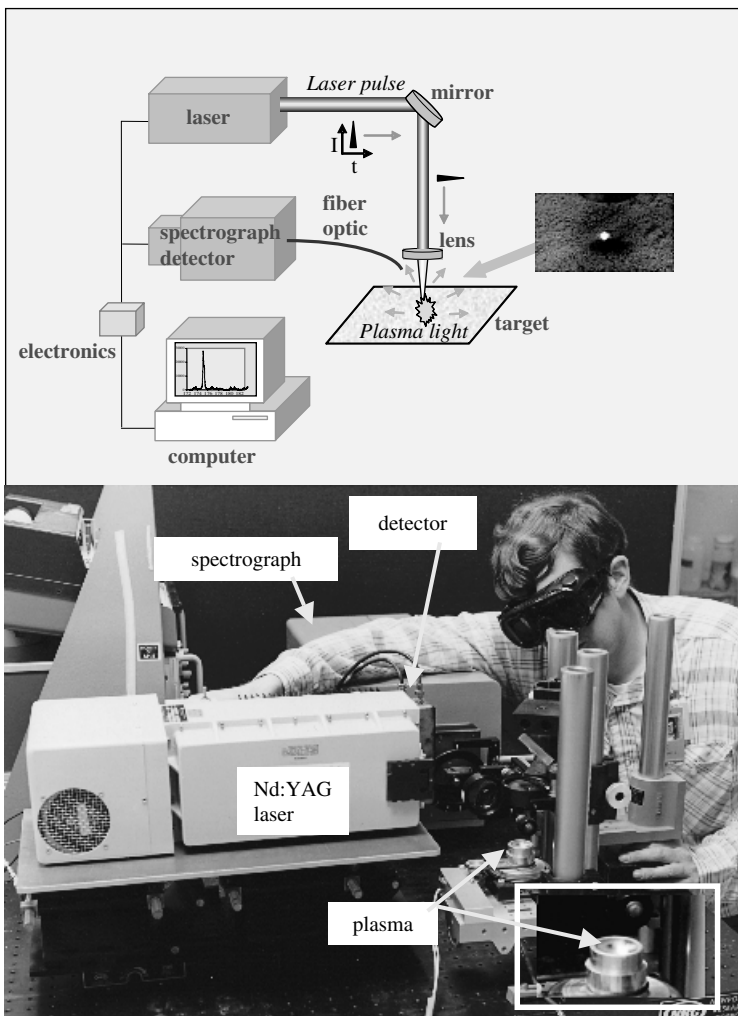


**Figure 3.1** Diagram of a typical LIBS set-up. The photo shows a simple LIBS set-up used to analyze material on a filter (see Plate 3)

## 3.2 LASERS

### 3.2.1 LASER FUNDAMENTALS

Principles of laser operation in general and the operation of specific lasers are described in detail in numerous books (Svelto, 2004). The discussion here will be limited to the fundamentals of the operation of the flashlamp-pumped Nd:YAG laser which is used for the majority of LIBS measurements. A basic Nd:YAG laser is

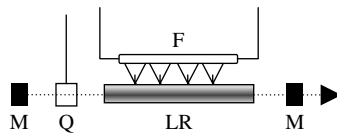


**Figure 3.2** Nd:YAG laser configuration. F, flashlamp; LR, laser rod; M, mirror; Q, Q-switch

shown diagrammatically in Figure 3.2. In brief, a flashlamp is fired to produce broadband light (pumping light) extending over the near UV, visible, and near IR spectral regions. A small percentage of this pumping light is absorbed by ions doped into the lasing material (Nd ions in a YAG crystal matrix; YAG, yttrium aluminum garnet). Due to the electronic energy levels of the Nd ions in the laser rod, if the flashlamp pumping is sufficiently strong, a population inversion is established in which the upper level of the lasing atomic transition is more populated than the lower terminating level of the transition. In this case, a photon passing through the laser rod at the same frequency as the lasing transition will experience gain or amplification by inducing decay of some of the ions from the upper to the lower state (stimulated emission). If the rod is surrounded by a resonant cavity composed of two mirrors in which some of this amplified light is directed back into the rod, significant amplification of light at the wavelength of the lasing transition can be achieved.

For LIBS, powerful laser pulses on the order of 5 MW are needed to form the microplasma when focused to a small spot. These high powers are easily achieved using a pulsed and Q-switched laser having moderate pulse energies. In this case, an electro-optic Q-switch shutter is positioned in the cavity to prevent photons at the laser wavelength from making a complete path through the cavity and inducing stimulated emission. In this way, the population inversion between the upper and lower levels of the lasing transition can become very large. When the Q-switch is activated by a suitably timed gate pulse, the Q-switch becomes transparent, allowing photons to make many traverses of the laser cavity resulting in a high power pulse of short duration. A fraction of this pulse leaves the cavity through a partially transmitting mirror (output coupler). For the Nd:YAG laser, the Q-switched pulse length is on the order of 5–10 ns. The pulse is of short duration because once lasing begins, the population inversion is rapidly depleted and lasing terminates. The Q-switch is intentionally closed shortly after the laser pulse to prevent the generation of additional pulses. The Q-switch can be pulsed more than once during the period of flashlamp pumping, however, to produce two powerful pulses for dual-pulse LIBS (Sections 3.2.5 and 8.6).

### 3.2.2 TYPES OF LASERS

Specifications of the pulsed and Q-switched Nd:YAG laser typically used for LIBS are listed in Table 3.1 along with specifications of some other lasers used for LIBS measurements. These other lasers include the excimer laser (UV wavelengths) and

**Table 3.1** Specifications of lasers used for LIBS

Type	Wavelength (nm)	Pulse width (ns)	Rep. rate (Hz)	Comments related to LIBS applications
Nd:YAG (s)	Fundamental: 1064 Harmonics: 532, 355, 266	6–15 4–8	ss to 20	(1) Fundamental wavelength easily shifted to provide harmonic wavelengths (2) Available in very compact form for small instrumentation (3) Good beam quality possible (4) Dual-pulse capabilities in single unit (5) Flashlamp or diode-pumped available
Excimer (g)	XeCl: 308 KrF: 248 ArF: 194	20 ns	ss to 200	(1) Requires periodic change of gases (2) Beam quality less than Nd:YAG laser (3) Provides UV wavelengths only
CO <sub>2</sub> (g)	10 600	200 (with 1000 ns trailing edge)	ss to 200	(1) Requires periodic change of gases or gas flow (2) Does not couple well into many metals (3) Beam quality less than Nd:YAG laser
Microchip	1064	<1 ns	1–10 k	(1) Good mode and beam quality (2) High shot-to-shot pulse stability (3) High rep. rates ~10 kHz

s, solid state laser; g, gas laser; ss, single shot.

the CO<sub>2</sub> laser (far IR wavelength) that use gas as the lasing medium. In this case an electrical discharge is produced in the gas that pumps the lasing species. The optimum type of laser used for LIBS depends on the application (Lorenzen *et al.*, 1992) and the desired laser wavelength.

Nd:YAG lasers (flashlamp pumped) are preferred for most LIBS applications because they provide a reliable, compact, and easy to use source of laser pulses of high focused power density. In addition, the fundamental wavelength can be easily shifted to generate pulses with fixed wavelengths ranging from the near IR to the near UV spectral regions. Typical laboratory and compact Nd:YAG lasers are shown in Figure 3.3. The latter type has been incorporated into compact, person portable instrumentation (Yamamoto *et al.*, 1996) and a cone penetrometer system (Miles and Cortes, 1998). Some important specifications of these two lasers are compared in Table 3.2. In a few cases, arc lamp pumped, acousto-optically Q-switched lasers have been used for LIBS (Ernst *et al.*, 1996; Yamamoto *et al.*, 2005). These lasers

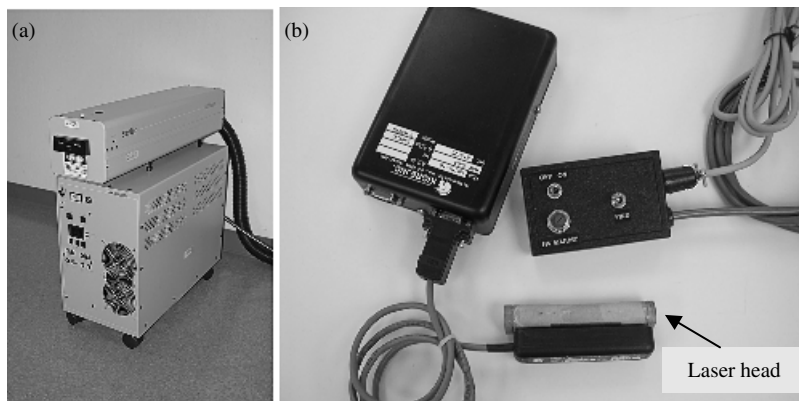


**Figure 3.3** (a) Typical laboratory Nd:YAG laser (Surelite laser; photo courtesy of Continuum, Inc.); (b) compact Nd:YAG laser (MK-367; photo courtesy of Kigre Laser, Inc.)

**Table 3.2** Specifications of the laboratory and compact Nd:YAG lasers of Figure 3.3

Parameter	Laboratory	Compact
Pulse energy (mJ) max.	450	25
Pulse width (ns)	5–8	4
Repetition rate (Hz)	10	1
Energy stability ( $\pm\%$ )	2	<10
Beam diameter (mm)	<10	3
Beam divergence (mrad)	0.5	1.1
Flashlamp lifetime ( $10^6$ shots)	10	0.3
Mass (kg)	71	1.2
Cooling	water	air
Power requirements	220 V AC; 12 A	12 V DC; 1.2 A

AC, alternating current; DC, direct current.

have repetition rates of several kilohertz but produce pulses with maximum energies up to 20 mJ. These have been used to sample solid surfaces such as metals and soils.

To increase the analytical performance of LIBS measurements, injection seeded Nd:YAG lasers have been investigated. Injection seeding is a method of producing laser output that operates on an ultra-narrow single longitudinal mode by injecting a ‘seed’ beam into the cavity from a single mode continuous wave diode pumped laser. The seed beam is typically injected into the Nd:YAG laser cavity through a fiber optic. The resulting laser pulse is near transform limited in linewidth and displays a smooth temporal profile in contrast to the intensity fluctuations normally observed from the unseeded laser operating multimode. The shot to shot stability of the laser pulse is enhanced using a seeded pulse. A recent study, however, has shown that in the analysis of gases, injection seeding did not improve analytical

precision (Hohreiter *et al.*, 2004). Other factors, such as the elimination of aerosol particles from the gas were found to significantly increase precision.

Pulse widths typically used for LIBS are in the range of 5–20 ns depending on the laser. In recent years there has been interest in evaluating the use of picosecond ( $10^{-12}$  s) (Eland *et al.*, 2001a) and femtosecond ( $10^{-15}$  s) pulses for LIBS. The majority of work appears to be devoted to femtosecond pulses (Eland *et al.*, 2001b; Scaffidi *et al.*, 2003). These pulses are usually generated by a mode-locked Ti-sapphire oscillator pumped by a continuous wave laser such as the solid-state Nd : YVO<sub>4</sub>. These lasers are not near the stage of development of the Nd:YAG laser for instrument applications and are more of a laboratory instrument. Use of these lasers, however, has revealed some interesting results in LIBS experiments and their use is expected to continue.

A new type of laser, the microchip laser (Zayhowski, 1999, 2000), has been demonstrated for LIBS analysis (Gornushkin *et al.*, 2004a). These lasers are made by dielectrically coating a thin piece of solid-state gain material to form a simple cavity which is then longitudinally pumped by a semiconductor laser. A saturable absorber is added to one end of the cavity to generate Q-switched pulses. A diagram of the components of the microchip laser is presented in Figure 3.4. Typically, these lasers produce pulses with durations of less than 1 ns and pulse energies in the low microjoule range. Because of the low energy, tight focusing of the laser pulse is needed to produce a plasma.

### 3.2.3 PROPERTIES OF LASER LIGHT IMPORTANT FOR LIBS

Properties of lasers important for LIBS include wavelength, pulse energy and focused pulse power density (irradiance). These determine whether an analytically useful laser plasma can be generated. For example, some laser wavelengths couple

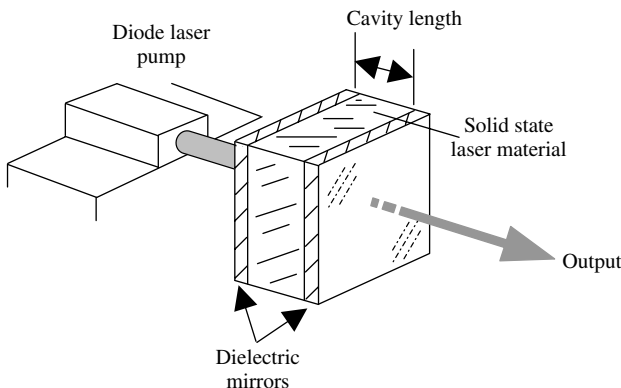


**Figure 3.4** Diagram of a micro-chip laser assembly. (After Zayhowski, 1999, with permission from Elsevier)

more readily into a specific material compared with other wavelengths. The CO<sub>2</sub> wavelength (10 600 nm) is highly reflected by a copper target as well as some other metals but this wavelength couples well into glasses and aqueous solutions which have high absorption in the IR. In addition, although a laser pulse may have focused power densities on the order of GW/cm<sup>2</sup>, if the pulse energy is too low, sufficient material may not be ablated and vaporized to provide a usefully strong emission signal.

Other important properties include the spatial quality of the laser pulse which determines the minimum spot size to which it can be focused. It may not be possible to focus a beam with poor quality to a sufficiently small spot to achieve power densities required to form a laser plasma. Some laser pulse properties are shown in Figure 3.5 and discussed below.

### 3.2.3.1 Irradiance

Lasers are unique sources of high irradiance (also termed intensity) light required to generate the laser plasma. The unit of irradiance is W/cm<sup>2</sup> or photons/cm<sup>2</sup>. The pulse energies used for LIBS typically range from 10 mJ up to 500 mJ. Given that the energy in a visible photon is  $\sim 10^{-19}$  J, the number of photons in a laser pulse used for LIBS ranges from  $10^{17}$  to  $5 \times 10^{18}$  photons. Note that these photons will be in a pulse having a duration of  $\sim 10$  ns for the usual LIBS experiment. For comparison, a thermal light source (blackbody) at a temperature of 1000 K will produce about  $10^{12}$  photons/s from a 1 cm<sup>2</sup> surface area within a bandwidth of 100 nm (a solid state laser will have a bandwidth  $< 0.001$  nm), or for comparison, only  $10^4$  photons in 10 ns.

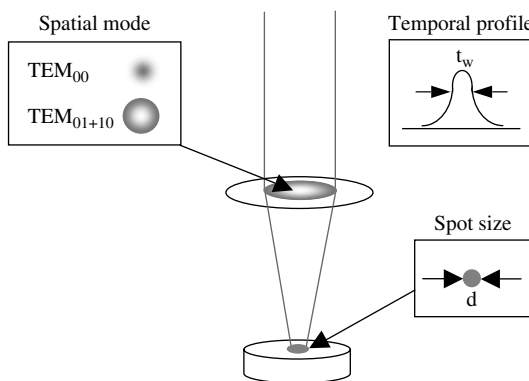


**Figure 3.5** Demonstration of some laser properties important for LIBS

### 3.2.3.2 Directionality

The ability of the laser pulse to propagate over long distances as a collimated beam is important for stand-off and remote LIBS measurements (Section 3.8 and Chapter 7). Here stand-off represents the projection of the laser pulse through the atmosphere or free space over a distance of many meters. Remote indicates transport of the laser pulse through a fiber optic cable. Both methods require a laser pulse with good directional beam qualities. A high quality laser which operates in a single lowest order mode (Gaussian mode) produces a laser beam that replicates closely a uniform plane wave having a constant phase distribution across the wavefront. Such a beam, emerging from the output coupler of the laser of diameter  $d$  will propagate as a highly directional, parallel beam for a distance given by  $\pi d^2/\lambda$ , often termed the Rayleigh range (Section 7.2.2). After this distance, the beam will begin to expand with an angular spread of  $\Delta\theta$  where  $\Delta\theta = d/\lambda$  is specified as the beam divergence.

### 3.2.3.3 Monochromaticity

Conventional light sources are broadband, generating light over a wide range of wavelengths. A laser on the other hand, has the ability to generate the majority of its output energy within a very narrow spectral range due to the laser light originating from a well-defined transition in the lasing medium. As noted above, for a solid state laser the bandwidth will typically be  $<0.001$  nm. In terms of excitation properties of the laser plasma, monochromaticity is not typically important. Analytically useful laser plasmas can be generated with IR, visible and UV wavelengths. Certain wavelengths couple more strongly into specific materials making wavelength important for ablation but a highly monochromatic beam is not important because the absorption spectra of bulk materials are usually slowing varying functions of wavelength. Monochromaticity may be important, however, in LIBS instrument design. That is, in some configurations, it may be desirable to use optical components that reflect the narrow band laser wavelength and then pass the broad spectrum of the laser plasma which is collected for analysis (open path LIBS, Section 7.2.3).

## 3.2.4 GENERATION OF ADDITIONAL WAVELENGTHS

For some target samples, the fundamental frequency of the laser (1064 nm for Nd:YAG) may not be optimum for LIBS analysis. Because of the typically good beam quality from Nd:YAG lasers and their high peak powers, a simple form of frequency conversion (or wavelength shifting) is possible to generate alternate wavelengths. This is accomplished using so-called harmonic generation simply by passing the laser pulse through a suitable birefringent material. Crystals of KDP (potassium dihydrogen phosphate) and KD<sup>+</sup>P (potassium dideuterium phosphate), which are relatively easy to produce in large sizes and which are transparent

**Table 3.3** Energy of fundamental and harmonic wavelengths of Nd:YAG

Wavelength (nm)	Energy (mJ)
1064	450
532	200
355	100
255	55

at the fundamental and shifted Nd:YAG wavelengths, are commonly used. Energy conversions are typically about 50%. In the simplest case, the 1064 nm fundamental is converted to 532 nm (2nd harmonic) which may be further doubled to 266 nm (4th harmonic). By combining the residual 1064 nm wavelength with converted 532 nm, the 3rd harmonic of 355 nm is generated. Table 3.3 lists typical energies available at the harmonic wavelengths for a laboratory Nd:YAG laser with specifications of Table 3.2.

These wavelengths can be used to generate other wavelengths not at harmonic frequencies using Raman shifting methods or by using them to pump dye lasers or OPOs (optical parametric oscillators). This adds complexity to the instrumentation, however.

### 3.2.5 DOUBLE PULSE OPERATION

Experiments have shown that in many cases the emission signals and signal-to-noise ratio in LIBS measurements can be enhanced through the use of dual laser pulses incident on the target in either a collinear or orthogonal configuration as shown in Figure 2.17 (Scaffidi *et al.*, 2006). For ultimate versatility, two independently operating lasers, separately triggered, provide the maximum versatility. That is, the pulses can be adjusted to overlap temporally or to be separated by any selected time interval and the pulse energies can be adjusted independently. The orthogonal pulse configuration will be easier to align compared with the collinear set-up when using two lasers but for implementation in the field, the collinear set-up is more feasible and will be useable for stand-off analysis. Also, the wavelengths of the lasers may be different to enhance certain effects. The use of a dual-pulse arrangement in which the pulses have different pulse widths has also been investigated (Scaffidi *et al.*, 2003).

In some experiments, where a pulse separation on the order of 40–160 µs is useful and the same wavelength is acceptable, a single laser can provide both pulses. An example is the detection of solids underwater (Pichahchy *et al.*, 1997). Specifically, Nd:YAG lasers that are electro-optically Q-switched can provide dual-pulse operation by using two Marx bank pulse generators to sequentially trigger the Q-switch. The triggering is set-up so the first Marx bank is triggered at the front of the pumping profile of the flashlamp and the second Marx bank is triggered at least 40 µs later but at a delay at which the flashlamp pumping rate is still sufficient to

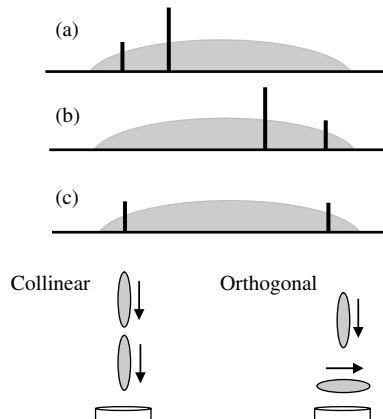


**Figure 3.6** Dual-pulse laser operation. Relative intensities of first and second pulses ( $E_1, E_2$ ) depending on positions relative to the flashlamp profile (shaded). (a)  $E_1 < E_2$ ; (b)  $E_1 > E_2$ ; (c)  $E_1 \sim E_2$ . Collinear and orthogonal dual-pulse configurations are shown

produce lasing. By adjusting the flashlamp pump energy, the timing between the two pulses and their positions within the envelope of the flashlamp profile, the relative pulse energies can be adjusted (Figure 3.6). Dual-pulse generation by the same laser is especially attractive for the collinear pulse configuration because the same optical system focuses the two pulses.

### 3.3 OPTICAL SYSTEMS

#### 3.3.1 FOCUSING AND LIGHT COLLECTION

In LIBS, laser pulses can be focused on the sample using lenses or mirrors as shown in Figure 3.7. Typically, a single lens is used to focus the laser pulses to a sufficiently small spot to achieve an analytically useful plasma (a). For systems requiring an adjustable focus, such as industrial process monitoring in which the lens-to-sample distance may be changing, a multi-lens system may be required with the relative positions of the lenses adjusted to locate the focal point on the target (b). Similarly, the laser pulses can be focused using a mirror (c).

Depending on the apparatus, a lens or mirror system may be used to collect the plasma light which is then directed into the detection system (e.g. spectrograph and detector). A single lens is the simplest optical arrangement to collect the plasma light although multiple lens systems may be used in certain cases. Unless constructed specifically to eliminate the effect, lens systems will exhibit chromatic aberration (Hecht, 2001), such that the focal position of the lens system is wavelength dependent (Figure 3.7d). This is due to the dependence of the refractive index of optical materials on wavelength. For example, for quartz, the refractive index

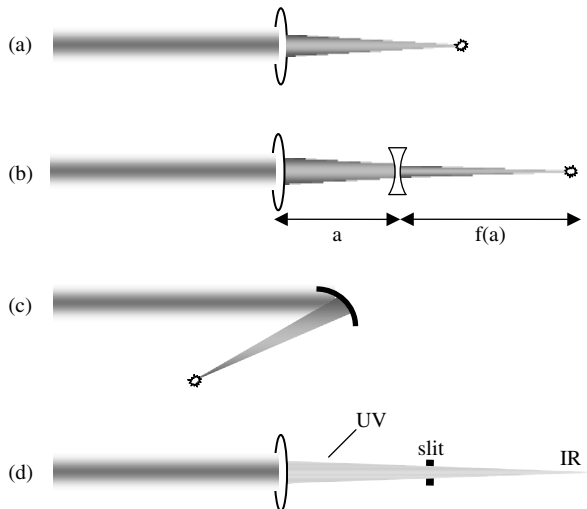


**Figure 3.7** Different arrangements for focusing laser pulses to generate a plasma

decreases with increased wavelength so that the focal length will increase with increased wavelength. An advantage of a mirror system is that all wavelengths will be focused at the same position. On the other hand, the use of a spherical mirror in an off-axis configuration will result in astigmatism and coma (Hecht, 2001) distorting the resulting image.

Typically, spherical optics are used to focus the laser beam, which is usually radially symmetric for an Nd:YAG laser. These result in a circular spot focused on the sample resulting in the plasma shown in Figure 3.1 which is radially symmetric with respect to the optical axis of the incident laser beam. By using cylindrical optics, however, a line or long spark can be formed on the target (Cremers and Radziemski, 1985; Arnold and Cremers, 1995; Mateo *et al.*, 2000; Rodolfa and Cremers, 2004). The area sampled by the long spark can be much larger than that sampled by the spark formed by a spherical lens allowing large areas to be more rapidly sampled. An example of such a focusing arrangement is shown in Figure 3.8 with the resulting spark shown in Figure 3.9. By using the donut mode from a laser with an unstable resonator, a long spark with a more uniform intensity distribution can be formed. When the long spark is formed by a Gaussian-like spatial mode, the ‘hot spot’ would be located in the center of the long spark.

### 3.3.2 LENSES

In the majority of LIBS systems, the laser pulses are focused into or on the sample using a simple lens. In addition, simple lenses are used to collect the plasma light and

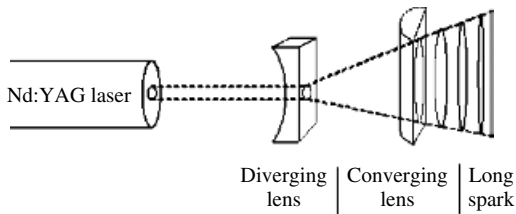


**Figure 3.8** Lens system used to form a long spark on a sample

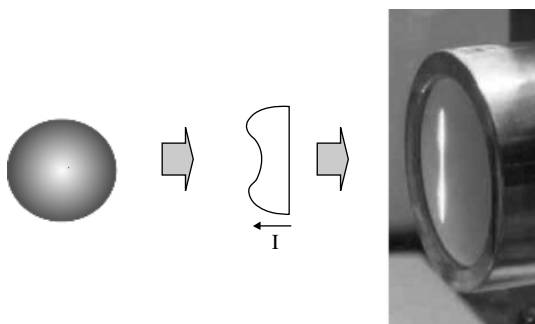


**Figure 3.9** Donut mode laser pulse produces a long spark with high intensity lobes at top and bottom. Shown on the right is the long spark formed on filter paper

either focus it into a spectrograph or onto a fiber optic cable. Important parameters of the lens are the focal length, diameter and material. Typical focal lengths for *in situ* measurements range from 50 to 150 mm with lens diameters of either 25 or 50 mm. The diameter of the laser beam from the majority of solid state lasers (or their harmonics) are on the order of 6–8 mm, suitable for the smaller lenses. More sophisticated, multilens focusing systems are needed, for example, for situations requiring variable focus, to focus the laser pulse over many meters, and to achieve the minimum spot size (highest power density on target).

Important properties of lenses are:

- (1) Material (e.g. bk-7, quartz, zinc selenide, germanium, NaCl). The lens should have maximum transmission at the laser wavelength and if used to collect plasma light, it must transmit efficiently at the wavelengths being monitored.
- (2) Anti-reflection coatings to minimize back reflections (to less than 0.5%, typical) and therefore maximize energy on target. This coating also minimizes reflections from the optic which may be directed back toward the laser or around the room. An uncoated optic will typically reflect about 4% of the light incident normal at each surface so a laser pulse traversing a lens will lose about 8% of the incident energy. For an optical system with many surfaces, the energy loss when using uncoated optics can be large.

- (3) Lens type (plano-convex, double convex, etc.). For critical applications, best form lenses that provide the minimum spherical aberration from a spherical lens may be preferred.
- (4) Scratch and dig is a measure of the visibility of surface defects, scratches and digs (pits). For most LIBS applications this is not a critical parameter.

### 3.3.3 FIBER OPTIC CABLES

Fiber optic cables (FOCs) are being used extensively with LIBS because they simplify collection of the plasma light (Figure 3.10). FOCs are particularly useful in applications in which the detection system cannot be positioned close to the target. An example is a subsurface cone penetrometer system in which the plasma may be generated many meters underground but the detection system is located at the surface (Theriault *et al.*, 1998). Prior to the use of FOC, the plasma light was either focused onto the spectrograph slit or the plasma was generated sufficiently close to the slit that a sufficient amount of light would pass through it. If focused on the slit, typically only a thin vertical slice through the plasma enters the spectrograph (Section 7.4.1). Small changes in the position of the plasma will greatly affect the intensity of observed light because the intensity and relative intensities of emissions are strongly dependent on position in the plasma.

A typical fused silica FOC design is shown in Figure 3.11. The fiber transmits the light using total internal reflection and those light rays entering the fiber within the acceptance cone angle (numerical aperture) will be reflected down the fiber with high efficiency (Figure 3.12). The acceptance angle of a fused silica fiber optic is  $\sim 26^\circ$  so that light will be collected from all parts of the plasma if positioned a few centimeters distant. Although the plasma emits UV light, in most applications ‘solarization,’ a UV light induced phenomenon that degrades the transmission efficiency of the fiber, does not appear to be a problem.



**Figure 3.10** Fiber optic cable used to collect plasma light. The SMA connector on this cable will interface to some types of spectrograph entrance slits

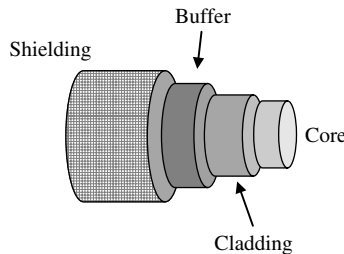


**Figure 3.11** Design of a fiber optic

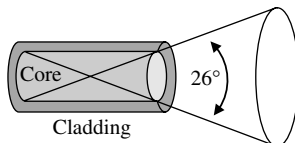


**Figure 3.12** Light rays entering the fiber within the acceptance cone will be transmitted

Fiber core diameters typically range from  $50\text{ }\mu\text{m}$  to 1 mm for fused silica. The fused silica can be high or low OH content with high OH fiber used in the UV/VIS and low OH fibers employed for the nearIR because of their low water content ( $<2\text{ ppm}$ ) and correspondingly lower absorption. A cladding material of lower refractive index ( $n_c$ ) than the core fiber ( $n_f$ ) is used to enhance the light guiding effect. Typical cladding is fluorine-doped silica producing a numerical aperture (NA) of 0.22, where  $\text{NA} = (n_f^2 - n_c^2)^{1/2}$ . Surrounding the cladding is a buffer to protect the cladding from scratches and other damage that may cause the fiber to break. The composition of the buffer determines the operating environment of the fiber. The typical polyamide buffer offers a wide temperature range ( $-100$  to  $400^\circ\text{C}$ ) and solvent resistance. For extremes of temperature ( $-90$  to  $750^\circ\text{C}$ ), a gold buffer is used.

Using a FOC, the plasma light can either be focused onto the fiber end to increase light collection or the fiber can simply be pointed at the plasma. Focusing on the fiber increases the sensitivity of light collection to alignment of the optical system. In contrast, pointing the fiber at the plasma reduces this alignment sensitivity (Section 7.4.1).

FOCs can be made in custom lengths having a variety of connector types (e.g. FCSMA905, ST, FC/PC). The composition of the FOC can also be custom tailored for the spectroscopic region of interest (Figure 3.13). For example, fiber materials are specially selected for the VIS/nearIR (350–2000 nm), UV/VIS (200–800 nm), and deep UV (solarization resistant fibers below 230 nm). Outer shielding is typically PVC, Kevlar reinforced PVC or metal shielding.

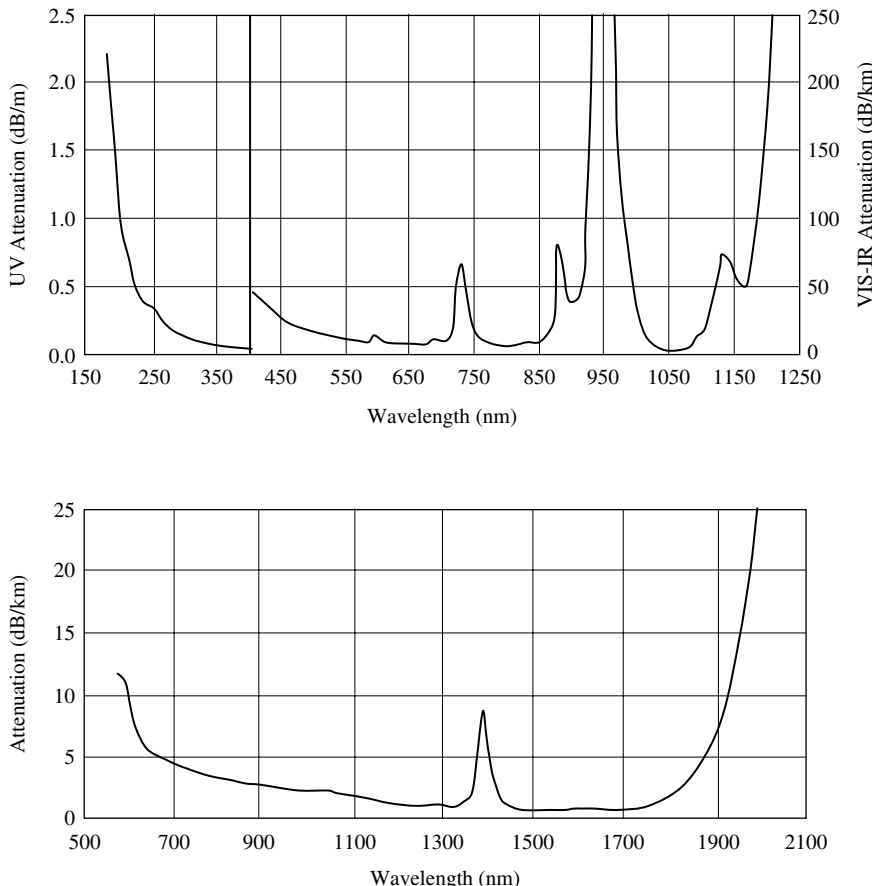


**Figure 3.13** Spectral transmission of UV (a) and IR (b) fiber optic materials. (Reproduced from *The Book on the Technologies of Polymicro*, 2005, with permission from Polymicro Technologies, LLC)

The discussion above relates to solid step index fused silica fibers. Other fiber types have been investigated for use with LIBS including graded index solid fibers, hollow-waveguide and photonic-crystal waveguide fibers, and hollow core fibers. Recently hollow-core photonic-crystal fibers have been used to deliver picosecond pulses which were then focused on a solid surface to form a laser spark (Konorov *et al.*, 2003). These fibers can transmit laser pulses having significantly higher fluences than is possible using fused silica fibers. Using the photonic-crystal fiber, however, it was not possible to form an air spark. Recently, it was demonstrated that by using a hollow-core fiber (cyclic olefin polymer-coated silver hollow fibers) an air plasma with high reproducibility can be formed for a straight or slightly curved fiber (Yalin *et al.*, 2005). The ability to form an air plasma was degraded

significantly as the fiber was bent further ( $1/R > 0.73/\text{m}$ ). Work remains to reduce bending losses to maximize energy transmission, but this demonstration opens up new possibilities for LIBS applications.

By using a bundle of individual fibers, custom FOCs can be constructed. Two examples are shown in Figure 3.14. One configuration involves a circular bundle at the light collection end of the fiber which is arranged as a linear array at the distal end. The linear array is positioned along the slit of a spectrograph to increase the amount of light directed into the instrument. In another arrangement (trifurcated cable), a circular fiber bundle of fibers is divided into separate bundled cables at the distal ends which can then be directed into different instruments. A common use is to route the collected light to different spectrographs each spanning different spectral regions. For commercial fiber optics, the specifications indicate that for a trifurcated bundle, 27% of the incident light is channeled into each leg while this increases to 43% for a bifurcated bundle. Losses are due to 4% reflection at each end and the packing fraction for fibers in the bundles, which is about 0.9. The positions of fibers in each bundle are randomized so that each of the divided ends will receive equal distributions of the light from the input end.

In addition to collecting plasma light, the FOC can also be used to deliver laser pulses to a remotely located sample (Cremers *et al.*, 1995; Davies *et al.*, 1995). The pulse energy leaving the fiber can be focused with a simple lens system to form the laser plasmas or the bare end of the fiber core may be ground smooth with a radius to serve as a short focal length lens. An example of a FOC probe delivering laser pulses is shown in Figure 3.15. The FOC shown here is delivering about 60 mJ of pulse energy.

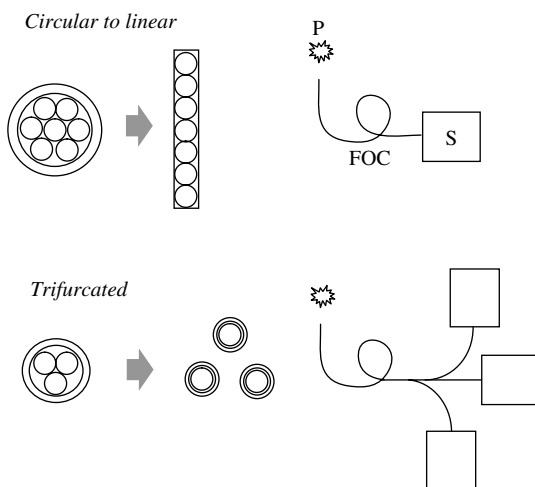


**Figure 3.14** Custom FOC configurations



**Figure 3.15** FOC probe for LIBS analysis. Using this probe, the plasma light was collected by the same fiber delivering the laser pulse. The plasma light was split off the distal end and directed into the detection system

### 3.4 METHODS OF SPECTRAL RESOLUTION

#### 3.4.1 INTRODUCTION

As described previously, the light from the laser plasma contains information about the elements composing the material via the set of emission lines characteristic of each element. The laser plasma can be considered as a sum of the white light continuum from the plasma and the discrete emissions from each atomic species and in some cases simple molecules. The complete emission spectrum of each element is unique, no two are identical. Figure 3.16 (Plate 4) demonstrates LIBS analysis using a low resolution spectral system and a higher resolution system. The light from the laser plasma on the right, when viewed through a simple transmission diffraction grating, shows a broad spectrum of low resolution. Strong emissions only from nitrogen in air are observed because air contains 80% nitrogen. When the same spectrum is viewed using a higher resolution spectral system, spectral features due to minor and trace elements in the soil are observed.

Figure 3.16 shows the importance of a high resolution detection system. When monitoring a single line as is often done in many types of atomic emission analyses, the possibility exists of spectral interferences, that is, that two or more elements may have the same emission wavelength or have emission lines sufficiently close in wavelength as to overlap. This overlap may prevent unambiguous monitoring of the element line of choice. If an atom is excited in a low density medium (e.g. a low pressure discharge tube or hollow cathode lamp), the emission lines can be very narrow, with a value of 0.01 nm typical. In a laser plasma, where the density of atomic species will be high, processes are active that will act to increase the width of the line. These include pressure broadening (due to collisions between species) and Stark broadening (due to the high electron density in the laser plasma). Because the plasma decays temporally after formation and the distribution of material in the plasma is very inhomogeneous, these widths can be reduced in some cases

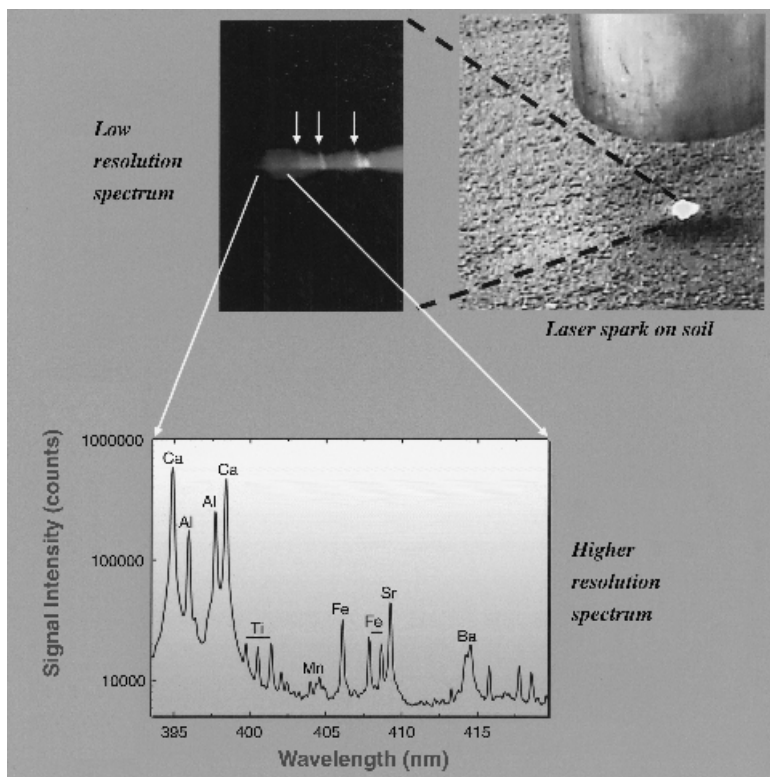


**Figure 3.16** LIBS spectrum produced by a simple transmission diffraction grating from the plasma formed at the right on soil. Here only strong lines of nitrogen from air are observed. Higher resolution of the spectrum shows emissions from major, minor and trace elements in the soil (see Plate 4)

by delaying observation to later times after the plasma has decayed, or viewing emissions from different areas of the plasma. Spectral overlap produced by broadening of lines by these processes is fundamental and determined by the physics of the atomic systems, as discussed in Chapter 2. Some practical aspects of measuring emission lines from LIBS spectra that partially overlap are discussed in Section 4.2.

There are several parameters important for describing the performance of a spectral resolution system. These will be discussed below in relation to a grating spectrograph.

### 3.4.2 SPECTRAL RESOLUTION DEVICES

The method of spectral resolution depends on the application and can be as simple as a spectral line filter to monitor a single wavelength or a sophisticated echelle

**Table 3.4** Comparison of methods of spectral resolution

Method	Characteristics
Spectral filter	Single fixed wavelength, small, inexpensive, useful for imaging
AOTF*	Single wavelength, tunable wavelength, useful for imaging
Grating monochromator	Single wavelength, high resolution, tunable, $f\#\sim 4$
Echelle spectrograph	High resolution, broadband spectral coverage, alignment more critical, typical $f\#>9$ , requires two-dimensional detector array
Grating spectrograph	Wide spectral coverage, high resolution, tunable, different gratings offers ability to tailor spectral resolution, $f\#\sim 4$

\* Acousto-optic tunable filter

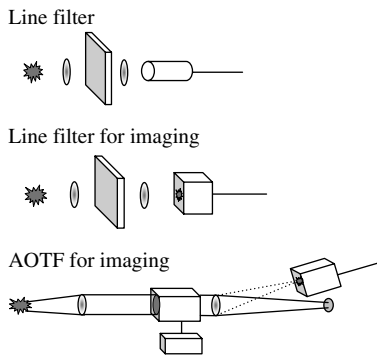


**Figure 3.17** Single emission line detection and imaging using a line filter and AOTF

spectrograph that can monitor simultaneously the majority of the useful LIBS spectral region (200–800 nm) for analysis in air. Table 3.4 lists methods of spectral resolution used for LIBS and some methods of single emission line detection are illustrated in Figure 3.17.

### 3.4.2.1 Spectral filters

Various types of filters are useful for LIBS (Figure 3.18). Long wave pass edge filters, for example, are useful to eliminate second order in spectrographs (e.g. 300 nm will appear at 600 nm unless it is removed by such a filter). Color filters can be used to transmit only the spectral region of interest to reduce light intensity at other wavelengths that may be particularly strong and may lead to high levels of scattered light in a spectrograph. A notch filter transmits over a broad spectral region but exhibits high attenuation within a small band. This filter will be useful for LIBS to filter out scattered 532 nm light when this wavelength is used to generate the laser plasma. This will be especially important if monitoring emission lines near 532 nm. Bandpass filters pass only a selected spectral region with high attenuation outside this region. The wavelength region passed by this filter is determined during

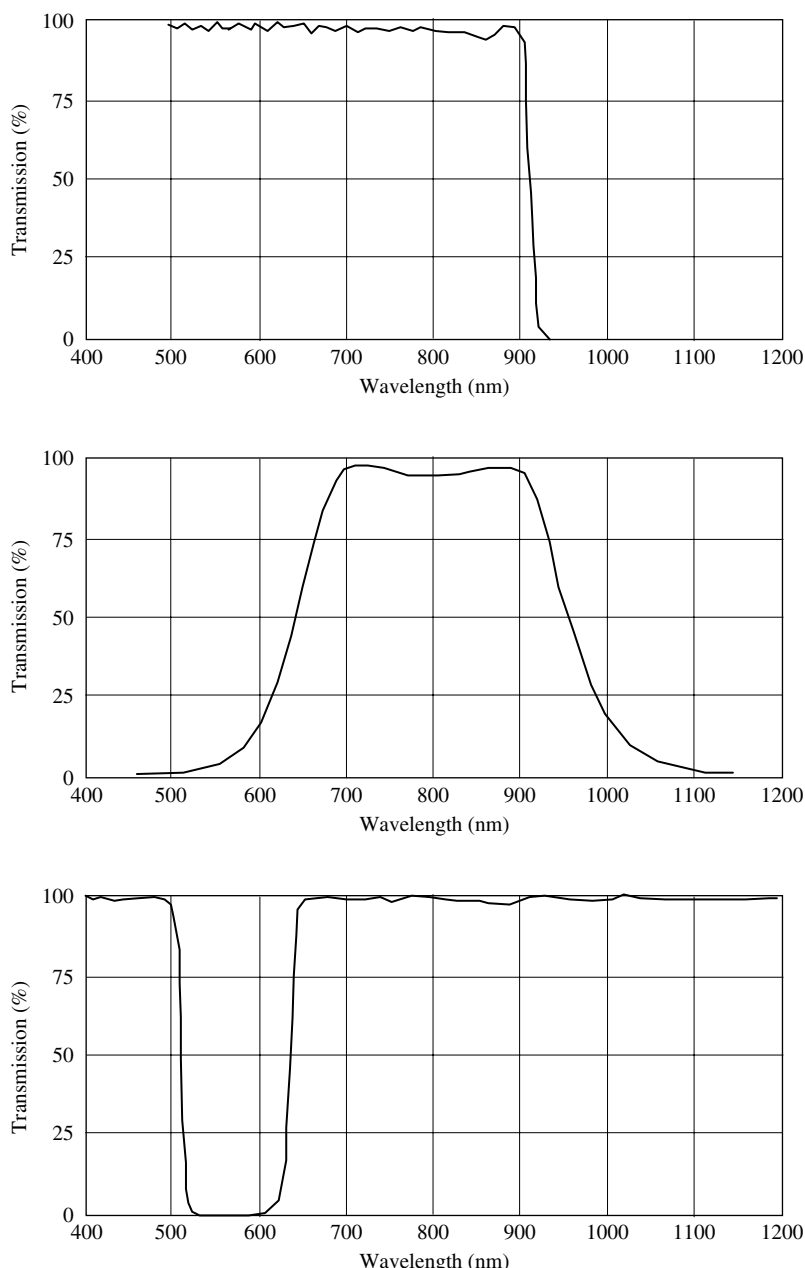


**Figure 3.18** Partial transmission curves for edge (a), bandpass (b) and notch (c) filters

fabrication and can be wide or narrow. Line filters or narrow bandpass filters are useful to transmit a certain emission line of interest. These filters would be useful for a simple LIBS instrument designed to monitor only a single or a few fixed emission lines. Such filters can be designed to transmit at a particular wavelength with a bandwidth down to 0.1 nm. They are manufactured using a series of dielectric coatings deposited on a suitable transmissive substrate (e.g. quartz for the UV). Tunable filters are angle sensitive and require a collimated beam of light to achieve maximum performance. Blocking of wavelengths outside the bandpass is typically  $10^{-4}$  and usable clear apertures are in the range 9 to 45 mm. Bandpass transmission at the center wavelength varies with filter specifications but is on the order of 40–70%.

### 3.4.2.2 Acousto-optic tunable filter (AOTF)

The AOTF is a solid-state electronically tunable spectral bandpass filter. It can be used for imaging in the light of a specific wavelength as well as serving as a simple spectral line selection device (Multari *et al.*, 1996). An AOTF consists of a crystal of tellurium dioxide or quartz with a piezoelectric transducer bonded to one side as shown in Figure 3.19. The piezo transducer is driven at radio frequencies (RF) to generate acoustical compression waves in the crystal that alter the refractive index of the crystal in a periodic pattern. This leads to the generation of a diffraction grating in the material so that a beam of collimated light incident at the Bragg angle is diffracted into the first-order beam. Changes in the frequency of the acoustic wave determine the spacing pattern in the crystal and hence the wavelength of the diffracted light. The power of the applied RF wave (5 W typical) determines the amplitude of the acoustic wave and hence the amplitude of the diffracted beam. The diffraction efficiency can reach  $\sim 80\%$  and the switching speed for both wavelength and power is on the order of megahertz. The AOTF requires collimated light (half-cone angle of  $\sim 5^\circ$ ) to achieve maximum performance. The use of a quartz crystal requires that the light be linearly polarized.

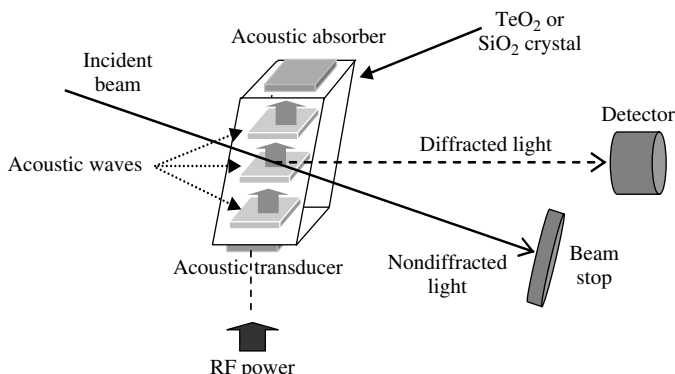


**Figure 3.19** Diagram of the operation of an AOTF device

An AOTF set-up is shown in Figure 3.17. AOTF systems can provide spectral selection from 230 nm to 4500 nm although a particular system is designed to operate efficiently over a narrower spectral range, typically 300 nm wide, with high efficiency selection of the desired wavelength ( $\sim 80\%$ ). For a particular device, the spectral resolution changes with wavelength over the operational range. For example, for one AOTF operating in the range 400–650 nm, the spectral resolution changes from 1 to 5 nm as the wavelength is scanned from the low to high wavelengths. Optical apertures range from  $2 \times 2$  to  $10 \times 10$  mm, useful for imaging. An example of an AOTF-filtered image of a LIBS plasma formed on a metal is shown in Figure 3.20 (Plate 5) (Multari and Cremers, 1996). Here the plasma was viewed in the light of the Cr(I) line at 425.4 nm. The evolution of the Cr emission from a tilted surface as a function of the time delay between plasma formation and observation of the light is shown here.

### 3.4.2.3 Spectrograph

A basic spectrograph is shown diagrammatically in Figure 3.21(a) (Plate 6). There are different designs (or mountings for the grating) such as the Littrow, Ebert-Fastie, Czerny-Turner, Paschen-Runge, and crossed-Czerny-Turner (James and Sternberg, 1969). The design differences relate to whether one or two mirrors are used for collimating and focusing the light and the position of the slits relative to the grating. The Czerny-Turner is shown in Figure 3.21 and is the most common variant in use. Here, light from the plasma is imaged onto the entrance slit. The light passing through the slit reaches the first mirror which collimates the light, directing it onto the grating. Ideally the grating will be filled with the light reflected by the mirror to achieve maximum resolving power. Light is reflected off the grating at different angles according to wavelength. This light then strikes a second mirror that focuses the light, now in the form of a spectrum, onto the focal plane. An array detector records the light preserving the horizontal distribution of light along the focal plane. In a spectrometer, a slit allows light over a selected narrow wavelength range to pass through to a detector.

Examples of spectra recorded with a spectrograph are shown in Figure 3.21(b). These demonstrate the operation of the spectrograph and the image presented at the focal plane. Here the spectrograph slits were set to a width of several millimeters compared with a usual setting of  $100\text{ }\mu\text{m}$ . In this case, an image of the laser plasma in the horizontal and vertical directions is formed at the focal plane at each wavelength of an emitting element. The elements observed here are N, Ca, Al and Si using Al metal as the target. The N emission originates from air. The spectra were obtained at different times after plasma formation and they show how the spectrum evolves with time. At the earliest time, the plasma spectrum is dominated by a spectrally broad background light that shows no strong emission features attributable to an element. At a later time, emissions from N(II) are observed and, as the plasma decays further with time, emissions from N(II) subside and are replaced by emissions from elements in the Al metal. These images show in effect the spatial dependence of the emission from the plasma in the light of each element observed.

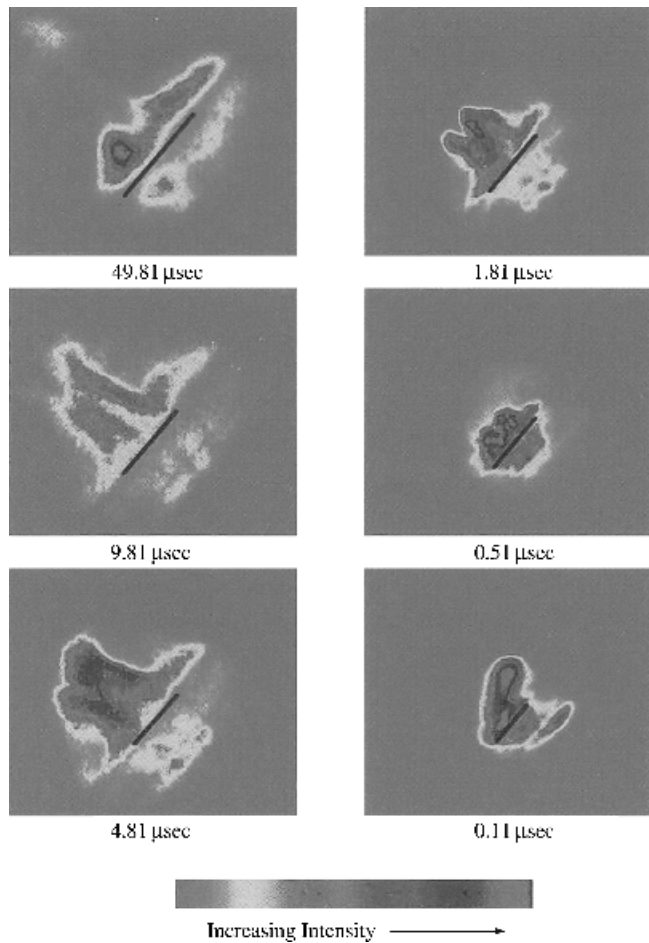


**Figure 3.20** Cr emission observed using the AOTF with an ICCD. (Reproduced from Multari and Cremers, Copyright 1996 IEEE) (see Plate 5)

Alternatively, individual slits can be located at the positions of emission lines along the focal plane. A light detector is then placed behind each slit to record the emission signal. An example is shown in Figure 3.22 together with a photograph of detectors positioned behind the focal plane of a 1 m focal length vacuum Paschen-Runge polychromator.

The  $f\# (=1/2 \times NA)$  of the spectrograph is determined by the diameter of the mirrors ( $d$ ) and the distance from the entrance slit to the first mirror ( $f$ ) according to  $f\# = f/d$ . The lower the  $f\#$ , the more light gathering capability of the instrument. For a 0.5 m spectrograph, a typical  $f\#$  is 4. The longer the focal length, the greater

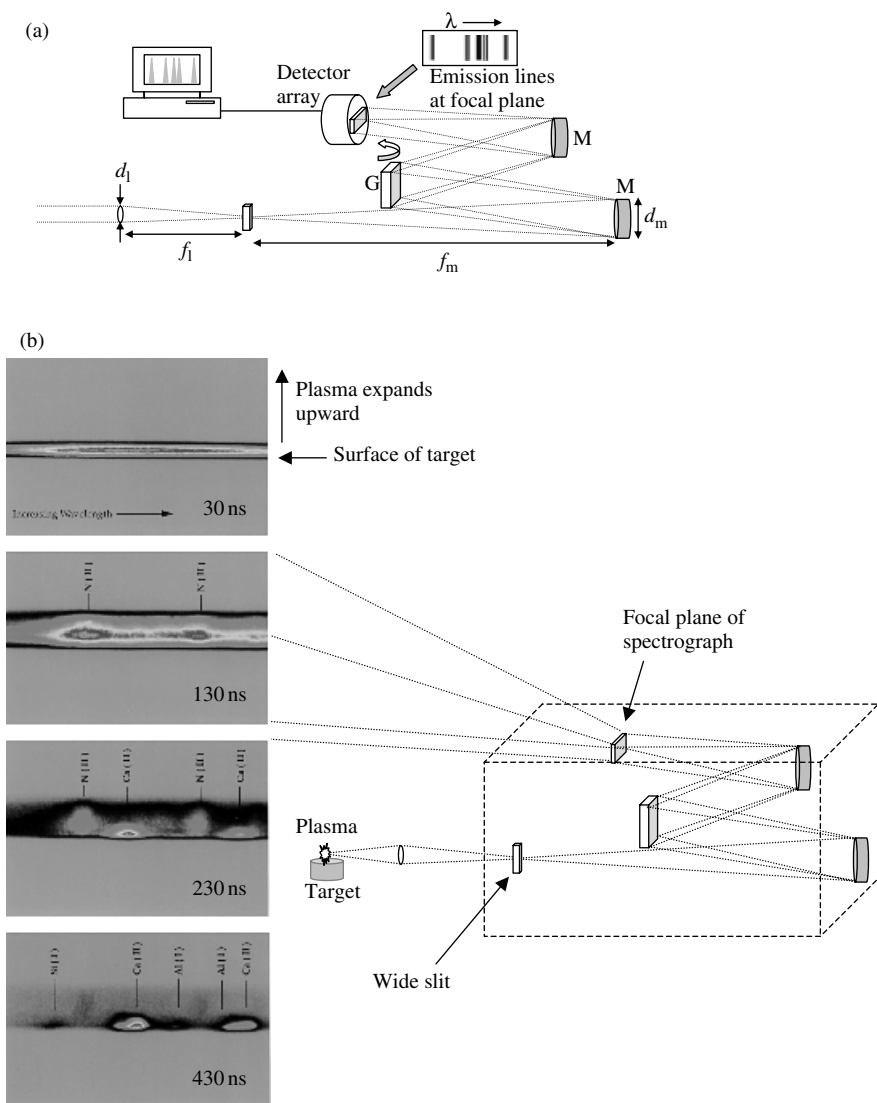


**Figure 3.21** (a) Detection of LIBS spectrum using a Czerny-Turner spectrograph and array detector. (b) Examples of LIBS spectra recorded at the focal plane of a spectrograph. (Multari *et al.*, 1996, with permission from Society for Applied Spectroscopy) (see Plate 6)

dispersion of the instrument. Typical specifications for a 0.5 m spectrograph are listed in Table 3.5.

To achieve maximum light throughput, it is important that the  $f\#$  of the spectrograph matches the  $f\#$  of the optical system directing the light onto the entrance slit. This is accomplished by proper selection of the lens (diameter and

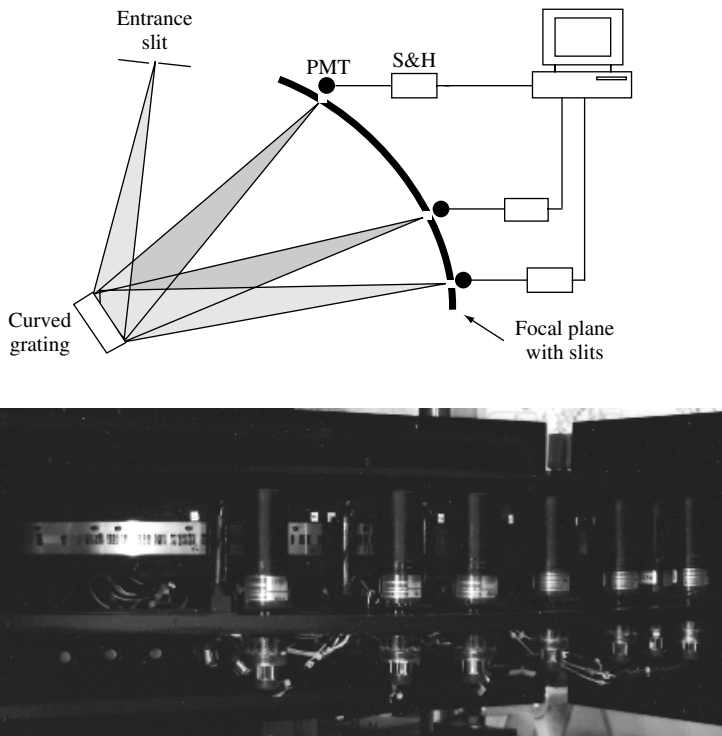


**Figure 3.22** Polychromator system with PMTs positioned behind slits in the focal plane. The PMT signal is processed, for example, using a sample-and-hold circuit (S & H). PMT = photomultiplier tube detector

**Table 3.5** Specifications for a 0.5 meter spectrograph

Optical design	Imaging Czerny-Turner
Focal length	500 mm
Grating	1200 lines/mm, 68 × 68 mm
Aperture ratio (f#)	4–6.5
Resolution (10 micron slit, 4 mm high)	0.05 nm
Reciprocal linear dispersion	1.7 nm/mm
Focal plane	27 mm wide × 14 mm high

focal length) used to focus the light onto the slit. Using an f# for the filling optics smaller than the f# of the spectrograph will overfill the mirror and grating resulting in scattered light.

An important parameter is the spectrograph resolving power expressed as:

$$R = \lambda / \Delta\lambda = nN \quad (3.1)$$

where  $n$  is the order of the spectrum and  $N$  is the number of lines on the grating illuminated by the light to be dispersed. Note that the resolving power is wavelength dependent and increases with the spectral order but it is independent of the size and spacing of the ruling in the grating. For a value of  $R = 2500$ , for example, at a wavelength of 250 nm, emission lines separated by 0.1 nm could be resolved. Spectrographs can have very high resolving powers, on the order of a million or higher.

The dispersion of a grating spectrograph is a measure of the spread of wavelengths. The angular dispersion, defined as  $d\theta/d\lambda$  is the angular separation of two wavelengths whose difference is  $d\lambda$ . It is readily obtained by differentiating the fundamental grating equation which results in:

$$d\theta/d\lambda = n/a \cos \theta \quad (3.2)$$

where  $\theta$  is the angle between the normal to the grating and the diffracted beam and  $a$  is the ruling spacing, the reciprocal of the number of lines per unit length. For example for a grating of 2400 grooves/mm, the ruling spacing is  $0.42 \mu\text{m}$ . As  $a$  gets smaller or the order number gets larger, the dispersion increases. However, the practicing spectrochemist is more interested in the spread of wavelengths across the width  $W$  of a focal plane, hence  $\Delta\lambda/W$ , called the reciprocal linear dispersion. To obtain that expression we start by defining the linear dispersion as:

$$dy/d\lambda = f d\theta/d\lambda \quad (3.3)$$

where  $y$  is a linear dimension in the focal plane parallel to the dispersion, and  $f$  is the focal length of the focusing optic, such as the second mirror in the Czerny-Turner arrangement. Then the reciprocal linear dispersion is:

$$d\lambda/dy = a \cos \theta / nf. \quad (3.4)$$

As a numerical example we will consider a fast (i.e. low f# value) vacuum spectrograph that we used for a vacuum ultraviolet (VUV) study (Radziemski *et al.*, 2005). It had 2400 lines/mm, 5 cm wide grating, a 30 cm focal length mirror, and was used in first order. For wavelengths between 150 and 200 nm the diffraction angle was close to  $45^\circ$ . So:

$$d\lambda/dy = 420 \text{ nm} \times (0.71)/300 \text{ mm} = 1.0 \text{ nm/mm}. \quad (3.5)$$

The CCD detector had  $1024 \times 1024$  pixels, each  $13 \mu\text{m}$  square. Hence the width  $W$  of usable focal plane was about 14 mm. Using the reciprocal linear dispersion, one could record about 14 nm of spectrum at one spectrometer setting.

Although spectrographs are more than a century old, new designs are being developed for LIBS. A high-resolution dual-grating Czerny-Turner spectrograph was

demonstrated for spectral imaging with LIBS (Gornushkin *et al.*, 2004b). In addition, high performance, very compact spectrographs incorporating array detectors are marketed by several manufacturers. An example is shown in Figure 3.23 along with some specifications.

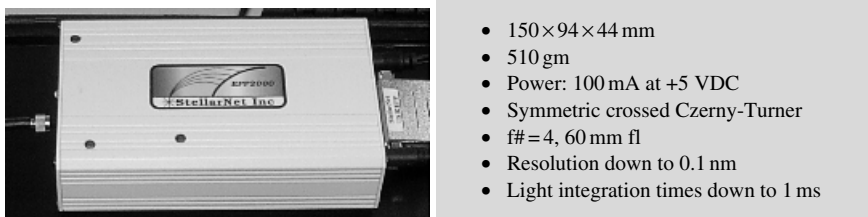


Figure 3.23 Compact, fiber-optic-coupled spectrograph. (Source: Stellar-Net [www.StellarNet.us](http://www.StellarNet.us))

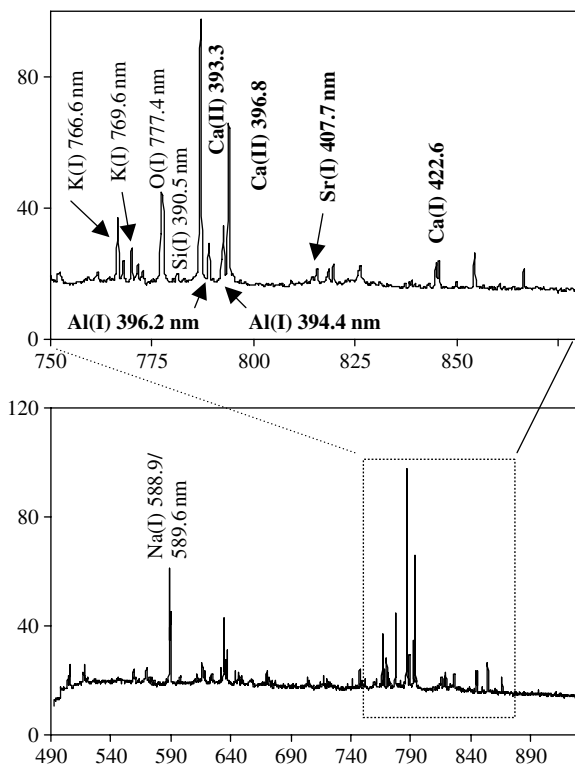


Figure 3.24 Spectrum obtained using a spectrograph similar to that shown in Figure 3.23

An example of a spectrum obtained with a similar instrument is shown in Figure 3.24. This is a spectrum of a certified soil sample obtained at a distance of 5.3 m with the sample maintained in 7 Torr of CO<sub>2</sub> to simulate the Mars atmosphere. The spectrum spans 490 to 930 nm and the detector was a CCD array. This spectrum demonstrates several issues discussed above. First, a limited, although wide spectral range is spanned by the spectrograph but many important lines of elements in soil below 490 nm are not observed in first order. Second, spectra of strongly emitting elements (Al, Ca, Sr, Si) are observed in second order at wavelengths above about 780 nm. These are shown in the expanded spectrum at the top. The lines of these elements appear at twice the wavelength. In this spectrum there is no strong interference of the elements appearing in second order with elements having emission lines in the range 750–775 nm. If there were strong interference between first- and second-order lines, an edge filter could be used to remove either element emissions above 750 nm (so second order would be observed unobstructed) or an edge filter could be used to eliminate emission below 450 nm so second order would not appear. Third, the wavelength spacing between elements in second order is double that for the first-order spectrum. Monitoring elements in second order is a method of achieving greater resolution and dispersion. Fourth, second order may be used to monitor elements at lower wavelength simultaneous with elements at greater wavelengths without requiring a second spectrograph tuned to lower wavelengths.

### 3.4.2.4 Echelle spectrograph

The ‘workhorse’ of LIBS analysis has been the spectrograph combined with either a photodiode array (PDA) or CCD array (Section 3.5). In recent years, however, the echelle spectrograph has been used more extensively and several compact versions have become available (Bauer *et al.*, 1998).

As shown in Figure 3.21, the conventional spectrograph uses a diffraction grating to produce the spectrum. This spectrum is recorded at the focal plane using a PDA or CCD. The spectral range recorded is limited by the width of the focal plane and the size of the array detector. Except in special cases, in which the vertical intensity distribution of the plasma light along the slit is used, the CCD is used in vertical binning mode with the intensities along the slit added to produce an intensity at each wavelength monitored along the focal plane.

Using an echelle spectrograph, the two-dimensional capabilities of the CCD can be utilized to increase the spectral range significantly. A diagram of an echelle spectrograph is shown in Figure 3.25. The echelle grating is a diffraction grating in which the number of lines/mm is much less than typically used in a conventional spectrograph (600 versus 2400). Because it is used at a high angle, the echelle produces spectra of very high dispersion but only over a short wavelength range in each grating order. The different orders of the grating will overlap and these are

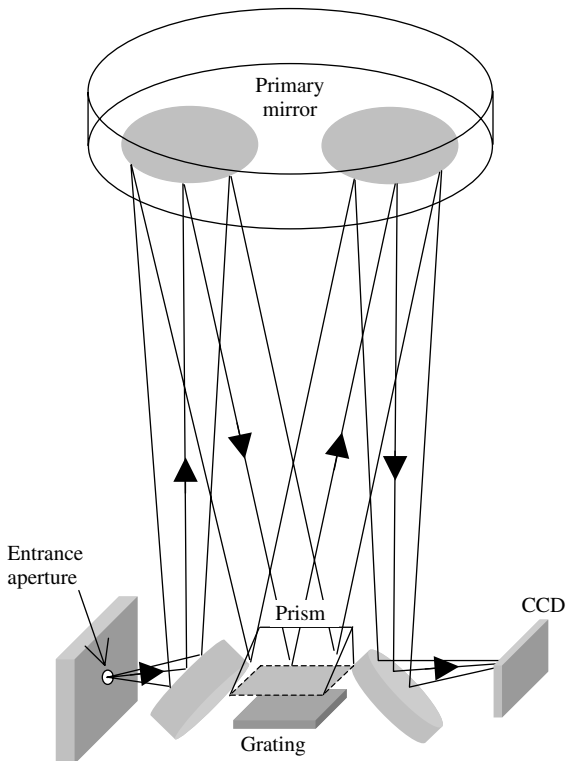


**Figure 3.25** Diagram of an echelle spectrograph. (Designed and Manufactured by Optomechanics Research Inc.)

spatially separated using a cross-dispersing element such as a prism. In this way, the various orders are stacked vertically in the echelle spectrograph focal plane. The two-dimensional detection capabilities of the CCD are then used to record the different orders resulting in the image of the orders or the echelleogram shown in Figure 3.26.

The different orders are easily seen in the echelleogram with longer wavelengths located at the bottom portion. The light ‘spots’ along the different orders correspond to emission from a specific element line. The echelleogram is useful to calibrate the echelle wavelength and adjust the optical alignment of the instrument. For spectral analysis, however, software is used to transform the echelle image to a spectrum. An example of a spectrum is shown in Figure 3.26. Note that the spectrum spans the main spectral region useful for LIBS analysis that extends from 200 to 800 nm. As with conventional spectrographs, different gratings can be used to increase instrument performance in certain spectral regions. Table 3.6 presents a comparison of two commercially available echelle instruments.

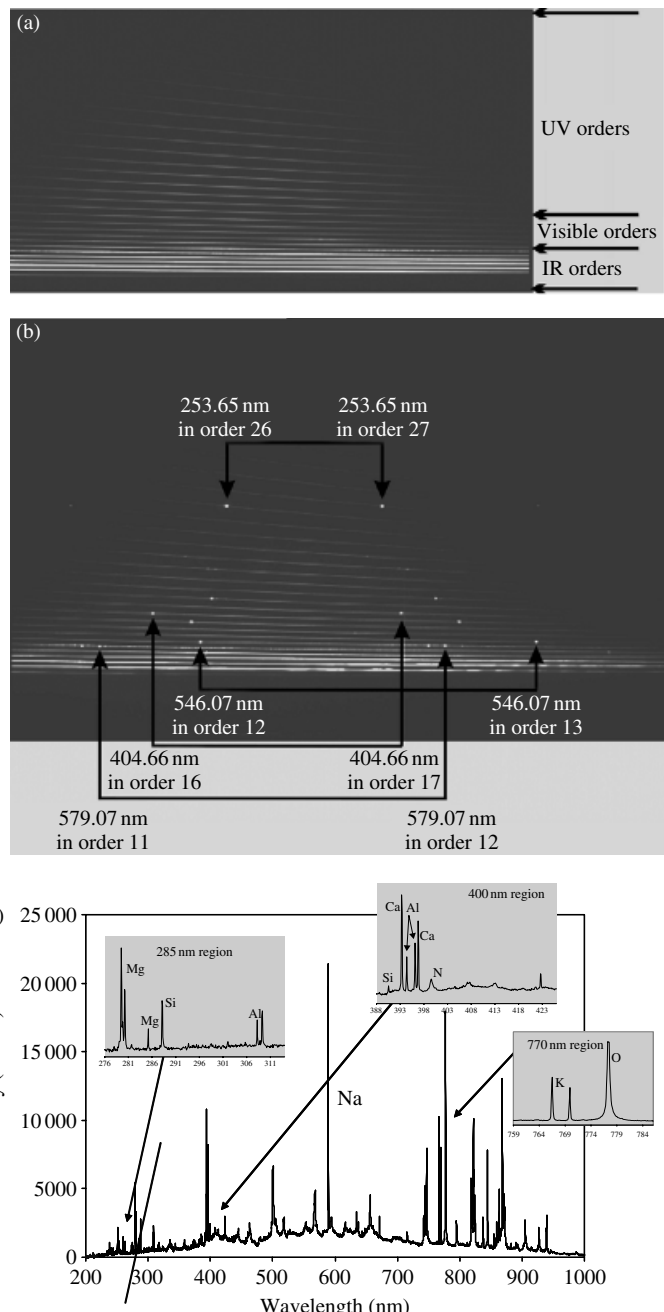


**Figure 3.26** (a) Arrangement of orders in the focal plane of an echelle spectrograph. (b) Emission lines from Hg lamp in the focal plane used to calibrate the wavelength. (c) LIBS spectrum of soil recorded using the echelle spectrograph and ICCD. (Photos courtesy of Catalina Scientific, Inc.)

**Table 3.6** Comparison of two echelle spectrographs (standard models, ICCD detector)

Parameter	Model 1	Model 2
Spectral range (nm)	190–1100	200–780
Spectral resolution ( $\lambda/\Delta\lambda$ )	1700	20 000
Focal length (cm)	20	25
Mass (kg)	4	4
Size (cm)	$12.7 \times 15.2 \times 32$	$14 \times 16 \times 32$

### 3.5 DETECTORS

The type of detector used with LIBS depends on many factors including the number of elements to be monitored and the type of spectral method used. A comparison of detectors typically used for LIBS is presented in Table 3.7. Using a line filter to monitor a single emission line as shown in Figure 3.17 requires only a sensitive light detector. Common examples are photomultiplier tubes (PMTs) or photodiodes, especially, sensitive avalanche photodiodes (APDs) (Squillante *et al.*, 2003). A variant of the APD, the Geiger photodiode has also been demonstrated for detection at low light levels (Myers *et al.*, 2003). The output of these devices is

**Table 3.7** Comparison of some detectors used for LIBS

Detector	Characteristics
Photomultiplier tube (PMT)	Measure instantaneous light intensity; temporal responses <1 ns; useful to map out decay response of plasma light; spectral response tailored to spectral region; inexpensive; compact; used with line filter or monochromator to provide single wavelength detection
Avalanche photodiode (APD)	Solid-state detector; high gain; fast response; rugged; compact; high signal-to-noise ratio; high quantum efficiency; fabrication as an array
Photodiode array (PDA)	Provides one-dimensional spatial information about light intensity along array; light intensity integrated with temporal response determined by readout time; used with spectrograph to provide simultaneous detection over a certain spectral range
Intensified PDA (IPDA)	PDA characteristics plus time-resolved detection down to few ns; more expensive than PDA
Charge coupled device (CCD)	Provides two-dimensional spatial information about light intensity on array; light intensity integrated with temporal response determined by readout time; used with spectrograph to provide simultaneous detection over a certain spectral range through vertical binning of pixel signals; intensity distribution along vertical dimension can be used in certain applications (e.g. long spark) or multiple FOC input at entrance slit to monitor spectra from different regions simultaneously
Intensified CCD (ICCD)	CCD characteristics plus time-resolved detection down to few ns; more expensive than CCD

a current in proportion to the intensity of incident light. These are not integrating devices as they provide a signal simultaneous in time with the incident light intensity. Therefore these can be used to monitor a selected spectral feature as a function of time. The current is typically integrated on a capacitor for a certain time period and the resulting voltage is the signal. Alternatively, the voltage can be digitized to produce a signal in the form of counts.

The ‘workhorse’ of photodetectors is perhaps the PMT which is compact, rugged, highly sensitive, and relatively inexpensive. PMTs come in a variety of sizes and the photocathode material is selectable to maximize sensitivity in certain spectral regions. A diagram of the operation of a PMT is shown in Figure 3.27(a). A light pulse striking the photocathode material results in the ejection of electrons that, through electrostatic focusing, travel through a set of dynodes coated with a secondary emissive material. An electron striking this material will eject additional electrons resulting in electron multiplication as the electron pulse produced by the light pulse, travels down the dynode chain. The large number of electrons is collected at the anode and results in a current signal with amplifications of  $10^6$  possible. In addition, PMTs that are ‘solar blind,’ that is, that do not detect IR or visible wavelengths are available. A diagram of a PMT and integrating circuit is shown in Figure 3.27(b).

Using a PDA, spectral information over a wide range can be recorded on each laser pulse. A diagram of a PDA is shown in Figure 3.28. The device is a linear array of closely spaced diodes with a typical diode size being  $25\text{ }\mu\text{m}$  wide  $\times 2.5\text{ mm}$  long.

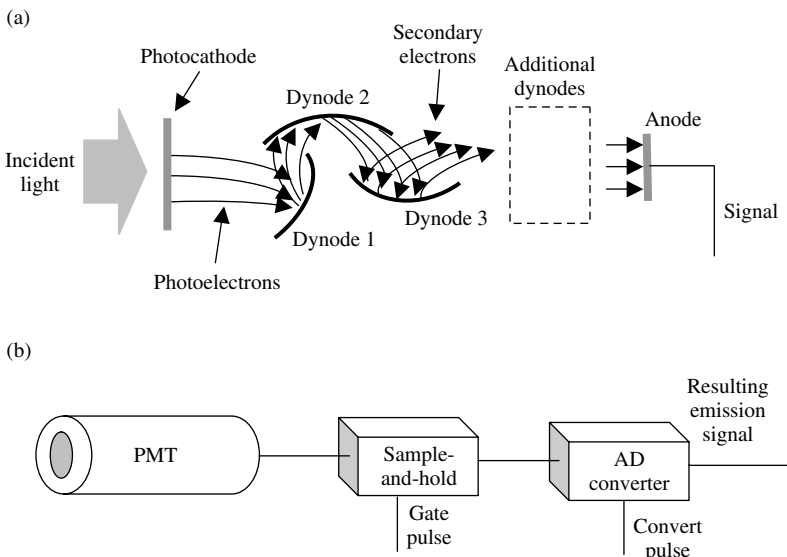


**Figure 3.27** (a) Diagram of the operation of a typical side-on PMT. (b) PMT with integrating and digitizing signal processing

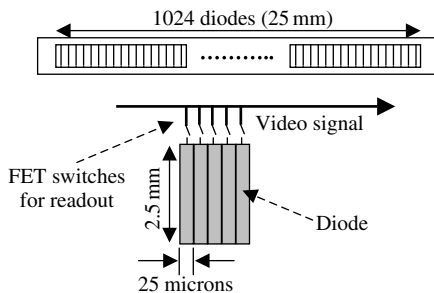


**Figure 3.28** Design of a linear PDA

The number of diodes ranges from 256 to 2048 although other configurations are possible. Light striking the diode removes charge and the amount of this charge is the signal. Following the exposure time period, the diodes are read out by measuring the amount of charge that must be added to each diode to achieve neutral charge. The diodes are read out sequentially.

Using a CCD, spectra over a wide range can also be recorded. The CCD, however, is a two-dimensional device so the  $x-y$  spatial distribution of light incident on the device can be recorded. Typical pixel sizes range from  $13 \times 13 \mu\text{m}$  up to  $26 \times 26 \mu\text{m}$ . The design of a CCD is shown in Figure 3.29. The arrangement shown here is  $512 \times 1024$  elements although many other array sizes are available. Like the PDA, the CCD integrates the incident light. Read-out of the array destroys the stored data and readies the array for the next record cycle. The CCD is readout by shifting all the rows vertically downward into the shift register which is then readout sequentially. After the pixel information (1024 separate pixels) in the shift register is read out, all rows are shifted down again and the new data in the

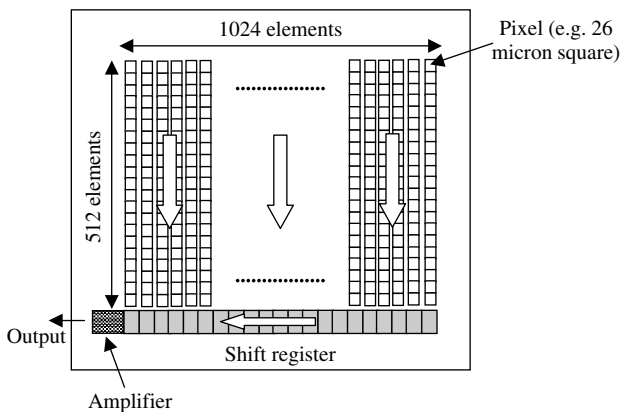


**Figure 3.29** Design of a CCD

shift register is read out. For a 512 pixel vertical array, 256 such shifts are required to completely read the array. Both the PDA and the CCD can be used to record a spectrum presented at the focal plane of the spectrograph. With the CCD, the intensity in the 512 pixels in each column are added or vertically binned to produce a single intensity at a particular wavelength in the focal plane. Using the CCD, however, information about the vertical distribution of light along the slit can be recorded also (Figure 3.21). This information can be useful, for example, if imaging a long spark along the entrance slit of a spectrograph. The vertical information will yield the distribution of a particular emission feature along the slit. That is, for each plasma, a map of the distribution of elements along the spark axis of those elements being monitored along the horizontal dimension of the CCD array (wavelength coverage) will be obtained. By scanning the long spark over a surface, a two-dimensional map of the intensity distribution can be constructed. An example is shown in Figure 3.30 (Plate 7).

A comparison of a typical PDA and CCD is presented in Table 3.8. An obvious advantage of the CCD is its two-dimensional capability, important for some applications such as imaging. For LIBS measurements in which the spectrum presented at the focal plane of the spectrograph is to be recorded, the two systems can be used somewhat interchangeably. There are certain applications, however, in which each has an advantage. For example, for low light levels, the CCD is preferred because of its lower dark current. The low dark current makes the CCD the detector

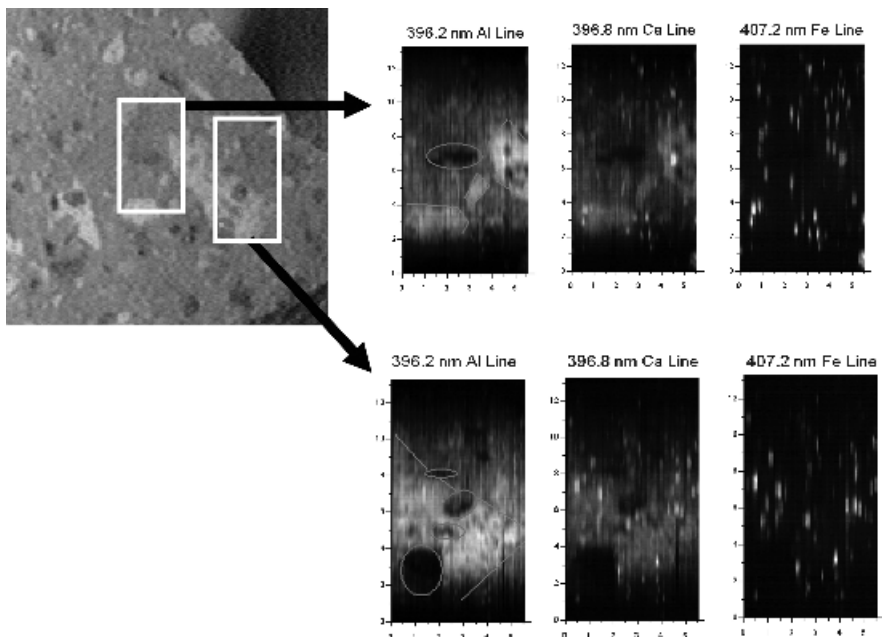


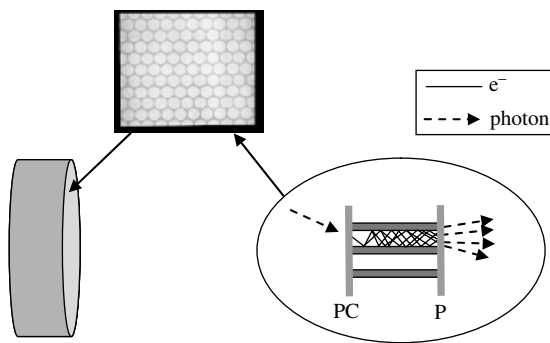
**Figure 3.30** Map of element emissions along a rock sample obtained by scanning a series of long sparks along the surface (see Plate 7)

**Table 3.8** Comparison of PDA and CCD array detectors (no MCP intensifiers)

Characteristic	PDA	CCD
Pixel size (example) ( $\mu\text{m}$ )	$25 \times 2500$	$13 \times 13; 26 \times 26$
Saturation level (no. e)	$125 \times 10^6$	650 000
Dark current (e/pixel/s)	600 000	100
Signal to noise (max.)	10 000:1	800:1
Electrons/count	1900	10
Spectral response (nm)	180–1100	180–1100

of choice for long integration times ( $>10\text{s}$ ) such as might be used with an echelle system where readout of the array after each shot is not feasible. On the other hand, the PDA is best for single shot measurements in which the signal levels are high or near the saturation level of the detector.

In LIBS, the decay of spectral features occurs on the microsecond time scale for a plasma generated using nanosecond laser pulses. On the other hand, typical readout times of  $1024 \times 1024$  arrays are on the order of a millisecond. Therefore, to obtain time resolved detection of an image, a shutter of some sort must be used to capture the image at a specific time after plasma formation. Clearly, for events on the microsecond time scale, mechanical shutters are too slow. An electronic shutter of some sort is required. Typical shutters used with array detectors are microchannel plates (MCPs) (Wiza, 1979). These are two-dimensional devices, like array detectors, that can be gated on and off very rapidly, on the order of a few microseconds for example, to permit or prohibit the passage of light. A diagram of an MCP is shown in Figure 3.31. MCPs consist of a thin sheet of glass tubes ( $\sim 10\text{--}100\,\mu\text{m}$  diameter) with length to diameter ratios of 40–100. The size of the MCP determines the number of tubes and arrays ranging from  $10^4$  to  $10^7$  individual



Typical size  $\sim 15\text{--}42\,\text{mm}$  diameter  
Gain  $\sim 10^3$   
No. channels  $\sim 10^4\text{--}10^7$

**Figure 3.31** Diagram of an MCP

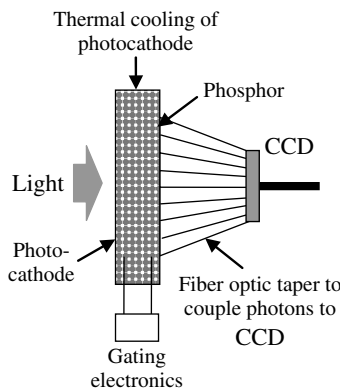


**Figure 3.32** Diagram of a typical ICCD

tubes. Gating is provided by applying a high voltage ( $\sim 1.5\text{ kV}$ ) between the front and back sides of the device. With the voltage applied, when a photon strikes the photocathode (PC), an electron is liberated that travels via multiple reflections down a narrow channel in the MCP. The insides of the tubes are manufactured to produce the desired secondary electron yield. In effect, each tube is a continuous dynode structure resembling a PMT. Because the electron is accelerated by the applied voltage, it acquires kinetic energy, and frees other electrons as it travels down the narrow channel. A single electron can give rise to as many as  $10^3$  electrons at the back end of the MCP. Electrons striking the luminescent phosphor screen (P) at the back of the MCP produce photons, many more photons than the single photon that initiated the electron cascade process. By adjusting the voltage, the gain of the MCP can be controlled. Note that MCPs are light gates only and do not record or store the incident light.

The detector of choice for many LIBS applications is the intensified CCD (ICCD) detector. These units are a CCD coupled to an MCP to provide time-gated detection of the laser plasma. A diagram of one configuration of an ICCD is shown in Figure 3.32. ICCDs can be used for time-resolved imaging, for example, with the AOTF or a line filter, or can be used with a spectrograph (Figure 3.21). Intensified PDAs (PDA + MCP) are also used for LIBS for time-resolved detection.

## 3.6 DETECTION SYSTEM CALIBRATIONS

### 3.6.1 WAVELENGTH CALIBRATION

In order to associate an emission line with a particular element, the recorded wavelength must be known within a certain precision. Following this, compilations of emission lines can be consulted to narrow down the choices and select the most appropriate element. Important factors to consider when selecting the appropriate

element of origin are discussed in Chapter 5. Single line filters are made for a particular wavelength ( $\pm$ tolerance) and these do not need to be calibrated although the bandpass wavelength can depend on extremes in temperature and the angle of incidence of the incident light on the filter surface. But polychromators and spectrographs must be wavelength calibrated using a calibration source having lines that can be unambiguously identified and associated with a specific wavelength. A common method of calibration uses a spectral lamp such as a ‘pencil style’ mercury or Hg lamp or hollow cathode lamp. The ‘pencil’ lamps are often preferred because they are a compact and stable source of narrow and discrete emissions lines. The Hg lamp in particular is widely used and the pattern of emissions lines readily identified for easy calibration. Lines for the Hg lamp are listed in Table 3.9 and in general these provide good spectral coverage for many important regions of the LIBS spectrum. For high resolution detection systems where wavelength coverage is reduced, another spectral source with a higher density of emission lines will be needed requiring the use of other calibration lamps, such as an iron hollow cathode. In addition to Hg, other readily available ‘pencil style’ lamps include Xe, Ar, Ne and Kr with lines in different spectral regions. The spectrum from these sources is recorded using the same experimental set-up used to record the LIBS spectrum. For calibration, at least two lines of known wavelength, ideally at each end of the recorded spectrum, are needed to calibrate the wavelength. When using only two lines, the assumption is that the dispersion remains linear across the spectral range

**Table 3.9** Hg calibration spectrum (Data sourced from Sansonetti *et al.*, 1996, with permission from Optical Society of America)

Wavelength (nm)	Intensity <sup>a</sup>
253.6521	300 000
289.3601	160
296.7283	2600
302.1504	280
312.5674	2800
313.1655	1900
313.1844	2800
334.1484	160
365.0168	5300
365.4842	970
366.2887	110
366.8284	650
404.6565	4400
407.7837	270
434.7506	34
435.8385	10 000
546.0750	10 000
576.9610	1100
579.0670	1200

<sup>a</sup> Relative units with the measured value of the 436 nm line arbitrarily set to 10 000.

so that a simple linear interpolation fit can be performed of wavelength versus position in the focal plane or versus wavelength setting on a monochromator. This approximation is fine for the width of array detectors, however, over a longer wavelength interval a better solution is to have identified lines at several positions across the focal plane so that a polynomial can be fit to the data to correct for nonlinear dispersion.

An example of wavelength calibration is shown in Figure 3.33. Figure 3.33(a) shows a LIBS spectrum obtained by analyzing a barium solution deposited on a filter. The detection system was an echelle spectrograph and ICCD detector. From the general area of the spectrum observed, a number of strong barium lines have been identified from compiled wavelength tables and these are labeled on the spectrum. The pixel number associated with each line is also indicated. Using the data of barium wavelength and corresponding pixel number (four points), we can fit the data as shown in Figure 3.33(b). The linear fit is excellent indicating constant linear dispersion across the focal plane. From the fit we can convert each pixel number to a corresponding wavelength and the resulting spectrum is shown in Figure 3.33(c). Using the calibrated spectrum, additional lines in the spectrum not used for calibration can be identified and these are listed on the calibrated spectrum. The H(I) line arises from the high concentration of hydrogen atoms from the filter material and sodium is ubiquitous in nature, found in many materials analyzed using LIBS.

### 3.6.2 SPECTRAL RESPONSE CALIBRATION

Each component of a LIBS detection system has a certain spectral response curve associated with it  $r(\lambda)$ . That is, the response depends on wavelength such that not all wavelengths are transmitted through or reflected off optical components with the same transfer efficiency. In addition, the detector used to record the light has a response function that is wavelength dependent. The end result is that the complete detection system (fiber optic, spectrograph, detector, lenses, etc.) will show a sensitivity that is wavelength dependent. In some cases it may be important to know how the response of the detection system varies with wavelength. As an example, the relative intensities of emission lines in different regions of the spectrum may be compared independent of the detection system response. In principle, the total response of a detection system may be computed from the separate response curves of the different components. Consider Figure 3.34 which shows response curves for the spectrograph, detector, and fiber optic cable. The responses have been normalized to 100 as most often it is the relative response of the system that must be computed with absolute response seldom used. By multiplying the different response curves, the total response  $r_{TOT}(\lambda)$  can be determined:

$$r_{TOT}(\lambda) = r_{FOC}(\lambda) \times r_{SPEC}(\lambda) \times r_{DET}(\lambda). \quad (3.6)$$

For the curves of Figure 3.34,  $r_{TOT}(\lambda)$  is plotted after normalization to 100. To correct a LIBS spectrum then for the spectral response of the detection system,

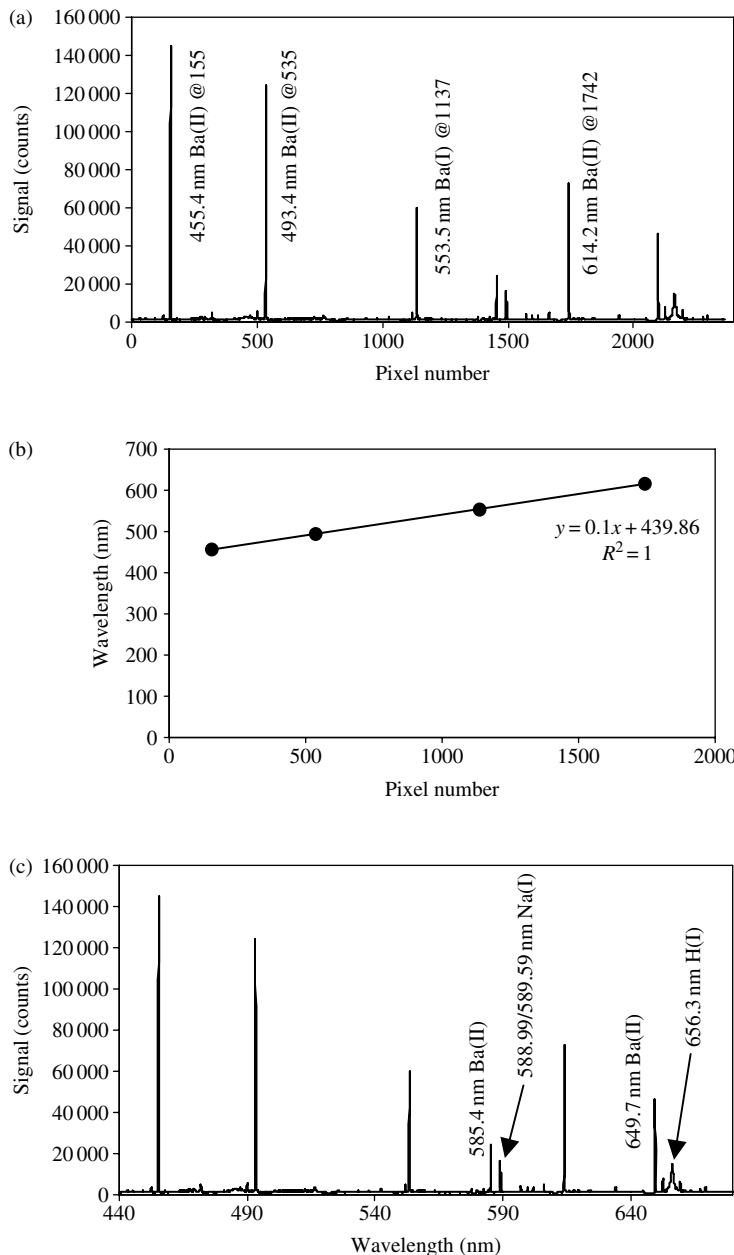


**Figure 3.33** Demonstration of wavelength calibration of a LIBS spectrum. (a) Recorded spectrum of signal versus pixel number. Four barium lines are identified and wavelengths indicated. (b) Barium wavelength versus pixel number for the four lines producing an equation relating wavelength ( $y$ ) to pixel number ( $x$ ). (c) Resulting calibrated spectrum with additional lines identified using wavelengths assigned by calibration

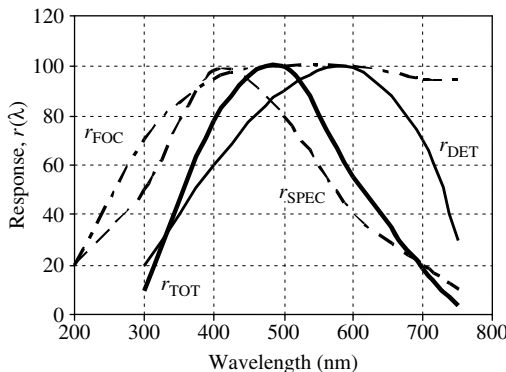


**Figure 3.34** Response curves for different components of a LIBS detection system along with the total response curve

the signal at each wavelength of interest  $s_{MEAS}(\lambda)$  is multiplied by the quantity  $r_{TOT}(\lambda')/r_{TOT}(\lambda)$  or

$$s_{CORR}(\lambda) = s_{MEAS}(\lambda) \times r_{TOT}(\lambda')/r_{TOT}(\lambda) \quad (3.7)$$

where  $\lambda'$  is some fixed wavelength to which the responses at the other wavelengths are compared. Typically,  $\lambda'$  may be selected as the wavelength for which  $r_{TOT}(\lambda) = 100$ .

In practice, the response of each detection system component will probably not be known accurately and there are differences between each individual component and the manufacturer's specification sheet. In addition, changes in components over time, due to factors such as degradation of spectrograph mirrors through oxidation of the coating and accumulation of surface contaminants such as pump oil, will change the response curve. The best method of correcting for spectral response is to use a calibrated light source. A tungsten lamp is used for wavelengths from about 250 to 2400 nm and deuterium lamps are used for UV wavelengths in the region 200–400 nm.

These lamps, typically traceable to a recognized calibration laboratory such as NIST (National Institute of Standards and Technology), are supplied with a calibration curve  $I_{CAL}(\lambda)$  or table of data from which such a curve can be prepared. The lamp will be operated at a specified current from a well-regulated power supply and in a certain geometrical set-up to direct light from a specific portion of the lamp into the detection system. The lamp will be positioned at the same location as the LIBS plasma would be formed and the lamp spectrum  $s_{LAMP}(\lambda)$  is recorded. Then  $r_{TOT}(\lambda)$  would be computed as:

$$r_{TOT}(\lambda) = s_{LAMP}(\lambda) \times I_{CAL}(\lambda')/I_{CAL}(\lambda). \quad (3.8)$$

The  $r_{TOT}(\lambda)$  values determined in this way would be used as described above to compute  $s_{CORR}(\lambda)$ . Here  $\lambda'$  is a selected fixed wavelength to which the other intensities are compared.

### 3.7 TIMING CONSIDERATIONS

In the case of time-resolved detection for either imaging or spectral detection, careful timing between the laser pulse and the gate pulse to the detector is essential. A timing diagram describing the timing events in a LIBS measurement is presented in Figure 3.35.

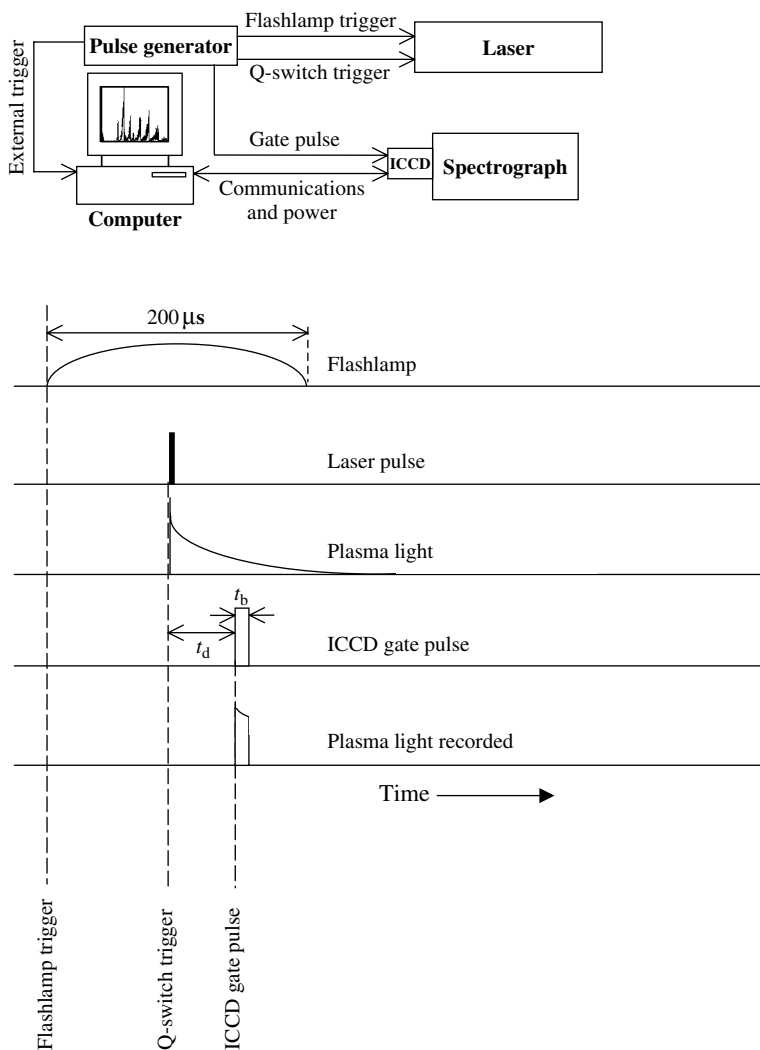


**Figure 3.35** Typical timing used in a LIBS experiment

In the case shown, the laser flashlamp and Q-switch are triggered by a pulse generator synchronized to the data acquisition system controller by a computer. The pulse generator produces an external trigger that clocks the detector readout with the laser pulse. A four-channel pulse generator is used so that each of the three pulses (flashlamp, Q-switch, gate, trigger) can be independently varied with respect to each other. This permits, among other things, the gate pulse to be positioned at zero delay with respect to the laser pulse or even positioned prior to the laser pulse (negative delay), useful for certain experiments.

In high repetition rate measurements, special care must be given to timing considerations. For example, a 1024 pixel PDA can be read out at a relatively fast rate so that the spectrum produced by each laser pulse can be independently recorded and stored. A typical rate will be 40 Hz. Readout times for a CCD detector can also be fast if the pixels are vertically binned, that is, if the CCD is not used in the image mode. When used in the image mode, however, as required by an echelle detector or for imaging studies, readout times will be much slower as each pixel must be read and stored separately. To prevent the finite readout time from limiting the repetition rate of the laser and hence the speed at which a measurement can be made, on chip averaging of the plasma light can be used. In this case, the CCD is not read out after each pulse but instead, the light from many plasmas are collected or averaged on the chip. The stored intensities are then read out after a certain number of pulses (e.g. 100 pulses, or 10 s for a 10 Hz) laser. Time resolved detection is still possible with an ICCD in this integrating mode as the intensifier can be gated rapidly on and off at the laser repetition rate. The integrated light in this case will represent time resolved detection.

### 3.8 METHODS OF LIBS DEPLOYMENT

Because the LIBS plasma is formed from laser light with its unique properties, LIBS is adaptable to a variety of different deployment methods. The typical LIBS set-up is shown in Figure 3.1. Additional arrangements are shown in Figure 3.36. Some of these are described later as examples of actual LIBS instruments. In Figure 3.36(a), the laser pulse is injected into a fiber optic cable for transport to the target. The emerging laser pulse is focused by a lens system to generate the laser plasma. The plasma light is then collected by either the same fiber optic or a second fiber and then transported back to the detection system. Obvious advantages of this system are that the laser and detection system can be positioned away from the target which may be located in a hazardous (e.g. high radiation) area. In addition, the probe at the end of the fiber can be very compact.

In a second configuration shown in Figure 3.36(b), a compact laser (e.g. Figure 3.3) can be housed in a small probe which is located adjacent to the target sample. The plasma light is collected by a fiber optic and transported back to the remotely positioned detection system.

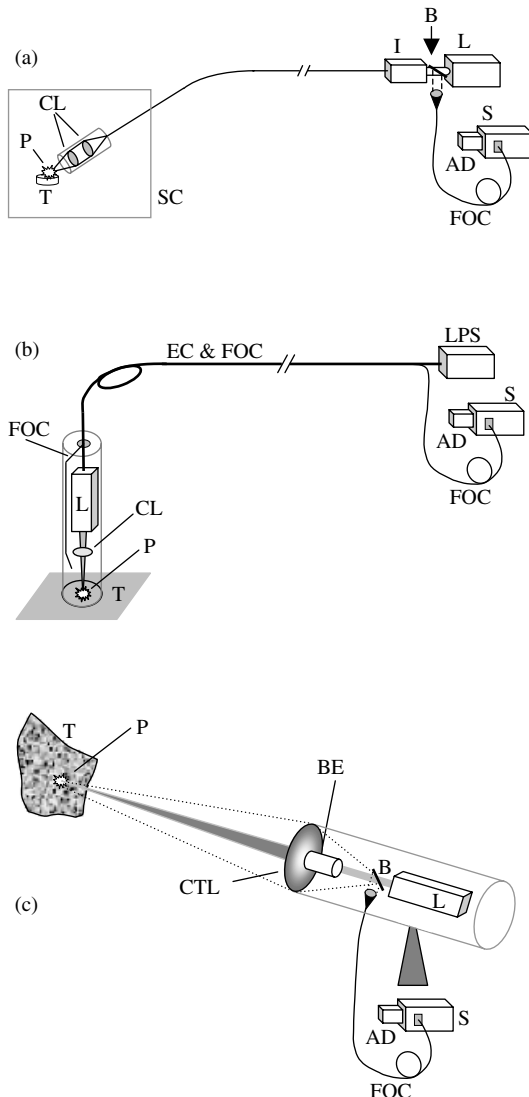


**Figure 3.36** Three possible configurations (a–c) for LIBS analysis in addition to direct analysis (Figure 3.1). L, laser; B, beamsplitter; FOC, fiber optic cable; I, pulse injector for FOC; CL, lens; T, target; P, plasma; S, spectrograph; AD, array detector; CTL, collection lens; EC, electrical cables; LPS, laser power supply; BE, beam expander

In the third configuration, the laser pulses are focused at a distance onto the remotely located target (Figure 3.36c). Typically, a beam expander will be used to expand the beam which is then focused onto the target using a multiple lens system. The plasma light can be collected by the same optical system as shown in Figure 3.36(c), or a

separate co-located light collection arrangement. This stand-off detection system can analyze samples at many meters distance. The achievable range depends on the spatial quality of the laser pulse as well as pulse energy and power density.

## REFERENCES

- Arnold, S.D. and D.A. Cremers (1995). Rapid determination of metal particles on air sampling filters using laser-induced breakdown spectroscopy. *Am. Ind. Hyg. Assoc J.* 56: 1180–1186.
- Bauer, H.E., F. Leis and K. Niemax (1998). Laser induced breakdown spectrometry with an echelle spectrometer and intensified charge coupled device detection. *Spectrochim. Acta Part B* 53: 1815–1825.
- Cremers, D.A. and L.J. Radziemski (1985). Direct detection of beryllium on filters using the laser spark. *Appl. Spectrosc.* 39: 57–63.
- Cremers, D.A., J.E. Barefield and A.C. Koskelo (1995). Remote elemental analysis by laser-induced breakdown spectroscopy using a fiber optic cable. *Appl. Spectrosc.* 49: 857–860.
- Davies, C.M., H.H. Telle, D.J. Montgomery and R.E. Corbett (1995). Quantitative analysis using remote laser-induced breakdown spectroscopy (LIBS). *Spectrochim. Acta Part B* 50: 1059–1075.
- Eland, K.L., D.N. Stratis, T. Lai, M.A. Berg, S.R. Goode and S.M. Angel (2001a). Some comparisons of LIBS measurements using nanosecond and picosecond laser pulses. *Appl. Spectrosc.* 55: 279–285.
- Eland, K.L., D.N. Stratis, D.M. Gold, S.R. Goode and S.M. Angel (2001b). Energy dependence of emission intensity and temperature in a LIBS plasma using femtosecond excitation. *Appl. Spectrosc.* 55: 286–291.
- Ernst, W.E., D.F. Farson and D.J. Sames (1996). Determination of copper in A533b steel for the assessment of radiation embrittlement using laser-induced breakdown spectroscopy. *Appl. Spectrosc.* 50: 306–309.
- Gornushkin, I.B., K. Amponsah-Manager, B.W. Smith, N. Omenetto and J.D. Winefordner (2004a). Microchip laser-induced breakdown spectroscopy: preliminary feasibility study. *Appl. Spectrosc.* 58: 762–769.
- Gornushkin, I.B., N. Omenetto, B.W. Smith and J.D. Winefordner (2004b). High-resolution two-grating spectrometer for dual wavelength spectral imaging. *Appl. Spectrosc.* 58: 1341–1346.
- Hecht, E. (2001). *Optics*, 4th edn, Addison-Wesley, Reading, MA.
- Hohreiter, V., A.J. Ball and D.W. Hahn (2004). Effects of aerosols and laser cavity seeding on spectral and temporal stability of laser-induced plasmas: applications to LIBS. *J. Anal. At. Spectrom.* 19: 1289–1294.
- James, J.F. and R.S. Sternberg (1969). *The Design of Optical Spectrometers*, Chapman and Hall, London.
- Konorov, S.O., A.B. Fedotov, O.A. Kolevatova, V.I. Beloglazov, N.B. Skibina, A.V. Shcherbakov, E. Wintner and A.M. Zheltikov (2003). Laser breakdown with millijoule trains of picosecond pulses transmitted through a hollow-core photonic-crystal fibre. *J. Phys. D: Appl. Phys.* 36: 1375–1381.
- Lorenzen, C.J., C. Carlhoff, U. Hahn and M. Jogwich (1992). Applications of laser-induced emission spectral analysis for industrial process and quality control. *J. Anal. At. Spectrom.* 7: 1029–1035.
- Mateo, M.P., S. Palanco, J.M. Vadillo and J.J. Laserna (2000). Fast atomic mapping of heterogeneous surfaces using microline-imaging laser-induced breakdown spectrometry. *Appl. Spectrosc.* 54: 1429–1434.

- Miles, B. and J. Cortes (1998). Subsurface heavy-metal detection with the use of a laser-induced breakdown spectroscopy (LIBS) penetrometer system. *Field Anal. Chem. Technol.* 2: 75–87.
- Multari, R.A. and D.A. Cremers (1996). A time-resolved imaging study of Cr(I) emissions from a laser plasma formed on a sample at nonnormal incidence. *IEEE Trans. Plasma Sci.* 24: 39–40.
- Multari, R.A., L.E. Foster, D.A. Cremers and M.J. Ferris (1996). Effect of sampling geometry on elemental emissions in laser-induced breakdown spectroscopy. *Appl. Spectrosc.* 50: 1483–1499.
- Myers, R.A., A.M. Karger and D.W. Hahn (2003). Geiger photodiode array for compact, lightweight laser-induced breakdown spectroscopy instrumentation. *Appl. Opt.* 42: 6072–6077.
- Pichahchy, A.E., D.A. Cremers and M.J. Ferris (1997). Detection of metals underwater using laser-induced breakdown spectroscopy. *Spectrochim. Acta Part B* 52: 25–39.
- Radziemski, L.J., D.A. Cremers, K. Benelli, C. Khoo and R.D. Harris (2005). Use of the vacuum ultraviolet spectral region for LIBS-based Martian geology and exploration. *Spectrochim. Acta Part B* 60: 237–248.
- Rodolfa, K.T. and D.A. Cremers (2004). Capabilities of surface composition analysis using a long laser-induced breakdown spectroscopy spark. *Appl. Spectrosc.* 58: 367–375.
- Sansonetti, C.J., M.L. Salit and J. Reader (1996). Wavelengths of spectral lines in mercury pencil lamps. *Appl. Opt.* 35: 74–77.
- Scaffidi, J., J. Pender, W. Pearman, S.R. Goode, B.W. Colston Jr, J.C. Carter and S.M. Angel (2003). Dual-pulse laser-induced breakdown spectroscopy with combinations of femtosecond and nanosecond laser pulses. *Appl. Opt.* 42: 6099–6106.
- Scaffidi, J., S.M. Angel and D.A. Cremers (2006). Recent and future trends in dual-pulse laser-induced breakdown spectroscopy. *Anal. Chem. Rev.* 78:A24–A32.
- Squillante, M.R., J. Christian, G. Entine, R. Farrell, A. Karger, M. McClish, R. Myers, K. Shah, D. Taylor, K. Vanderpuye, P. Waer and M. Woodring (2003). Recent advances in very large area avalanche photodiodes. *Proc. SPIE* 5071: 405–410.
- Svelto, O. (2004). *Principles of Lasers*, 4th edn, Springer, Berlin.
- Theriault, G.A., S. Bodensteiner and S.H. Lieberman (1998). A real-time fiber-optic LIBS probe for the in situ delineation of metals in soils. *Field Anal. Chem. Technol.* 2: 117–125.
- Wiza, J.L. (1979). Microchannel plate detectors. *Nucl. Instrum. Methods* 162: 587–601.
- Yalin, A.P., M. DeFoort, B. Wilson, Y. Matsura and M. Miyagi (2005). Use of hollow-core fibers to deliver nanosecond Nd:YAG laser pulses to form sparks in gases. *Opt. Lett.* 16: 2083–2085.
- Yamamoto, K.Y., D.A. Cremers, L.E. Foster and M.J. Ferris (1996). Detection of metals in the environment using a portable laser-induced breakdown spectroscopy (LIBS) instrument. *Appl. Spectrosc.* 50: 222–233.
- Yamamoto, K.Y., D.A. Cremers, L.E. Foster, M.P. Davies and R.D. Harris (2005). LIBS analysis of solids using a long-pulse (150 ns) Q-switched Nd:YAG laser. *Appl. Spectrosc.* 50: 1082–1097.
- Zayhowski, J.J. (1999). Microchip lasers. *Opt. Mater.* 11: 255–267.
- Zayhowski, J.J. (2000). Passively Q-switched Nd:YAG microchip lasers and applications. *J. Alloys Compd.* 303–304: 393–400.

---

# 4 Determining LIBS Analytical Figures-of-Merit

---

## 4.1 INTRODUCTION

Analytical figures-of-merit (FOM) are used to benchmark the capabilities of an analysis method and to compare the performance of distinct analytical techniques using a common set of parameters. The main FOM often used to characterize an analytical method are: (1) limits of detection, (2) precision and (3) accuracy, although other parameters such as (4) sensitivity and (5) selectivity are sometimes included. Definitions of FOM and standardized methods of determining them can be found in publications by the International Union of Pure and Applied Chemistry (IUPAC, 1997) and the International Organization for Standardization (ISO, 1993, 1997, 2000). Here we present a discussion of the more important FOM and how they are used to characterize LIBS.

## 4.2 BASICS OF LIBS MEASUREMENTS

Whether qualitative or quantitative analysis, the basic component of any LIBS measurement is the emission spectrum recorded from a single plasma. Each firing of the laser atomizes a portion of the sample in the pulse focal volume and produces a plasma that excites and re-excites the atoms to emit light. The plasma light is collected and recorded resulting in a measurement. The recorded quantities may be a spectral region (e.g. obtained using an ICCD detector) or the emission wavelength of a single line or set of lines (e.g. PMT detection using a polychromator) as described in Chapter 3. From the spectrum, the intensities of the analyte(s) emission line(s) is (are) determined. Here we discuss details related to analysis of the emission spectrum.

Examples of LIBS analyses that produce complex (Cr) and relatively simple (Be) spectra are shown in Figure 4.1. These spectra were obtained by scanning a series of laser sparks along filter paper on which atomic absorption standard (AAS) solutions were deposited. These solutions are relatively free of contaminants so the observed

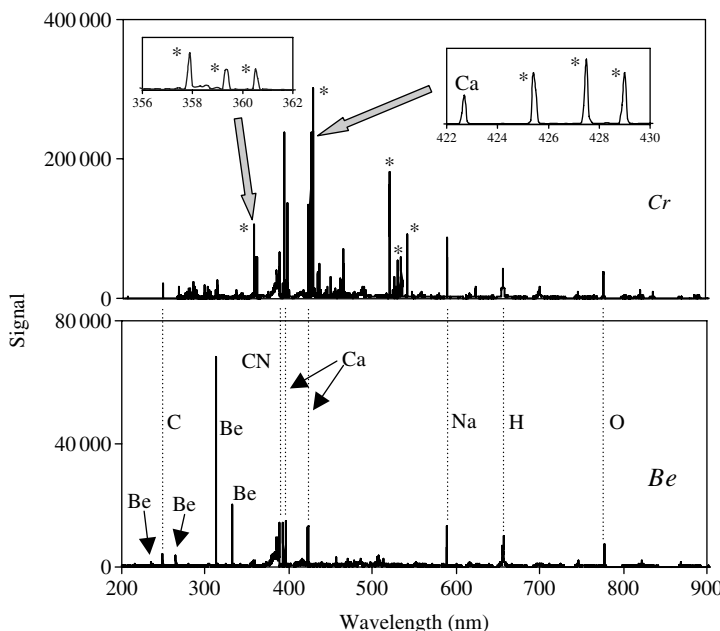


**Figure 4.1** Comparison of LIBS spectra of Cr and Be solutions deposited on a filter showing differences in complexity (line density). Emissions from C, H and O are due to the filter material. Cr lines indicated by an asterisk (\*)

lines, with the exception of C, H and O from the filter material, are due to the deposited element. The elements Ca and Na are ubiquitous in nature and are also observed. The elements in the filter have a few strong lines to interfere with lines due to Cr and Be. The insets on the Cr spectrum show, at higher spectral resolution, the strong Cr lines in the UV and blue spectral regions. Strong emission from the molecule CN is also observed as described below.

The LIBS spectrum resulting from interrogating a basalt rock sample is shown in Figure 4.2. This spectrum spans the most important spectral region for LIBS, 200 to 800 nm, over which most elements exhibit at least a few strong emission lines. This spectrum shows a very high density of emission lines resulting from the complex composition of the basalt rock and the sensitivity of the LIBS method.

There are several factors to consider in identifying an emission line with a particular element and these are discussed in Chapter 5. In all cases, however, the wavelength of the emission line is the prime identification parameter. Element wavelengths are listed in a number of compendiums (Striganov and Sventitskii, 1968; Reader *et al.*, 1980; Phelps, 1982; Winge *et al.*, 1985; Sobel'man, 1996; Reader and Corliss, 1997; Payling and Larkins, 2000). Typical entries by element in such compilations include the wavelength, ionization stage, relative intensity

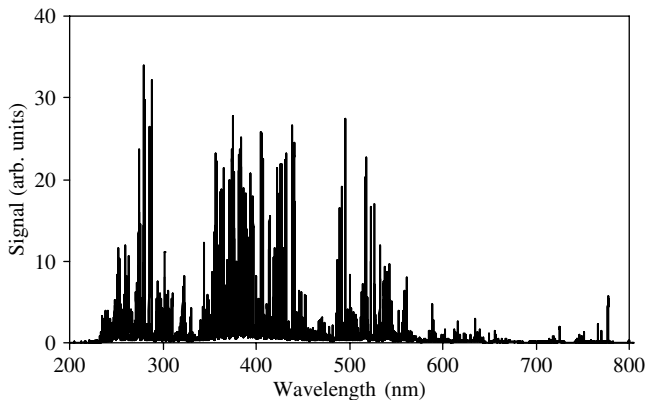


**Figure 4.2** LIBS spectrum of basalt recorded using an echelle spectrograph

and energy level designations with energies. Here we use the nomenclature that (I) signifies the neutral atom, (II) represents the once-ionized atom, etc., so that O(I), O(II) and O(III) represent the neutral, once-ionized and doubly ionized oxygen atom, respectively.

In addition to emissions from atoms, emissions from simple molecules are observed from some samples. In general, high concentrations of the elements composing the molecules must be present for molecular emissions to be observed. Typical examples include AlO (Chapter 5) from Al metal interrogated in air, YO from the superconductor ( $\text{YBa}_2\text{Cu}_3\text{O}_7$ ), and  $\text{C}_2$  and CN from graphite sampled in air. These simple molecules are formed as the atoms recombine in the cooling plasma. Typically, the ambient air supplies the O atom of the molecule. An example of a LIBS spectrum from graphite analyzed in air is shown in Figure 4.3. A compilation

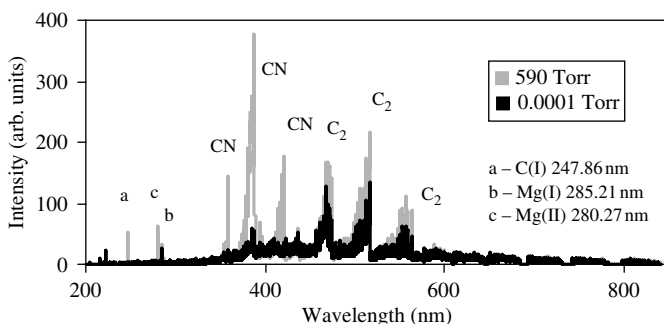


**Figure 4.3** LIBS spectrum of graphite in air showing emissions from a few elements and simple molecules formed as the plasma temperature decays

of emission wavelengths for simple molecules likely to be found in a LIBS plasma is presented in Pearse and Gaydon (1963).

Examination of the LIBS spectrum will reveal those elements in the sample that are present at concentrations above the minimum detectable by the method. Compiling a list of elements in a sample is useful for qualitative analysis (Chapter 5). In most cases, however, the interest lies in the intensity of an emission line or set of lines which is used for quantitative analysis (Chapter 6). The discussion of methods to determine the intensity of an emission line begins with a closer look at a very small spectral region of the complex spectrum of Figure 4.2. This is shown in Figure 4.4 with lines due to the elements Ti, Al and Ca labeled. The strongest line shown is that of Ca(II) at 396.2 nm. The Ti line lies in a spectral region where it is free of a spectral interference (i.e. overlap) with another line. The Al line, on the other hand, shows interference from lines on the long and short wavelength sides of this line. The cross-hatched region in each case is the sum of the emission line intensity and the background or white light from the plasma. Depending on the detector, background due to dark noise in the detector can be subtracted out of the recorded spectrum, often automatically, which we will assume is the case here. It should be noted that a detection system such as a polychromator with PMTs mounted behind a slit will record the sum of the emission signal and white light background. Because the recorded light intensity is ascribed to a single wavelength corresponding to an analyte wavelength, the sum of the signals will be processed. There is no way to determine what fraction is due to the emission line and what part is due to the background light when recording a single wavelength. In contrast, in the case of an array detector (PDA, CCD or ICCD, etc.) the intensity as a function of wavelength is recorded and processing of the line and line shape and background subtraction can be carried out.

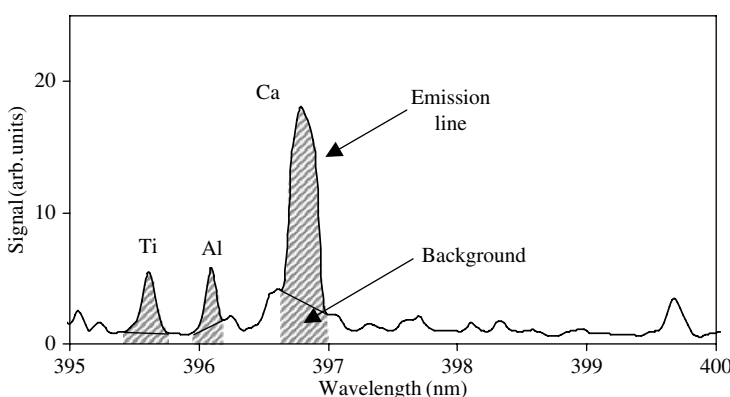


**Figure 4.4** Expanded region of Figure 4.2 showing individual lines

In determining a line intensity, the simplest case to consider is that of Ti in Figure 4.4. The net emission signal is determined by establishing the baseline on either side of this ‘clean or isolated’ line, drawing an imaginary line between these two points and computing the area or height above this line. A simple algorithm can be written to readily process this type of data. The software for some array detector systems has this capability built in. Determining the analyte signal in the case of Al is more complex as there is an adjacent line that represents a small interference with the Al line. The simplest method of determining the net emission signal is the same as described above – draw an imaginary line between the low and high wavelength side of the Al line which, in our example, is still well defined even in the presence of the interference. As in the case for Ti, the net emission signal is computed as the area above the imaginary line. The most complex case is that of Ca with interferences on either side but here again a good approximation to the net Ca emission signal can be determined by computing the area of the imaginary line between the low and high wavelength side of the Ca line. This procedure, although containing some error, has been shown to give adequate results.

Another method of determining the area of a line is shown in Figure 4.5 for the 422.6 nm Ca(I) line from the spectrum of Figure 4.2. There is an interference on the left side of this line but the right side is free of interference. A baseline level can be established using the flat region around 423 nm and this is indicated by the dashed line. Finding the peak of the line and computing the area in the shaded region yields one half of the line area with background. One-half the baseline is easily subtracted and the resulting value is doubled to give the net analyte signal.

The calculations of line areas described above can easily be carried out by writing simple computer programs to process the spectral information from an array

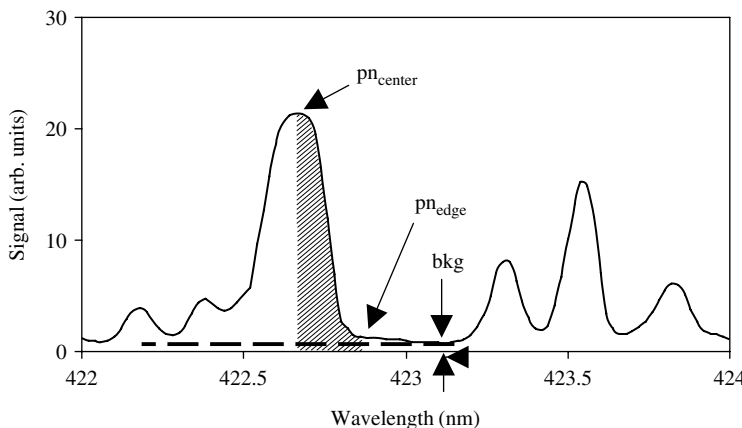


**Figure 4.5** Determining the area of the Ca(I) 422.6 nm line by splitting the line

detector. These data will be in the form of signal at a particular pixel number (pn) which corresponds to a certain wavelength:  $\text{signal}(\text{pn})$ . In the case of Figure 4.5, the line area will be computed as:

$$\text{Area} = 2 \times [\sum \text{signal}(\text{pn}_i) - \text{bkg}] \quad (4.1)$$

where the sum extends from  $\text{pn} = \text{pn}_{\text{center}}$  to  $\text{pn}_{\text{edge}}$  and bkg is the background intensity adjacent to the line. The background (bkg) is that corresponding to one-half the line width.

In the most rigorous evaluation of line intensities, each emission peak could be fitted with an assumed line shape. Then the intensity of the analyte of interest is de-convoluted from the other interfering lines (Kauppinen *et al.*, 1981; Barth, 2000). This is illustrated in Figure 4.6. From the line shape, the net analyte signal can be extracted. Whether this procedure leads to improved data is a function of the degree of overlap and the relative intensities of the analyte and the interferent(s). Clearly, as the analyte intensity decreases in intensity relative to the interferent(s) intensity(ies), such a procedure will improve the data. On the other hand, it is often possible to use another emission line of the element of interest if the line of choice exhibits strong interferences.

In the majority of cases, essentially the same results will be obtained using the peak height and peak area of a line. This is shown on Figure 4.7 where the height and area of the 769.9 nm K(I) line are plotted on the same calibration curve graph versus concentration. The height values were normalized to the area value at the maximum concentration to accentuate the similarities in the results. On the other hand, if comparing the intensities of two lines, one of which may be strongly affected by Stark broadening, for example the H(I) (alpha) line at 656.29 nm, the integrated intensities should be used.

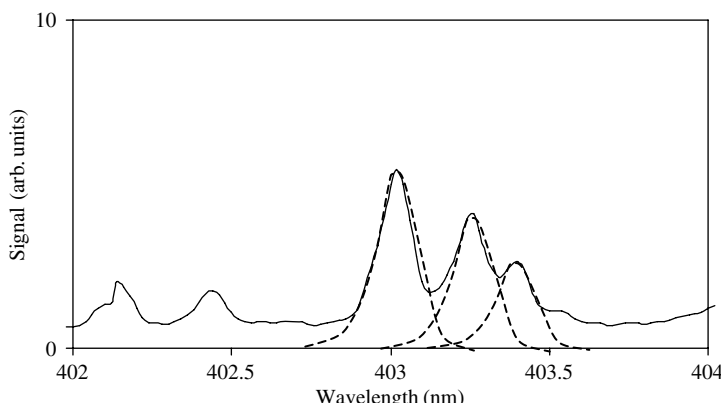


**Figure 4.6** Mn line spectrum extracted from Figure 4.2 showing the overlap of the adjacent lines at 403.08, 403.31 and 403.45 nm

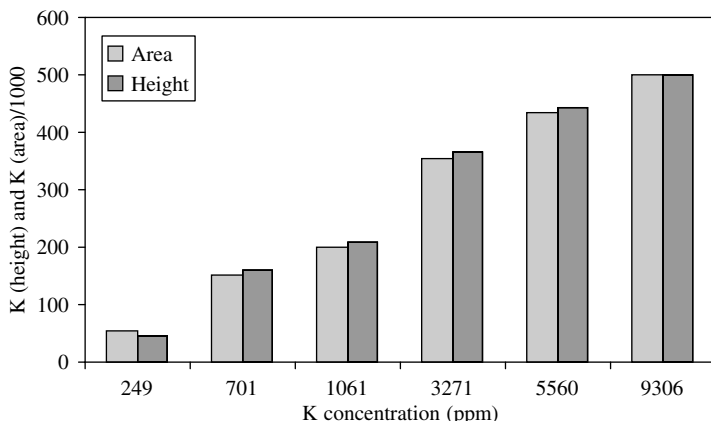


**Figure 4.7** Comparison of peak heights and areas obtained for the K line at 769.9 nm for powdered basalt samples spiked with different concentrations of KCl

### 4.3 PRECISION

Emission of light from the LIBS plasma is a short-lived event (Figure 2.1) that involves collecting light over a time period of only  $\sim 20\text{ }\mu\text{s}$ , for example. For comparison, a measurement using a continuous excitation source such as the inductively coupled plasma (ICP) may involve collection of light from the excited analyte over a period of 5 s which corresponds to collecting the light from 250 000 laser plasmas or running a 10 Hz laser for 6.9 h! Clearly, the total signal recorded in a practical LIBS measurement is much less than that recorded using a continuous source, assuming equal excitation. In addition, the laser plasma is a pulsed excitation source that both prepares (atomizes) and excites the sample on each shot. Inherent shot-to-shot instabilities related to the achievable stability of the repetitive laser pulses and perturbations of the plasma by characteristics of the sample and the sampling procedure, all serve to limit measurement ‘repeatability.’ Here repeatability is the closeness of one measurement with other measurements carried out under the same experimental conditions.

Measurement repeatability is described by the term precision – a measure of the agreement of a set of results ( $x_i$ ) among themselves. Precision is usually expressed in terms of the deviation of a set of measurements (number =  $n$ ) from the arithmetic mean ( $M$ ) of the set of repeated measurements. This deviation is calculated as the standard deviation ( $s$ ) given by

$$s = [\sum(x_i - M)^2/n - 1]^{1/2}. \quad (4.2)$$

Using  $s$ , the percent relative standard deviation (%RSD) can be computed as:

$$\%RSD = 100\% \times (s/M). \quad (4.3)$$

It should be noted that in some cases, a measurement will involve a single LIBS spectrum. An example is the determination of the composition of a single small particle such as in an aerosol laden air stream. In other cases, a series of individual measurements will be collected and the shot-to-shot evolution of the LIBS spectrum is analyzed. An example is repetitive ablation of a geological sample to monitor the change in composition as the outer (weathered) layers are ablated away and the composition of the underlying bulk sample is analyzed. The result is a histogram of composition as a function of depth. Another example is the real-time monitoring of material flow for process control or effluent analysis. Note that for these single shot measurements, precision cannot be determined ( $n = 1$ ) and would not have any significance as the sample would be changing shot-by-shot. On the other hand, computing  $s$  for such a set of data could be used as a designator for the extent of change observed in a sample or process, rather than a measure of the repeatability of the process itself (e.g. the standard deviation in the sample composition among individual particles exhibited a value of 30%).

Aside from these ‘special cases,’ to increase LIBS analytical performance, typically, many individual measurements (i.e. individual spectra) are recorded and the results are combined to produce an average measurement. The average measurement may be repeated several or many times using the same experimental parameters. Each of these similar measurements is called a ‘replicate.’ In a measurement, the sample is assumed to be a constant or that a sufficiently large number of individual spectra are averaged to account for variations in sample properties. Spectra are also averaged to account for shot-to-shot differences that may result from somewhat different plasma excitation on each shot. The number of measurements averaged together to produce a single LIBS measurement is determined by many factors including:

- (1) sample homogeneity (depth and lateral homogeneity, more uniform samples will require fewer measurements to obtain a representative determination of composition);
- (2) desire to maximize precision and accuracy within the performance of the method;
- (3) required analysis duty cycle (number of measurements/time);
- (4) sampling method. (Is the lens-to-sample distance constant? Are ablated particles intercepting subsequent laser pulses and perturbing plasma formation?)

When making replicate measurements, the experimental conditions are maintained constant. The results of these replicate measurements (e.g. six is typical) are used to determine measurement precision and increase the accuracy of a determination. A demonstration of the change in precision with number of individual spectra averaged to produce a single measurement is shown in Figure 4.8. The sample was a homogeneous uranium solution with the laser pulses focused on the surface of the liquid to form the plasmas. In this example, averaging a large number of spectra to produce a single measurement was found to increase precision which, in these

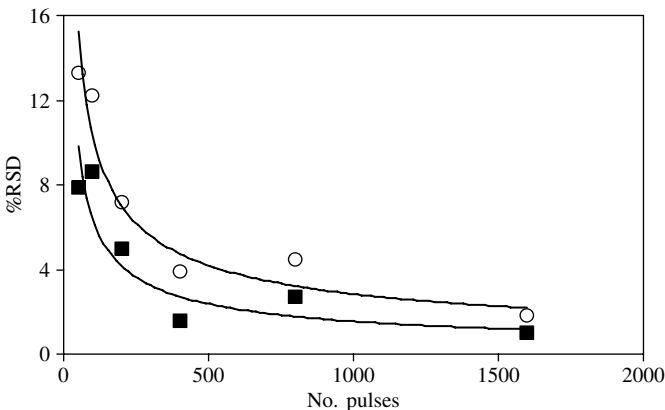


**Figure 4.8** Measurement precision (%RSD) versus number of pulses used for a measurement. Sample was uranium metal in nitric acid (Wachter and Cremers, 1987). Net uranium signal (open circles) and uranium signal ratioed to an adjacent region of background continuum light (black squares)

measurements, was limited by movements of the liquid surface due to the shock wave produced by the laser pulse. These data show a significant gain in precision as the number of averaged pulses increased from 50 to 500 and that a precision of 1% was obtained for the ratioed analyte signal using 1600 laser pulses (10 Hz laser, 2.7 min analysis time).

It should be emphasized that precision is a measure of the repeatability of a measurement. High precision does not imply an accurate measurement.

## 4.4 CALIBRATION

### 4.4.1 CALIBRATION CURVES

For quantitative analysis, a calibration curve of instrument response (e.g. element signal) versus absolute mass (gram, nanogram, etc.) or concentration (% parts-per-million or ppm) of the element to be detected is usually prepared. A general calibration curve is shown in Figure 4.9 and some aspects of this curve are sometimes seen in LIBS literature for calibration over a wide range. Ideally, there will be a linear relationship between the element response and the mass or concentration over the entire range investigated and a linear fit to the data would pass through the origin (0,0). Also, in the best case, the signal will double in magnitude if the concentration doubles. Actual calibration curves deviate from these ideal qualities. The range of concentration of mass (or concentration) over which the calibration curve is linear is termed the *linear dynamic range*. Nonlinear behavior is sometimes observed at the lower and higher concentrations. The slope of the calibration curve

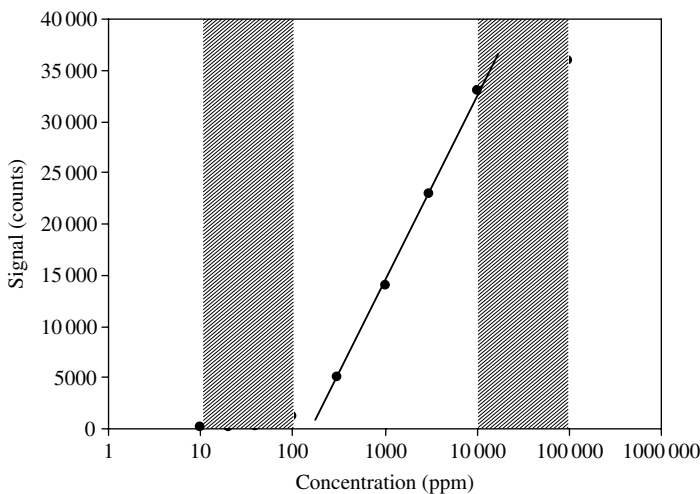


**Figure 4.9** Generalized calibration curve with three regions of different sensitivity clearly evident

at a certain concentration is termed the sensitivity and it is the change in signal for a given incremental change in the concentration (or mass). Clearly, as the slope increases, a fixed change in the observed signal relates to a smaller change in the concentration. Often the calibration curve will be plotted as mass (or concentration) versus signal.

The curve of Figure 4.9 shows a loss of sensitivity at high and low concentrations, on either side of the central linear region. The loss of sensitivity, or flattening of the curve, at low concentrations can be due to:

- (1) a spectral interference with the analytical line with the concentration of the interfering species remaining constant as the analyte concentration decreases;
- (2) a constant background concentration of the analyte being determined that is not included in the stated concentration of the analyte;
- (3) incorrect determination of the analyte signal so that a portion of the background signal is included in what is assumed to be only the analyte signal.

An example of an unexpected source of error related to (2) occurred in our laboratory during a measurement of Hg in soil. Using the 546 nm Hg(I) line as the analyte LIBS signal, a strong signal at 546 nm was recorded even for ‘pure’ or ‘clean’ soil. The line was observed when analyzing other materials and the signal was finally traced to a light leak in the plasma light collection system. The Hg emission from fluorescent lights in the laboratory contributed a constant signal to the analyte signal excited by the laser plasma.

Considering (1), whether a species interferes with or overlaps the analyte emission signature in a LIBS measurement is related to the resolution of the detection system and the timing parameters used to record the spectrum. A review of wavelength tables will show that few analyte lines have true spectral interferences in the sense of

two adjacent lines having the identical wavelengths. There will be some difference in the wavelength but perhaps a very small difference, on the order of 0.01 or 0.001 nm or even less. In practice however, the line width and the spectral resolution method will determine if the lines interfere. The lower the resolution of the method, the greater will be the chance of spectral interference.

At early times (e.g.  $t_d < 1\text{ }\mu\text{s}$ ), the spectral lines may be broadened to the extent that they overlap whereas for a longer delay ( $t_d \sim 2\text{ }\mu\text{s}$ ) the broadening may decrease so the lines are sufficiently resolved to be individually monitored without interference. This time dependent broadening is due to effects such as Stark broadening and Doppler broadening (see Chapter 2) that vary with the decaying plasma. In the presence of such broadening, interfering lines cannot be resolved using even a high resolution spectrograph, as the broadening occurs in the analyte itself. Some of these line broadening processes become less important as the plasma decays after formation. A good demonstration of such line broadening is provided by the hydrogen line at 656 nm. At early times in the LIBS plasma,  $t_d \sim 0.1\text{ }\mu\text{s}$ , this line can be on the order of 10 nm wide whereas at later delays,  $t_d \sim 1\text{--}2\text{ }\mu\text{s}$ , this will be reduced to a few tenths of nanometers. The sensitivity of this hydrogen line to the electron density (Stark effect) is sometimes used as a measure of the plasma electron density (Section 2.1.2).

The loss of sensitivity at high concentrations is most often due to ‘self-absorption.’ Self-absorption typically is observed for emission lines in which the lower level of the transition is the ground state or close to the ground state. Because transitions are element specific and quantized or of a specific wavelength, a given species has the highest probability of reabsorbing a photon emitted by a member of the same species. Because of the high density of atoms in the microplasma and its characteristically high temperature and electron density gradients, the outer layer of the plasma will be populated by ‘cool’ atoms, residing mostly in the ground state. The central core of the plasma will contain a higher density of excited atoms. As these atoms decay to the ground state, the emitted photons corresponding to resonance transitions will have a high probability of being absorbed by the ‘cooler’ atoms in the outer layers, thereby reducing the observed intensity of the emission line. As the concentration of the atoms in the target sample increases, the number of ‘cooler’ atoms in the outer layer increases and self-absorption becomes evident (Figure 4.10). A good example of self-absorption observed in a LIBS experiment is shown in Figure 4.11. Here the shapes of the emission lines depend on ambient pressure with the peaks recorded for 580 Torr reduced in intensity at the center (self-reversed). The lines appear broad in relation to their height because of the high concentration of K(I) in the sample. These K(I) emissions end in the ground state and the upper levels are at 1.6.1 and 1.62 eV making them particularly susceptible to self-absorption. The effect of self-absorption on the ability to obtain quantitative results using LIBS has been considered in detail (Lazic *et al.*, 2001).

A loss of sensitivity in the calibration curve can also be due to saturation of the detector response, that is, the intensity of light upon the detector is so great that there no longer is a linear response of the detector signal to the change in light

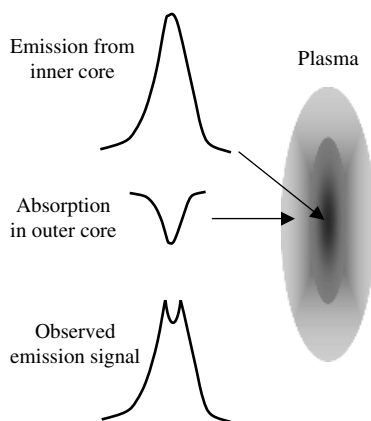


**Figure 4.10** Diagram illustrating the origin of self-absorption

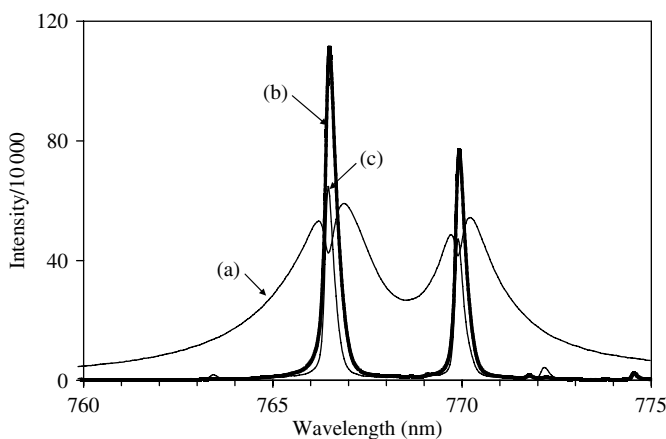


**Figure 4.11** Example of strong self-absorption observed from a laser plasma formed on pressed KCl powder. The two large peaks correspond to strong K emissions. (a) 580 (b) 7 and (c) 0.0001 Torr pressure (Harris *et al.*, 2004)

intensity. In the linear operating regime of the detector, a change in the incident light intensity by  $x\%$  should change the signal by  $x\%$ . This is most often evaluated using a neutral density filter to reduce the light intensity a known amount and monitoring the resulting signal.

If the nonlinear behavior of a calibration curve is due to some change in excitation provided by the plasma as the sample changes, the curve can often be ‘straightened out’ by plotting the analyte signal ratioed to another element known to be in the sample at a constant concentration. An example is shown in Figure 4.12. The left plot displays a calibration curve that is clearly not linear with the absolute Cu signal

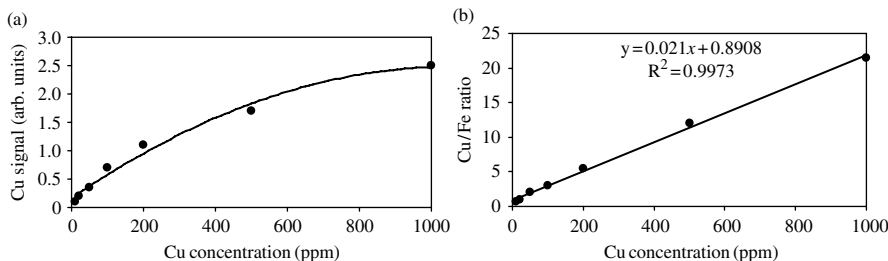


**Figure 4.12** LIBS calibration curves for Cu in a synthetic silicate sample using 10 mJ pulses

plotted versus Cu concentration from a set of synthetic silicate samples. There is a significant loss of sensitivity at the higher concentrations. Plotted in Figure 4.12(b) is the ratio Cu/Fe. The resulting calibration curve is linear. Plotting the analyte signal ratioed to an ‘internal standard’ element is a well known method of correcting for some nonlinear behavior. The caveat is that the concentration of the internal standard element must be constant.

The slope or sensitivity of the linear portion of the calibration curve in Figure 4.9 is dependent on experimental factors. Shown in Figure 4.13 is the relationship between

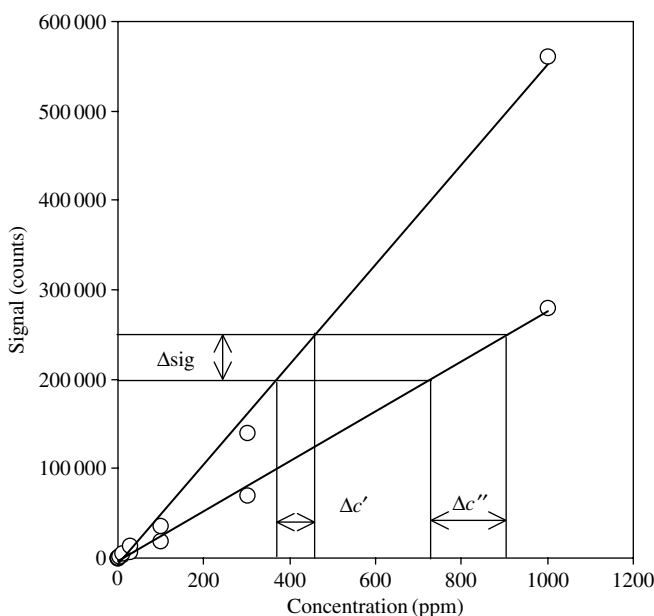


**Figure 4.13** For a given uncertainty in the analyte signal ( $\Delta \text{sig}$ ), the uncertainty in the concentration determination decreases with increased sensitivity ( $\Delta c' < \Delta c''$ )

a change in the signal and a corresponding change in the analyte concentration. Clearly, as the slope increases, for a given uncertainty in the signal ( $\Delta\text{sig}$ ), the uncertainty in the concentration to be determined decreases. Therefore, it is desirable to have maximum sensitivity in the technique.

For LIBS, increases in the laser pulse energy and the gain of the detection system, both instrumental parameters, will increase the slope. The slope will also be affected by sampling conditions such as the atmosphere above the sample. An example of the change in calibration curve slope with laser pulse energy is shown in Figure 4.14. The increase in slope with energy can be traced to (1) increased mass ablation of the sample leading to a higher number of excited species and (2) an increase in the size of the plasma producing greater excitation of ablated species.

The dependence of slope on pressure shown in Figure 4.15 requires some explanation. The increase in slope observed for 7 Torr pressure is the net result of the competing processes of increased ablation and reduced excitation. The number of collisions decreases as the pressure is reduced but the number of atoms in the plasma increases with ablation. The latter is the predominate mechanism down to a pressure of a few torr. Ablation increases with reduced pressure because of reduced plasma shielding that permits more of the incident laser pulse energy to reach the sample surface. For pressures below about 1 Torr, plasma shielding becomes negligible and the mass ablated remains uniform for further pressure decreases. In this low pressure regime, reduced excitation due to reduced pressure (reduced collisions) controls species excitation and the element signals decrease with pressure. For pressures below about 0.001 Torr, ablated species are no longer confined near the surface as these are ejected out into the surrounding free space immediately upon irradiation by the laser pulse. In this case the time between collisions becomes so great that further pressure decreases do not affect species excitation.

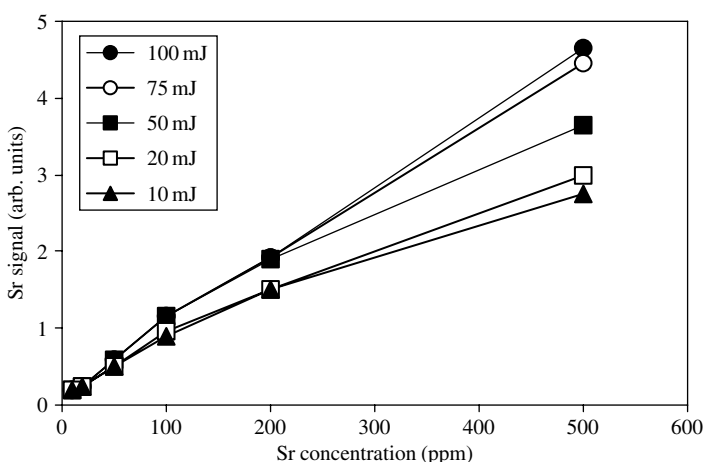


**Figure 4.14** Sr calibration curve as a function of laser energy

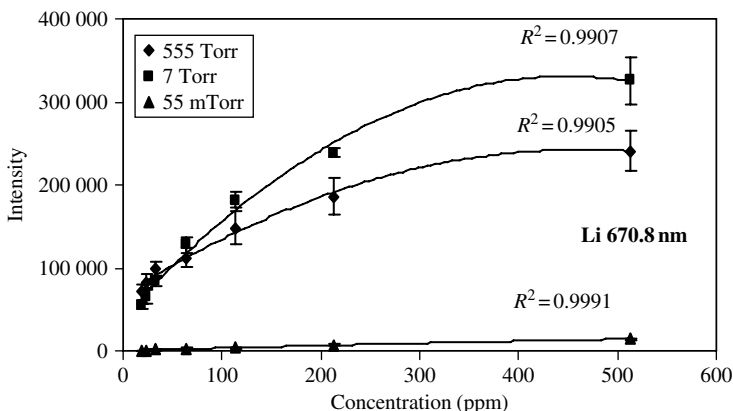


**Figure 4.15** Calibration curves for Li at various pressures. The distance between the target and the LIBS system was 4 m (stand-off measurement, Chapter 7)

#### 4.4.2 CALIBRATION STANDARDS

The LIBS method, as any other analytical technique, requires calibration to obtain optimum results in a quantitative analysis. As discussed in Chapter 8, methods are being developed for calibration free-LIBS but this technique has not been widely deployed as the method is still being refined and the quality of the results has been sample dependent. For this reason, active calibration is typically employed with the calibration curve developed using a set of standards or calibration samples having a composition as close as possible to the unknown sample. This provides for the best results as factors such as matrix effects are minimized because the standards and the unknown samples have the same bulk composition. Of course, in some cases the sample to be analyzed may be a true unknown with little or no knowledge about the matrix.

Calibration standards for soil analysis can be prepared, for example by obtaining clean soil and then adding known amounts of the analyte of interest (e.g. potassium), as a compound for example (potassium chloride), to the soil to produce a set of samples having analyte concentrations spanning the range of interest. By weighting out the samples fairly precisely, acceptable calibration samples can be prepared. It may be, however, that the chemical form of the analyte compound added to the calibration samples may be different from the form of the analyte in the unknown specimen thereby possibly affecting the observed emission signals through matrix effects.

Because LIBS interrogates a sample with little or no preparation, the method requires that the form of the calibration standard match that of the interrogation method. That is, solid samples will be used to calibrate a LIBS system developed to analyze metal samples, airborne samples will be used to calibrate the response of a LIBS air sampling system in which the laser plasma is formed directly in

air, and surface depositions of a material will be developed to calibrate a method of analyzing swipes upon which contaminated material has been deposited. Some different calibration samples are shown in Figure 4.16 (Plate 8).

Calibration standards for many types of samples can also be obtained commercially from a large number of governmental and industrial laboratories. These include reference materials, certified reference materials, primary standards, etc. Table 4.1 lists the definitions of these different sample types as they relate to LIBS and which may be encountered in selecting and developing calibration samples.

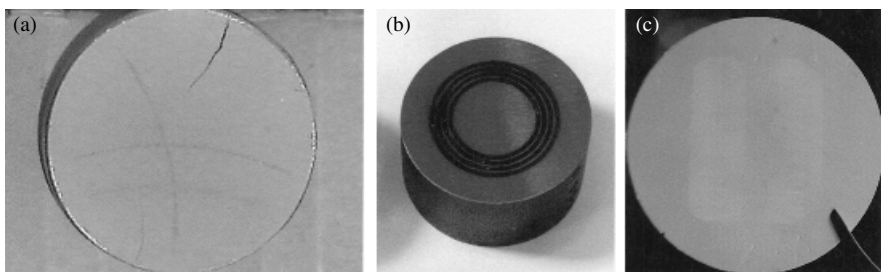


**Figure 4.16** Examples of some calibration samples. (a) Pressed basalt certified reference material showing the tracks produced by translating the sample under repetitive laser sparks. (b) Steel certified reference material showing concentric tracks produced by a high repetition rate laser. (Yamamoto *et al.*, 2005, with permission from Society for Applied Spectroscopy.) (c) Calibration filter containing an analyte at a certain surface concentration (e.g.  $\text{ng}/\text{cm}^2$ ). The tracks produced on the sample by scanning the filter under a series of long sparks formed on the surface are visible (see Plate 8)

**Table 4.1** Some definitions related to LIBS calibration

Calibration curve	A graphical representation of the relationship between a signal and the amount of an analyte in a sample. Additional variables or analytes may be used in calibration in which case a calibration surface or hypersurface is formed (multicomponent analysis)
Standard or calibration sample	A material having one or more composition values of interest that can be presented to the analytical instrument for calibration purposes
Reference material (RM)	A material having one or more composition values of interest that are sufficiently homogeneous and well established within certain limits to be used for the calibration of an analytical instrument, the assessment of an analytical method, or for assigning values to other materials
Certified reference material (CRM)	A reference material, accompanied by a certificate, having one or more composition values of interest certified by a procedure or a series of procedures which establishes traceability assuring an accurate realization of the composition value. The certified value is usually accompanied by an uncertainty at a stated level of confidence

#### 4.5 DETECTION LIMIT

The limit of detection (LOD) as defined by the IUPAC is (IUPAC, 1997):

*The limit of detection, expressed as the concentration,  $c_L$ , or the quantity,  $q_L$ , is derived from the smallest measure,  $x_L$ , that can be detected with reasonable certainty for a given analytical procedure. The value of  $x_L$  is given by the equation  $x_L = x_{bi} + ks_{bi}$  where  $x_{bi}$  is the mean of the blank measures,  $s_{bi}$  is the standard deviation of the blank measures, and  $k$  is a numerical factor chosen according to the confidence level desired.*

Because the relationship between the measure (or signal) and the concentration (or mass) is given by the slope of the calibration curve  $m = \Delta c_L / \Delta x_L$ , we have  $c_L = c_{bi} + ks_{bi}m$  but  $c_{bi}$  is typically zero (no analyte concentration in the blank sample) so that  $c_L = ks_{bi}m$ . This is the formula that is often used to compute the LOD with  $k = 3$ . Ideally, a  $k = 3$  value would correspond to a confidence level of 95% but because  $s_{bi}$  is determined from a small number of measurements, a 90% confidence level is more reasonable. The detection limit should be considered the minimum amount of the analyte that can be present and be determined to be present, rather than the minimum amount of the sample that can be actually measured. For quantification purposes,  $k = 10$  and the limit of quantification is given by  $LOQ = 10s_{bi}m = 3.3LOD$ . Debate over FOMs, especially the detection limit, is ongoing and a bibliography relating to the detection limit is presented at the end of this chapter.

It should be realized that the LOD can be affected by many measurement parameters such as laser pulse energy and the values of  $t_d$  and  $t_b$  used for detection as well as sample characteristics. The condition of the surface polish of a metal sample and laser pulse irradiance, for example, have been shown to affect the LOD for Mo in stainless steel (Cabalín *et al.*, 1999).

#### 4.6 ACCURACY

Accuracy is a measure of how close a measurement result is to the ‘true’ value of the property measured. Of course, the true value would have to be determined by a perfect measurement technique which in reality does not exist. Even if an ‘unknown’ sample were made from pure components, there would always be some uncertainty in measuring out the compounds that would be combined to make the ‘unknown’ sample. We therefore resort to what is termed the ‘conventional true value’ or ‘accepted true value.’ An example would be the concentration of an analyte specified for a certified reference material (Table 4.1). The ‘certified concentration’ would be determined by averaging analytical determinations of that analyte from a number of different analytical methods.

The error in accuracy may be defined as the difference between the measured value ( $x_m$ ) and the ‘accepted true value’ ( $x_{atv}$ ):

$$\text{Error} = x_m - x_{atv} \quad (4.4)$$

Errors in accurately measuring a quantity can be due to many factors and these can be classed as systematic (or determinate) errors and random errors. Systematic errors are due to a fault in a procedure or instrument. For example, in a LIBS measurement, if the laser pulse energy was not maintained constant (instrument drift) or it had a different value than the laser energy used for measurements used to construct the calibration curve, errors in determining an analyte concentration will occur. Such an error can be minimized by assuring the constancy of laser pulse energy and other experimental parameters.

Random errors cannot be avoided and are due to fundamental limitations on the experimental procedure. For example, the laser pulse energy can never precisely be set to the same value used to construct the calibration curve and there will always be some drift in the laser energy at a level below which the energy cannot be controlled any more precisely. From this definition, it is clear that random errors can be minimized to some extent by making replicate measurements. It is just as likely that a random error will produce a positive error as a negative error and to a certain extent these will cancel out.

The accuracy is often expressed as percent accuracy error which is computed as:

$$\% \text{accuracy error} = \text{absolute value of } [(x_m - x_{atv})/x_{atv}] \times 100\%. \quad (4.5)$$

Accuracies of LIBS measurements determined using geological samples and in direct air sampling evaluations are presented in Section 6.8.

## REFERENCES

- Barth, A. (2000). Fine-structure enhancement – assessment of a simple method to resolve overlapping bands in spectra. *Spectrochim. Acta Part A* 56: 1223–1232.
- Cabalín, L.M., D. Romero, J.M. Baena and J.J. Laserna (1999). Effect of surface topography in the characterization of stainless steel using laser-induced breakdown spectrometry. *Surf. Interface Anal.* 27: 805–810.
- Harris, R.D., D.A. Cremer, C. Khoo and K. Benelli (2004). Unpublished data.
- IUPAC (1997). *Compendium of Chemical Terminology*, 2nd edn, IUPAC, Research Triangle Park, NC.
- ISO 3534-1 (1993). *Statistics—Vocabulary and Symbols – Part 1: Probability and General Statistical Terms*, ISO, Geneva.
- ISO 11843-1 (1997). *Capability of Detection – Part 1: Terms and Definitions*, ISO, Geneva.
- ISO 11843-2 (2000). *Capability of Detection – Part 2: Methodology in the Linear Calibration Case*, ISO, Geneva.
- Kauppinen, J.K., D.J. Moffatt, H.H. Mantsch and D.G. Cameron (1981). Fourier transforms in the computation of self-deconvoluted and first-order derivative spectra of overlapped band contours. *Anal. Chem.* 53: 1454–1457.
- Lazic, V., R. Barbini, F. Colao, R. Fantoni and A. Palucci (2001). Self-absorption model in quantitative laser induced breakdown spectroscopy measurements on soil and sediments. *Spectrochim. Acta Part B* 56: 807–820.
- Payling, R. and P. Larkins (2000). *Optical Emission Lines of the Elements*, John Wiley & Sons, Ltd, Chichester.
- Pearse, R.W.B. and A.G. Gaydon (1963). *The Identification of Molecular Spectra*, Chapman and Hall, London.

- Phelps III, F.M. (Ed.) (1982). *MIT Wavelength Tables, Volume 2: Wavelengths by Element*, MIT Press, Cambridge, MA.
- Reader, J., C.H. Corliss, W.L. Wiese and G.A. Martin (1980). *Wavelengths and Transition Probabilities for Atoms and Atomic Ions*, Natl. Stand. Ref. Data Ser., Natl. Bur. Stand. (US) 68: Part I.
- Reader, J. and C.H. Corliss (1997). Line spectra of the elements. In *CRC Handbook of Chemistry and Physics*, 77th edn, ed. D.R. Lide, CRC Press, Boca Raton, FL.
- Sobel'man, I.I. (1996). *Atomic Spectra and Radiative Transitions*, 2nd edn, Springer-Verlag, Berlin.
- Striganov, A.R. and N.S. Sventitskii (1968). *Tables of Spectral Lines of Neutral and Ionized Atoms*, IFI/Plenum, New York.
- Wachter, J.R. and D.A. Cremers (1987). Determination of uranium in solution using laser-induced breakdown spectroscopy. *Appl. Spectrosc.* 41: 1042–1048.
- Winge, R.K., V.A. Fassel, V.J. Peterson and M.A. Floyd (1985). *Inductively Coupled Plasma-Atomic Emission Spectroscopy, Physical Sciences Data Volume 20*, Elsevier, Amsterdam.
- Yamamoto, K.Y., D.A. Cremers, L.E. Foster, M.P. Davies and R.D. Harris (2005). Laser-induced breakdown spectroscopy analysis of solids using a long-pulse (150 ns) Q-switched Nd: YAG laser. *Appl. Spectrosc.* 59: 1082–1097.

## BIBLIOGRAPHY FOR DETECTION LIMITS

- Analytical Methods Committee (1987). Recommendations for the definition, estimation and use of the detection limit. *Analyst* 112: 199–204.
- Analytical Methods Committee (2001). Measurement of near zero concentration: recording and reporting results that fall close to or below the detection limit. *Analyst* 126: 256–259.
- Boumans, P.W.J.M. (1994). Detection limits and spectral interferences in atomic emission spectrometry. *Anal. Chem.* 66: 459A–467A.
- Currie, L.A. (Ed.) (1988). *Detection in Analytical Chemistry: Importance, Theory and Practice*, ACS Symposium Series 361, American Chemical Society, New York: Ch. 1.
- Currie, L.A. (1997). Detection: international update, and some emerging dilemmas involving calibration, the blank, and multiple detection decisions. *Chemom. Intell. Lab. Syst.* 37: 151–181.
- Currie, L.A. (1999). Detection and quantification limits: origins and historical overview. *Anal. Chim. Acta* 391: 127–134.
- Garner, F.C. and G.L. Robertson (1988). Evaluation of detection limit estimators. *Chemom. Intell. Lab. Syst.* 3: 53–59.
- Long, G.L. and J.D. Winefordner (1983). Limit of detection: a closer look at the IUPAC definition. *Anal. Chem.* 55: 712A–724A.

---

# 5 Qualitative LIBS Analysis

---

## 5.1 INTRODUCTION

As discussed in Chapter 4, the basis of any LIBS measurement is the plasma spectrum which contains information about the elements in the target sample. This information is in the form of emission lines located at specific wavelengths, the intensity of the lines and the relative intensities of the lines. This information is important for analyzing the sample. The analysis can either be qualitative or quantitative. *Qualitative analysis* seeks to establish the presence of a given element in a sample. *Quantitative analysis* seeks to establish the amount of a given element in a sample. As a subset of qualitative analysis we can add material identification. This type of analysis can arise if the identification of the samples lies within a certain limited set of materials. An example is the identification of metal alloys of which there are a limited number (Jurado-Lopez and Luque de Castro, 2003). Some examples of the different types of qualitative analysis that have been used with LIBS are listed in Table 5.1. In this chapter we discuss qualitative analysis and material identification.

## 5.2 IDENTIFYING ELEMENTS

The basalt spectrum of Figure 4.2 contains a high density of lines. Due to the high resolution of the echelle spectrograph used to record this spectrum, many closely spaced lines can be resolved and elements identified. Analysis of this spectrum indicates emission lines attributed to the elements (e.g. Al, Ba, Ca, Fe, K, Li, Mg, Mn, Na, Sr, Ti). In all cases, each element in the basalt has many lines of different intensities in the spectrum. The assignment of a line is a blend of science, art, and experience. Topics to consider when identifying lines are presented below.

- (1) *Knowledge of the sample.* For example, basalt is known to have high concentrations of Si, Al, Ca, Fe, K, Mg, Mn, Na, P and Ti, etc., but recordable concentrations of other elements such as Eu, Sm, U, elements that may have lines closely adjacent in wavelength to the strong lines of these elements (spectral interference) are unlikely to be found, unless the sample is contaminated by these elements.

**Table 5.1** Examples of qualitative analysis using LIBS

Purpose	Procedure
Identification of complex molecules by element intensities (Dudragne <i>et al.</i> , 1998)	Ratios of slopes of calibration curves were compared with stoichiometric atom ratios to identify starting molecules
Sorting of wood products treated with CCA (copper chromated arsenate) (Moskal and Hahn, 2002)	Form laser plasmas on wood surface and monitor for Cr emission
Identification of organic compounds in air (Portnov <i>et al.</i> , 2003)	Intensity ratios of C, H, O, N, C <sub>2</sub> and CN
Identification of alloys used in jewelry manufacture (Jurado-Lopez and Luque de Castro, 2003)	Rank correlation method used to compare spectra of ‘unknown’ samples with those in a spectral library
Identification of precipitates on surfaces of Al alloys (Cravetchi <i>et al.</i> , 2003)	Spectra in the region 320–410 nm were compared to distinguish the precipitate from the Al alloy
Identification of the composition of dirt on steel plates during manufacture (Orzi and Bilmes, 2004)	The presence of Fe particles in the surface dirt layers of manufactured steel plates

- (2) *Relative intensities of lines from wavelength tables.* From wavelength tables (references in Chapter 4), the relative intensities of lines can be determined and these can be used as a guide to assist in identifying lines. It should be realized, however, that relative line intensities are source dependent and that current wavelength tables were not compiled using the laser spark.
- (3) *The ionization stage of the element.* Assume that two elements are equally likely to be found in a sample. If the two elements have lines that spectrally interfere and one line belongs to a neutral species and the other belongs to a doubly or triply ionized species, it is most likely that the line belongs to the neutral species. Although once-ionized species are often observed in a LIBS plasma, the observation of higher ionization stages is unlikely in air. The lines of species with ionization potentials of 6 eV or less are more likely to be observed whereas species corresponding to >10 eV are unlikely to be present in sufficient numbers to be observed.
- (4) *The experimental conditions.* Certain experimental conditions can determine the species observed. For example, in air, emissions due to Fe(I) and Fe(II) are observed with the ionization potential of Fe(I) being 7.87 eV. In a vacuum, however, Fe(III) can be observed even though the second ionization potential is 16.18 eV. In another example, focused power densities on the order of 1 MW/cm<sup>2</sup>, corresponding to a welding laser pulse, incident on an aluminum sample creates a plume that results in the excitation of neutral species but no ionized species are observed. The temperature of the plume measured using a Boltzmann plot (Chapter 2) indicates 3000 K.

- (5) *Observation of multiple strong lines.* Many elements have several strong emission lines and if one line is observed the other strong lines of the element should be present. For example, if the strong Al(I) lines at 394.4 and 396.1 nm appear, the strong Al(I) lines at 308.2 and 309.3 nm should also be observed.

An example using the basalt spectrum of Figure 4.2 and the tentative identification of the strong line at 288.1 nm as due to Si(I) will demonstrate the procedure of line identification. Within 0.05 nm of the 288.1 nm line are lines due to Sm, Gd, Cd, Cs, Pr, Ca and Tm with the Gd line being somewhat strong as listed in the wavelength tables. However, from knowledge of typical soil composition, it is very unlikely that Sm, Gd, Pr and Tm will be in soil unless it happens to be contaminated. In addition, these are not usual contaminants found in soils unlike Pb, As, Zn, etc., which can occur due to mining and industrial processes. On the other hand, Ca is ubiquitous in nature being found almost everywhere naturally and it is present in soil at a high concentration. A look at wavelength tables, however, will show that the Ca line in question is due to doubly-ionized Ca, with Ca(III) having an ionization potential of 11.871 eV which is very high. For this reason, we would not expect to see strong Ca(III) lines appearing in a LIBS spectrum. The element Cs is also observed in many materials so it could be a candidate for the line we are tentatively attributing to Si(I). The Cs line is due to once-ionized Cs with the first ionization potential being 3.894 eV, sufficiently low that the Cs(II) line would be observed in a LIBS plasma. To further evaluate the presence of Cs we look for the two strong blue lines of Cs at 455.528 and 459.317 nm. In our spectrum there is a line close to 455.528 nm which could be due to Cs if the wavelength calibration of the spectrograph is off a small amount. There does not appear a feature at or near 459.317 nm, however, that we can attribute to the other strong Cs line. Therefore, it seems like Si(I) is the best identification of the 288.1 nm line. This is further supported by the appearance of a relatively strong line at 390.55 nm that is listed in the wavelength table as being about one-third the intensity of the 288.1 nm Si(I) line.

One factor that affects all LIBS measurements, even the simple identification of elements in a sample, is the condition of the surface. LIBS is essentially a surface analysis technique although repetitive sampling at the same location can be used to ablate through the surface to underlying layers. Surface detection is a useful capability in some applications, however, for example, to detect stains on a surface in the presence of a large mass due to the underlying substrate. Other analytical methods which can penetrate through the surface layer (e.g. x-ray fluorescence) to sample a large volume of the substrate composition would be attempting to monitor a small signal from a thin layer of surface material on top of a large signal from the bulk target. On the other hand, repetitive ablation at the same spot can be used to ablate through a thin weathered layer on a rock ( $\sim 100 \mu\text{m}$  thick) to record changes in composition as the underlying bulk rock is approached. An example of this is shown in Figure 5.1. Figure 6.8, discussed below, shows the spectrum from a Tl stain on an aluminum plate.

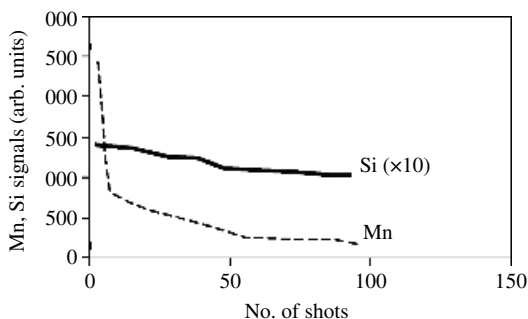
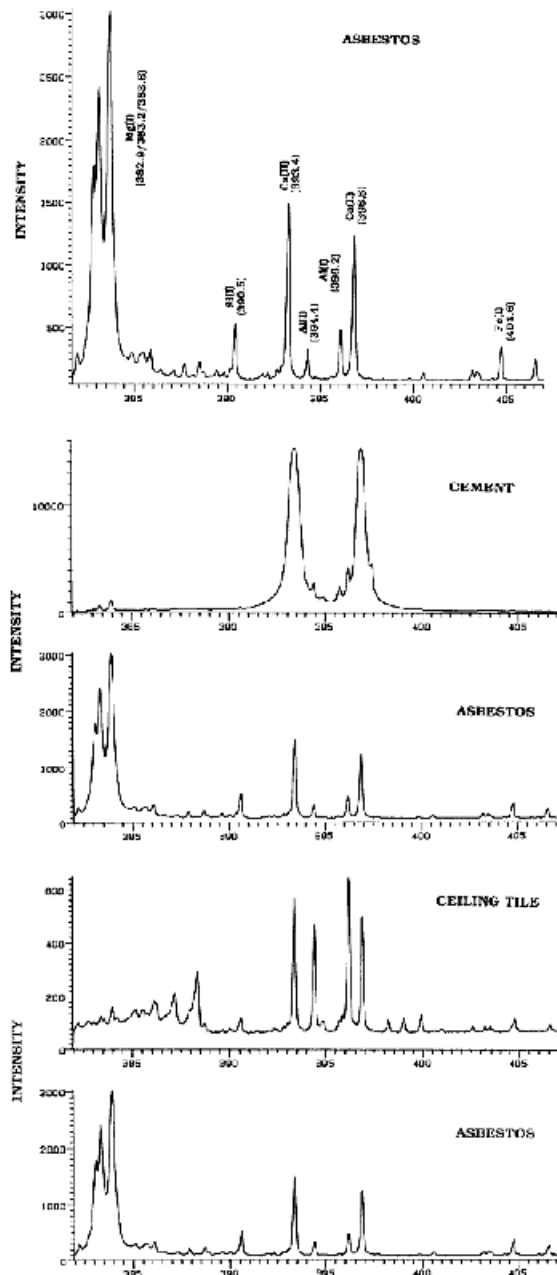


**Figure 5.1** Change in element signals as the weathered surface of a granite rock is repetitively ablated. The Si(I) signal was multiplied by a factor of ten for plotting here

### 5.3 MATERIAL IDENTIFICATION

Patterns in the spectrum formed from element line intensities can be used to identify a material from a given set of materials. Consider asbestos, a highly fibrous silicate mineral composed of the elements Mg, Ca, Si, Al, O, H and C which are ubiquitous in nature. It is not the elements in asbestos that are dangerous but the structure of this material that determines toxicity. Fibers longer than  $5\text{ }\mu\text{m}$ , less than  $5\text{ }\mu\text{m}$  wide with a length/width ratio  $>3$  are most toxic. Sensitive detection is needed to monitor for residues of asbestos as according to one study the ‘evaluation of all human data provides no evidence for a threshold or a safe level of asbestos exposure.’ Fortunately, LIBS has good detection capabilities for the elements in asbestos. Asbestos is typically found around construction areas as it was added to building materials to give them strength, fire retardant abilities, color, and in some cases, simply as filler because it was an inexpensive material. For this reason, because LIBS is an element detector, to identify asbestos using LIBS its spectrum must be distinguishable from common building materials. A comparison of the asbestos LIBS spectrum in the wavelength range 382–406 nm is shown in Figure 5.2 along with LIBS spectra of cement and a ceiling tile. Upon inspection of the spectra they are clearly distinguishable based on the appearance/absence of some lines and the relative intensities of lines due to different elements. The results of a comparison of the asbestos spectrum with four different ceiling tile compositions, cement, wallboard and pipe insulation is presented in Table 5.2. The results show that based on mostly qualitative evaluation of the different spectra, using three different classes of signal levels (low, medium and high), asbestos can be identified from the other materials.

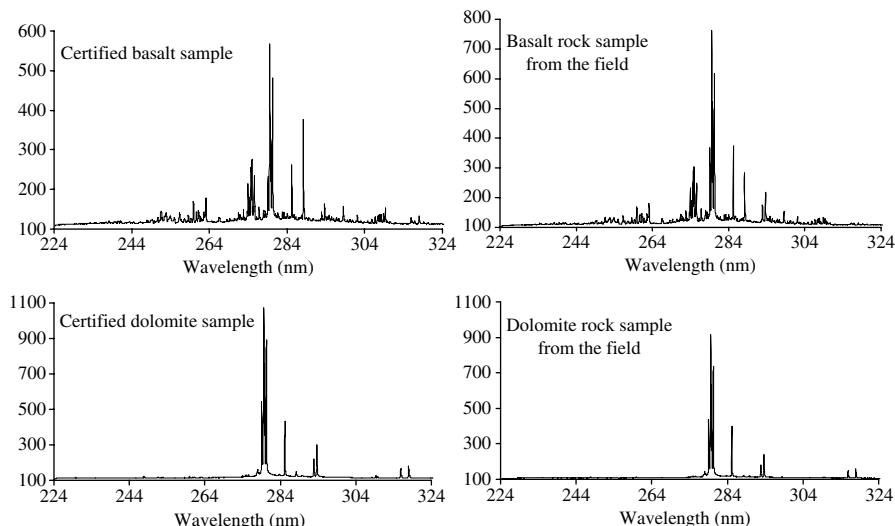
As another example, consider the identification of rock type based on recorded emission lines in the UV spectral region. Figure 5.3 displays spectra from bulk rock samples of basalt and dolomite and certified rock powder standards of these same rock types. The bulk rock and powders originated from different geological locations. A cursory examination of the different spectra and evaluations based on



**Figure 5.2** Qualitative analysis using LIBS. Comparison of LIBS spectra of asbestos, cement and ceiling tile in the region 382–407 nm. Although composed of ubiquitous elements (Al, Mg, Ca, Fe), these different materials, likely to be found together, are easily distinguished by inspection of the spectra

**Table 5.2** Comparison of asbestos and building materials spectra

Material	Element detected					
	Mg	Si	Ca	Al	Ti	Fe
Asbestos	XXX	X	XX	X		
Tile 1	X	X	XX	X		
Tile 2			XXX	XX	XX	
Tile 3	X		XX	XX	X	
Tile 4	X	X	XX	X		X
Pipe insulation		XX	X	XXX	X	
Wallboard	X		XXX			
Cement		X	XXX	XX		

**Figure 5.3** Comparison of spectra from bulk rock and powdered samples of basalt and dolomite

the positions of lines and relative line intensities show that the bulk rock and powder standards for the common rock types agree and are significantly different from the other type. Including other rock types such as granite would show the ability of LIBS to distinguish this variety from basalt and dolomite.

Another type of material identification can be practiced by ‘atom counting.’ Although LIBS cannot give structural information directly about the starting target material, it can reveal in certain circumstances, the number of a certain atomic species in a sample. An example is shown in Figure 5.4. Here two CFCs (chlorofluorocarbons) and the gas SF<sub>6</sub> as pure materials were mixed with Ar gas and were analyzed using the same apparatus under identical analysis conditions. The F/Ar ratio was determined over a certain concentration range. The slope of the

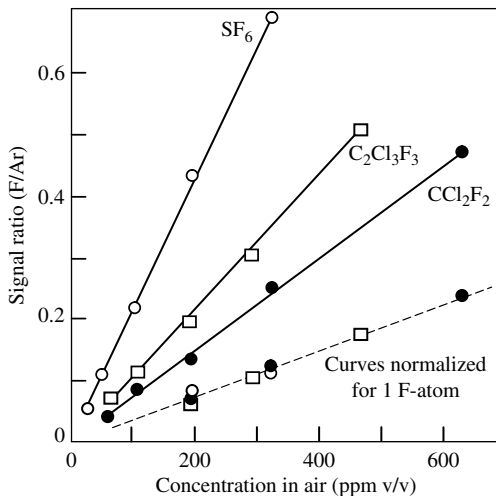


**Figure 5.4** Calibration curves for different F-containing atoms. The dashed curve results from dividing the data for each species by the number of F atoms in that species (i.e. 6, 3, 2) (After Cremers and Radziemski, 1983)

calibration in each case is related to the number of F atoms on the pure gas species. Dividing each signal of the corresponding species by the number of F atoms results in the overlapping dashed line curve shown in the figure. This indicates that in the case of pure materials and a calibrated system, a material can be identified from a certain set of possible species. By including other atoms in the calibration procedure, the identification can be made more selective. In the case of CFCs, the Cl atom could be included in a LIBS analysis and these atoms counted.

#### 5.4 PROCESS MONITORING

Besides acting as an excitation source to form a plasma that can be analyzed to determine composition, the laser pulse can also process a material to do work. An example is surface cleaning. Surface cleaning using a high repetition rate (kHz) acousto-optically Q-switched laser is shown in Figure 5.5. Some advantages of using a laser for cleaning are (1) fine control of the cleaning operation as the laser pulse spatial size and location can be precisely controlled, (2) remote cleaning because only optical access to the sample is required (e.g. through a window) and (3) the ability to monitor in real-time and remotely the cleaning process spectroscopically. As a demonstration of laser cleaning and process monitoring, a brief study of removing and monitoring AlO layers from aluminum is described. This work (1) demonstrates surface cleaning, specifically that oxide layers can be removed from an Al surface easily, rapidly and remotely using a laser and that (2) the oxide removal process can be monitored optically in-process and *in situ*.

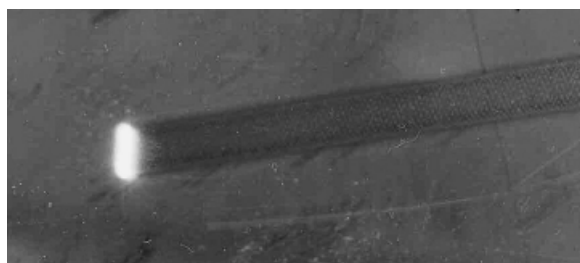


**Figure 5.5** Laser cleaning of a surface using a high repetition rate laser. The laser beam (kHz repetition rate) is rastered across the surface as the Al sample is translated below the beam generating the cleaned area (Yamamoto *et al.*, 2005, with permission of Society for Applied Spectroscopy)

#### 5.4.1 EXPERIMENTAL

The experimental arrangement is shown in Figure 5.6. Pulses from a Q-switched Nd:YAG laser were focused on the surface of aluminum samples using a cylindrical lens (150 mm focal length). The samples were contained in a large chamber purged with Ar gas to minimize re-oxidation of the surface following oxide removal by the laser pulses. High-purity Ar (less than 20 ppm impurities) was used as the purge gas. The laser pulse energies were between 100 and 400 mJ, the pulse width was 10 ns, and the laser repetition rate was 1–25 Hz. The aluminum samples were 0.64 cm thick disks mounted axially to permit rotation during the experiments so fresh aluminum surfaces could be continually exposed to the laser pulses. A small motor was used to rotate the samples. Because of the high peak power densities of the focused laser pulses, ‘line sparks’ about 5–7 mm long could be formed on the samples. Examples of line sparks are shown in Figures 1.5 and 3.9. These sparks ablated the surface material from the samples and at the same time atomized and excited the removed material for a LIBS analysis. In these experiments, the spark light was imaged onto

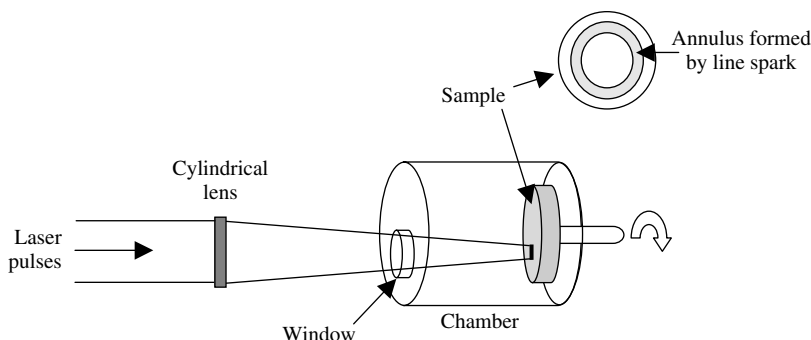


**Figure 5.6** Apparatus used to monitor plasma emissions during surface cleaning of Al metal in an Ar gas atmosphere

the entrance slit of a small spectrograph and the light detected by an intensified array detector. Two types of samples were used: Al disks as machined and Al disks that had been black anodized to increase the thickness of the oxide surface layer.

The removal of oxide from the sample surface was monitored spectrally during the cleaning operation by recording emissions from (1) a trio of neutral oxygen lines [O(I)] near 777.4 nm and (2) a series of aluminum oxide bands (AlO) in the blue spectral region. The O(I) lines were not spectrally resolved in these experiments. The AlO spectrum monitored here is shown in Figure 5.7. Because the atmosphere surrounding the sample was purged with pure Ar gas, the spectral features due to O(I) and AlO recorded here were due mainly to the evolution of O from the surface of the sample by the action of the laser pulses.

## 5.4.2 RESULTS

### 5.4.2.1 Monitoring Oxide Removal Using O(I) Emissions

Figure 5.8 shows spectra obtained by repetitively sparking the same area of an unanodized aluminum surface. The strong line on the left of each spectrum is due

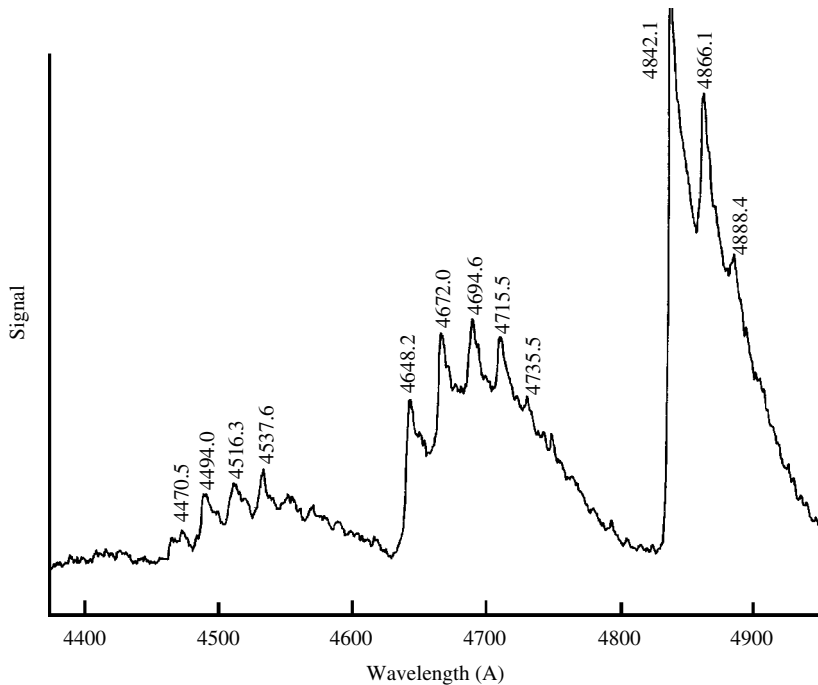


**Figure 5.7** AlO emission recorded from the laser plasma formed on oxidized Al metal

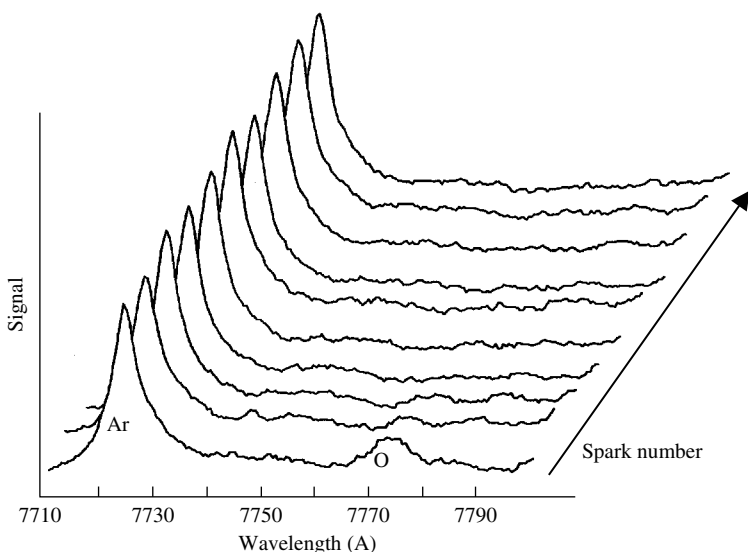
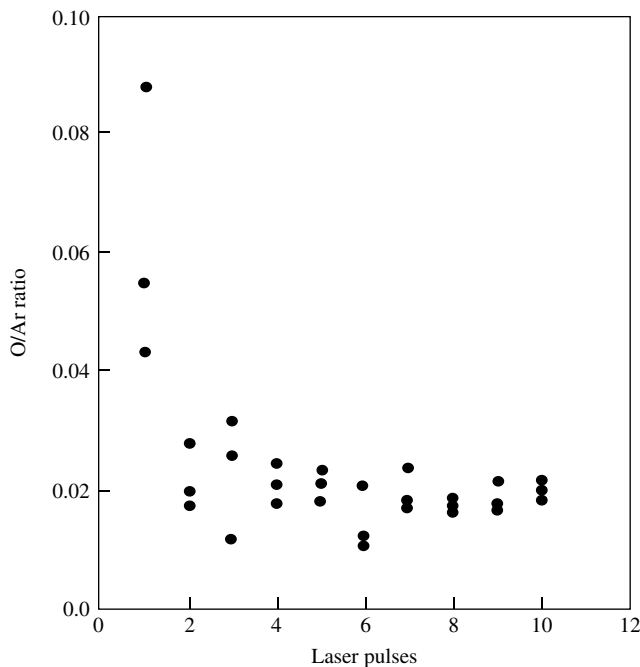


**Figure 5.8** LIBS spectra recorded from a bare (unanodized) Al metal plate

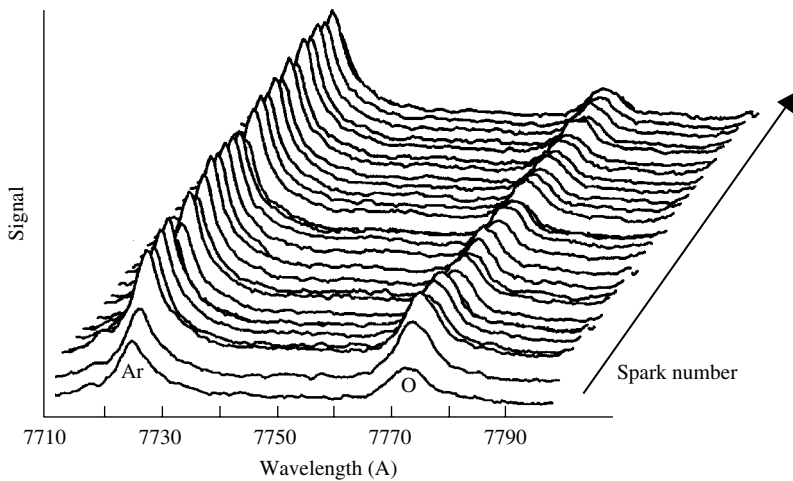
to argon emission. The oxygen line is small but clearly shown on the first spectrum on the right at 777.4 nm. The strength of the oxygen line decreased rapidly as the number of sparks increased and it is absent from the last spectrum shown here. The intensity of the O(I) line is plotted in Figure 5.9 versus shot number for three different independent experiments. Essentially the same temporal histories were obtained in each experiment.

Figure 5.10 shows the results of an identical experiment carried out using an anodized aluminum sample. The oxygen line is much stronger on these spectra because of the greater thickness of the oxide layer. In fact, the oxygen emission increased during the first few sparks, then decreased somewhat and eventually leveled off to a nearly constant value. The increased O(I) signal [and Ar(I) signal] observed on the first few shots can be attributed to increased coupling of the laser energy due to repetitive sparking at the same area. Data for two similar experiments carried out under these conditions are plotted in Figure 5.11.

The residual oxygen signal observed even after 49 shots had been formed at the same location on the anodized aluminum sample (Figure 5.11) can be attributed to the residual oxide layer at the perimeter of the ablation region. This oxide layer was evidently still being sampled by the 49th pulse. The validity of this explanation was verified by ablating a small continuous region of the surface by slowly rotating the sample while repetitively sparking the surface at 25 Hz. The sample was then exposed to air to produce oxidation and then the center portion of the previously ablated region was resparked and the O(I) emission recorded. These results are presented in Figures 5.12 and 5.13 and they show that when the heavily oxidized



**Figure 5.9** Intensity of O(I) emission versus shot number for a bare Al metal plate. Results for three experiments are shown



**Figure 5.10** LIBS spectra recorded from an anodized Al metal plate

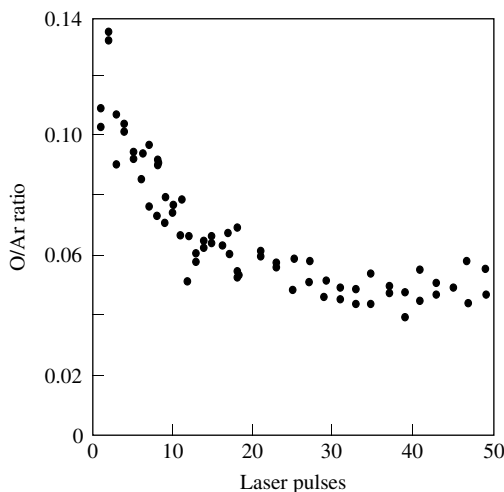


**Figure 5.11** Intensity of O(I) emission versus shot number for an anodized Al metal plate. Results for two experiments are shown

region around the ablated area was removed, the O(I) emission signals were reduced to a very low level after several shots.

#### 5.4.2.2 Monitoring Oxide Removal Using AlO Emissions

A series of experiments similar to those described above was carried out by monitoring the AlO emission in the blue spectral region. Signals from the unanodized aluminum were weak and not useful to monitor the change in oxide thickness. Figure 5.14 shows the AlO signals recorded by repetitively sparking an anodized surface. As observed for O(I) emissions (Figure 5.11), even after many shots the AlO signal remained strong. These data are plotted in Figure 5.15. Data obtained by repetitively sparking a previously cleaned region of an originally anodized sample is shown in Figure 5.16. Here, as shown above in the case of O(I) emissions, the AlO signals recorded after many shots were smaller than those observed by sparking a fresh anodized surface.

#### 5.4.2.3 Rate of Oxide Removal

The rate of removal of oxide from the anodized samples was observed visually: the gray metallic color of aluminum metal was clearly distinguishable from the black color of the anodized coating. By rotating the sample under the laser pulses and changing the laser repetition rate it was possible to determine an approximate rate of removal of the heavy anodized layer. This rate was about  $0.3 \text{ cm}^2/\text{s}$  for the laser operating at 10 pulses/s. The time required to clean an area of  $1300 \text{ cm}^2$  is about 72 min under these conditions: lasers of the type used here, however, can be

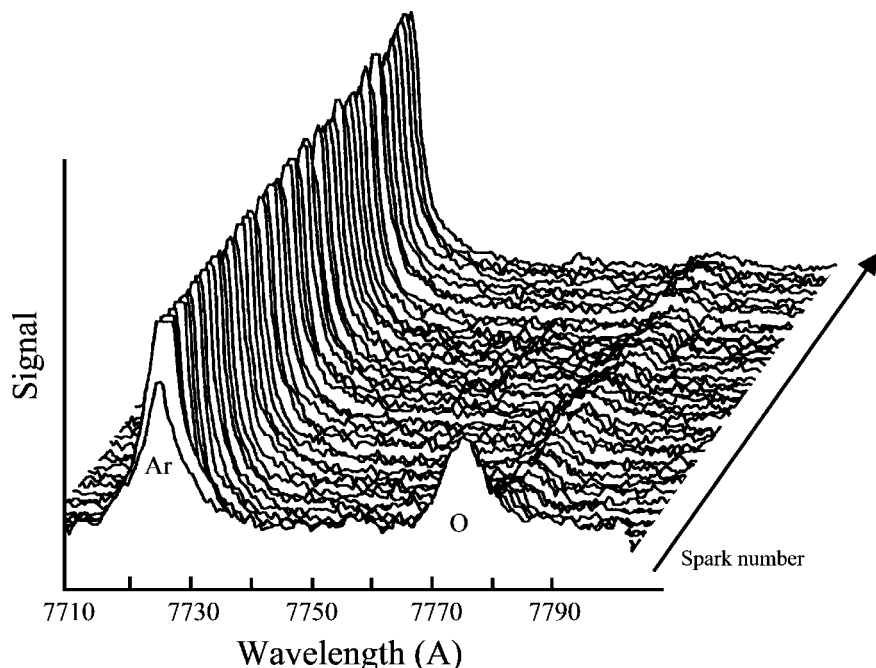


**Figure 5.12** Intensity of O(I) emission after removal of anodized area surrounding the ablation region showing much reduced residual O(I) signal compared with Figure 5.10

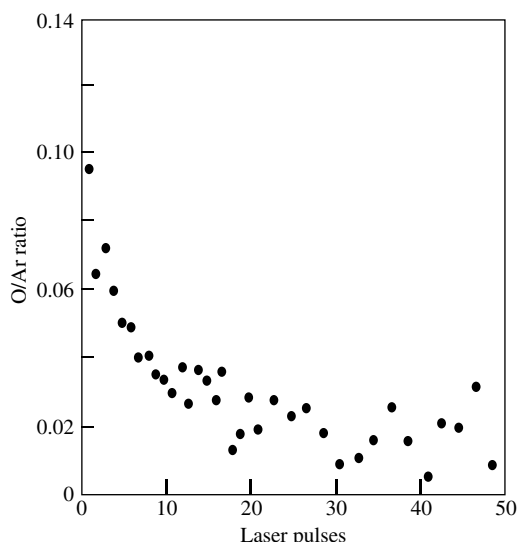


**Figure 5.13** Intensity of O(I) emission versus shot number for an anodized Al metal plate after removal of anodized region surrounding the ablation region. Compare with data of Figure 5.11

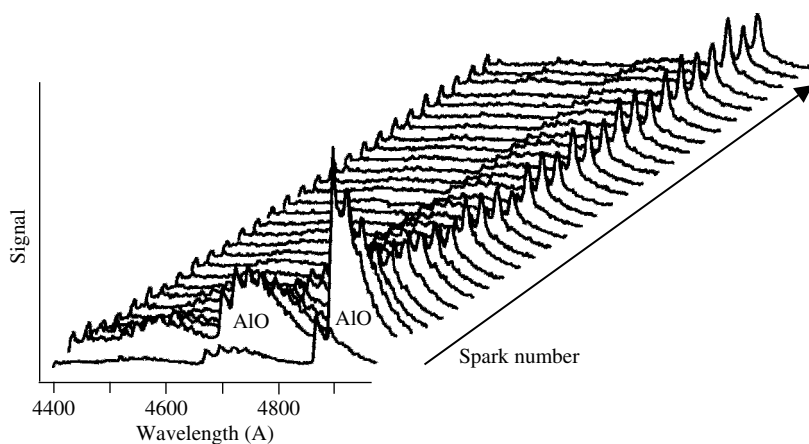


**Figure 5.14** AlO emission recorded from repetitively ablating an anodized Al metal plate

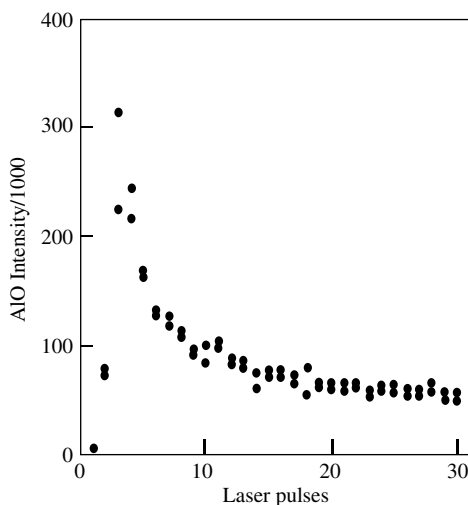


**Figure 5.15** Intensity of AlO emission versus shot number for ablation of an anodized Al metal plate

operated at 30 Hz and the laser beam expanded in one dimension to generate a ‘long spark’ about 12 mm long on the sample. This effectively increases the cleaning rate by a factor of  $(30/10\text{Hz}) \times (12/6\text{mm}) = 6$  so the area of  $1300\text{cm}^2$  could be cleaned in about 12 min. It should also be pointed out that excimer lasers with pulse repetition rates of 100–200 Hz having beam dimensions larger than those used here could be used to increase the cleaning rate significantly compared with that calculated here.

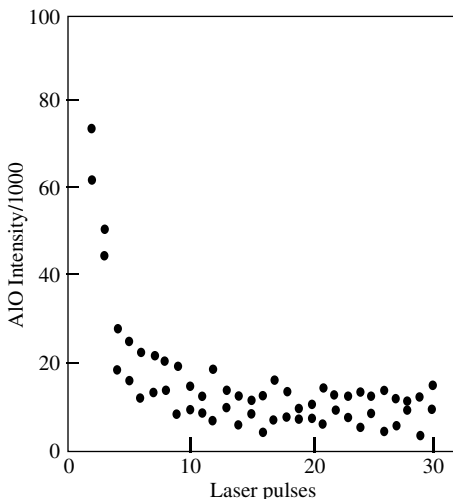


**Figure 5.16** Intensity of AlO emission versus shot number for an anodized Al metal plate after removal of anodized area surrounding the ablation region. Compare with data of Figure 5.13

#### 5.4.2.4 Surface Condition after Cleaning

The condition of the aluminum surface after cleaning depends to some extent on the parameters of the laser pulse and how it is focused on the sample. In the experiments described here, there was some reduction in the macroscopic smoothness of the surface as observed visually under a microscope. Much of this roughness occurred at the perimeter of the long sparks and was due to the strong focusing of the laser pulses.

#### 5.4.3 CONCLUSIONS

The work described here has shown that (1) a previously oxidized surface can be efficiently cleaned by scanning the surface with a repetitively pulsed laser beam, (2) the metal surface can be roughened to some extent by the action of the laser pulses, and that (3) the removal of the oxide can be determined spectroscopically by monitoring the O(I) emission in the case of a light or heavily oxidized surface or by monitoring the AlO emission in the case of heavy oxidation. It may also be possible to monitor oxide removal via an increase in emission from the metal lines as the oxide layer is ablated.

### 5.5 MATERIAL SORTING/DISTINGUISHING

The ability to perform a LIBS measurement using only a single pulse has a number of applications. One application is the sorting of a group of materials according to composition. The speed with which such sorting can be carried out depends on

several factors including (1) surface condition of samples in the group, (2) the type of analysis (only major elements or minor elements, trace elements) and (3) the closeness of compositions of samples in the group.

### 5.5.1 SURFACE CONDITION

Clearly, because LIBS is a surface analysis method, it is important that the surface composition be indicative of the bulk composition. Repeated ablation by a series of laser sparks can be used to ablate away unrepresentative surface layers but this will preclude a rapid analysis. Depending on the surface condition only a few laser ablations may be needed to obtain a representative sample or 10 s or 100 s of ablative shots may be needed. The repetition rate of the laser will of course enter into the analysis as a higher repetition rate laser will allow a more rapid analysis if many ablative pulses are needed to interrogate the bulk sample.

In cases where the bulk composition is of interest, the surface contamination thick and repetitive sampling is not feasible, LIBS can yield ambiguous results. Examples are shown in Figure 5.17. Here we present spectra abstracted from spectral signatures of an aluminum metal substrate. Aluminum samples were retrieved from a recycling operation feedstock and interrogated without cleaning using a single LIBS spark (50 mJ energy pulse) directed at each sample. The clean sample shows only strong emissions from Al lines at 394.4 and 396.1 nm. Weathered surface #1 shows some traces of dirt (no loose dirt) on the surface but the underlying aluminum was visible. In this spectrum the strong Al lines are apparent along with weak lines due to strong emissions from Ca, a common contaminant. Sample weathered #2 (clearly dirty, but the underlying surface still visible) shows strong emission from lines attributed to Al (the substrate), Ca (stronger than recorded from weathered #1 relative to Al), Pb and Fe. The Al samples were collected along with other metals and would have come into contact with these metals during handling. The heaviest surface contamination was observed for sample weathered #3 which visually showed heavy accumulation of dirt that completely obscured the surface. The corresponding spectrum shows strong emissions from Ca (stronger than Al, the substrate), Fe and again Pb. The Al emissions are actually weaker in intensity than many of the lines due to other elements. Because the surface was completely obscured for this sample, the origin of the Al emission was from the contaminant(s) rather than the bulk metal.

### 5.5.2 TYPE OF ANALYSIS

The criteria for sorting materials can be designated at different levels. For example, if the starting group contains a number of materials differing only by a few elements and those elements are minor or trace levels, then the surface condition of the samples will require more averaging to increase data quality to more accurately

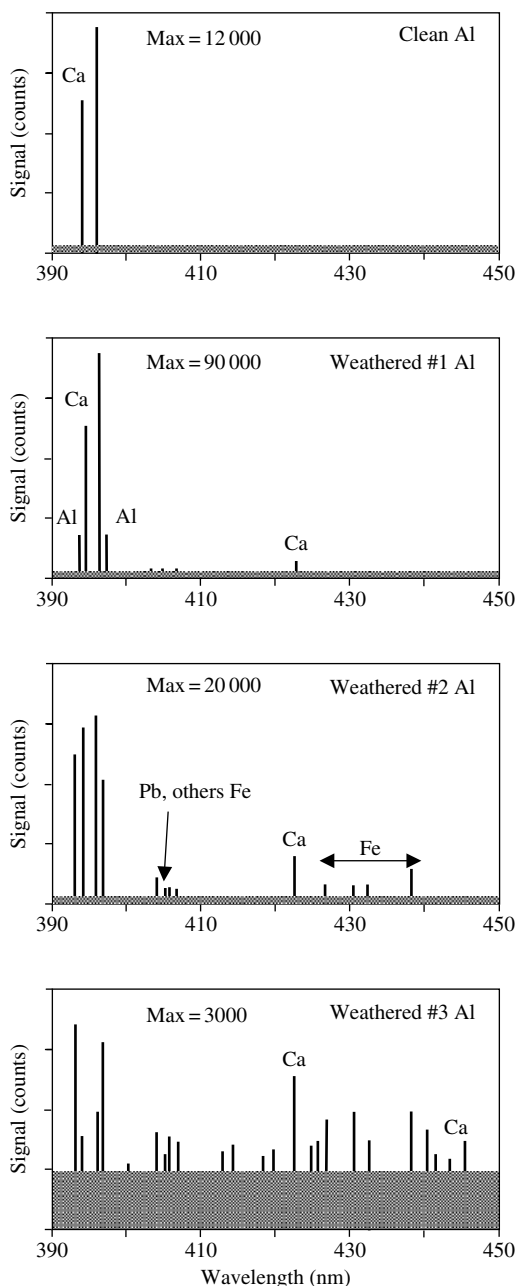


**Figure 5.17** LIBS spectra from aluminum metals with different degrees of surface contamination. The grey area indicates the average height of the background intensity

determine the sample composition and to observe differences in concentrations between these elements in the samples which, depending on the sample, may differ by only a few percent. On the other hand, if sorting is to only be carried out at a level corresponding to sorting by only the main element with differences between minor and trace elements unimportant (e.g. ferrous alloys from aluminum alloy and copper alloys) then only a few shots may be needed. This is demonstrated in Figure 5.18 in which a series of nine different metals (Al, Ti, In, Fe, Cu, etc.) were presented to a series of repetitive laser sparks and a single spectrum from a single spark recorded from each sample. As the results show, and detailed analysis of the data verifies, using only a single spectrum, the different metals can be sorted with 100% accuracy. Note that only a small spectral region (317.9 to 418.0 nm) was used for this type of sorting. Other spectral regions could be included to increase the accuracy of sorting and to include other metals not having distinct spectral features in the region displayed in Figure 5.18.

### 5.5.3 SORTING MATERIALS OF CLOSE COMPOSITION

The more difficult type of analysis is that involving a set of samples having small compositional differences. Examples include steel alloys and aluminum alloys, which can differ by only a few percent in a few elements. Another example occurs with the identification of different rock samples within a type. As shown above, it is relatively easy to discern the differences between different rock types such as

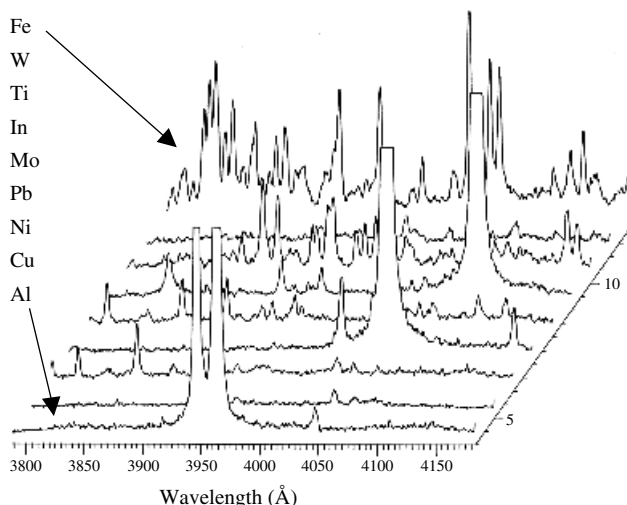


**Figure 5.18** Sequential LIBS spectra recorded from nine different metals each ‘analyzed’ by a single laser plasma at a rate of 19 samples/s. The list of elements corresponds to the order of the spectra shown

**Table 5.3** Composition differences between six basalt samples

	Columbia	688 Rock	Olivine	GUW BM	NCS GBW	Hawaiian
Sr (ppm)	346	169.2	468	220	1100	389
Si (%)	79.4	48.4	46.85	49.51	44.64	73.2
Ba (ppm)	683	200	172	250	527	130
Ti (%)	3.61	1.17	1.62	1.14	1.42	4.36
Mn (%)	1.52	0.167	0.15	0.14	1.31	1.29
Ca (%)	12.21	12.17	9.6	6.47	8.81	19.57
Al (%)	20.64	17.36	17.06	16.25	13.83	20.66
Fe (%)	23.46	17.99	10.09	9.67	21	20.93

basalt, dolomite, granite, etc. Sorting materials within a rock type, looking for small compositional differences is more demanding. A simple experiment will demonstrate, however, the use of LIBS for this application. Consider six basalt samples having the compositions listed in Table 5.3. Spectra of these six basalts are presented in Figure 5.19 for the spectral region from 380 to 470 nm. The spectra are overlapped and appear to be very similar. By constructing calibration curves for the six basalts for the elements listed in Table 5.3, linear calibration curves are obtained and the element concentrations for the corresponding basalt sample lie in the correct position on each curve. Representative curves for barium and silicon are shown in Figure 5.20. Using these results, it is possible to unambiguously identify each of the six basalts using the calibration curves.

## 5.6 SITE SCREENING USING LIBS

LIBS instruments can be readily deployed to evaluate areas for high and low levels of contaminant materials. This includes monitoring the workplace to determine the presence and locations of contaminant dusts (in air and on surfaces) and the screening of soils for toxic materials such as result from mining operations (e.g. Berkely Pit, Montana). LIBS instruments can be readily configured for this application and examples are shown in Figure 5.21. These include instruments that can be transported to a field site to provide on-site analysis in a mobile laboratory or instruments that can be deployed in the field for *in-situ* measurements. The basic design of these instruments follows the general LIBS configuration shown in Figure 3.1. The actual application will determine the type of components used (e.g. laser energy, repetition rate) and the sampling configuration. The instruments shown in Figure 5.21 include a backpack LIBS system that is battery-operated, with the laser mounted in the hand-held probe to directly sample surface or soil contamination. The second device is a transportable LIBS system into which collected samples are introduced and analyzed in less than 1 min by a series of laser plasmas directed at the surface. The third instrument, shown in Figure 5.22, is intermediate to these two instruments. It can be deployed in the laboratory or field and accepts collected samples of about 4 g soil.

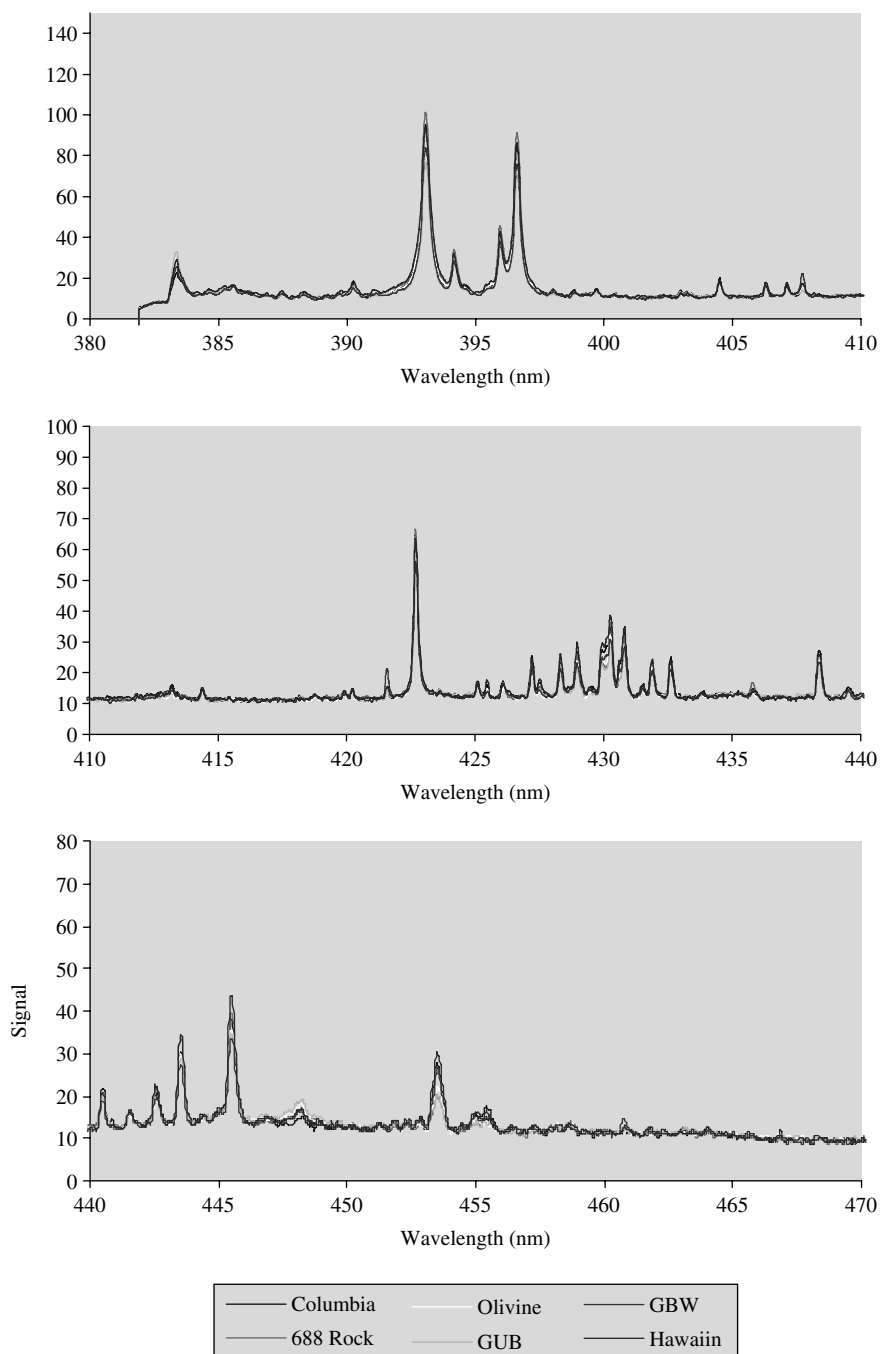


**Figure 5.19** Overlapped spectra of six basalts samples (Table 5.3) showing similarity of the spectra

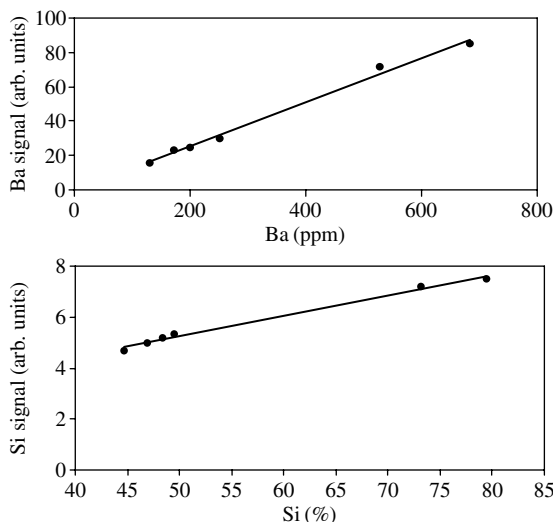


**Figure 5.20** Calibration curves for Ba and Si using the six basalt samples of Table 5.3

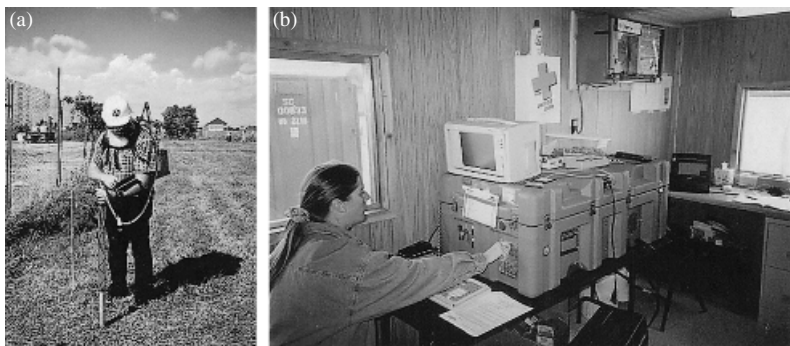


**Figure 5.21** (a) Backpack LIBS instrument shown here for direct soil analysis. (b) Transportable LIBS instrument for the analysis of collected samples. Both units were deployed at Luckey, Ohio to characterize a former beryllium processing site. (Photos courtesy of Science and Engineering Associates, Inc.)

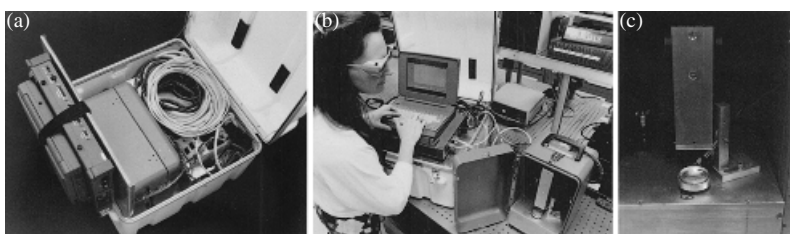


**Figure 5.22** Portable soil analyzer (ca. 1994). (a) Packaged instrument. (b) Instrument in use. (c) Analysis of loose soil sample. Soil samples are placed in small cup, rotated and analyzed using a compact Nd:YAG laser, a 0.125 m spectrograph, and a CCD



**Figure 5.23** (a) Aerial photo of a former beryllium facility at Luckey, Ohio, USA. (b) Map of main features and locations of high and low beryllium concentrations. (Photo and figure courtesy of Science and Engineering Associates, Inc.) (see Plate 9)

Actual screening results are shown in Figure 5.23 (Plate 9). An aerial view of a former beryllium processing plant at Luckey, Ohio is shown together with a map of beryllium contamination throughout the property. This map was produced from data obtained using the instrumentation shown in Figure 5.21. High

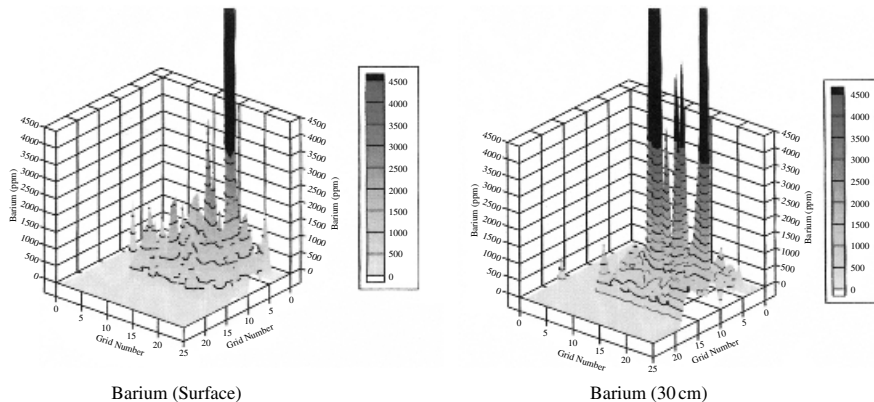


**Figure 5.24** Barium concentrations in soil determined using the field portable LIBS instrument of Figure 5.21(b). The grid refers to spatial position along the area of contamination with the determined concentrations plotted on the vertical axis. Each measurement required about 2 min, including sample exchange in the instrument (see Plate 10)

beryllium concentrations are indicated by red and the blue areas reveal lower level contamination.

Another example of soil screening is shown in Figure 5.24 (Plate 10). An open field area was contaminated by barium nitrate. The area had been exposed to the weather for many years and some of the water soluble compound had leached into the ground. Using the transportable instrument shown in Figure 5.21(b), collected samples were analyzed and maps of barium concentrations at depths down to 30 cm were developed. Two such maps are shown in Figure 5.24.

## REFERENCES

- Cravetchi, I.V., M. Taschuk, G.W. Rieger, Y.Y. Tsui and R. Fedosejevs (2003). Spectrochemical microanalysis of aluminum alloys by laser-induced breakdown spectroscopy: identification of precipitates. *Appl. Opt.* 42: 6138–6147.
- Cremers, D.A. and L.J. Radziemski (1983). Detection of chlorine and fluorine in air by laser-induced breakdown spectrometry. *Anal. Chem.* 55: 1252–1256.
- Dudragne, L., Ph. Adam and J. Amouroux (1998). Time-resolved laser-induced breakdown spectroscopy: application for qualitative and quantitative detection of fluorine, chlorine, sulfur, and carbon in air. *Appl. Spectrosc.* 52: 1321–1327.
- Jurado-Lopez, A. and M.D. Luque de Castro (2003). Rank correlation of laser-induced breakdown spectroscopic data for the identification of alloys used in jewelry manufacture. *Spectrochim. Acta Part B* 58: 1291–1299.
- Moskal, T.M. and D.W. Hahn (2002). On-line sorting of wood treated with chromated copper arsenate using laser-induced breakdown spectroscopy. *Appl. Spectrosc.* 56: 1337–1344.
- Orzi, D.J.O. and G.M. Bilmes (2004). Identification and measurement of dirt composition of manufactured steel plates using laser-induced breakdown spectroscopy. *Appl. Spectrosc.* 12: 1475–1480.

- Portnov, A., S. Rosenwaks and I. Bar (2003). Identification of organic compounds in ambient air via characteristic emission following laser ablation. *J. Lumin.* 102–103: 408–413.
- Yamamoto, K.Y., D.A. Cremers, L.E. Foster, M.P. Davies and R.D. Harris (2005). LIBS analysis of solids using a long-pulse (150 ns) A-switched Nd: YAG laser. *Appl. Spectrosc.* 50: 1082–1097.

---

# 6 Quantitative LIBS Analysis

---

## 6.1 INTRODUCTION

The ultimate goal of any analysis technique is to provide a highly quantitative analysis, that is, to determine with high precision and accuracy the concentration of a species in a sample (e.g. parts-per-million), the absolute mass of a species (for example, ng in a particle), or determine a surface concentration (e.g. ng/cm<sup>2</sup>). A quantitative analysis begins with determining the response of a system for a given concentration or mass of the analyte of interest. This usually takes the form of a calibration curve as discussed in Chapter 4. As noted there, the calibration is usually strongly dependent on the analysis conditions. So for quantitative analysis, the conditions used to prepare the calibration curve must be the same when the ‘unknown’ sample is analyzed. In a LIBS analysis there are many parameters that affect the precision and accuracy of a measurement. Some of these can be controlled, such as the stability of the laser pulse energy, and others are dependent on the sample and sampling procedure over which there may not be a high degree of control. The advantage of LIBS, that materials can be sampled directly with little or no sample preparation, is also a challenge to the method, because the physical and chemical properties of the sample can have a strong effect on the ability to obtain quantitative data. A list of important parameters that affect a LIBS analysis is presented in Table 6.1 and some of these are shown in Figure 6.1.

## 6.2 EFFECTS OF SAMPLING GEOMETRY

It has been well documented in LIBS measurements that changes in the geometrical aspects of the measurement system can strongly affect analysis results. This includes the methods of focusing the laser pulses on the target and of collecting the plasma light. For example, the power density incident on the sample is a strong function of the lens-to-sample distance (LTSD) and the power density determines, in part, emission line intensities, the relative intensities of lines, and the mass of sample ablated. The dependence of mass ablated from aluminum metal on the LTSD, for laser pulses focused by spherical and cylindrical lenses of 75 mm focal length, is shown in Figure 6.2 (Multari *et al.*, 1996). The mass ablated is clearly a strong

**Table 6.1** Factors affecting quantitative analysis using LIBS

Source	Factor	Comments
Laser	Laser pulse energy, laser pulse power, repetition rate	Typically stable to within a few percent for constant temperature operation
Detector	Detector gain	Keep constant or calibrate response if gain is changed
	Linearity of response	Operate in region of linear response or change gain to maintain linearity
Sampling parameters	Lens-to-sample distance	May be maintained through an automated focusing system; less a problem for longer focal lengths; use of a collimated beam to form the plasma can minimize effects
	Changes in optical path transmission to/from sample	Absorption/scattering of laser pulse over optical path to sample by gases and aerosols
	Change of atmosphere above sample	Gas pressure and composition affect ablation and plasma properties
Sample	Uniformity of composition	Sufficient averaging to obtain representative sample
	Uniformity of surface	Sufficient averaging to obtain representative sample
	Chemical matrix effects	Under certain experimental conditions, effect may be reduced
	Physical matrix effects	Under certain experimental conditions, effect may be reduced

function of LTSD with the cylindrical lens showing a stronger variation with changes in the sampling geometry. The total mass ablated from the metal was measured in these experiments. It should be noted, however, that the distribution of total ablated sample between atoms and sample mass removed as particles may change with LTSD. Clearly, changes in the distribution of ablated material between atomized sample and particles will affect the observed emission signals.

The plasma temperature is also a function of LTSD as shown in Figure 6.3, again for the two types of lenses and an aluminum metal sample used for Figure 6.2 (Multari *et al.*, 1996). These data were recorded using a fiber optic cable pointed at the plasma formed on the samples to collect light from all parts of the plasma. In addition, the position of the focusing lens was changed rather than the sample position so the geometry between the fiber optic and sample would remain constant for the different LTSD settings. Both lenses show a strong dependence of temperature on LTSD with a temperature variation of about 30% for the spherical lens for the range over which a useful analytical plasma could be formed. As with ablation, the cylindrical lens shows a more restricted range over which a plasma was initiated.

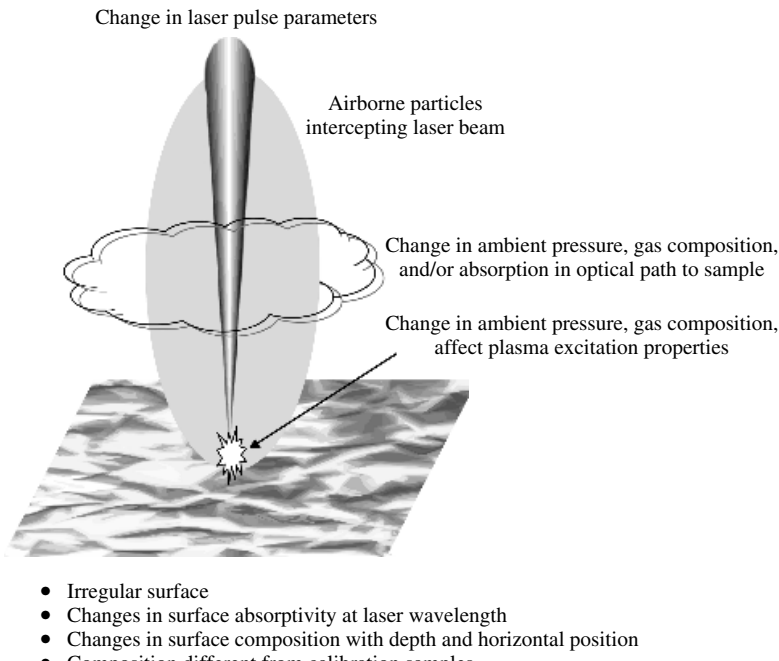


**Figure 6.1** Some factors affecting quantitative analysis in LIBS

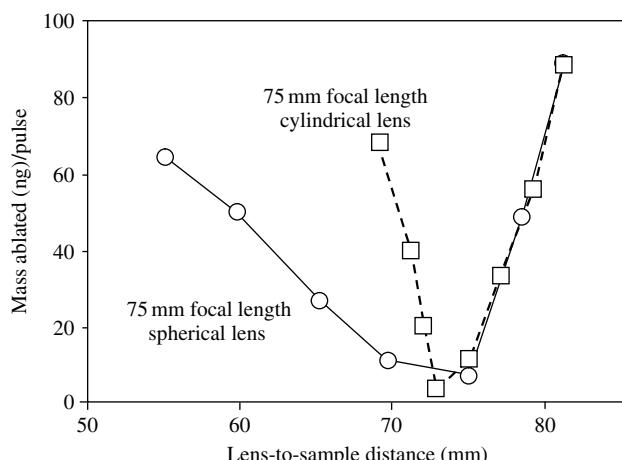


**Figure 6.2** Mass ablated from aluminum metal as a function of LTSD for spherical and cylindrical lenses (75 mm focal length). (After Multari *et al.*, 1996, with permission from Society for Applied Spectroscopy)

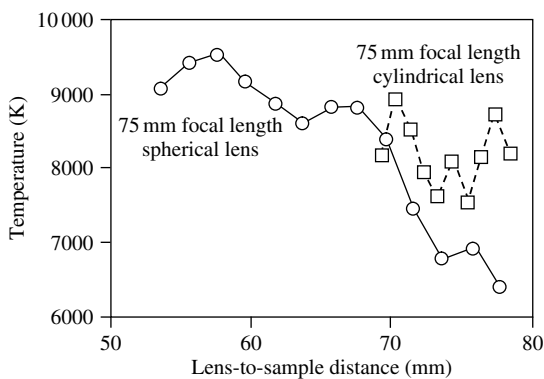


**Figure 6.3** Dependence of plasma temperature on LTSD for plasmas formed by spherical and cylindrical lenses (75 mm focal length). (After Multari *et al.*, 1996, with permission from Society for Applied Spectroscopy)

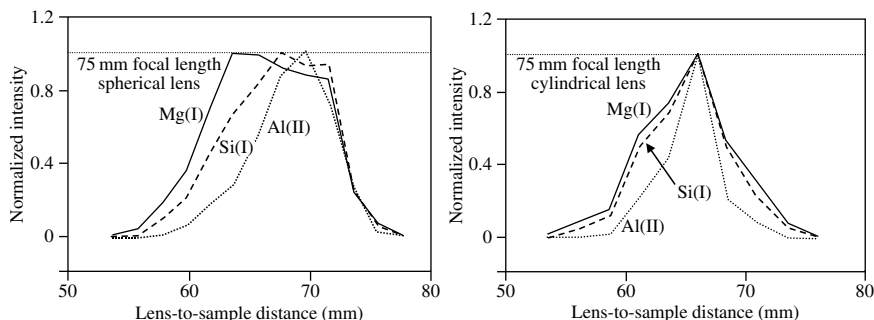


**Figure 6.4** Normalized intensities of three emission lines as a function of LTSD. Plasmas were formed by spherical and cylindrical lenses. (After Multari *et al.*, 1996, with permission from Society for Applied Spectroscopy)

The results of a different experiment are shown in Figure 6.4, which contains the normalized dependence of emissions from Al(II), Mg(I) and Si(I) as a function LTSD on soil samples, for the same two lenses (Multari *et al.*, 1996). The emission lines used were 281.62, 285.21 and 288.16 nm, respectively. Samples were soil pressed into a pellet to provide a smooth and uniform surface for analysis. These were translated under the repetitive laser sparks and the spectra were averaged. As the data show in both cases, the emission signals are a strong function of the LTSD for the two lenses, the most intense emissions occurring at a LTSD less than the lens focal length. For the spherical lens, the emission intensities remain above the normalized value of 0.5 over a range of about 14 mm ( $60 \text{ mm} < \text{LTSD} < 73 \text{ mm}$ ), while for the cylindrical lens the range is somewhat smaller, about 10 mm ( $60 \text{ mm} < \text{LTSD} < 69 \text{ mm}$ ).

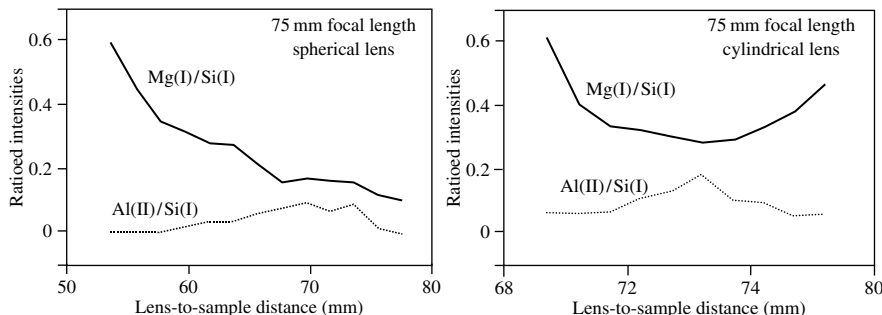


**Figure 6.5** Ratioed intensities of two emission lines as a function of LTSD. Plasmas were formed by spherical and cylindrical lenses. (After Multari *et al.*, 1996, with permission from Society for Applied Spectroscopy)

Figure 6.5 shows the intensity ratios of  $\text{Mg(I)}/\text{Si(I)}$  and  $\text{Al(II)}/\text{Si(I)}$  as a function of LTSD for the two lenses. Ideally, the ratio should be independent of LTSD assuming that excitation parameters (e.g. temperature, Figure 6.3) within the plasma change the same for the two species involved in the ratio. The somewhat large variation in the ratio with LTSD shown by these data suggests that the different species are experiencing different excitation with LTSD values.

### 6.3 OTHER SAMPLING CONSIDERATIONS

The calibration curve is one good diagnostic to probe different matrix effects in LIBS analysis. The dependence of calibration curves on pressure has already been briefly discussed in Chapter 4. Specifically of interest is Figure 4.15, which shows that as the ambient air pressure is reduced, the slope of the calibration changes significantly. With reduced pressure, the slope increases and maximizes for pressures in the region around 10–100 Torr. Then the slope decreases significantly as the pressure is further reduced. The two main competing processes at work here are changes in mass ablated and changes in excitation parameters with pressure (e.g. electron density and temperature; Knight *et al.*, 2000). As the pressure is decreased, the mass of material ablated increases significantly but it levels off for pressures below about 10 Torr. On the other hand, as the pressure is reduced, the excitation of species in the plasma decreases because the collision rate, responsible for excitation in the cooling, decaying plasma, decreases linearly with pressure. The net result of the two competing processes is a peak in element excitation at pressures of a few tens of torr. It must be realized, however, that other factors are at work which also affect the observed element emission intensity. As the pressure is reduced, the atomic species are no longer confined to the initial plasma volume at the surface and they can escape more readily into the region above the surface. At very low pressures, on the order of microns, atoms are ejected from the surface and are quickly transported

out of the region of the laser pulse/material interaction zone at the surface. Because of its low mass, hydrogen would escape more quickly than any other element. Under these conditions, after the laser pulse is turned off ( $\sim 10$  ns for Q-switched Nd:YAG lasers), the excited species may no longer be in the field of view of the light collection system giving an apparent decrease in excitation, which may also be different for different atoms. All of these factors are active and must be considered.

Another interesting effect of pressure is demonstrated by Figure 6.6 (Sallé *et al.*, 2005). Here we show calibration curves for Ca(II) at 393.3 nm for certified

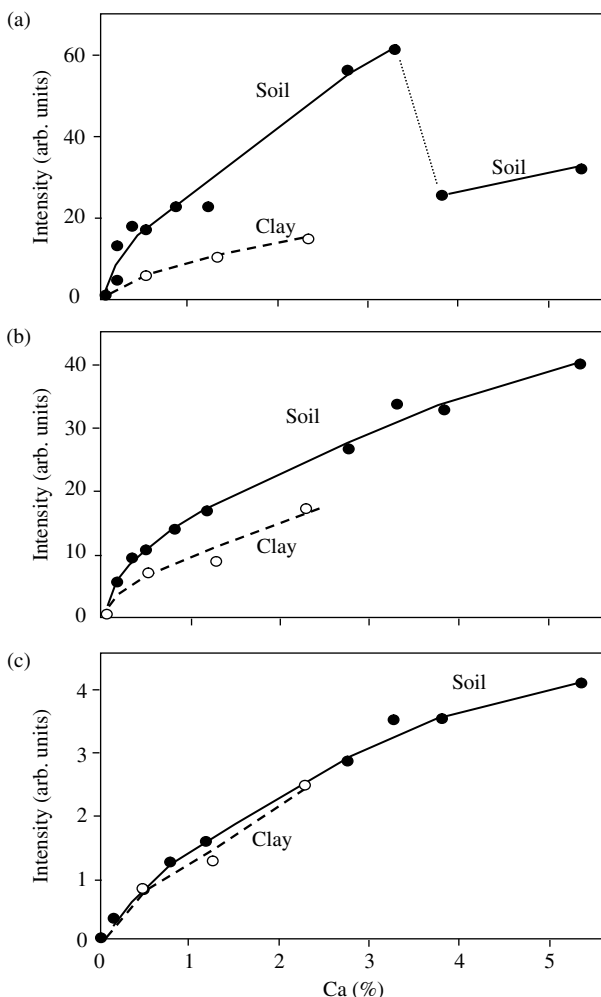


**Figure 6.6** Comparison of calibration curves for Mn in soil and clay samples at three pressures. (a) 585 Torr; (b) 7 Torr; (c) 50 mTorr. (After Sallé *et al.*, 2005, with permission from Elsevier)

soil and clay samples at three different pressures. The compositions of these matrices are significantly different with clay samples being characterized by high aluminum content. These data show two interesting effects. First, at 585 Torr (Figure 6.6a), the calibration curves for the two matrices are significantly different with a greater slope observed for the soil sample. As the pressure is reduced, the slopes of both curves decrease but the slope of the curve corresponding to soil decreases to a greater extent compared with the curve for clay. At the lowest pressure, 50 mTorr, the curves appear to overlap. That is, reduced pressure has reduced significantly a matrix effect yielding highly collinear calibration curves.

Secondly, we note that the soil data for the curve at 585 Torr do not show a steady correlation of Ca signal with Ca concentration. The data appear ‘noisy’ and at the two highest concentrations the correlation breaks down completely. As noted above, however, as the pressure is reduced the soil data become more smoothly correlated and this is especially evident for the two highest Ca concentrations as these values now lie along a smooth calibration curve. At the lowest pressures, the correlation among the soil data becomes even stronger. Clearly, the sampling parameter of ambient pressure significantly affects the analytical results and it does so by reducing some chemical matrix effect.

Because LIBS is a surface analysis method, surface deposits such as weathered layers (Figure 5.1) or dirt (Figure 5.17) can interfere with the determination of the underlying bulk composition. In some cases, repetitive ablation can remove these layers sufficiently to permit sampling of the bulk materials. In addition to such surface effects, the inherent inhomogeneity of the sample can complicate a determination of sample composition. In fact, the question may arise as to what is the true composition of an inhomogeneous sample. Differences in composition can be spatially large so that if 1 mm<sup>3</sup> of a sample was extracted and analyzed the results may be quite different from those obtained by extracting and analyzing a 1 cm<sup>3</sup> volume of the sample. This is demonstrated by the photo of a rhyolite rock surface shown in Figure 6.7 (Plate 11). The close up photo shows visual inhomogeneities in the rock surface that are on the order of 1–3 mm. Because of the typically small size of the focused spot used to form the laser plasma (100–200 µm), the element signals will be strongly dependent on the position of the focal spot on the sample. A long spark, also shown in Figure 6.7, can be used to average over some of these inhomogeneities.

Another example of sampling characteristics is presented in Figure 6.8 which shows the results of scans with a long spark over an aluminum surface contaminated with a Tl containing solution. The features show how the Tl is distributed on the surface. As the sparks are scanned along the surface, emissions from Al and Fe from the metal are clearly evident in the spectral region around 358 nm. As the sparks begin to interrogate the Tl deposited as a solution (then dried) on the plate, strong Tl emissions are observed in combination with a suppression of emissions from the Al and Fe in the substrate. Effectively, the dried deposited solution is inhibiting sampling of the underlying metal: the dried layer is shielding the metal

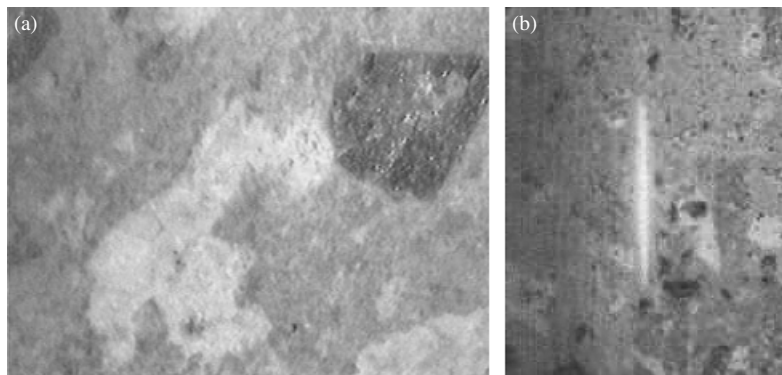


**Figure 6.7** (a) Close-up photo of a ground surface of a rhyolite rock sample. Distinct features are 1–2 mm in size. (b) Analysis of the same rock using a long spark (1 cm) to average over inhomogeneities (see Plate 11)

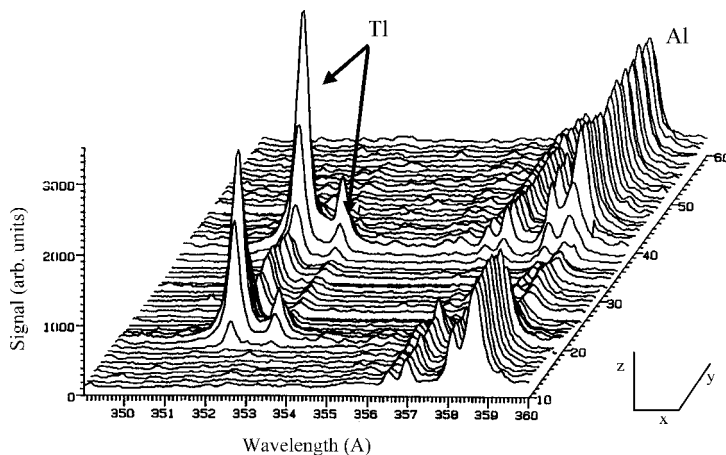


**Figure 6.8** Sequential spectra recorded by scanning a series of long laser sparks along an Al metal plate contaminated by a Tl solution. The three lines to the left of the Al line are due to Fe. The location of the Tl is coincident with a suppression of emissions from Al and Fe in the metal. Wavelength (x); shot number (y); signal (z)

surface from the incident laser energy. It is interesting to observe how the Tl signals increase at the start and finish of the scan across the Tl contaminated region. This correlates with a visible inspection of the dried Tl containing solution on the metal, which shows deposition as a ring-shaped pattern on the surface.

## 6.4 PARTICLE SIZE AND INCOMPLETE VAPORIZATION

Physical factors can affect LIBS analysis. When analyzing a powdered sample or an aerosol, one such factor is particle size. This was demonstrated by one set of experiments. BeCu particles of four different size groups were deposited on filters and interrogated using LIBS. The particles were sized in a cyclone separator, collected and then suspended in water. By placing a known volume of the well-stirred suspension on filter paper (6.4 mm diameter), a known mass was deposited. The actual Be mass in an aliquot of each suspension size was determined by depositing an aliquot of each solution on replicate filters which were then analyzed using ICP analysis.

Six replicate LIBS analyses were performed using a freshly prepared filter for each analysis. The laser pulse energy was 20 mJ. The Be signal data for each particle size group were plotted and are shown in Figure 6.9. There is a strong dependence of the calibration curve slope on particle size (in  $\mu\text{m}$ ), with the slope increasing as particle size decreases. The results indicate that a greater mass of Be is being accessed as the particle size decreases suggesting a physical matrix effect. If the larger particles are incompletely vaporized, the resulting Be signal will be lower than that obtained from smaller particles that are completely vaporized. The data of Figure 6.9 indicate that the boundary between complete and incomplete vaporization resides around a particle size of about  $2 \mu\text{m}$ . These results agree with a separate determination of complete particle vaporization which indicated that, for 320 mJ, the maximum size particle that could be vaporized is on the order of  $2.1 \mu\text{m}$  (Carranza and Hahn, 2002). Assuming that all laser pulse energy is directed toward ablation, a simple calculation predicts that a copper particle (the major component of BeCu used here) of diameter  $\sim 150 \mu\text{m}$  should be completely ablated by 20 mJ. Therefore, it appears that only a fraction of the laser energy is going into vaporization.

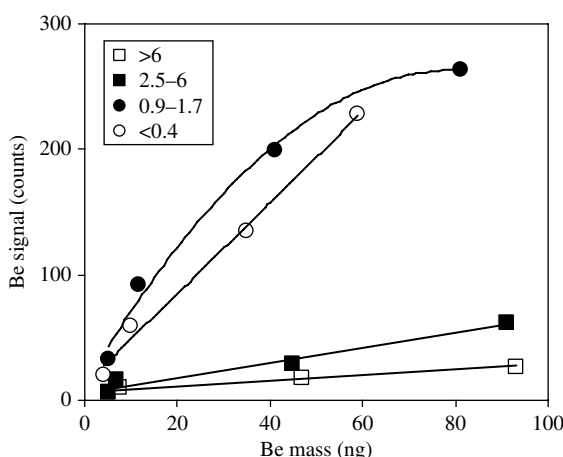


**Figure 6.9** Calibration curves for Be(II) at 313.1 nm for different sizes of BeCu metal particles (in  $\mu\text{m}$ )

## 6.5 USE OF INTERNAL STANDARDIZATION

As discussed in Chapter 4, use of an internal standard can often minimize shot-to-shot variations in the LIBS emission signal, increasing measurement precision and correcting nonlinear behavior in calibration curves. The LIBS signal in this case is the analyte signal ratioed to the emission from the internal standard element. This correction was demonstrated in Figure 4.12. Another example of the use of an internal standard is shown in Figure 6.10. To obtain these data, a series

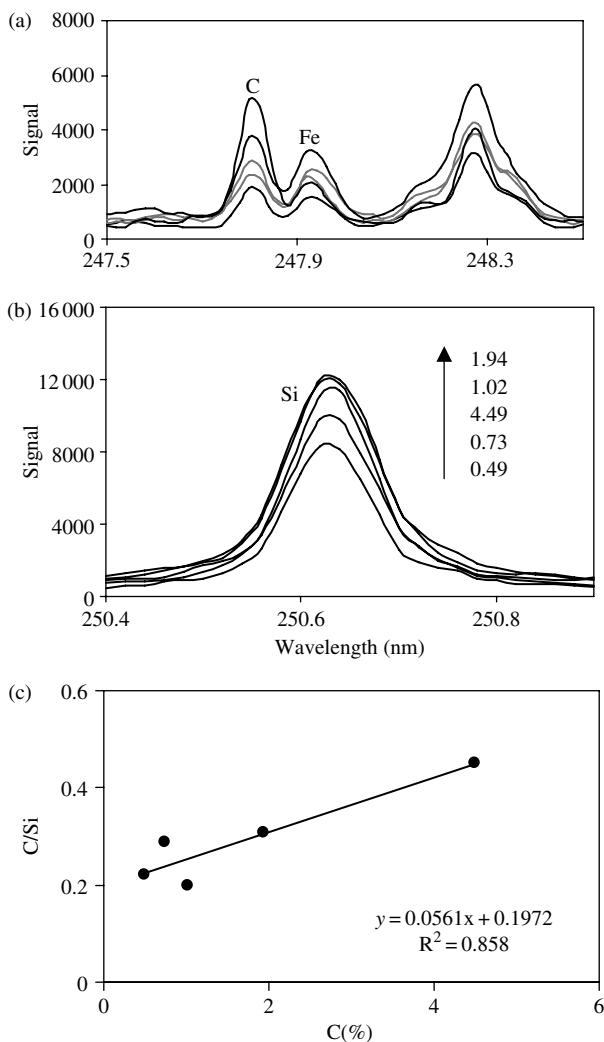


**Figure 6.10** Internal standardization in the detection of carbon in soil

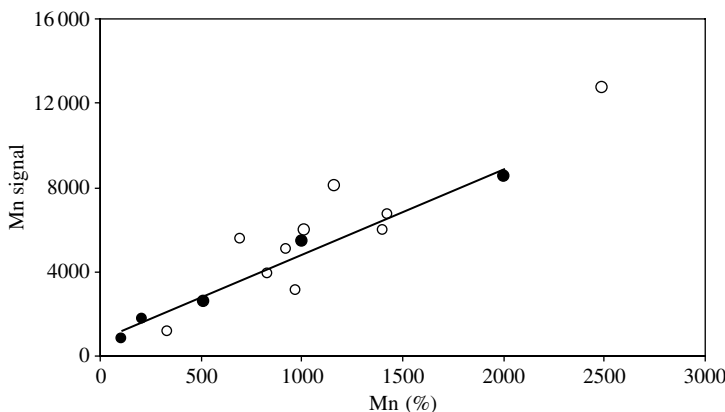
of soil samples from approximately the same geographical location were collected, homogenized, and then analyzed by a conventional combustion analysis method to determine total carbon content. The values found for the different samples were 0.49, 0.73, 1.02, 1.94 and 4.49 wt%. These samples were then analyzed using the laser plasma from pressed samples of each member of the collected soil series. The C(I) line at 247.86 nm was recorded simultaneously with the Si(I) line at 250.6 nm using an echelle spectrograph. These emissions are shown in Figure 6.10 for each of the five samples. Silicon was assumed to be at a constant concentration in the soils as the samples were obtained from approximately the same location. The carbon content will vary more widely than silicon with changes in location due to processes such as plant growth and decay which produce large changes in carbon content over a small area.

Figure 6.10(a) shows the carbon and iron signals for the five samples. The spectra as grey lines are out of order with respect to the carbon concentration in the samples. The carbon peak should increase in intensity with carbon concentration in the soil. Figure 6.10(b) shows the silicon signal for the different samples. The curves are labeled as indicated by the arrow according to the corresponding carbon content of the soil sample. Ideally, the silicon signals would overlap to a high degree showing concentration uniformity in the samples but here we see that there is a strong variation in the silicon signal with the sample. This is true even though the experimental conditions were kept constant for all measurements and the variation was attributed to differences in ablation and plasma excitation occurring during the different analyses. Figure 6.10(c) shows the resulting carbon calibration curve using silicon as an internal standard. The results indicate that even though the carbon signals do not monotonically increase with carbon content and the silicon signal, the internal standard, varies strongly from sample to sample, a usable, though not perfect, calibration curve can be prepared using internal standardization.

## 6.6 CHEMICAL MATRIX EFFECTS

The effect of different species on the analyte in the LIBS plasma is a manifestation of a chemical matrix effect. Other plasma sources exhibit matrix effects but the LIBS plasma can be highly sensitive to these because of the high density of material in the plasma. It is well known that in some plasma sources the introduction of an easily ionizable element, such as cesium, can move the neutral – ion equilibrium concentration of an analyte toward the neutral species (e.g. Le Chatelier's principle). The increase in electron concentration introduced by the easily ionizable element will increase electron–ion recombination and hence result in a greater number of neutral species (Eppler *et al.*, 1996).

A good example of a matrix effect is shown in Figure 6.11. Here we show LIBS data for Mn(I) (set of lines around 403 nm) obtained using certified stream sediment samples and synthetic silicate samples. The concentrations of the major elements in the sediment samples vary from sample to sample but the concentrations of these



**Figure 6.11** Calibration curve for Mn in (open circles) sediments and (closed circles) synthetic silicate samples. The linear fit is to the (closed circles) data

same elements in the synthetic silicate samples remain constant. Major element concentrations for both sample matrices are listed in Table 6.2 with the ranges of major species for the sediment samples listed as they are sample dependent. The data of Figure 6.11 show that greater correlation between Mn signal and Mn concentration was obtained using the constant matrix composition of the synthetic silicates compared with the sediment samples. These data suggest that the variations in the major element concentrations of the sediment samples perturb the Mn emission intensities precluding a high correlation between signal and concentration.

LIBS measures the total abundance of an element in a sample because the plasma breaks down the original target sample into its component parts (e.g. F-atom counting, Section 5.3). In principle, all information about the starting material structure and bonding is lost. It has been shown, however, that the signals obtained from an element depend on the compound form of the starting material (Eppler *et al.*, 1996). A simple example of this is shown in Figure 6.12. Here we show signals from Pb(I) (405.7 nm) and Ba(II) (233.5 nm) compounds ratioed to C(I) (247.8 nm) and Cr (425.4 nm). Masses of the compounds were added to the soil so the concentration

**Table 6.2** Major elements in synthetic silicate and stream sediment samples

Sample	Major species (wt%)									
	SiO <sub>2</sub>	Al <sub>2</sub> O <sub>3</sub>	Fe <sub>2</sub> O <sub>3</sub>	CaMg(CO <sub>3</sub> ) <sub>2</sub>	Na <sub>2</sub> SO <sub>4</sub>	K <sub>2</sub> SO <sub>4</sub>	Na <sub>2</sub> O	K <sub>2</sub> O	CaO	MgO
Synthetic silicates (all)	72	15	4	4	2.5	2.5	—	—	—	—
Sediments (range)	32–75	10–29	2–13	—	—	—	0.1–3.3	0.2–3.4	0.2–8.3	0.3–2.4

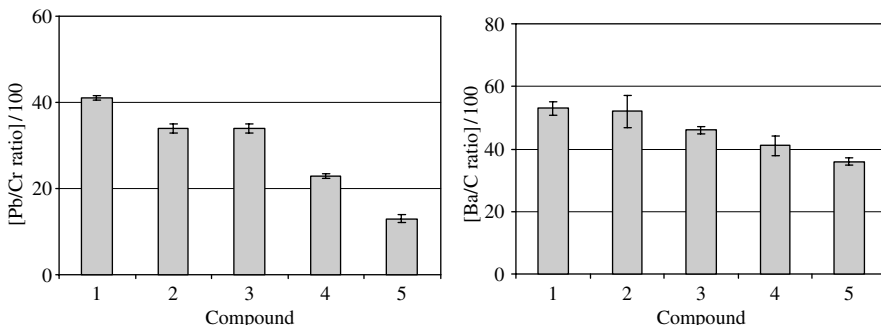


**Figure 6.12** Dependence of Pb(I) and Ba(II) signals on compound form in a solid matrix. For Pb(I): 1, -O; 2, -CO<sub>3</sub>; 3, -Cl<sub>2</sub>; 4, -SO<sub>4</sub>; 5, (NO<sub>3</sub>)<sub>2</sub>. For Ba(I): 1, -CO<sub>3</sub>; 2, -O; 3, -SO<sub>4</sub>; 4, -Cl<sub>2</sub>; 5, (NO<sub>3</sub>)<sub>2</sub>. (Data from Eppler *et al.*, 1996)

of the analyte was constant. The precision bars indicate one standard deviation from a set of six replicate measurements. As the data show, the Ba(II) and Pb(I) signals depend on the compound when ideally they should be comparable. The source of these differences could be due to a chemical matrix effect in which the element constituents of the counter ions (e.g. CO<sub>3</sub>, Cl<sub>2</sub>SO<sub>4</sub>, etc.) in the compounds change the excitation and emission characteristics of Ba(II) and Pb(I). Alternatively, the differences could be due to difference in the mass of each compound ablated because of the different heat capacities, vaporization temperatures, and/or absorption at the laser wavelength, characteristic of the different compounds.

## 6.7 EXAMPLE OF LIBS MEASUREMENT: IMPURITIES IN LITHIUM SOLUTIONS

The report presented below demonstrates the procedures, analyses and results used to evaluate LIBS for the detection of impurities in LiCl solutions. The report was prepared for an industrial sponsor and was aimed at benchmarking LIBS capabilities. Of particular importance was the ability to perform such measurements on samples contained in a sealed environment, such as a processing stream with no direct physical access. The results demonstrate many aspects and characteristics of a quantitative LIBS study. Certain aspects of LIBS measurements discussed in other chapters of this book (e.g. Chapter 4), such as self-absorption, spectral interferences, and the calculation of precision and detection limits are demonstrated.

### 6.7.1 OBJECTIVE

The objective of this study was to assess the analytical capabilities of LIBS for the detection of impurities contained in aqueous solutions of 10 M LiCl.

The impurities are Ca, Mg, Si, Cl, K, Na, Fe, Cr, Ni and C. This report describes: (1) the experimental instrumentation and test methods used for LIBS measurements; (2) calibration curves for each impurity over the range 50–2000 ppm; and (3) detection limits and measurement precision for each impurity over the concentration range of interest.

## 6.7.2 EXPERIMENTAL

### 6.7.2.1 Apparatus

The experimental set-up used for the LIBS measurements is shown in Figure 6.13. The pulses from a Q-switched laser were focused on the surface of the solutions contained in sealed quartz vials through the side of the vial as shown. Surface excitation was used instead of forming the laser spark in the bulk liquid because of previous indications of improved detection limits. The light from the spark was collected by a lens and imaged onto the entrance slit of a spectrograph. The spectrally resolved light was detected by a time-gated intensified photodiode array. A pulse generator was used to trigger the laser and to send a gate pulse to the detector head. The gate pulse determined the time interval over which the detector collected light from the spark. This interval was in most cases 2–200 µs after spark formation. In this way, the strong background continuum radiation from the plasma, which occurs within the first few microseconds after spark initiation, was eliminated from the measurements. The experimental equipment and conditions are listed in Table 6.3.

### 6.7.2.2 Preparation of Solutions

The solutions were prepared in the following manner. First, a large volume of a 10 M solution of LiCl/water was prepared from analytical grade powders of the salts and deionized water. Then, smaller volumes of each of these solutions were measured out and known masses of analytical grade powdered salts containing each of the impurities were weighed out and dissolved in the LiCl volumes to produce a

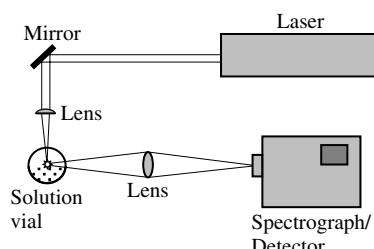


**Figure 6.13** LIBS apparatus to evaluate the detection of impurities in Li-containing solutions

**Table 6.3** Experimental conditions for LIBS experiments

Laser	Quanta-Ray DCR-1A, Nd:YAG
Wavelength	1064 nm
Pulse length	10 ns
Pulse energy	200 mJ
Repetition rate	10 Hz
Optics	
Focusing lens	2.54 cm diameter, 5 cm focal length
Imaging lens	quartz, 2 in. diameter, 10 cm focal length
Detection system	
Spectrograph	0.5 m focal length, SPEX Industries
Gratings	1200, 2400 and 3600 lines/mm
Detector	Tracor Northern TN-6500 controller with TN-6132 photodiode array
Vials	Analabs, type 35 quartz spectrometer cell (50 mm diameter × 50 mm long)

2000 ppm solution. Portions of these solutions were then diluted with the portions of the master LiCl solutions to give impurity solutions having concentrations of 50, 100, 200, 400 and 800 ppm. Only one impurity was present in each solution (i.e. the impurities were not mixed). For the LIBS measurements, a fixed volume of each solution was put into a clean vial and sealed. Keeping the volume constant maintained the distance between the liquid surface and focusing lens constant.

### 6.7.2.3 Experimental Procedure

#### *Calibration Curves*

Calibration curves were prepared by measuring the emission signal averaged from 600 laser sparks formed on the surface of each solution containing a specific impurity over the 50–2000 ppm concentration range. The photodiode array controller automatically averaged the spectra as they were accumulated and calculated the area under the emission peak. The area of the peak obtained by analyzing each of the six different solutions for a specific impurity was plotted against impurity concentration to produce a calibration curve. A curve was prepared for each impurity in this way.

A list of the analytical lines used for each impurity is presented in Table 6.4. These lines are, in general, those that give the maximum detection sensitivity in emission spectrochemical analysis. Compared with other elements, lithium has few emission lines and the strongest unresolved emissions of Li(I) at 670.78 and 670.79 nm did not interfere with detection of the impurity atoms examined here.

#### *Measurement Precision*

The precision of the LIBS measurements was determined by performing ten replicate measurements of the impurity signals at high and low concentrations and calculating

**Table 6.4** Analytical lines of impurity elements

Element	Line (nm)	Element	Line (nm)
Ca	393.37 (II)	Na	589.59 (I)
Mg	279.55 (II)	Fe	248.33 (I)
Si	288.16 (I)	Cr	267.716 (I)
Cl	837.59 (I)	Ni	231.60 (II)
K	766.49 (I)	C	247.86 (I)

(I), neutral atom; (II), once-ionized atom.

the standard deviation. Elemental signals were averaged from 200, 600 and 1800 laser sparks corresponding to measurement times of 0.33, 1 and 3 min, respectively.

### **Detection Limits**

The limit of detection (LOD) was determined by computing the slope ( $m$ ) of the calibration curve ( $\Delta c/\Delta x$ , where  $x$  is the signal) at low concentrations and using the formula  $LOD = 2sm$ , where  $s$  is the standard deviation of 10 measurements made for a specific impurity at the lowest concentration of 50 ppm (Chapter 4).

## 6.7.3 RESULTS

### **6.7.3.1 General Considerations**

Typical spectra obtained for this report are shown in Figure 6.14. Here the strong emissions from once-ionized Mg are clearly evident in Figure 6.14(a) obtained by averaging the light from 100 sparks. The detector gate was set so the spark light from 1 to 201  $\mu$ s after spark formation was integrated. Emissions from Li(I) and Mg(I) are also evident in the spectrum. The spectrum shown in Figure 6.14(b) was obtained by integrating the light from 10 to 210  $\mu$ s. The intensities of the Mg(II) lines shown here relative to the Li(I) and Mg(I) lines are much less than that shown in the spectrum in Figure 6.14(a). This demonstrates the general rule that lines from ions decay more rapidly than neutral lines as the plasma cools. Figure 6.15 shows the spectrum obtained from a 250 ppm Ni in 10 M LiCl solution (Figure 6.15a) and the spectrum recorded from a ‘pure’ 10 M LiCl solution (Figure 6.15b) over the same spectral region. The Ni emission lines are clearly evident and no ‘background’ spectral features are present from the solution containing only LiCl. Figure 6.16 shows the spectrum obtained from a 250 ppm Cr in 10 M LiCl solution (Figure 6.16a) and the spectrum obtained from a 10 M LiCl solution (Figure 6.16b) over the same spectral region. Two Cr lines are completely free of spectral interferences but a strong Li line interferes with a strong Cr line in this spectral region.

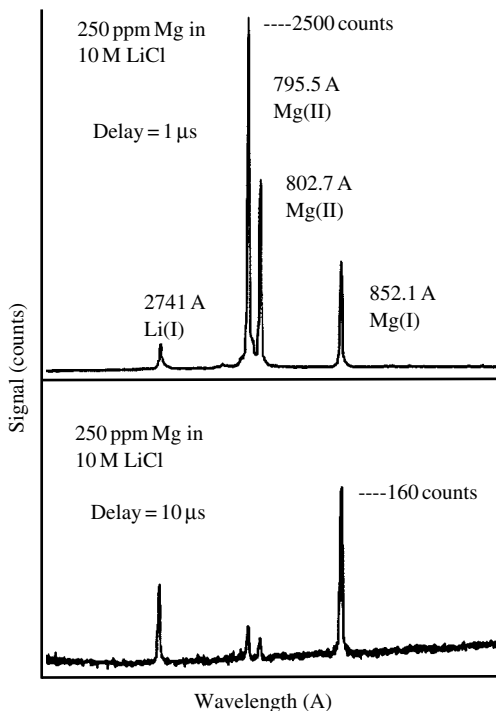


**Figure 6.14** LIBS spectrum of Mg lines at two delay times. Sample was Mg in a LiCl solution

Analysis of carbon with LIBS presented a problem at the carbon concentrations of interest here. Carbon signals were obtained from a ‘pure’ solution of 10 M LiCl and even from deionized water. The latter was attributed to excitation of carbon dioxide in the air above the solution. This carbon signal was reduced significantly by purging the vial with argon gas before sealing it prior to analysis. A strong residual carbon signal was obtained from the 10 M LiCl solution even when it was purged with argon gas. Initially, this emission signal was attributed to a somewhat strong Li(I) line located at 247.5 nm but the dispersion of the detection system was such that features 0.3 nm apart [the C(I) line lies at 247.8 nm] were easily identifiable as distinct lines. Therefore, the carbon signal in the LiCl solution was attributed to carbon impurities in the powder used to prepare the solution.

### 6.7.3.2 Calibration Curves

Calibration curves for the LIBS measurements are presented in Figures 6.17, 6.18 and 6.19. The elemental signals have been normalized to the signal measured at the

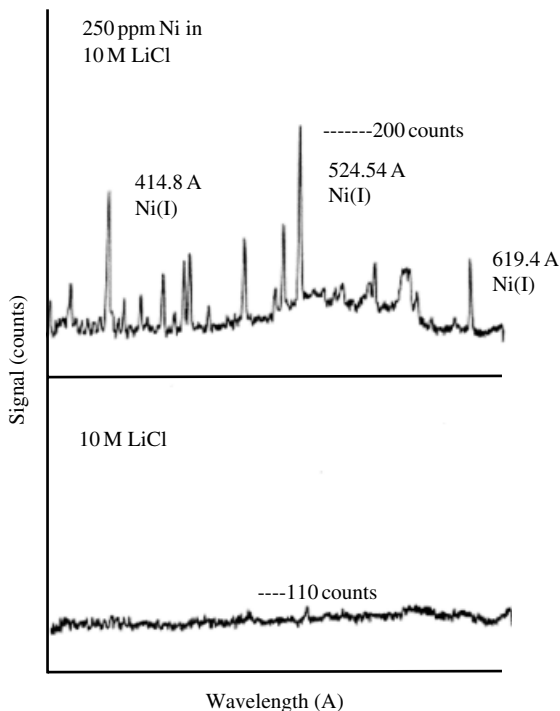


**Figure 6.15** LIBS spectrum of Ni in a LiCl solution (a) and the spectrum recorded from the neat LiCl solution (b)

highest concentration of 2000 ppm studied here. In most cases, the calibration curves are linear over the range shown. The two exceptions are calcium and carbon. At high calcium concentrations, the calibration curve shows a loss of sensitivity (slope) which is probably due to self-absorption. The calibration curve for carbon shows a loss of sensitivity at low concentrations. This is probably due to a background carbon signal from carbon in the atmosphere above the solution in the vial which could not be eliminated completely and carbon impurity believed to be in the LiCl powder as discussed above. Chlorine could not be detected in these solutions even at concentrations as high as 2000 ppm. This is probably due to the high energy (10.4 eV) of the strong IR neutral chlorine transition normally used for analytical work and the weaker excitation obtained by forming the spark on a liquid.

#### 6.7.3.3 Precision

The precision of the LIBS measurements is presented in Table 6.5. The values listed in this table are a compilation of results obtained for the different impurities. In general, the same range of measurement precision was obtained for the different

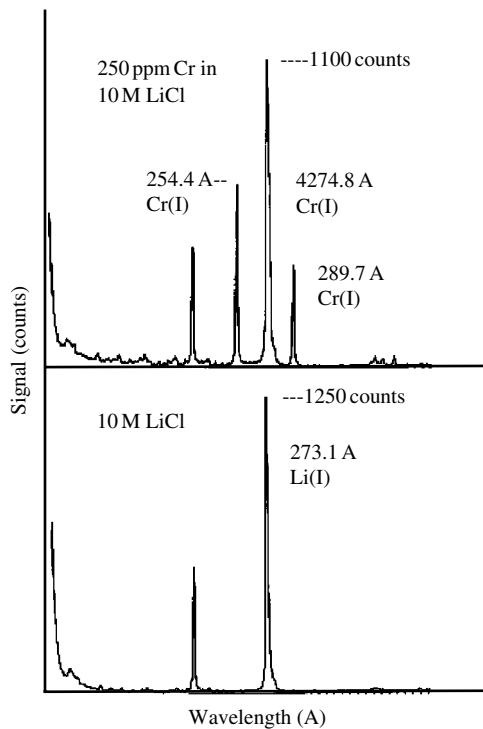


**Figure 6.16** LIBS spectrum of Cr in a LiCl solution (a) and the spectrum recorded from the neat 10 M LiCl solution (b). Two Cr lines are completely free of spectral interferences but a strong Li line interferes with a Cr line in this spectral region

**Table 6.5** Measurement precision

Integration period (sparks)	Precision (%)
200	5–8
600	4–6
1800	1–3

impurities and no distinct trends were observed (i.e. in repeated measurements, no impurity appeared to yield better measurement precision than another impurity) indicating the measurement precision obtained was characteristic of LIBS itself. As expected, there was an increase in precision as the integration period (number of sparks or elapsed time) increased.

#### 6.7.3.4 Detection Limits

The detection limits for the different impurities are listed in Table 6.6.

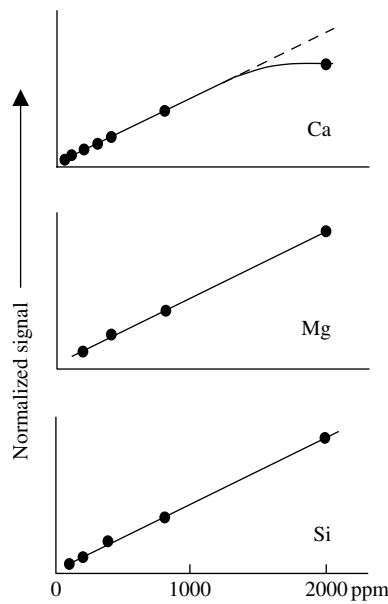


**Figure 6.17** Calibration curves for the impurities Ca, Mg and Si in LiCl solutions

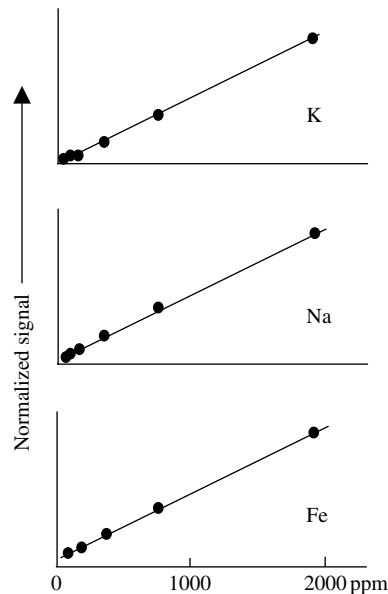


**Figure 6.18** Calibration curves for the impurities K, Na and Fe in LiCl solutions

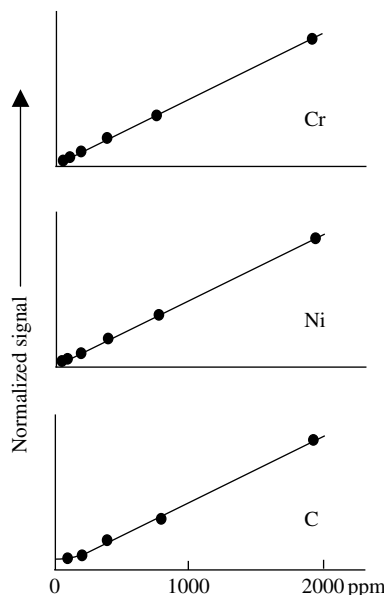


**Figure 6.19** Calibration curves for the impurities Cr, Ni and C in LiCl solutions

**Table 6.6** Detection limits (in ppm) for impurities in LiCl solutions

Impurity	LOD	Impurity	LOD
Ca	1	Na	0.02
Mg	200	Fe	20
Si	60	Cr	20
Cl	—	Ni	20
K	1	C	50

LOD, limit of detection.

#### 6.7.4 DISCUSSION OF RESULTS

The LIBS detection limits determined for many impurities are sufficiently low to meet requirements of certain applications. The detection of carbon, however, one important impurity, will be compromised for analyses conducted in air. In addition, the analyses are sufficiently rapid to provide for real-time continuous monitoring. Because the surface of the solution is significantly agitated by the shock waves set-up by the spark, the mass of sample analyzed varies from spark to spark. This can be averaged out of the measurements to some degree by averaging a large number of sparks for each measurement.

The advantages of the LIBS method are its noninvasive and remote detection capabilities. Samples can be analyzed in place, all that is required is optical access to the material to form the spark and collect the emitted light. For maximum measurement accuracy, the LIBS method must be periodically calibrated using standards similar to the unknown solutions to be determined. A method must be developed to introduce the calibration samples into the sealed environment containing the unknown samples. There are many variables that depend on experimental conditions that can affect the excitation properties of the plasma. For example, it has been shown that the LTSD is critical in LIBS analysis so the calibration samples must be introduced in such a way as to duplicate this parameter.

## 6.8 REPORTED FIGURES-OF-MERIT FOR LIBS MEASUREMENTS

LIBS analytical figures-of-merit (FOM) have been reported in the literature for a variety of samples under different measurement conditions. The majority of these measurements have been conducted in the laboratory but there have been some reports of tests done in the field with LIBS results compared with analyses obtained using conventional methods. An extensive list of detection limits derived from the LIBS literature is presented in Appendix C. When reviewing this list it should be noted that detection limits were determined in different ways, some based on the procedures of Chapter 4, and with others estimated based on the signal to noise ratio at one concentration. In addition, specific experimental parameters (e.g. laser pulse energy, delay times, etc.) varied between different studies. The literature reference should be consulted for specific information regarding the detection limit computation.

In determining LIBS accuracy, the LIBS result must be compared against the true or assumed concentration of an element in the sample. Care must be exercised in comparing such results, with special consideration given to evaluating the method or methods used to determine the ‘accepted true’ concentration in a sample (Section 4.6). For example, some accepted methods of determining elements in soils do not necessarily access all forms of the element. These may only determine the concentration of the element that is in a certain oxidation state with the other oxidation states representing compounds that are not accessed by the analytical technique. LIBS, however, accesses all forms of an element. In such cases, the LIBS value can be expected to be higher than the value determined by the other method.

The accuracy of LIBS has been determined less often than measurement precision and detection limits but there are several reports that show the capability of LIBS using different data reduction methods. For example, Figure 6.20 presents data obtained from the analysis of standard reference materials (SRMs; Colao *et al.*, 2004) using calibration-free LIBS (CF-LIBS), a method discussed in Section 8.3.

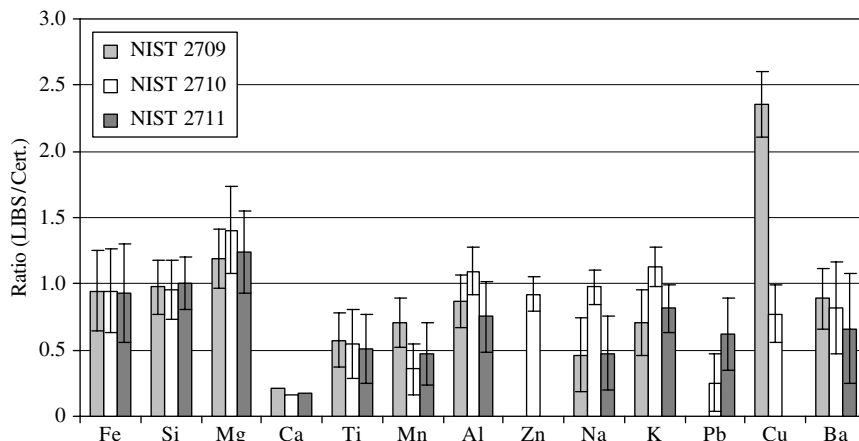


**Figure 6.20** Display of LIBS accuracy using certified standard reference materials. (Data from Colao *et al.*, 2004)

The SRMs were powdered samples having a high uniformity of composition with the accepted true values of element concentrations determined by several methods and then averaged. Using such samples represents a good test of LIBS analysis capabilities. Plotted in Figure 6.20 is the predicted element concentration divided by the certified concentration. Ideally, the ratios will be unity but we note there is element dependent deviation from this value. The precision bar on each result denotes the  $\pm$  uncertainty in the predicted values indicated by the authors. The underestimations of the concentrations of Ca, Na and K were attributed to saturation of the observed emission lines although an effort was made to exclude lines known to exhibit strong saturation effects from the analysis. The data show that the best correlations were obtained for the major elements Fe, Si and Mg.

The same authors, using CF-LIBS and mineral samples, compared LIBS results with those obtained by SEM-EDX (scanning electron microscope equipped with an energy dispersive x-ray spectrometry micro-analytical tool). These results are shown in Figure 6.21 plotted in the same way as described for Figure 6.20.

In data from another study, LIBS results for Antarctic sediments were compared with certified values (Lazic *et al.*, 2001). These results are presented in Table 6.7. The accuracy error was computed according to Equation (4.5) except the absolute value was not included to show over- and underestimations of the concentrations. The predicted concentrations were based on an algorithm that takes into account self-absorption and contributions from regions in the plasmas with different densities resulting in a model that corrects for nonlinearity between emission intensities

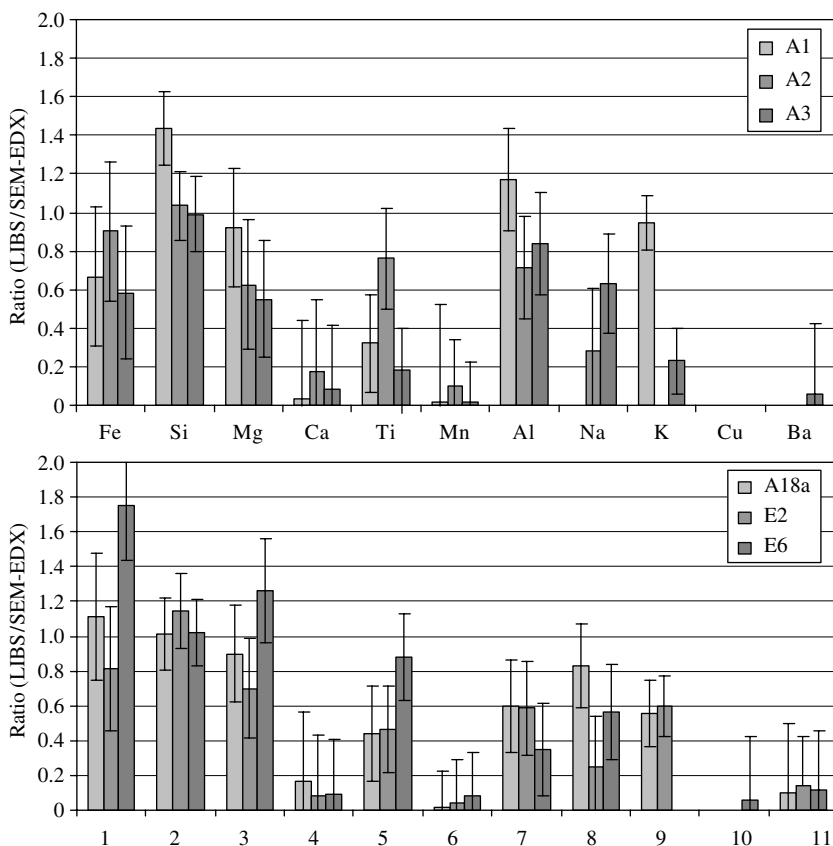


**Figure 6.21** Comparison of LIBS and SEM-EDX determinations of elements in mineral samples. (Data from Colao *et al.*, 2004). The labels A1, A2, etc. refer to different samples

and element concentrations. The achieved accuracy was related to the element type and its concentration in the samples as well as the number of samples used to develop the initial calibration data. Elements at high concentrations (Na and Al) were underpredicted and this was related to incomplete correction for self-absorption in the outer plasma layers. The high value obtained for zinc was attributed to some overlap of the Zn line with adjacent strong intensity emission lines.

In another test of LIBS analysis accuracy, or at least, correspondence with accepted analysis methods, on-line continuous monitoring was demonstrated for emissions from incinerators (Buckley *et al.*, 2000). The LIBS plasma was generated in the exhaust stream of the incinerators and metals were injected into the exhaust stream for analysis. Along with *in situ* LIBS sampling, exhaust samples were

**Table 6.7** Accuracy of LIBS measurements for Antarctic reference sediments (Lazic *et al.*, 2001)

Element	Certified concentration (ppm)	Accuracy error (%)	Element	Certified concentration (%)	Accuracy error (%)
Zn	53.3	+40	Na	1.97	-32
Ni	9.56	10	Mg	1.52	-14
Mn	446	-5	Fe	2.44	-17
Cr	42.1	2	Ca	1.58	6
Ba	464	1	Al	6.71	-35

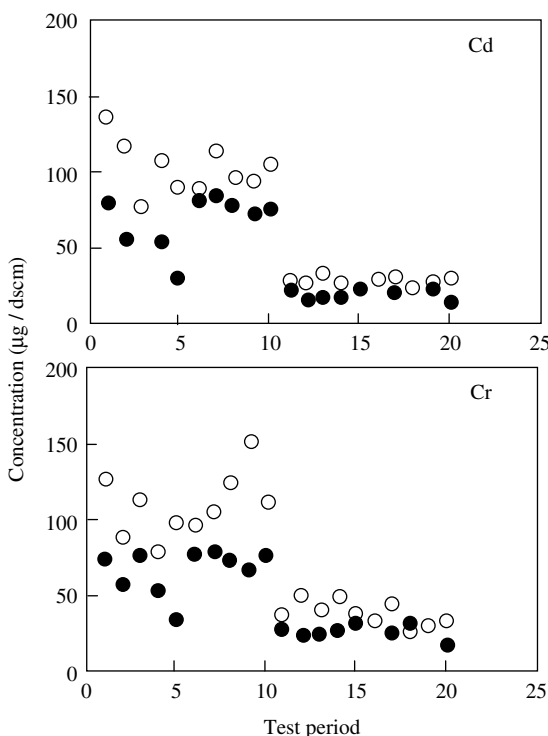


**Figure 6.22** LIBS analysis results compared with Method 29 for *in situ* monitoring of elements in an incinerator. LIBS (open circles) and Method 29 (closed circles) data. (Data from Buckley *et al.*, 2000). dscm, dry standard cubic meters

removed and element concentrations were determined using EPA Method 29 (EPA Multi-Metals Sampling Train). The results for cadmium and chromium are shown in Figure 6.22. Each test period corresponded to 1 h of system operation. Each measurement involved averaging spectra from 600 laser plasmas.

Depending on the test period, the results show moderate or high discrepancy between the LIBS measurements and those made using Method 29. On the other hand, in general, the trends in the airborne concentrations of these two elements and other elements monitored tracked reasonably well with the changes determined using Method 29. The overall results for all elements monitored indicate an average difference or accuracy error between the two methods of 63% with beryllium showing the greatest deviation. If the beryllium results were excluded, the overall difference was reduced to 37%.

## 6.9 CONCLUSIONS

LIBS can be used to provide quantitative analysis of a variety of samples in many settings, both in the laboratory and in the field. As shown here by example, however, each application has some unique characteristics which must be dealt with in order to optimize performance. As the practice of LIBS develops, procedures for obtaining quantitative results reproducibly will be developed, probably for the easiest cases first. These would likely be analysis of metals under reproducible conditions, in a quasi-laboratory environment. Quantitative measurements in the field will likely be the most difficult situation. Nevertheless the method has prospects for providing some information rapidly in field conditions, which cannot be said of most other analytical techniques.

## REFERENCES

- Buckley, S.G., H.A. Johnsen, K.R. Hencken and D.W. Hahn (2000). Implementation of laser-induced breakdown spectroscopy as a continuous emissions monitor for toxic metals. *Waste Manage.* 20: 455–462.
- Carranza, J.E. and D.W. Hahn (2002). Assessment of the upper particle size limit for quantitative analysis of aerosols using laser-induced breakdown spectroscopy. *Anal. Chem.* 74: 5450–5454.
- Colao, F, R. Fantoni, V. Lazic, A. Paolini, F. Fabbri, G.G. Ori, L. Marinangeli and A. Baliva (2004). Investigation of LIBS feasibility for in situ planetary exploration: an analysis on Martian rock analogues. *Planet. Space Sci.* 52: 117–123.
- Eppler, A.S., D.A. Cremers, D.D. Hickmott, M.J. Ferris and A.C. Koskelo (1996). Matrix effects in the detection of Pb and Ba in soils using laser-induced breakdown spectroscopy. *Appl. Spectrosc.* 50: 1175–1181.
- Knight, A.K., N.L. Scherbarth, D.A. Cremers and M.J. Ferris (2000). Characterization of laser-induced breakdown spectroscopy (LIBS) for application to space exploration. *Appl. Spectrosc.* 54: 331–340.
- Lazic, V., R. Barbini, F. Colao, R. Fantoni and A. Palucci (2001). Self-absorption model in quantitative laser induced breakdown spectroscopy measurements on soil and sediments. *Spectrochim. Acta Part B* 56: 807–820.

- Multari, R.A., L.E. Foster, D.A. Cremers and M.J. Ferris (1996). The effects of sampling geometry on elemental emissions in laser-induced breakdown spectroscopy. *Appl. Spectrosc.* 50: 1483–1499.
- Sallé, B., D.A. Cremers, S. Maurice and R.C. Wiens (2005). Laser-induced breakdown spectroscopy for space exploration applications: influence of the ambient pressure on the calibration curves prepared from soil and clay samples. *Spectrochim. Acta Part B* 60: 479–490.

---

# 7 Remote LIBS Measurements

---

## 7.1 INTRODUCTION

Remote measurements using LIBS are carried out in three ways. In the first method, the laser beam is directed over an open path (through air, gas or vacuum) to the target on which a plasma is formed and then the plasma light is collected at a distance. The distances achievable depend on the method of forming the plasma (conventional focusing using a lens or mirror system or femtosecond-induced ‘filamentation’) and on the method of collecting the plasma light. Even though a robust plasma may be formed, sufficient light must be collected to record a useful spectrum. This method puts severe requirements on laser, optics and detection system performance. In the second method, the laser pulses are injected into a fiber optic and transported to the remotely located target sample. The pulses exiting the fiber are focused to form a plasma on the adjacent sample and the plasma light is collected using the same fiber optic or a second fiber. The advantages of these two methods are that the LIBS instrumentation (laser, spectrograph and detector) can be located at a distance from the target. This opens up a range of new applications for the technique and for this reason remote LIBS analysis has been an area of intense activity in recent years. In the third method, less often used than the other methods, a compact probe containing a small laser is positioned next to the remotely located sample and the plasma light is sent back to the detection system over a fiber optic cable.

Advantages common to all remote LIBS methods are:

- Ability to analyze targets located in certain environments where access by personnel and/or nondisposable equipment is limited (e.g. areas of contamination by toxic, radioactive materials or a confined area).
- Application to process control where analysis must be done rapidly and from a distance (e.g. molten metals and glasses).

Open path LIBS has the added advantages of:

- analysis of physically inaccessible targets (e.g. geological features on cliff faces);
- interrogation of targets located in hazardous environments where any physical access is prohibited but optical access is possible (e.g. through a window on a glove box);

- rapid analysis of distinct, widely separated targets from a single vantage point;
- screening of large surfaces by scanning laser pulses along a surface;
- no possibility of damage to or contamination of equipment by locally harsh environments.

Fiber optic LIBS has the advantages of:

- reduced requirements on instrument performance in comparison with the laser (e.g. greater pulse energies) and optical system (high light collection efficiency) required for open path LIBS;
- direct line of sight to the target is not required;
- shielding of personnel from the open path laser beam;
- greater stand-off distances possible than with open path LIBS.

Compact probe fiber optic LIBS has the advantages of:

- high beam quality delivered to the adjacent target by laser pulses directed to the sample without the use of a fiber optic;
- higher pulse powers can be directed onto the target compared with fiber delivery;
- no damage to fiber optic by high power laser pulses;
- lower pulse energies can be used as the laser pulse is focused directly onto the adjacent target;
- shielding of personnel from open path laser beam;
- greater stand-off distances possible than with open path LIBS.

Open path, remote laser-based spectroscopic measurements have been carried out for many years under the umbrella name of LIDAR (light detection and ranging). These measurements include elastic scattering, absorption, fluorescence and Raman spectroscopy, which offer particle and molecular detection at distances exceeding a kilometer. LIBS has not been included in LIDAR because until recently, these measurements have been restricted to a maximum distance of only a few tens of meters. Recent developments, however, aim to extend the range to a kilometer or more in the near future. Because LIBS is an element detection method, it will provide a new capability to LIDAR methods, complementing the chemical molecular information available from current LIDAR methods.

Of all the remote LIBS techniques, open path LIBS is of particular interest because measurements can be carried out in a truly ‘stand-off’ mode without any intrusion into the sample region. The only requirement is line-of-sight optical access. In contrast, remote LIBS with a fiber optic and conventional methods of elemental analysis require that some physical device, be it a source and/or detector, be positioned adjacent to the sample or that the sample be retrieved and then transported to the analyzer. Such conventional analysis methods include electrode spark and arc spectroscopy which use metal electrodes, the inductively coupled plasma which sustains the continuous plasma using RF power directed into a coil, and x-ray fluorescence which requires that the source and detector be close to

the target. These requirements limit the use of these methods for some important applications and often increase analysis times. In contrast, the unique capability of open path LIBS, combined with the other LIBS advantages, opens up exciting new applications of the technology that cannot be addressed by any other elemental analysis methods.

Two different methods of open path LIBS measurements have been demonstrated which generate the analytical plasmas based on different physical processes. The first method demonstrated we call ‘conventional remote LIBS’ in which the laser pulse is focused onto the target by a lens or mirror-based optical system to produce power densities sufficiently high to induce ablation and form the microplasma. This method typically has used nanosecond laser pulses with the required energy dependent on the target distance and the characteristics of the optical system. Conventional open path LIBS has been demonstrated at a range of 80 m using nanosecond lasers typically used for *in-situ* LIBS. The second method employs nonlinear processes induced by the high power densities achievable using femtosecond laser pulses. The properties of these pulses can be tailored to form self-guided ‘filaments’ in a transparent medium (e.g. air) that will propagate over long distances and produce LIBS excitation of a sample. Currently, this method requires the use of large sophisticated laser systems but it has the potential to extend LIBS analysis capabilities to very long distances with kilometer ranges predicted.

Because LIBS uses powerful lasers to generate the laser plasma, extreme care must be taken in deploying LIBS systems for remote analysis. The laser pulse can represent an ocular and skin hazard to the public and the operator and can serve as an ignition source for explosive/flammable materials. Safety concerns are especially paramount for open path LIBS where it may be difficult to control access to the laser beam. The hazards will generally increase as the path length increases and procedures should be developed to ensure the safe use of all remote LIBS systems. These concerns may preclude the use of remote LIBS in some cases. Other safety issues associated with LIBS are discussed in Appendix A.

## 7.2 CONVENTIONAL OPEN PATH LIBS

### 7.2.1 APPARATUS

The vast majority of open path LIBS measurements have been conducted using the ‘conventional’ method of forming the plasma at a distance. A generalized apparatus is shown in Figure 7.1.

Two important requirements of remote conventional LIBS are (1) generating a robust plasma at distance and (2) collecting sufficient light for analysis. These requirements put constraints on the specifications of the laser, optical system, spectrograph and detector. As the distance increases, system requirements become more critical.

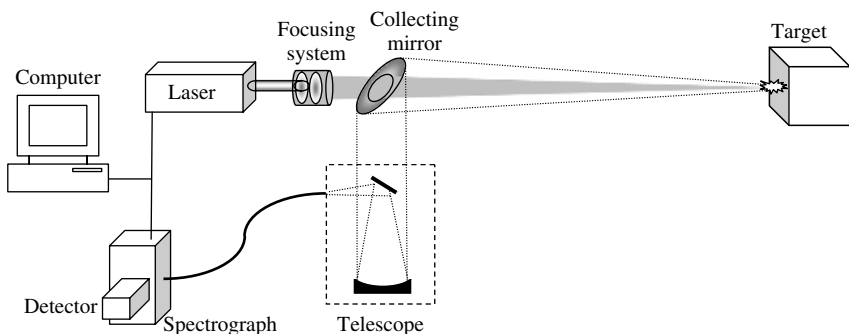


**Figure 7.1** Schematic of a LIBS system for conventional open path, remote LIBS

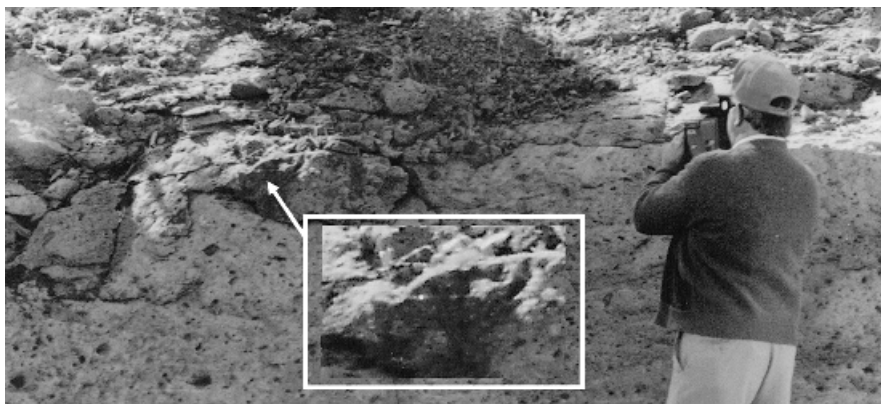


**Figure 7.2** Demonstration of stand-off LIBS using a laboratory instrument to interrogate a cliff bank. The spark is shown in the inset. The distance was 24 m between the spark and the optical system (focusing and light collection) (see Plate 12)

The visual appearance of the laser plasma formed on a cliff face is shown in Figure 7.2 (Plate 12). This plasma was formed at a distance of 24 m using a laboratory Nd:YAG laser (10 Hz, 300 mJ/pulse). At this distance, useful spectra were recorded using a 100 mm diameter collection lens with the light focused on a fiber optic connected to a 0.3 m spectrograph equipped with an ICCD (Blacic *et al.*, 1992).

## 7.2.2 FOCUSING THE LASER PULSE

Depending on the analysis distance, the laser pulses may be focused using a simple lens, a pair of lenses (to vary the position of the focal point), or a more elaborate optical system may be employed to first expand the diameter of the laser pulse and then focus the pulse at a distance onto the target. The use of high quality

anti-reflection coated optics is important to maximize the power density on the target. In situations where instrument mass is important (e.g. spacecraft), a mirror system, such as a Cassegrainian telescope, may be desirable as mirrors can generally be fabricated having less mass than an equivalent lens. Mirrors have the added advantage of being free of chromatic aberration. Typically, the focusing system would be adjustable so targets at various ranges can be interrogated from a fixed position.

To form a robust laser plasma, a minimum power density on the target is required. For a given laser pulse power, the power density generated on a remote sample will depend mainly on the minimum achievable spot size which is a function of distance. For a high quality (e.g. Gaussian) laser beam, the spot size is governed by spherical aberrations in the optical system and by the diffraction limit. The laser pulse power directed toward the sample can be reduced through absorption and scattering by the atmosphere and by aerosol particles and this possibility must be considered for each application.

To demonstrate some concerns that must be considered for a remote LIBS system, we first evaluate factors affecting the minimum spot size for a simple single lens system. As noted above, the main factors are spherical aberration and diffraction. For spherical aberration, the smallest spot size ( $d_{\text{aber}}$ ) at the focus is given by:

$$d_{\text{aber}} = f(d/f)^3[n^2 - (2n+1)k + (n+2)k^2/n]/32(n-1)^2 \quad (7.1)$$

where  $d$  is the input beam diameter,  $n$  is the refractive index of the lens material at the laser wavelength,  $f$  is the lens focal length and

$$k = R_2/(R_2 - R_1) \quad (7.2)$$

where  $R_1$  and  $R_2$  are the radii of curvature of the lens. Using the usual sign convention for lenses, for a plano-convex lens with light incident on the plane side  $k = 0$  and for light incident on the convex side  $k = 1$ .

On the other hand, the spot size determined by diffraction for a beam of wavelength  $\lambda$  is given by:

$$d_{\text{diff}} = 2.44\lambda f/d. \quad (7.3)$$

Insight as to which effect predominates for given  $f$  and  $d$  values can be obtained by setting  $d_{\text{aber}} = d_{\text{diff}}$  and solving for  $f$  as a function of  $d$ . An example is shown in Figure 7.3 for 1064 nm light.

For practical LIBS systems, the diameter of the laser beam, even after expansion by a simple Galilean telescope will typically be less than 4 cm whereas focal lengths of interest will be several meters or more. In this case, according to Figure 7.3, the minimum spot size attainable at the focus will be determined by the diffraction limit rather than spherical aberration which becomes important for shorter focal length lenses and smaller beam diameters. For  $d = 4\text{ cm}$ , spherical aberration determines the minimum achievable spot size for  $f < \sim 40\text{ cm}$  whereas

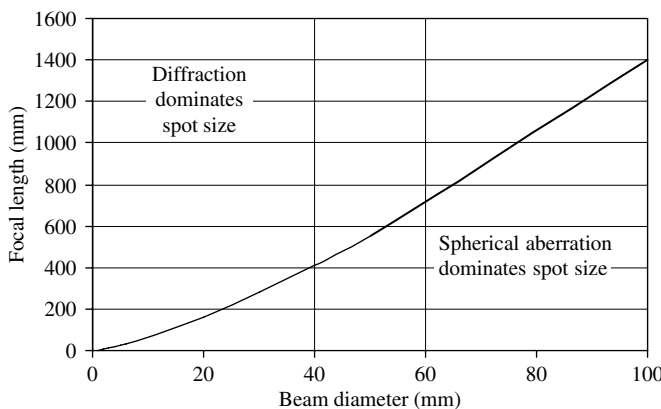


**Figure 7.3** Relationship between  $f$  and  $d$  for  $d_{\text{aber}} = d_{\text{diff}}$

diffraction is the determining factor at longer focal lengths. Therefore, if working in the diffraction limited focusing regime, expanding the beam diameter prior to focusing will produce smaller spot sizes and higher power densities on the distant sample.

Another important parameter is the Rayleigh range ( $z_R$ ) of the beam at focus which is given by (assuming a diffraction limited spot size,  $d_0 = d_{\text{diff}}$ ):

$$z_R = \pi d_0^2 / \lambda = \pi 5.95 \lambda (f/d)^2 \quad (7.4)$$

and is shown in Figure 7.4. The Rayleigh range is important because it is one computable measure of how accurately the focus must be adjusted to produce the greatest power density on the remote target. Note that  $z_R$  is defined as the distance from the beam waist ( $d_0$ ), or point of minimum beam diameter after focus, to the position at which the area of the beam has doubled. Symmetry of the Rayleigh range before and after the beam waist is assumed. According to Equation (7.4), the Rayleigh range varies as the square of the focal length and as the reciprocal of the square of the input beam diameter. As a sample calculation, for  $d = 4\text{ cm}$ ,  $f = 10\text{ m}$  and a 1064 nm Nd:YAG beam,  $z_R = 124\text{ cm}$ .

For conventional remote LIBS, the spot size on the sample must be minimized to generate the strongest plasma. Operationally this condition may be achieved by

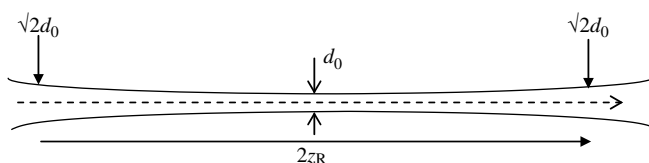


**Figure 7.4** Rayleigh range for a focused Gaussian beam in relation to the minimum spot size  $d_0$

repetitively firing the laser and adjusting the focal position until the ‘best’ plasma is formed on the sample. The ‘best’ plasma can be indicated by the intensity of white light from the plasma, or by the sound produced by the laser pulse induced shock wave, or by monitoring the intensity of element emissions. At best focus, these should all be maximized. In an automated system, target distance can be determined using a rangefinder based on a number of methods including time-of-flight, phase shift, triangulation and interferometry. The first two listed are appropriate for LIBS instruments and some characteristics are summarized in Table 7.1.

The precision to which the focus must be determined to form a useful plasma depends on distance. The greater the distance, the longer the Rayleigh range and hence precise focusing becomes less crucial.

The Rayleigh range is a parameter useful to estimate an operating range for an optical system in which the diffraction limited spot size must remain below a certain value assuming a certain laser beam quality. The useful operating range for a LIBS system can be determined operationally and provides actual performance capabilities. An example of data recorded during such an evaluation is shown in Figure 7.5. To obtain these data, a  $\times 20$  beam expander was used to expand and then focus at a distance Nd:YAG pulses of about 3 mm starting diameter. The pulse energy was 100 mJ. For each selected distance, the LIBS signal from Al metal was maximized by adjusting the beam expander focus to produce the maximum LIBS signal from Al(I) at 394.4 nm. Then the metal sample was moved both toward and away from the beam expander and the position in each direction at which the signal decreased to 10% of its maximum value was noted. For the particular system used here, the value of 10% was selected because the Al(I) signal at this intensity was still regarded as sufficiently strong to be useful for quantitative measurements. The total distance between the two end 10% end points is plotted in Figure 7.5 as a function of target distance. For comparison, the Rayleigh range for  $d = 20 \times 3 \text{ mm} = 60 \text{ mm}$ ,  $f = 10 \text{ m}$ , and the Nd:YAG fundamental wavelength is 55 cm for this system. This compares well ( $z_R = 2 \times 55 \text{ cm} = 110 \text{ cm}$ ) with the usable range of about 1 m displayed in Figure 7.5.

**Table 7.1** Methods of measuring target distances for LIBS

Method	Operation	Range	Accuracy	Laser
Time-of-flight	Round trip travel time of a short duration laser pulse directed at the target is measured	10 m–tens of km	<1 mm	Pulsed laser diode
Phase shift	Shift in phase between a reference pulse and the pulse reflected off the distant target is measured	0.2–200 m	<1.5 mm	Pulsed laser diode (beam divergence = $0.16 \times 0.6 \text{ mrad}$ ; 15 ns pulse; 0.95 mW)

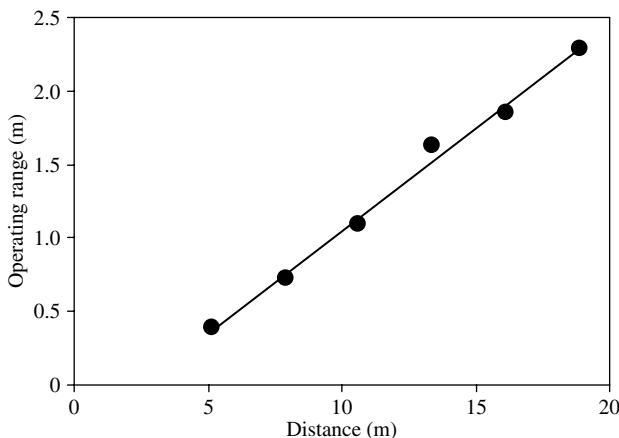


**Figure 7.5** Useful operating range of a LIBS system over a range of stand-off analysis distances

### 7.2.3 COLLECTING THE PLASMA LIGHT

Remote LIBS systems have been developed in which the plasma light is collected collinear with or off-axis to the path of the laser pulses directed to the target. Collection along the same axis as the laser pulses eliminates parallax as the distance to the target ( $r$ ) changes. In the collinear arrangement, the plasma light is diverted from the path of the laser pulses using, for example, a beam splitter or mirror with a central clear aperture. In one configuration the beam splitter will have a coating that passes the laser wavelength but reflects the plasma light over a wide spectral range. Such coatings are not ideal for wide spectral band detection as there will be some spectral regions that are not efficiently reflected from the beam splitter due to the coating. Using a mirror with a central open aperture as shown in Figure 7.1 avoids this problem but some fraction of the returning plasma light is lost. Of course, here again it is a trade off. For long distances, the outgoing laser beam will be expanded requiring a large central aperture resulting in greater loss of returning light. In either case, the diverted and collected light is then directed into the detection system.

The plasma light can also be collected using the arrangement shown in Figure 7.6. A lens is shown here as focusing the laser pulses onto a fiber optic and the laser pulses are directed onto the target by a 100% reflecting mirror, the converse arrangement of Figure 7.1. A mirror could be used to collect and focus the returning plasma light onto the fiber optic in place of the lens. If using a lens, an important consideration is chromatic aberration. This effect is a result of the refractive index of the lens material being wavelength dependent so that different wavelengths will be focused at different points along the optical axis (Figure 3.7d). Unless achromatic lenses, lenses in which the effect has been corrected, are used, lens focusing will require that the fiber optic be moved relative to the collecting lens to optimize the recorded intensity for different spectral regions. Chromatic aberration becomes an

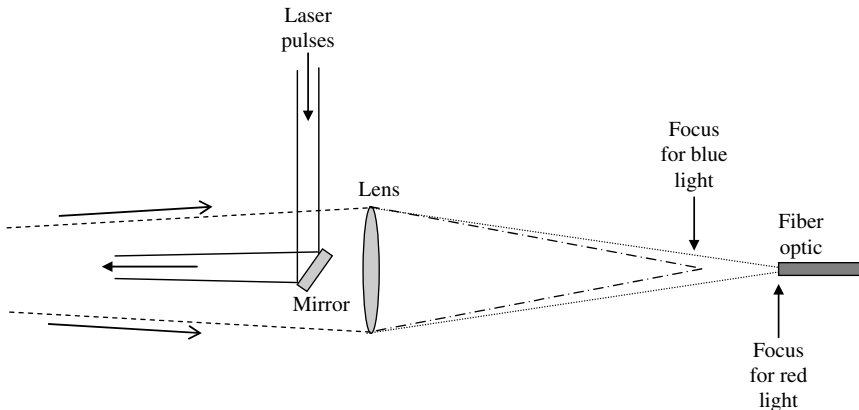


**Figure 7.6** One method of collecting plasma light using a single lens. Unless the lens is achromatic, the optimum focal position on the fiber will be wavelength dependent

important consideration, especially when using an echelle spectrograph (Section 3.4) where the spectrum collected on a single shot can encompass a large spectral range (e.g. 200–800 nm). The apparatus shown in Figure 7.1 and the arrangement of Figure 7.6 with the lens replaced by a mirror will be free of this effect.

Of course, with either mirror or lens focusing, some adjustment of the light collection system, just as in the case of focusing the laser pulse, will be required to inject maximum collected light into a fiber as the distance from the target to the optical system ( $r$ ) changes. Note that in all the light collection configurations discussed here, the collected light will vary as  $1/r^2$ .

#### 7.2.4 RESULTS USING CONVENTIONAL LIBS

Remote LIBS based on conventional focusing has been used mainly for the analysis of solid targets with ranges up to 80 m reported. Liquid samples have been interrogated at distances of a few meters. Because of the high power densities required to induce air breakdown, the analysis of gases at long distances has not been reported using conventional focusing methods and practical size lasers.

One of the first reports of remote LIBS analysis was described in 1985 by Zuev *et al.* (Zuev *et al.*, 1985). A ‘spectrochemical LIDAR’ instrument was developed based on a Cassegrainian telescope, spectrograph, and photographic or photomultiplier detection of the collected light. A CO<sub>2</sub> laser (300 µs pulse width and 500 J) was used to generate the laser plasma. Although the focused power densities at distance were not sufficient to produce an air plasma, plasmas were formed on aerosol particles within the telescope focal region at ranges of 50 to 150 m. The elements Ca, Al and Na from the particles were detected along with oxygen and nitrogen emissions from air.

Another early report of stand-off analysis of solids was published in 1987 (Cremers, 1987). One goal of this work was to demonstrate the rapid sorting of metals according to the main metal constituent rather than long range measurements so distances were less than 3 m. Laser pulses were focused on metal samples using a single lens and the light was collected by a bare fiber optic bundle pointed at the plasma. No attempts were made to optimize the experimental set-up to extend the range, but using this simple arrangement, useful signals were obtained as far as 2.4 m using a single focusing lens and no spatial expansion of the laser pulse. This work showed 100% success at the rapid identification of metals according to their main element component (Cu, Zn, Al, Ni, Sn, Mo, Ti or Fe). The use of repetitive ablation to clean a surface was described and the method was evaluated for the analysis of steel at 0.55 m.

In 1991, LIBS was demonstrated for the remote analysis of geological samples outdoors in air at a distance of 24 m using a laboratory laser and detection system (Blacic *et al.*, 1992). The equipment was positioned on a cart and moved outside the laboratory to interrogate a cliff bank (Figure 7.2). A simple three-lens system was used to focus the pulses so the focal distance could be adjusted to achieve different stand-off distances. Spectra were readily collected in bright sunlight allowing an evaluation of the target material composition. The goal of this preliminary work was to promote LIBS as an instrument for future planetary missions. Subsequent investigations on the development of LIBS for space exploration are discussed in Chapter 8.

Although stand-off analysis is usually performed using solid samples, one study has described the analysis of liquids at distances of 3–5 m using both off-axis and on-axis methods of plasma light collection (Samek *et al.*, 2000). Plasma light was collected on-axis using a novel method of separating the laser beam from the plasma light based on frustrated total internal reflection. Different methods of sampling liquid samples were investigated with the majority of measurements employing a laminar flow water jet. In one experiment, however, a radioactive solution of Tc in a Petri dish was analyzed at a distance of 3 m. A low pulse repetition rate of 1 Hz was used to minimize splashing of the solution. Based on the concentration of Tc in the sample and the signal strength it was estimated that Tc levels down to 25 mg/l should be observable.

A custom, mobile LIBS system was developed for stand-off analysis (1 m) of major elements in a mineral melt (1600°C) in an industrial environment (Panne *et al.*, 2002). The plasma light was collected at an angle to the path of the laser pulses instead of collinearly. A variation in the LIBS signal of Si was observed due to changes in position of the mobile instrument in relation to the melt. This was believed to be due to collection of the light at an angle which resulted in monitoring different regions of the expanding plasma. Variations in signals could probably be minimized through a collinear geometry (Figure 7.1). Operational parameters such as pulse irradiance and gate delay and width of ICCD detection were optimized in terms of the signal to noise ratio. This permitted all major elements in the melt (Ti, Fe, Mn, Mg, Ca, Si, Na, Al) to be identified within the brief interrogation time of 1 s corresponding to ten laser pulses. To evaluate process monitoring, LIBS

measurements were made from a melt at analysis intervals separated by 60 s along with manual retrieval of a sample from the melt for subsequent analysis by x-ray fluorescence. Runs extending over 80 and 130 min were carried out and compared. Good correlation was observed between the LIBS and x-ray fluorescence data (elements Si, Fe, Al, Ca, Mn, Mg) with a slight shift in the pattern (element signal versus time) attributed to a small mismatch between the sampling times.

Analysis of stainless steel at a distance of 40 m was demonstrated using an open-path LIBS system (Palanco *et al.*, 2002). Light was collected off-axis to the path of the laser pulses. The long Rayleigh length of the beam at 40 m was found useful to minimize the effect of surface irregularities on the analysis with an RSD of 14% determined for the absolute signal precision as the sample position varied  $\pm 1$  m from the position of optimum laser focus. The ratio Cr/Fe was found to be highly uniform over the range  $\pm 5$  m from the laser focus. In addition, spectra from six stainless steels samples were collected and emissions from Ni, Mo and Ti compared. Using these data in a three-dimensional pattern recognition algorithm showed that the six steels could be accurately classified using only three elements.

Based on a collinear optical design in which the plasma light was collected along the same path as the laser pulses, Palanco and Laserna (Palanco and Laserna, 2004) developed and described an open-path LIBS analysis system. Performance of the system was evaluated and the feasibility of extending the analysis range of such a LIBS system based on conventional focusing was discussed.

Using a Nd:YAG laser, spectrograph, and ICCD, samples including plant material, soil, rock and cement collected from an industrial environment were analyzed at 12 m distance in the laboratory (Lopez-Moreno *et al.*, 2004). The experimental arrangement was similar to that of Figure 7.1. Depth resolved measurements and the effect of surface condition on the analysis were evaluated. Factors affecting analysis results such as moisture content, surface uniformity and sample orientation were evaluated. Detection limits for Cr and Fe were determined to be about 0.2 wt% from calibration curves prepared using a set of slag standards. These curves were then used to determine the Cr levels in some of the collected environmental samples. The change in Cr signals (concentration) with shot number on the different samples was used to draw conclusions regarding aspects of environmental pollution. Using the large depth of focus of the optical system at 12 m, three-dimensional maps of Cr, Fe, Ca and Mg distributions in a rock sample were made over the volume 20 mm  $\times$  18 mm  $\times$  0.54 mm depth.

Using the same apparatus, except that the collected plasma light was directed into a fiber optic and a HeNe laser, collinear with the Nd:YAG pulses, was used to aim the system, the same group monitored the corrosion of stainless steels in a high temperature environment (Garcia *et al.*, 2004). The experiments were conducted in the laboratory at a distance of 10 m with the steel samples maintained in an oven. The oxidation of the surface was monitored and qualitative differences observed between the intensity of element emissions from the corroded, scaled steel surface and a clean steel surface. Specifically, after only 10 min exposure at 1200°C, the scaled layer was found to be Fe-rich with reduced levels of Cr, Ni and Mo compared

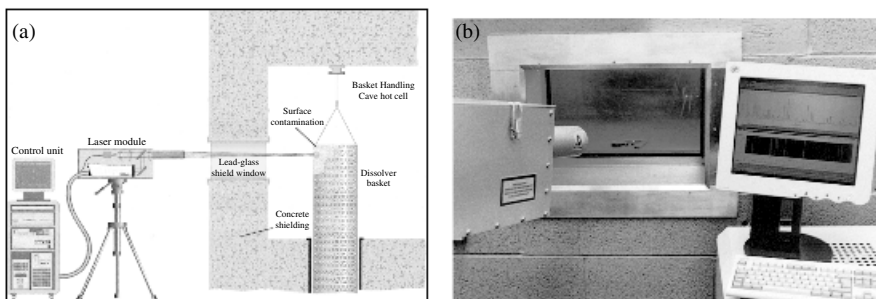


**Figure 7.7** (a) Schematic showing the deployment of the remote LIBS instrument to monitor surface contamination. (b) Laser beam of the instrument being directed through the lead glass shield window (Applied Photonics, 2004a. Courtesy of Applied Photonics, Ltd) (see Plate 13)

with the starting material. Depth profiling of the corroded layer showed depletion of Cr at the surface with the Cr signals increasing as a result of repetitive ablation that interrogated the underlying bulk material.

An open-path transportable LIBS apparatus was used to analyze molten steel on a factory floor (Palanco *et al.*, 2004). The sample was heated in a crucible in a small scale induction furnace of 1 kg capacity. The distance between the instrument and the crucible was about 7.5 m with two mirrors in between to direct and focus the laser pulses vertically downward onto the molten sample surface. Measurements showed the ability to monitor in real-time changes in the composition of the melt (e.g. Ni added). Calibration curves for Ni and Cr were prepared by adding these elements to stainless steel. From the curves, detection limits of 1190 and 540 ppm were determined for Ni and Cr, respectively.

Stand-off LIBS was used at a distance of about 5 m to determine the composition of contaminants deposited on dissolver baskets at a spent nuclear fuel reprocessing plant (Applied Photonics, 2004a). Radiometric analysis of the contaminants had identified the radionuclide components but another method was needed to identify the nonradioactive materials. An analyzer system was deployed including the laser and optics to form the laser plasma remotely on the basket through a thick lead-glass window and collect the plasma light [Figure 7.7 (Plate 13)]. The material was analyzed *in situ* and determined to be zirconium molybdate which was an insoluble material formed during the reprocessing procedure.

### 7.3 STAND-OFF LIBS USING FEMTOSECOND PULSES

#### 7.3.1 CONVENTIONAL REMOTE LIBS USING FEMTOSECOND LASER PULSES

LIBS measurements are typically carried out using nanosecond laser pulses. These pulses are 5–10 ns in duration, contain energies ranging from a few millijoules

up to 500 mJ, with the fundamental wavelength of 1064 nm preferred for most applications. The pulse powers are in the range of 0.3 to 50 MW with corresponding focused power densities of 3.8 to 6.4 GW/cm<sup>2</sup> (for a 0.1 mm diameter spot size). Nanosecond lasers are preferred for LIBS because they are technologically well-developed, rugged and reliable, and very compact systems are available for incorporation into instruments. Picosecond and femtosecond lasers, however, generating pulses of durations on the order  $10^{-12}$  and  $10^{-14}$  s, respectively, have been investigated for LIBS applications and some advantages have been found. Unfocused powers from these lasers range from hundreds of megawatts to tens of terawatts.

Because of the broad spectral content of femtosecond pulses, an important concept in discussions of femtosecond lasers is chirp. A chirped pulse is one in which the different wavelengths or colors are not distributed uniformly over the envelope of the pulse. Chirp may be viewed as an increase or decrease in the frequency of a light pulse with time as monitored from a stationary position as the pulse passes by the observer. Chirp can be used to tailor certain pulse properties to maximize excitation characteristics when used for LIBS.

A pulse can be positively or negatively chirped. Positive chirp occurs when the leading edge of the pulse is red-shifted in relation to the central wavelength and the trailing edge is blue-shifted. Negative chirp is the opposite situation. Because the refractive index of a material depends on wavelength, different wavelengths pass through a medium at different velocities. In this way, by passing a chirped pulse through a sequence of prisms, the chirp can be adjusted to be either positive or negative. The refractive index of glass and most materials (e.g. air) increases as the wavelength decreases so that longer wavelengths travel with greater velocities. Therefore, a positively chirped pulse will become more positively chirped and show an increase in pulse width as it passes through air. For instance, a 70 fs pulse of 16 nm spectral content will be chirped into a 1 ps pulse after traversing 1 km of air and the peak pulse power is reduced by a factor of 10 (Wille *et al.*, 2002). On the other hand, a negatively chirped pulse transmitted through the atmosphere will exhibit reduced chirp and a shorter pulse width (Figure 7.8). By controlling the chirp in an output pulse, the pulse width, the pulse power, and hence the position of plasma formation from the laser can be controlled.

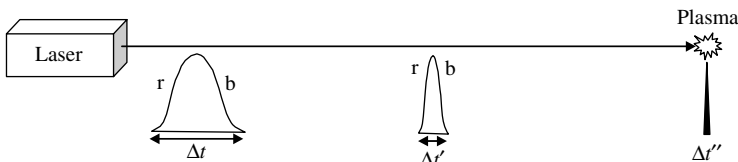


**Figure 7.8** A negatively chirped pulse [blue (b) precedes red (r)] is temporally compressed by traveling through an atmosphere ( $\Delta t > \Delta t' > \Delta t''$ ). When the pulse has been sufficiently compressed, producing a high power density, a plasma is formed at a certain distance

Remote LIBS analysis of targets has been carried out using femtosecond pulses focused onto a target as in conventional LIBS (Figure 7.1). Femtosecond pulses (795 nm, 10 Hz, up to 350 mJ, 75 fs) were directed from the laboratory onto the solid target at 25 m using a simple mirror telescope to expand ( $\times 3$ ) and then focus the pulses (Rohwetter *et al.*, 2004). The femtosecond laser could also be adapted to produce picosecond and nanosecond pulses for comparison of results. A second telescope (10 cm primary mirror diameter) was used to collect the plasma light at a position adjacent to but not collinear with the path of the incident laser pulses. Some main results of this study were: (1) femtosecond and picosecond pulses can be used for remote analysis with a detection limit of 100 ng computed for Cu at 25 m using femtosecond pulses; (2) femtosecond pulses produced a cleaner LIBS spectrum than either the picosecond or nanosecond pulses, with the femtosecond spectrum free of emissions from elements in the ambient gas; (3) emissions from the femtosecond- and picosecond-produced plasmas decayed at about the same rate as those from a ns-pulse produced plasma (microsecond timescale); (4) adjusting the femtosecond-pulse chirp to produce the minimum duration laser pulse at the target (i.e. maximum power density) does not produce the strongest emission signal. The optimum signals were obtained by adjusting the chirp for each type of target material.

### 7.3.2 REMOTE ANALYSIS BY FEMTOSECOND PULSE PRODUCED FILAMENTATION

As noted above, using nanosecond pulses of reasonable energy (i.e. <500 mJ), ranges of tens of meters are possible with LIBS. For this reason, LIBS has not been included in the arsenal of spectroscopic methods employed for long range LIDAR measurements ( $\sim$ km). Because of the high optical powers generated by femtosecond pulse lasers, on the other hand, a variant of LIBS is possible based on atmospheric filamentation produced by these pulses (Kasparian *et al.*, 2003). Filamentation occurs when a sufficiently powerful femtosecond pulse propagates through air or other medium transparent at the laser wavelength. The process is based on the Kerr effect in which the refractive index of a medium is changed by an applied electric field. The induced change ( $\Delta n$ ) is given by:

$$\Delta n = n_2 I \quad (7.5)$$

where  $n_2$  is the nonlinear index of refraction particular to the medium and  $I$  is the optical intensity. When a Gaussian-shaped light pulse passes through the transparent medium the change in refractive index will be greater at the spatial center of the pulse and less at the edges, following the intensity distribution across the pulse profile. For air  $n_2 = 3 \times 10^{-19} \text{ cm}^2/\text{W}$  and the induced changes will form a positive lens acting to focus the light pulse. This focusing results in ionization of the transparent medium and formation of a plasma that acts to defocus the beam. When the pulse power exceeds a certain critical power, a dynamic equilibrium exists

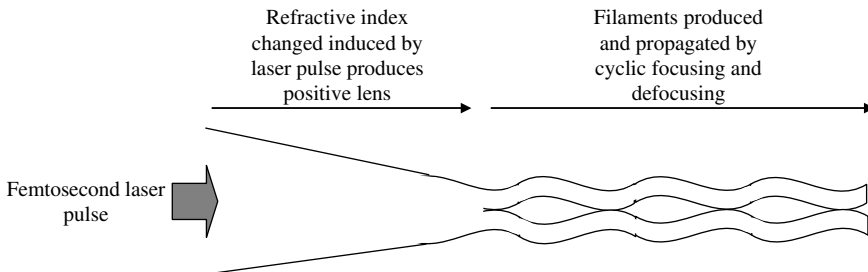


**Figure 7.9** Filaments over long path lengths are generated by the dynamic equilibrium between focusing (Kerr effect) and defocusing (plasma formation) which occurs along the path of the laser pulses

between the two processes resulting in self-trapping of the propagating laser beam near the optical axis of the beam. For air, the critical power is several gigawatts. This trapping is shown in Figure 7.9. The self-trapping generates filaments of ‘white light’ or a spectral continuum over distances much longer than is achievable using a conventionally focused beam. Images of filaments produced in air are shown in Figure 7.10 (Plate 14). About 10–20% of the laser pulse energy is directed into the filaments.

Filament lengths of 200 m are typical with filaments up to 2 km long being observed. Filament diameters have been measured to be about 0.1 mm. The intensity inside the filaments is on the order of  $4 \times 10^{13} \text{ W/cm}^2$  (Kasparian *et al.*, 2000). At powers 10–100 times above the critical value, multiple filaments are formed that propagate along the beam direction. Frequencies other than the laser frequency are generated as a result of self-phase modulation within the filament producing a ‘white light.’ A significant portion of this continuum is radiated in the forward and backward direction of pulse propagation aiding remote detection of the spectroscopic signal from the filaments.

### 7.3.3 TERAMOBILE

Currently compact and field-deployable nanosecond laser systems are available for stand-off LIBS using conventional focusing. On the other hand, femtosecond laser systems generating powers on the order of  $10^{14} \text{ W}$  that are needed for filamentation studies are currently laboratory instruments because of their complexity, size and requirement for a controlled operating environment. These laboratory devices will become more readily adapted for field use as the technology improves. These efforts will be driven by the unique capabilities that femtosecond lasers promise in several areas related to LIBS and other applications. For the past several years, field applications of femtosecond pulse technology have been demonstrated and evaluated by the Teramobile, a joint collaboration between French and German organizations (Wille *et al.*, 2002). The Teramobile is a laboratory contained inside

Publisher's Note:  
Permission to reproduce this image  
online was not granted by the  
copyright holder. Readers are kindly  
requested to refer to the printed version  
of this chapter.

**Figure 7.10** CCD camera images of filaments produced by a femtosecond laser beam propagating vertically through the atmosphere. The femtosecond pulses were produced by the Teramobile. (A) Fundamental wavelength, exhibiting signals from more than 20 km and multiple-scattering halos on haze layers at 4- and 9-km altitudes. (B–D) White light (385 to 485 nm) emitted by the femtosecond laser beam. These images have the same altitude range, and their common color scale is normalized to allow direct comparison with that of (A). (Reprinted with permission from Kasparian *et al.*, Copyright 2003 AAAS) (see Plate 14)

a standard freight container that can be transported to different field sites. The laboratory includes a transportable femtosecond laser system producing terawatt laser pulses and associated detection and analysis instrumentation for evaluating the operation of the system for different applications.

#### 7.3.4 REMOTE LIBS USING FEMTOSECOND PULSES

Using self-guided filaments produced by femtosecond laser pulses, remote filament-induced breakdown spectroscopy (R-LIBS) has recently been demonstrated (Stelmaszczyk *et al.*, 2004). The output pulses (80 fs, 250 mJ, 10 Hz) of the Teramobile were collimated to 3 cm diameter and directed at metal targets (Cu and steel) located 20–90 m distant. The pulses leaving the laser system were negatively chirped (corresponding pulse width of 800 fs) to begin filament production in front of the target at 7–8 m. In this way, filaments were produced on the target surface and one pattern is shown in Figure 7.11. The backward emitted light

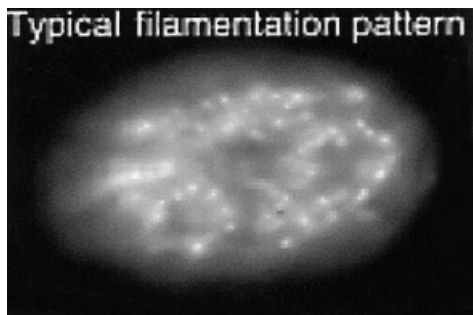


**Figure 7.11** Filaments produced on a metal target at >20 m. (Reprinted with permission from Stelmaszczyk *et al.*, 2004. Copyright 2004, American Institute of Physics)

from the filaments was collected by a telescope (20 cm) and recorded by a spectrograph and ICCD. The LIBS spectrum was examined in the 500–550 nm region and emissions from Cu(I) and Fe(I) were recorded at 90 m. Over the 20–90 m range investigated, the LIBS signal from the target surface was independent of distance, indicating that target excitation by the filaments did not change with distance. Considerations of signal-to-noise changes with distance showed that with this nonoptimized system, a distance of 150 m could be realized for LIBS detection (signal to noise ratio  $\sim 1$ ). Expected improvements in the detection system efficiency on the order of 100 should permit measurements at  $\sim 1$  km range, comparable with the distance observed for filament propagation (Rodriguez *et al.*, 2004).

In a subsequent study by the same group, the range of R-FIBS was extended to an Al target located 180 m from the laser (Rohwetter *et al.*, 2005). Comparisons were made between the R-FIBS spectra and the spectra from conventional LIBS produced by picosecond and nanosecond lasers. The main result was that the R-FIBS spectra were free of emission lines due to oxygen and nitrogen similar to the spectra obtained using femtosecond pulses for conventional LIBS (Rohwetter *et al.*, 2004). Based on the results of this work, the feasibility of kilometer range R-FIBS was considered and experimental requirements estimated.

## 7.4 FIBER OPTIC LIBS

### 7.4.1 FIBER OPTICS FOR LIGHT COLLECTION

The use of fiber optics has greatly benefited applications of LIBS in two ways: by providing new methods of collecting the plasma light and by delivering the laser energy to the target. In this section we discuss benefits related to collection of the plasma light. Using a fiber, the plasma light does not need to be directly focused onto the entrance slit of a spectrograph or passed directly through a filter, etc.,

using a relay optical system. This lends great versatility to instrument design and permits the detection system to be remotely located away from the target as shown in Figure 3.36. Fiber lengths of many tens of meters have been reported in the literature. In addition, with lens focusing onto a slit, typically only a portion of the plasma volume is monitored (Figure 7.12). Because of the highly inhomogeneous distribution of material in the plasma and the strong spatial gradients in excitation parameters in the small plasma, minute changes in the position of the plasma on the slit can significantly change the appearance of the recorded spectrum in terms of emission line intensities as well as relative intensities. For *in-situ* measurements, this sensitivity to alignment is reduced by collecting the plasma light with a bare fiber optic pointed at the sample. Because of the wide acceptance angle of the fiber optic (26° and 58°, respectively, for a fused silica and glass fiber) small changes in the plasma position will not significantly affect the collected plasma light (Figure 7.12). In addition, using a fiber in this way provides collection of light from all parts of the plasma, that is, the plasma light is spatially averaged. Data showing the dependence of the Fe signal on plasma position are shown in Figure 7.13 for each arrangement. In the first case, the plasma light is imaged on a spectrometer slit (100 μm wide) by a 50 mm focal length lens (1:1 magnification). Movements of the lens by 0.5 mm reduce the signal to half the maximum value. Movements become more sensitive as the lens focal length increases. Using a fiber optic to collect the plasma light decreases the sensitivity to plasma position. As shown in Figure 7.13, a change in the plasma position on the target in the vertical direction of 3.5 cm produces a 25% change in the observed signal. The fiber to plasma distance was 55 cm.

The amount of light collected by a fiber decreases with distance ( $r$ ) as  $1/r^2$ , the same as for lens imaging. Because the end of the fiber is typically small, say 0.6–1 mm diameter, the collection angle from a point source like the laser plasma is also very small with the equivalent f# of the system being about 116 (for 55 cm distance). The amount of light into the fiber can be increased using a lens to focus the plasma light onto the end of the fiber. The cone of light focused onto the fiber

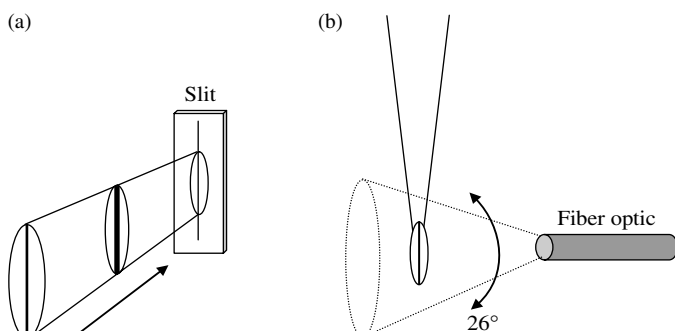


**Figure 7.12** (a) Focusing the plasma light onto a spectrograph slit. Because of the narrow slit (e.g. 100 μm), the signal is sensitive to image position. (b) Collecting light with a fiber optic reduces sensitivity because of the 26° acceptance angle for light

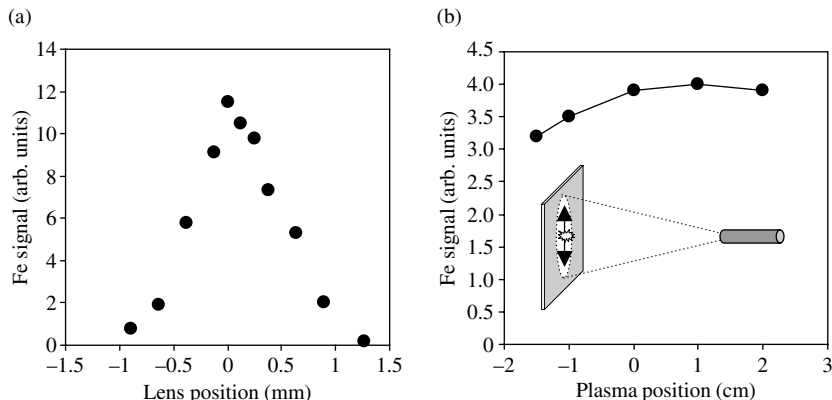


**Figure 7.13** Variation of recorded signal as a function of (a) lens imaging plasma on a slit and (b) position of the plasma on the target in the vertical direction with plasma light collected by a fiber optic. The distance between the fiber and sample was 55 cm for (b)

by the lens should be within the acceptance angle of the fiber so that the majority of light incident on the fiber will be transmitted (matching the numerical apertures, Section 3.3.3). Light outside the acceptance cone will not be transmitted. Of course in using lens light collection with a fiber, the sensitivity to plasma position increases as for direct imaging on a slit with a lens. The advantages of remote detection capability as regards light collection are still preserved, however.

#### 7.4.2 FIBERS FOR LASER PULSE DELIVERY

A second benefit of fiber optics is the ability to transmit sufficiently high pulse irradiance through a fiber so an analytically useful plasma can be formed at the distal end of the fiber. In this way, the laser system as well as the detection system can be located remotely from the target as shown in Figure 3.36. It is even possible to collect the plasma light using the same fiber optic that transmits the laser pulse. A probe incorporating these capabilities is shown in Figures 3.15 and 7.14. Typically, low OH fused silica step indexed fiber optics are used to transmit the laser pulse. The fibers used to transport the laser pulse have diameters in the range of 0.4–1 mm. Smaller diameters cannot handle the pulse energies required to form the laser plasma and larger diameters, although available, are not flexible enough for some applications. The laser pulse can be injected into the fiber using the arrangement shown in Figure 7.15. The fiber is positioned behind the focus of a long focal length lens (>200 mm) with the distance between the lens and fiber input face adjusted so that the diverging beam fills about 75% of the fiber end. A lens with a short focal length will generate an air spark at the focus and will introduce rays into the fiber at an angle that exceeds the acceptance angle, resulting in high transmission losses.



**Figure 7.14** Generation of a laser plasma on soil using a small probe with a single fiber that delivers the laser pulse and collects the plasma light

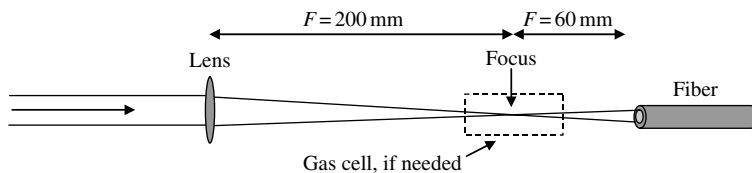


**Figure 7.15** Method of injecting laser pulses into a fiber to remotely form the laser plasma

The air spark can be eliminated by placing an evacuated or gas-filled cell at the focus (Davies *et al.*, 1995). The divergence of the laser beam into the fiber can also be controlled using a simple Galilean telescope which eliminates the sharp focus that may produce a laser spark in air. This arrangement is shown in Figure 7.16. In this case, the evacuated cell is not needed.

Generally, the fiber can accommodate the pulse powers used for LIBS, but coupling the energy into the fiber without damaging the fiber input face is the major problem. To achieve maximum power transmission, the end face of the fiber must be optically smooth and perpendicular to the beam. Proper focusing of the beam is critical to prevent intense laser light leaking into the cladding that may damage the polymer cladding or buffer coating. The epoxy used for bonding the fiber to the connector can be affected as well. For this reason, a silica/silica fiber

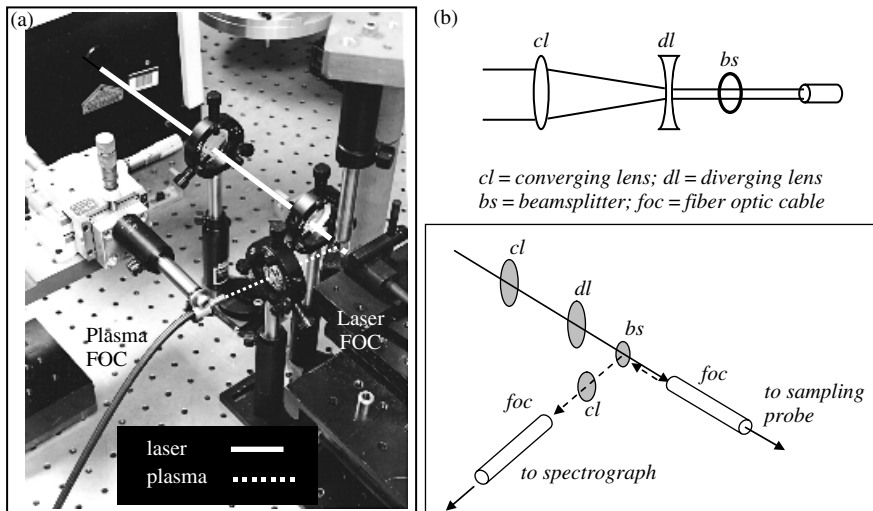


**Figure 7.16** (a) Photo and (b) diagram showing one method of using the same fiber to transport the laser pulse and collect the plasma light. A Galilean telescope is used to inject the pulses into the fiber optic

is often used in a specially designed mounting or connector to better tolerate the high power densities and rapid heating levels. It is also recommended that the beam not completely fill the core diameter. Some factors affecting fiber damage by laser pulses are listed in Table 7.2.

The coupling efficiency of the laser energy into a fiber may be increased through the use of a fiber optic with an integral taper at the end. With the larger area of the taper input end, the pulse power incident on the fiber can be reduced to minimize damage and for beams that are multimode and not easily focused, more energy can be injected into the larger taper end. It should be realized that in using a tapered fiber, the numerical aperture (NA) of the light into the taper must satisfy certain conditions to achieve maximum coupling down the fiber. The important relationship is:

$$\text{NA}_{\text{in}} = \text{NA}_{\text{out}} (d_{\text{out}}/d_{\text{in}}). \quad (7.6)$$

Here  $\text{NA}_{\text{in}}$  and  $\text{NA}_{\text{out}}$  refer, respectively, to the numerical aperture of the taper input and of the base (nontapered) main fiber over which the laser pulse will be transmitted. The input and output diameters of the taper are  $d_{\text{in}}$  and  $d_{\text{out}}$ , respectively. For a fused silica base fiber,  $\text{NA}_{\text{out}} = 0.22$  and for a taper of  $d_{\text{in}}/d_{\text{out}} = 3/1$ , the result is  $\text{NA}_{\text{in}} = 0.073$ . A value greater than this will result in losses of the input beam energy through the core/cladding interface due to a reflection angle inside the core exceeding the angle for total internal reflection. Tapers as large as 5/1 can be accommodated in fiber manufacture with the taper occurring over 10–15 mm of the fiber end.

A system of using the same fiber for transporting the laser beam and collecting the plasma light is shown in Figure 7.16. Here a Galilean telescope (single converging

**Table 7.2** Factors influencing fiber damage for laser pulse transport

Fiber input face condition	<ul style="list-style-type: none"> <li>• quality of end polishing</li> <li>• cleanliness</li> <li>• cleaving</li> </ul>
Fiber material	<ul style="list-style-type: none"> <li>• purity/quality of silica</li> <li>• optical attenuation of laser wavelength</li> </ul>
Laser parameters	<ul style="list-style-type: none"> <li>• wavelength</li> <li>• pulse power, pulse width, pulse energy</li> </ul>
Launch conditions	<ul style="list-style-type: none"> <li>• power density on fiber input face</li> <li>• spot size on face</li> <li>• spatial distribution of light at input face</li> <li>• alignment on input face</li> <li>• numerical aperture of input optics</li> </ul>

and diverging lenses) was used to generate a slightly diverging beam going into the fiber optic. The return light from the plasma was collected using a beamsplitter consisting of a small quartz plate (~8% reflection collection efficiency).

#### 7.4.3 APPLICATIONS OF FIBER OPTICS

An early investigation of the use of fiber optics to deliver a laser pulse of sufficient power density to perform a LIBS measurement was reported for underwater analysis (Nyga and Neu, 1993). Separate XeCl lasers (308 nm) were employed, each laser being fiber optic (600 µm core diameter) coupled to deliver pulses to the surface of a calcite sample located under water. The first pulse formed a bubble on the sample and the second laser pulse interrogated the calcite surface inside the bubble simulating in this way interrogation of the calcite in air. The plasma light was collected by the fiber delivering the second laser pulse. A portion of this light was split off and the LIBS spectrum recorded using a spectrograph and ICCD.

The first extensive investigation of the use of optical fibers to deliver the laser pulse to the sample over a long distance was described by Davies *et al.* (1995). A separate fiber was used to collect the plasma light. As the application was intended for eventual use in a nuclear reactor with doses of gamma radiation, attenuation of wavelengths ranging from 296 to 1064 nm was investigated for certain radiation exposure times. A core diameter of 550 µm was chosen for use with laser pulses of 50 mJ energy to accommodate the high power densities without damaging the fiber. Concentrations of some elements of interest were observed as low as 200 ppm and calibration curves were prepared for several elements using certified ferrous metal standards. Use of the system for distances up to 100 m was demonstrated.

In the same year Cremers *et al.* described the use of the same fiber optic to deliver laser pulses to a sample for LIBS and to collect the plasma light (Cremers *et al.*, 1995). Detection limits for Ba and Cr in soil were presented along with calibration curves. Detection limits obtained using the fiber were comparable with

those determined for the same elements using direct focusing (nonfiber optic coupled) LIBS.

There have been several other published works dealing with fiber optic coupled LIBS. A representative list is presented in Table 7.3. Some of these involved fiber optic delivery of the laser pulse energy and fiber collection of the plasma light at the source. Others have used a small laser in a probe positioned adjacent to the target with the plasma light collected by a fiber and transported back to the remotely located detection system.

**Table 7.3** Literature relating to fiber optic coupled LIBS

Application	Comments (ref.)
Cone penetrometer system	Describes the construction and use of a truck mounted system for subsurface analysis of contaminated sites (Saggesen and Greenwell, 1996)
Fiber optic system for detecting lead in paint	Some analytical results are presented for the detection of Pb in paint using the fiber optic system (Marquardt <i>et al.</i> , 1996)
Transportable LIBS analyzer for soil contamination	Soil sample analyzer either by insertion into device or through fiber optic coupling of laser pulses to soil. Instrument shown in Figure 7.17 (Cremers <i>et al.</i> , 1996)
Cone penetrometer system	Subsurface sampling head designed in which plasma is formed at the interface between a quartz window and soil. Single fiber used for laser and plasma light (Theriault <i>et al.</i> , 1998)
Fiber optic probe that combines LIBS, Raman and imaging	LIBS measurements demonstrated using granite rock. Raman spectra obtained of single TiO <sub>2</sub> and Sr(NO <sub>3</sub> ) <sub>2</sub> particles and Raman images of the same particles were recorded (Marquardt <i>et al.</i> , 1998)
Aspects of injecting high power laser pulses into a fiber	Useful technical information for those interested in getting started with fiber delivery of pulses for LIBS (Neuhäuser <i>et al.</i> , 2000)
Fiber optic probe described and used to analyze Al alloy samples	Detection limits for elements in Al alloys obtained with the fiber optic probe were compared with those obtained by direct focusing of the laser pulses (Rai <i>et al.</i> , 2001)
Fiber optic probe developed for the <i>in situ</i> determination of the elemental composition of a molten alloy	Experimental parameters of the system (e.g. laser pulse energy, gate delay, etc.) were evaluated for different solid alloys. Following this, the system performance was tested using molten alloys in a laboratory size furnace (Rai <i>et al.</i> , 2002)
Determine the Cu content of stainless steel steam generator tubes in the reactor of a nuclear power station	A fiber optic coupled LIBS system (75 m umbilical length), shown in Figure 7.18, was used with separate fibers for laser pulse delivery and plasma light collection (Whitehouse <i>et al.</i> , 2001; Applied Photonics, 2004b)
Nuclear reactor control rods were screened to determine those containing low Si concentrations subject to corrosion and failure	Control rods were interrogated using a fiber optic coupled probe positioned in a hot-cell through a 10 m umbilical cable. The control rod target was first cleaned using several hundred shots. This was followed by the LIBS analysis using 100 shots (Applied Photonics, 2004c). The LIBS system was similar to that of Figure 7.18



**Figure 7.17** Transportable LIBS system soil analysis. (a) Fiber optic delivery of pulses to soil mound. (b) Insertion of soil samples into instrument for analysis (see Table 7.3)

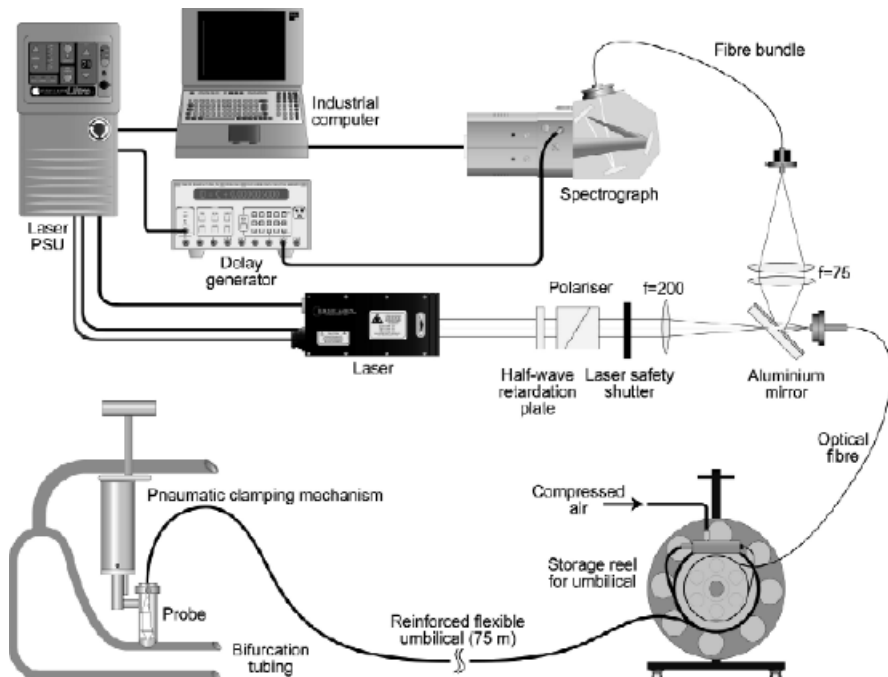


**Figure 7.18** Fiber optic coupled LIBS system used for analysis of nuclear reactor components. (Courtesy of Applied Photonics, Ltd, see Table 7.3)

## REFERENCES

- Applied Photonics (2004a). Remote characterization of high-level radioactive waste at the THORP nuclear reprocessing plant: laser-induced breakdown spectroscopy (LIBS): application note 002. Applied Photonics Limited, North Yorkshire, UK ([www.appliedphotonics.co.uk](http://www.appliedphotonics.co.uk))
- Applied Photonics (2004b). In-situ compositional analysis of economizer tubes within the sub-boiler annulus of an AGR pressure vessel: application note 005. Applied Photonics Limited, North Yorkshire, UK ([www.appliedphotonics.co.uk](http://www.appliedphotonics.co.uk))
- Applied Photonics (2004c). In-situ batch identification of Magnox reactor control rods: application note 006. Applied Photonics Limited, North Yorkshire, UK ([www.appliedphotonics.co.uk](http://www.appliedphotonics.co.uk))
- Blacic, J.D., D.R. Pettit and D.A. Cremers (1992). Laser-induced breakdown spectroscopy for remote elemental analysis of planetary surfaces. Proceedings of the International Symposium on Spectral Sensing Research, Maui, HI.
- Cremers, D.A. (1987). The analysis of metals at a distance using laser-induced breakdown spectroscopy. *Appl. Spectrosc.* 41: 572–579.
- Cremers, D.A., J.E. Barefield and A.C. Koskelo (1995). Remote elemental analysis by laser-induced breakdown spectroscopy using a fiber optic cable. *Appl. Spectrosc.* 49: 857–860.
- Cremers, D.A., M.J. Ferris and M. Davies (1996). Transportable laser-induced breakdown spectroscopy (LIBS) instrument for field-based soil analysis. *SPIE 2835*: 190–200.
- Davies, C.M., H.H. Telle, D.J. Montgomery and R.E. Corbett (1995). Quantitative analysis using remote laser-induced breakdown spectroscopy (LIBS). *Spectrochim. Acta Part B* 50: 1059–1075.
- Garcia, P.L., J.M. Vadillo and J.J. Laserna (2004). Real-time monitoring of high temperature corrosion in stainless steels by open-path laser-induced plasma spectrometry. *Appl. Spectrosc.* 58: 1347–1352.
- Kasparian, K., R. Sauerbrey and S.L. Chin (2000). The critical laser intensity of self-guided light filaments in air. *Appl. Phys. B* 71: 877–879.
- Kasparian, J., M. Rodriguez, G. Méjean, J. Yu, E. Salmon, H. Wille, R. Bourayou, S. Frey, Y.-B. André, A. Mysyrowicz, R. Sauerbrey, J.-P. Wolf and L. Wöste (2003). White light filaments for atmospheric analysis. *Science* 301: 61–64.
- Lopez-Moreno, C., S. Palanco and J.J. Laserna (2004). Remote laser-induced plasma spectrometry for elemental analysis of samples of environmental interest. *J. Anal. At. Spectrom.* 19: 1479–1484.
- Marquardt, B.J., S.R. Goode and S.M. Angel (1996). In situ determination of lead in paint by laser-induced breakdown spectroscopy using a fiber-optic probe. *Anal. Chem.* 68: 977–981.
- Marquardt, B.J., D.N. Stratis, D.A. Cremers and S.M. Angel (1998). Novel probe for laser-induced breakdown spectroscopy and Raman measurements using an imaging optical fiber. *Appl. Spectrosc.* 52: 1148–1153.
- Neuhäuser, R.E., U. Panne and R. Niessner (2000). Utilization of fiber optics for remote sensing by laser-induced plasma spectroscopy (LIPS). *Appl. Spectrosc.* 54: 923–927.
- Nyga, R. and W. Neu (1993). Double-pulse technique for optical emission spectroscopy of ablation plasmas of samples in liquids. *Opt. Lett.* 18: 747–749.
- Palanco, S., J.M. Baena and J.J. Laserna (2002). Open-path laser-induced plasma spectrometry for remote analytical measurements on solid surfaces. *Spectrochim. Acta Part B* 57: 591–599.
- Palanco, S. and J. Laserna (2004). Remote sensing instrument for solid samples based on open-path atomic emission spectrometry. *Rev. Sci. Instrum.* 75: 2068–2074.
- Palanco, S., S. Conesa and J.J. Laserna (2004). Analytical control of liquid steel in an induction melting furnace using a remote laser induced plasma spectrometer. *J. Anal. At. Spectrom.* 19: 462–467.

- Panne, U., R.E. Neuhauser, C. Haisch, H. Fink and R. Niessner (2002). Remote analysis of a mineral melt by laser-induced plasma spectroscopy. *Appl. Spectrosc.* 56: 375–380.
- Rai, A.K., H. Zhang, F.Y. Yueh, J.P. Singh and A. Weisburg (2001). Parametric study of a fiber-optic laser-induced breakdown spectroscopy probe for analysis of aluminum alloys. *Spectrochim. Acta Part B* 56: 2371–2383.
- Rai, A.K., F.Y. Fang and J.P. Singh (2002). High temperature fiber optic laser-induced breakdown spectroscopy sensor for analysis of molten alloy constituents. *Rev. Sci. Instrum.* 73: 3589–3599.
- Rodriguez, M., R. Bourayou, G. Méjean, J. Kasparian, J. Yu, E. Salmon, A. Scholz, B. Stecklum, J. Eisloffel, U. Laux, A.P. Hatzes, R. Sauerbrey, L. Wöste and J.-P. Wolf (2004). Kilometer-range non-linear propagation of fs laser pulses. *Phys. Rev. E* 69: 036607-1–036607-7.
- Rohwetter, Ph., J. Yu, G. Méjean, K. Stelmaszczyk, E. Salmon, J. Kasparian, J.-P. Wolf and L. Wöste (2004). Remote LIBS with ultrashort pulses: characteristics in the picosecond and femtosecond regime. *J. Anal. At. Spectrom.* 19: 437–444.
- Rohwetter, Ph., K. Stelmaszczyk, L. Wöste, R. Ackermann, G. Méjean, E. Salmon, J. Kasparian, J. Yu and J.-P. Wolf (2005). Filament-induced remote surface ablation for long range laser-induced breakdown spectroscopy operation. *Spectrochim. Acta Part B* 60: 1025–1033.
- Saggese, S. and R. Greenwell (1996). LIBS fiber optic sensor for subsurface heavy metals detection. *Proc. SPIE* 2836: 195–205.
- Samek, O., D.C.S. Beddows, J. Kaiser, S.V. Kukhlevsky, M. Liska, H.H. Telle and J. Young (2000). Application of laser-induced breakdown spectroscopy to in situ analysis of liquid samples. *Opt. Eng.* 39: 2248–2262.
- Stelmaszczyk, K., Ph. Rohwetter, G. Méjean, J. Yu, E. Salmon, J. Kasparian, R. Ackermann, J.-P. Wolf and L. Wöste (2004). Long-distance remote laser-induced breakdown spectroscopy using filamentation in air. *Appl. Phys. Lett.* 85: 3977–3979.
- Theriault, G.A., S. Bodensteiner and S.H. Lieberman (1998). A real-time fiber-optic LIBS probe for the in situ delineation of metals in soils. *Field Anal. Chem. Technol.* 2: 117–125.
- Whitehouse, A.I., J. Young, I.M. Botheroyd, S. Lawson, C.P. Evans and J. Wright (2001). Remote material analysis of nuclear power station steam generator tubes by laser-induced breakdown spectroscopy. *Spectrochim. Acta Part B* 56: 821–830.
- Wille, H., M. Rodriguez, J. Kasparian, D. Mondelain, J. Yu, A. Mysyrowicz, R. Sauerbrey, J.P. Wolf and L. Wöste (2002). Teramobile: a mobile femtosecond–terawatt laser and detection system. *Eur. Phys. J. AP* 20: 183–190.
- Zuev, V.E., A.A. Zemlyanov, Y.D. Kopytin and A.V. Kuzikovskii (1985). *High Power Laser Radiation in Atmospheric Aerosols*, D. Reidel, Boston.

---

# 8 Examples of Recent LIBS Fundamental Research, Instruments and Novel Applications

---

## 8.1 INTRODUCTION

We began this book by a thorough review of experiments and results on LIBS from the years 1960 through 2002. After that we reviewed the fundamentals of the physics of the plasma, the apparatus, and the analytical considerations. Throughout the book, some examples of complete LIBS systems have been discussed. In this chapter we look at the recent history from 2003 onward with a view towards emphasizing the latest trends in LIBS research and applications, in general focusing on what a new practitioner needs to know to perform state-of-the-art LIBS experiments.

Although the thrust of much recent LIBS work has been on applications, a review of recent activity shows that much is also being done on the fundamental physics of plasma formation and expansion, as well as modeling of the ablation process. Because the understanding of the plasma and ablation influences the choice of apparatus and its settings, we deemed this an important area to review.

## 8.2 FUNDAMENTALS

Energy absorption in and propagation through a plasma is an older area of investigation that has been revisited. Bindhu *et al.* (2004) described the energy absorption and propagation of laser created sparks in air and in argon using as a diagnostic a high-speed 2 ns resolution camera to photograph the plasmas. All plasmas were generated with the 532 nm second harmonic of Nd:YAG, with an 8 ns pulse width. One of the results was a new measurement of the breakdown threshold in atmospheric air yielding  $2.5 \times 10^{12} \text{ W/cm}^2$ . The temperatures and electron densities were determined through standard techniques, the latter using the widths of N(II) and Ar(II) lines. The authors estimated the free-electron bremsstrahlung

absorption depth (in/cm) using an expression given originally by Zel'dovich and Raizer (Zel'dovich and Raizer, 2002):

$$\alpha_b = 1.37 \times 10^{-35} \lambda^3 n_e^2 T_e^{-1/2} \quad (8.1)$$

with the wavelength in micrometers and electron density per cm<sup>3</sup>. Using this expression, they calculated the absorption depth in argon and in air at a variety of energies and axial spark distances. The absorption depths ranged from 0.02 (air, 200 mJ) to 0.14/cm (Ar, 200 mJ). Their conclusions supported many previous observations, for example that the plasma appears to shift towards the laser. Figure 8.1 shows the estimated speed of plasma propagation towards the laser beam for air and argon sparks, as a function of laser energy. The speeds vary from about 1 to  $3 \times 10^7$  cm/s. They also plotted the amount of laser energy lost in the forward direction of the beam, due to absorption and scattering, as a function of laser energy. Above 50 mJ per pulse, more than 80% of the laser energy is lost to the forward direction.

The LIBS plasma has inhomogeneities that can lead to spatial differentiation. This fact could be important in choosing the temporal window in which to accumulate spectroscopic data. The following papers highlight different aspects related to inhomogeneities.

Corsi *et al.* (Corsi *et al.*, 2003) monitored the spatial and temporal evolution of a plasma from a steel target using time of flight and shadowgraph techniques.

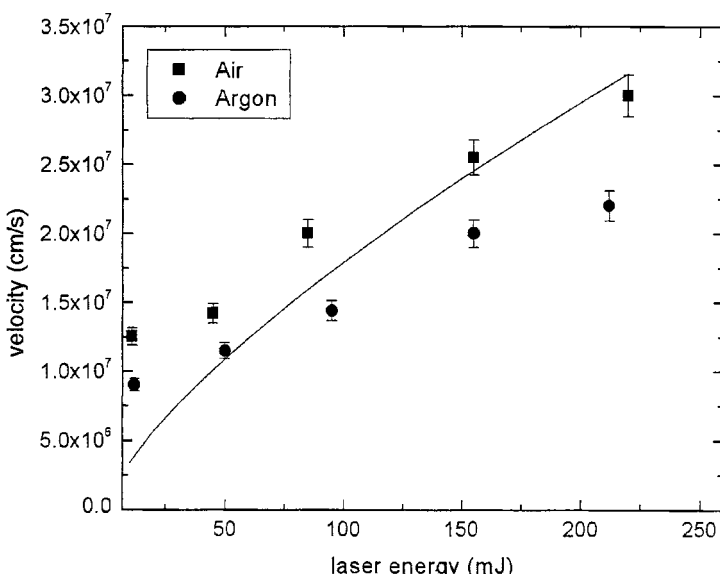


**Figure 8.1** The estimated propagation velocity of the spark towards the laser beam as a function of laser energy, for sparks in argon and in air. (Reproduced from Bindhu *et al.*, 2004, with permission from Society for Applied Spectroscopy)

The laser was a Nd:YAG with a maximum energy of 600 mJ at 1064 nm, and a 7 ns pulse width. They found two regions in the plume, one characterized by air and continuum emissions produced by shock wave ionization, and the other by emissions from ablated material. At 250  $\mu\text{m}$  from the target they calculated speeds of expansion of  $1.2 \times 10^6 \text{ cm/s}$  and  $1.2 \times 10^5 \text{ cm/s}$  for the continuum and neutral chromium fronts. More separation is seen at lower laser irradiances as shown in Figure 8.2. At  $2 \times 10^9 \text{ W/cm}^2$  the nitrogen emission intensity peaks considerably earlier than the iron or chromium lines monitored. At  $2 \times 10^{11} \text{ W/cm}^2$ , all species lie on the same rise-time curve although their decays differ. They concluded that one needed a sufficiently high laser fluence and acquisition delay time to assure the homogeneity needed for analytical applications.

The homogeneity of laser plasmas was investigated using the curve of growth method, using five Fe(I) lines (Aguilera *et al.*, 2003). The laser was a Nd:YAG at 1064 nm with a 4.5 ns pulse length. Two time windows were observed, 4–5 and 15–18  $\mu\text{s}$ . The curve of growth technique was used to determine plasma parameters. In that formalism, the line shapes as a function of temperature and concentration were modeled, and their widths compared with observed line widths. During the early temporal interval, large gradients between inner and outer plasma areas in temperature and iron atom densities were observed. By the later window, with the plasma expanded and somewhat cooled, a single region model explains the uniform temperature and ion atom density. In the 4–5  $\mu\text{s}$  window, the inner region was 1 mm long, had an iron atom density of  $4 \times 10^{16}/\text{cm}^3$  and a temperature of 9400 K. The longer outer region was 4 mm in length, and exhibited an iron atom density of  $2 \times 10^{14}/\text{cm}^3$  and a temperature of 7800 K. At 15–18  $\mu\text{s}$ , a single and more uniform regime was observed, with a length of 4 mm, density of  $6 \times 10^{14}/\text{cm}^3$ , and a temperature of 6700 K. The agreement between modeled and experimental line shapes implied that the Stark effect was the dominant broadening mechanism in the plasma.

Aguilera and Aragón focused on temperatures obtained from neutral and ion spectral lines, and on the errors that can result from the inhomogeneous nature of the plasma (Aguilera and Aragón, 2004). They studied the different temperatures that can be obtained from Boltzmann and Saha plots. Experimentally they generated a LIBS plasma using a Nd:YAG laser with 100 mJ per pulse, and investigated the results in a temporal window of 3–3.5  $\mu\text{s}$ . Abel inversions coupled with curves of growth were used to obtain a three-dimensional picture of the plasma. When spatially integrated, the Saha and Boltzmann approaches gave different temperatures, 9100 K versus 13 700 K. However, when spatially resolved, data from the same volume gave the same temperature, 13 160 K. The difference was explained by the spatial variation of the plasma temperature and densities leading to a difference in spatial locus for populations in the upper levels of transitions for neutrals and ions.

Plasma models are becoming more comprehensive and detailed. The paper by Gornushkin *et al.* reported on experiments performed to validate a radiative model of a LIBS plasma expanding into a vacuum (Gornushkin *et al.*, 2005). They specifically addressed the inverse problem, which means finding initial conditions by comparing

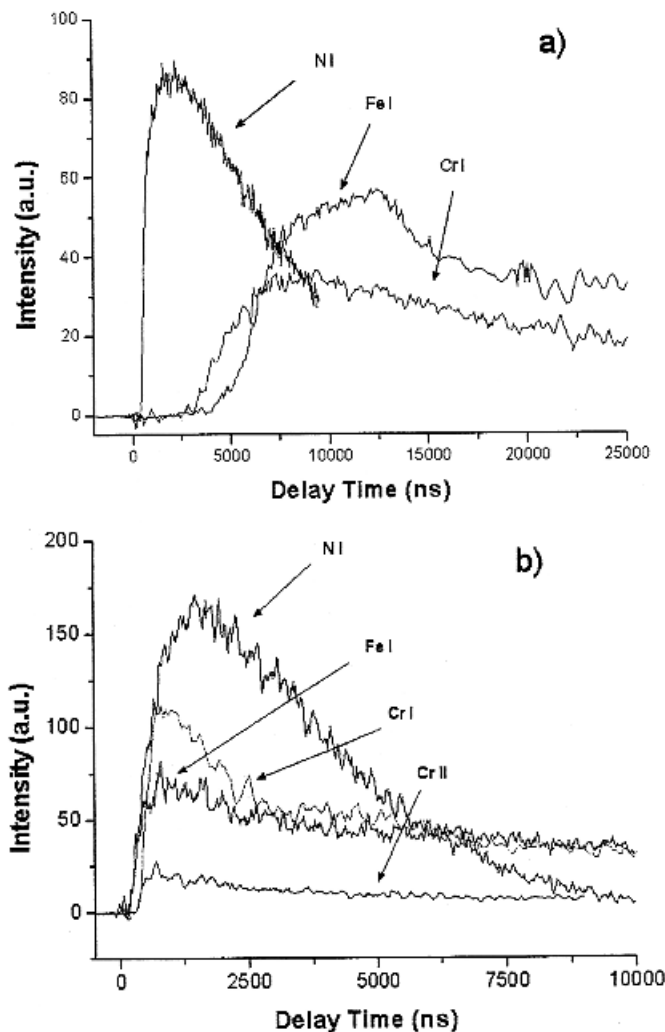


**Figure 8.2** Intensity of emission lines as a function of time, at a distance of 1.5 mm from the target. The irradiance values were (a)  $\sim 1.5 \times 10^9 \text{ W/cm}^2$  and (b)  $\sim 2 \times 10^{11} \text{ W/cm}^2$ . At the higher irradiance the rise times for all lines are very similar. (Reproduced from Corsi *et al.*, 2003, with permission from Society for Applied Spectroscopy)

calculated synthetic spectra with experimentally measured ones. Effectively they deduced the composition of the material from the calculated spectra. The plasma was considered to be characterized by a single temperature and electron density. Two separate problems were considered, first reproduction of the spectra from a single element like aluminum, and then multicomponent samples. From two to six elements and up to 500 spectral lines were involved in these calculations.

The experimental part used a Nd:YAG laser at 1064 nm producing a 0.2 mm spot at 16 GW/cm<sup>2</sup>. They calculated the Boltzmann temperature with Fe(II) lines, as a function of position and time, centered around 60 ns into the plasma. The calculated value, averaged over all space and time points around that window, was 17 200 K, compared with the measured value of 16 500 K. The next step in their work will be to include expansion into an atmosphere through shock waves and introducing a second temperature and other factors that could be responsible for deviation from equilibrium.

Bogaerts *et al.* (2003) combined a review with original modeling work on laser evaporated plasma plume expansion into a vacuum, and ablation as it leads to vaporization and particle formation. They modeled the interaction of a nanosecond pulse with a copper target in vacuum. Some of the parameters studied were melting and evaporation of the target, the plume expansion and plasma formation, the ionization degree and density profiles of neutral, once-ionized and doubly ionized copper and electrons, and the resultant plasma shielding. Calculations were performed for a 266 nm wavelength with a 10 ns Gaussian pulse width. The peak irradiance chosen was 10<sup>9</sup> W/cm<sup>2</sup> which, when integrated over the pulse, corresponded to a fluence of 10.6 J/cm<sup>2</sup>.

We highlight a few of the many interesting results of this work. The first is the surface temperature as a function of time at the conditions specified above. In the model, the temperature rises to 6000 K during the laser pulse and then decays over the next 100 ns to about 2000 K. The surface recession rate peaks at the peak of the laser pulse, then decreases and slows considerably when the surface temperature drops below the boiling temperature. They also calculated the variation of these quantities as a function of irradiance between 1 × 10<sup>7</sup> and 1 × 10<sup>10</sup> W/cm<sup>2</sup>. Plasma formation takes place at 5 × 10<sup>8</sup> W/cm<sup>2</sup>. The surface temperature is about 2000 K at 1 × 10<sup>8</sup> W/cm<sup>2</sup>, and begins to level off at about 7000 K shortly after plasma formation. The surface recession rate has a similar dependence on irradiance, although the melt depth continues to increase through 1 × 10<sup>10</sup> W/cm<sup>2</sup> where it is 200 nm. At higher irradiance values, the leveling off of surface temperature and recession is due to the onset of plasma shielding and the direction of energy into increasing the plasma ionization. The authors make many comparisons with experimental work that confirm their general direction. The next step in this evolving work is to model the expansion into one atmosphere of a cover gas, such as air or argon.

### 8.3 CALIBRATION-FREE LIBS (CF-LIBS)

The technique of calibration-free LIBS (CF-LIBS) (Ciucci *et al.*, 1999) is gaining acceptance in certain experimental situations. Starting from the relative intensities of spectral lines, one constructs a family of Boltzmann plots corresponding to all constituents in the plasma. The concentration of the constituents can then be calculated from the intercepts of the lines on the y-axis. One then forces the

concentrations of the observed constituents to add up to 100% of the material in the plasma. In CF-LIBS, the plasma is assumed to be in local thermodynamic equilibrium (LTE) and optically thin. It is often not optically thin for strong lines, however. Then spectral-line self-absorption becomes a major issue for the technique. Many lines ending on the ground states of elements, often suspect for self-absorption or self-reversal, have been excluded from the analyses to avoid prejudicing the results. Research recently focused on correction for self-absorption.

The basis of the correction scheme proposed in Bulajic *et al.* (Bulajic *et al.*, 2002) is to construct curves of growth for spectral lines of interest. Figure 8.3 shows calculated profiles for Cu(I) 324.7 nm as a function of species density. In this simulation, the line starts to become flat-topped at an electron density of  $5 \times 10^{15}/\text{cm}^3$ . Further increases in electron density over  $10^{17}/\text{cm}^3$  would have shown self reversal at the line center.

The recursive algorithm developed proceeds to calculate species densities from input parameters, estimates self-absorption, recalculates species densities, and so on. The intricacies of Gaussian, Doppler and Voigt profiles are considered. According to the authors, convergence takes place in 10–15 cycles. They compared LIBS results with and without corrections applied to values from standard NIST steel and precious alloy samples. For the NIST 1172 sample, the improvement they achieved is shown in their experimental values reproduced in Table 8.1. The span of concentrations over which this method works is impressive.

An additional difficulty in CF-LIBS arises in accounting for the contributions of all species. Many of the elements detected by LIBS will have neutral and

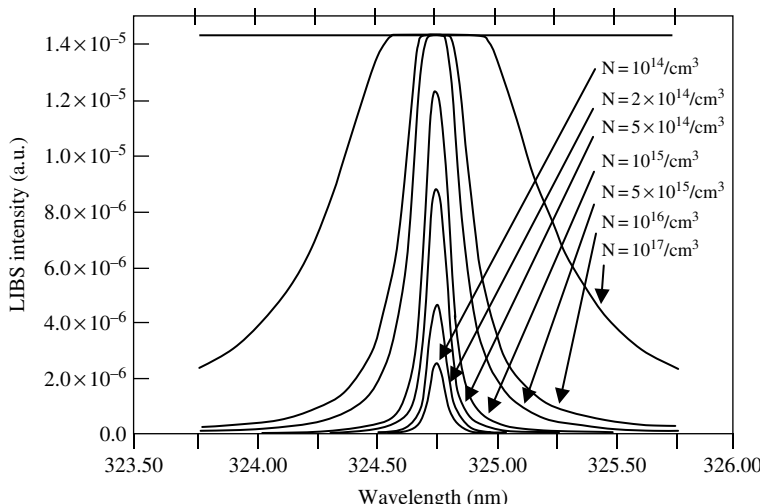


**Figure 8.3** Modeled intensity profile of the Cu(I) line at 324.7 nm as a function of species density. (Reproduced from Bulajic *et al.*, 2002, with permission from Elsevier)

**Table 8.1** Improvement in analytical performance when a self-absorption correction is added to CF-LIBS. Concentrations are in w%. The standard is a NIST 1172 certified value

Element	CF-LIBS	Corrected for self-absorption	Certified value
Mn	$2.0 \pm 0.5$	$1.7 \pm 0.2$	1.76
Cr	$22 \pm 6$	$19.9 \pm 1$	17.4
Fe	$60 \pm 8$	$68.5 \pm 2$	67.72

Data from Bulajic *et al.* (2002), with permission from Elsevier

once-ionized states. If spectral lines from both states have not been observed, it is necessary to use the Saha equation to calculate the missing species concentration. The neutral and once-ionized contributions must be added together in order to get the total concentration of that particular element. One assumes that the temperatures of all the elements are the same, which would be the case in LTE. That is likely to be the case for neutral elements, but there is evidence of deviation in temperatures between neutral and once-ionized species. Also, as demonstrated above, plasmas can have different temperatures in different spatial regions.

Calibration-free LIBS has been tested for applications of LIBS on Mars. Colao *et al.*, in a thorough, practical study, applied the technique to terrestrial samples of soils and volcanic rock, similar to what can be expected on Mars (Colao *et al.*, 2004a). The laser was a tripled Nd:YAG operating at 355 nm, and the atmosphere simulated was that of Mars. Validation was performed with standard reference materials and scanning electron microscopy coupled with energy-dispersive x-ray analysis (SEM-EDX) on the same samples of siliceous soils and rocks. In summary, LIBS provided an accuracy better than 20% on all major elements except calcium, and better than 60% on minor elements. The conclusion was that, as a remote system operating in real-time without internal standards, it would be very useful for preliminary analyses. A prior knowledge of the sample composition, through combination with data from a different technique such as x-ray fluorescence, would enhance the LIBS results. Sallé *et al.* (Sallé *et al.*, 2005a) reported continued development of this method at the 36th Lunar and Planetary Science Conference.

## 8.4 LASER AND SPECTROMETER ADVANCES

Gornushkin *et al.* (Gornushkin *et al.*, 2004a) reviewed the rapidly developing microchip-laser as it might apply to LIBS. The ones used for LIBS are passively Q-switched Nd:YAG sources of sub-nanosecond, multikilowatt pulses at high repetition rate. Pumping is done by continuous wave diode lasers to produce 1064-nm pulses a few hundred picoseconds long. Advantages include single mode output which contributes to stability, low pulse to pulse amplitude variation, almost Gaussian intensity profiles, 10 kHz repetition rates, a single linear polarization state, and small  $\sim 2$  mrad divergence. The short pulse length combined with the  $\sim 10 \mu\text{J}$

output are disadvantages, however, in plasma formation. Tight focusing is necessary to achieve breakdown, which leads to a short working distance. In their feasibility study, they demonstrated that quantitative analysis was possible using nongated detectors. Their microchip laser was a diode-pumped passively Q-switched Nd:YAG laser, operated at 1064 nm, 550 ps pulse widths, 7  $\mu$ J pulse energy, with a repetition rate of 5.45 kHz. The laser pulse was focused to a spot of 8  $\mu$ m diameter. It was necessary to keep the target rotating to sustain the plasma because at the high repetition rate the melt does not have time to solidify between laser pulses, and the threshold for breakdown on the melt is significantly higher than on the solid. They observed that 0.5 to 20 ng per pulse could be removed from metal foils and silicon wafers and with that they obtained detectable spectra. The zinc resonance line was self-reversed. Comparison of cadmium spectra with a spectral library allowed qualitative identification. Limits of detection were poor, however. They concluded that more powerful microchip lasers with energies of more than 50  $\mu$ J per pulse would be needed to make this technology useful. These devices are beginning to appear commercially.

A flashlamp-pumped acousto-optically Q-switched Nd:YAG laser (AO-laser) was used to study the effect of high frequency 150 ns pulses for LIBS analysis (Yamamoto *et al.*, 2005). Pulse energies of 10 mJ and frequencies up to 6 kHz were investigated. The typical laser power was 0.07 MW, with a spot size of about 0.25 mm, hence an irradiance of 140 MW/cm<sup>2</sup>. The high repetition rate led to increased spatial and depth sampling. Targets included steels, soils, surface stains and dusts on aluminum. Detection limits for Cr, Cu, Mn, Ni and Si in steel were obtained from calibration curves, and ranged from 0.11 to 0.24%. The minimum detectable mass of 1.2 pg/shot was achieved for strontium. Plasma characteristics were compared with those generated by the more common electro-optically Q-switched Nd:YAG laser. Temperatures varied from 7000 to 4000 K over the first 2  $\mu$ s of the plasma. The authors commented that the maximum sampling rate for time-resolved detection of light from individual plasmas will be limited by the readout time of the detection system.

Recently a clever design for a dual-grating high-resolution spectrometer was described by Gornushkin *et al.* (Gornushkin *et al.*, 2004b). At its core it is a Czerny-Turner spectrometer but with a second grating placed close to and almost at right angles to the first grating. A spectrum from the first grating continues through the spectrometer as usual. The zero-order light reflected from the first grating falls on the second grating, is dispersed, and turned by a mirror so that it too proceeds to the focal plane. A two-dimensional CCD detector in the focal plane of the spectrometer allows simultaneous recording of two spectral intervals which are offset vertically to be distinguished, one from the other. The two gratings can be driven independently; hence two intervals between 200 and 800 nm can be observed and imaged. These are 2–3 nm wide for a 2400 grooves/mm grating and 4–5 nm for a 1200 grooves/mm grating. This instrument will be useful in applications where two simultaneously displayed spectral windows are needed. This includes cases where two or more lines need to be observed in different spectral regions for temperature measurements.

## 8.5 SURFACE ANALYSIS

Vadillo and Laserna reviewed the use of LIBS for surface analysis (Vadillo and Laserna, 2004). They considered many issues: the thermodynamic factors governing plasma formation, energy threshold effects, the ablation threshold fluence, coupling efficiency, the effect of laser pulse width, the sensitivity to the surface, and the effect of the lateral resolution. Material begins to be removed at the ablation threshold fluence, when the energy deposited exceeds the local heat of vaporization. They then considered surface applications, the lateral distribution of elements, depth profiling, and the imaging of different atomic species. Some of the factors that interact include spatial resolution (one wants smaller spot size), data acquisition speed (one wants high speed) and sampling flexibility. Their ample discussion of depth resolution merits comment. Depth resolution was defined as the depth range over which the signal observed changes a specified amount, when profiling a sharp interface between two media. The depth resolution  $\Delta z$ , by convention, is the depth range over which the signal changes from 84 to 16% of its full value. In mathematical form  $\Delta z$  is given by:

$$\Delta z = \Delta p \text{ AAR} \quad \text{with AAR} = d(p_{0.5})^{-1} \quad (8.2)$$

where  $\Delta p$  is the number of laser shots needed to reach 84 and 16% of the signal, AAR is the averaged ablation rate,  $d$  is the thickness of the layer being investigated, and  $p_{0.5}$  is the number of laser shots required to reach the interface. Although Equation (8.2) predicts the best resolution (lowest  $\Delta z$ ) when the ablation rate is lowest, the authors comment that experiment has shown this occurs at moderate irradiance levels (Mateo *et al.*, 2001). Their overall conclusion is that surface analysis is a field which is growing quickly and will move forward with new applications year after year.

Scanning across a surface with an elongated spark to map inclusions or other deviations from the substrate has become an area of interest. Rodolfa and Cremers investigated the rapid determination of the spatial distribution of elements on surfaces like aluminum and rhyolite rock (Rodolfa and Cremers, 2004). Cylindrical optics were used to create a linear spark  $\sim 1$  cm in length, as shown in Figure 8.4. Light emitted by atoms excited along the spark was collected and provided a spatial profile of elemental composition in the sample when analyzed with a spectrometer and gated ICCD detector. Two configurations were used. With a slit in the focal plane, the resulting data represented the emission intensity along the exit slit at a single wavelength. Replacing the slit with a two-dimensional ICCD detector allowed multiple elements to be monitored at the same time resulting in a two-dimensional intensity graph of the elemental distributions. Moving the spark across the sample surface as spectral data were recorded at regularly spaced intervals allowed them to determine spatial distributions across an area, as illustrated in Figure 8.5. There an image made by printer toner on paper was detected through the iron spectral signature. In another experiment, rescanning the same barium spot six times showed a lower than exponential decay of the signal, and by implication the material was lost to the next scan.

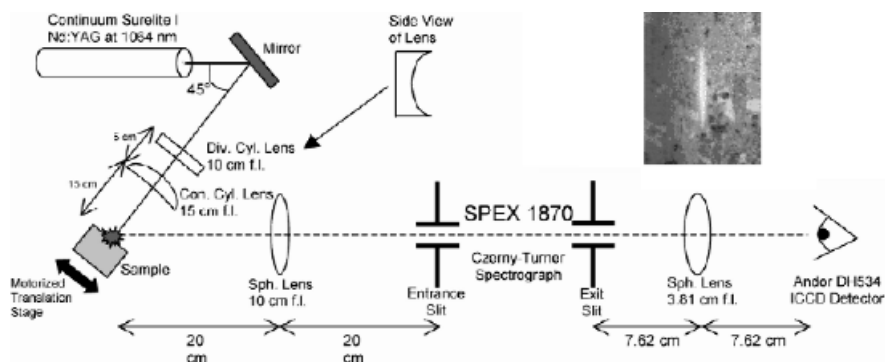


**Figure 8.4** Experimental apparatus for surface scanning techniques using LIBS. A Nd:YAG pulse goes through a diverging cylindrical lens of focal length 10 cm with its axis arranged horizontally. The beam then goes through a converging cylindrical lens of focal length 15 cm with a vertical axis to produce the long spark on the sample. Light from the plasma is imaged on the spectrometer slit using a spherical lens of 10 cm focal length, and light from the exit slit is focused on the camera with a spherical lens of focal length 3.81 cm. The schematic illustrates the production of the long spark. The inset is a photo of a long spark on rhyolite. (Reproduced from Rodolfa and Cremers, 2004, with permission from Society for Applied Spectroscopy)

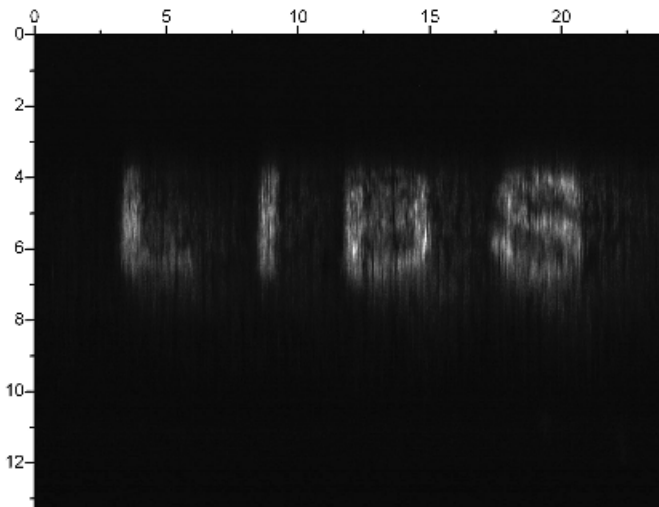


**Figure 8.5** An intensity map across printed text, a 14-pt sans-serif LIBS, in the light of Fe(I) at 404.6 nm. Dimensions on the axes are millimeters. (Reproduced from Rodolfa and Cremers, 2004, with permission from Society for Applied Spectroscopy)

Mateo *et al.* reported an automated line-focused laser ablation method for mapping of inclusions in stainless steel (Mateo *et al.*, 2003). The Nd:YAG laser beam at 532 nm was focused to a micro-line on the sample surface. That reduced the number of laser pulses necessary to generate chemical maps and hence improved the speed of data collection. It resulted in a flat topped beam profile which led to very

reproducible craters in terms of depth per pulse. Resolution was about  $5\text{ }\mu\text{m}$  along the line and  $50\text{ }\mu\text{m}$  between lines. Light from the sample was projected through a Czerny-Turner imaging spectrograph onto a CCD detector, resulting in two- and three-dimensional maps of inclusions in the steel sample. The constituents included Mn, Mg, Ca, Al and Ti. There was an approximately 50-fold reduction in the number of pulses and the time to complete an analysis using the micro-line method over the point to point method. Topographic studies were conducted to demonstrate the utility of the method. In one of these, they generated a three-dimensional map of aluminum inclusions in stainless steel. The dimensions of the volume sampled were  $875\text{ }\mu\text{m}$  in length,  $600\text{ }\mu\text{m}$  in width and  $56\text{ }\mu\text{m}$  in depth. The depth profiling of the aluminum inclusions stood out in this three-dimensional representation. The laser energy was  $33\text{ mJ/pulse}$ . It required  $2.5\text{ min}$  to scan this volume, much improved over the point to point method. Nevertheless the total volume interrogated was less than  $0.03\text{ cm}^3$ , so the method will still be limited to extended spot sampling on a steel surface.

Bette *et al.* demonstrated high speed scanning LIBS at up to  $1000\text{ Hz}$  for the detection of inclusions in and on steel (Bette *et al.*, 2005). Simple grinding of the sample surface was sufficient for preparation. A Paschen-Runge spectrometer with an individual photomultiplier for each line was used and covered the wavelength range from  $130$  to  $777\text{ nm}$  (oxygen emission lines at each end). Up to  $24$  elements could be monitored simultaneously. The system could analyze areas with dimensions up to  $110$  by  $45\text{ mm}$ . For the first time, light elements such as C, N, O, P and S could be quantified simultaneously. A diode-pumped Nd:YAG laser at  $1064\text{ nm}$  was used to scan the sample. Only one laser pulse was applied per position. The spherical lens focusing arrangement resulted in crater diameters of  $16$ – $20\text{ }\mu\text{m}$ . Figure 8.6 shows a  $40 \times 40\text{ mm}$  area of a steel sample scanned with a step of  $100\text{ }\mu\text{m}$ .

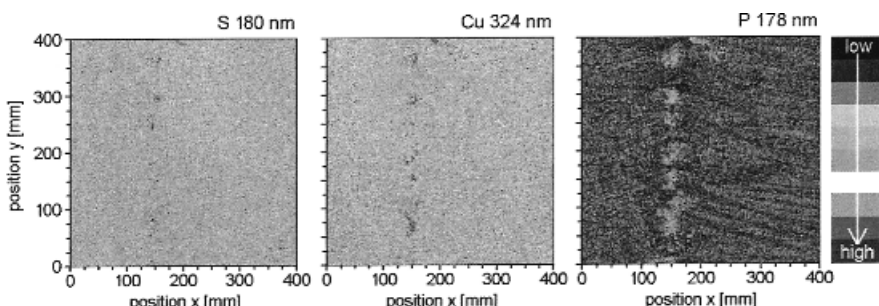


**Figure 8.6** Segregation and dendrites in steel. A  $40 \times 40\text{ mm}$  area of a steel sample was scanned with a step of  $100\text{ }\mu\text{m}$ , with  $400 \times 400$  measurement points performed in  $15\text{ min}$ . All mappings were captured during the same scanning measurement. The sulfur, copper and phosphorus channels show a segregation zone oriented in the  $y$  direction. (Reproduced from Bette *et al.*, 2005, with permission from Journal of Laser Applications. Laser Institute of America\*, Orlando, Florida. [www.laserinstitute.org](http://www.laserinstitute.org). All rights reserved)

Note: \*The Laser Institute of America disclaims any responsibility or liability resulting from the placement and use in the described manner.

A total of  $400 \times 400$  measurements were made in 15 min. The sulfur, copper and phosphorus channels showed a segregation zone, a linear zone of enhanced elemental concentrations, oriented in the y direction.

## 8.6 DOUBLE PULSE STUDIES AND APPLICATIONS

Advances in double pulse techniques through 2002 were reviewed in Chapter 2. Figure 2.17 shows different geometrical arrangements in use and these are summarized below:

- (1) collinear multiple pulses within the same flashlamp pulse;
- (2) collinear beams from two lasers focused on the same spot on the target;
- (3) orthogonal beams, typically with one beam perpendicular and one parallel to the surface:
  - (a) where the pulse for the beam parallel to the surface is first in time forming an air spark (pre-ablative);
  - (b) where the pulse for the beam parallel to the surface is second in time, and reheats the material ablated by the first pulse (reheating).

Several experiments and papers have recently tried to address the causes of the 10- to 100-fold increase in intensities with double-pulse LIBS.

The Saclay group investigated quantifying the intensity changes for double pulse LIBS in orthogonal geometry (Gautier *et al.*, 2005). This paper starts with a good summary of the major variations of this technique and appropriate references. They carried out their double pulse experiments on aluminum samples in atmospheric pressure air. Two lasers were used, one at 532 nm and a second at 1064 nm. Experiments were done in the 3a and 3b arrangements using pre-ablation and reheating schemes. In the reheating experiments, only emissions from lines with high excitation energy levels were enhanced. The results are summarized in Figure 8.7 which shows, for the Mg(II) line at 280.27 nm, the increase in intensity for double pulses compared with simple pulses of increasing laser energy. At the same ablation laser energy, the reheated signals always were greater than the simple-pulse signals by factors of 3 to 5. Results were related to the capacity of the plasma to absorb the energy of the reheating pulse leading to increases of plasma temperature. However the same enhancements were not found in reheating for the Mg(I) 285.2 nm line, because the principal effect of the reheating pulse was to increase the temperature of the plasma. This in turn led to higher ionization, which depleted the neutral fraction, counteracting the thermal increase in the neutral Boltzmann population. In the pre-ablation spark dual pulse scheme (3a), the increases might be linked to the change of atmospheric pressure created by the spark before the ablation step. For their orthogonal beam experimental set up, the reheating scheme (3b) was found to be better than the pre-ablation method for improving LIBS sensitivity.

In this study by the Pisa group (Cristoforetti *et al.*, 2004), single pulse and double pulses were introduced in the parallel configuration (2) using two Nd:YAG lasers

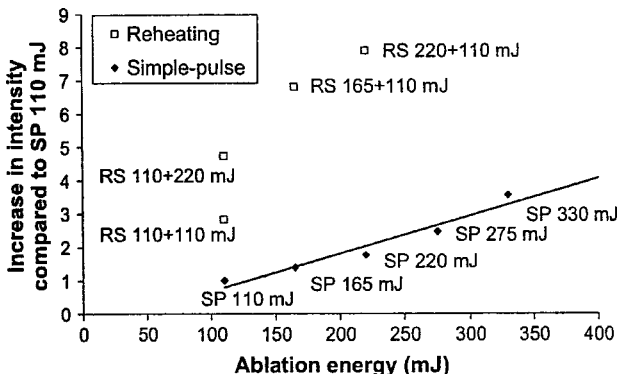


**Figure 8.7** Results obtained with different laser energies in the reheating scheme (RS, open squares) and simple pulse (SP, black diamonds) for the Mg(II) 280.27 nm line. The delay between the two pulses in the RS scheme was 200 ns. (Reproduced from Gautier *et al.*, 2005, with permission from Elsevier)

at 1064 nm. The target was a brass sample and air pressures were varied from 0.1 Torr to atmospheric pressure. Neutral and ionized lines were used as diagnostics. Several pressure dependent phenomena were recorded. In one case, the double pulse enhancement of 4 for the Cu(I) 521.5 nm line at atmospheric pressure disappeared below 100 Torr. In another, the pressure effect on the enhancement due to double pulse delay was recorded. The group interpreted these effects as being consistent with changes, as a function of pressure, in the shock wave expansion and gas density in the cavity caused by the laser plasma. The authors concluded that a more detailed model accounting for residual plasma atom effects and electron densities found by the second laser pulse would be useful for more complete modeling of the double pulse process.

Laser microablation and plasma reheating with collinear laser pulses in the 50 fs to 10 ps regime were studied by Semerok and Dutouquet (Semerok and Dutouquet, 2004). A laser at 800 nm with a maximum of 20  $\mu$ J per pulse was incident upon a Michelson interferometer to provide the two beams. The results were divided into three delay regions. For delays less than 1 ps, the double pulse effect was similar to that of one pulse of the same energy. The 1–10 ps regime was one of partial plasma shielding. The 100–200 ps delay was found optimum for plasma re-heating by the second pulse, favoring plasma reproducibility and maximizing radiation intensity.

Despite the many experiments, the explanations of the enhancement effects observed are only slowly emerging. They will certainly depend strongly on interpulse delay. At delays below 1 ps, as indicated above, the effects diminish, showing no improvement over single pulse excitation. Once the plasma is formed coupling enhancement may dominate and then plasma shielding. At longer delays, sample heating and atmospheric number density may affect enhancement mechanisms. At even longer delays, the first plasma may have sufficiently cooled and recombined as to present ambient conditions to the next pulse. Much interesting work remains to be done.

## 8.7 STEEL APPLICATIONS

Steel analysis has always been a popular application for LIBS. It has been applied to multi-elemental analysis of slag samples from a steel plant, as reported by Kraushaar *et al.* (Kraushaar *et al.*, 2003). Avoiding sample preparations, liquid slag was captured in special probes, cooled, and then analyzed with LIBS. In order to obtain useful results, a preliminary chemical analysis of the slag is an essential input parameter because elemental concentrations can range up to 30%. In this work the authors compared four methods of standardizing the LIBS spectra: using (1) no internal standard; (2) one internal standard; (3) a sum of internal standards; and (4) a multi-variate calibration. In the latter case, all the integrated signals are chosen as input parameters, and they span a vector space. The calibration model determines the direction in the vector space that correlates most closely with the reference concentrations of the calibration samples. This direction is used for a linear calibration function. To test which of the calibrations matched most closely the x-ray fluorescence (XRF) determination of concentrations, the mean  $r^2$  coefficient was determined. It varied in the order given above as: 0.65, 0.85, 0.90 and 0.96. Calibration curves show a much better fit of the calibration line for the multi-variate analysis. Much of the work was done on homogeneous samples of representative concentrations, to avoid confusing sample inhomogeneities with fundamental capability. The next major step in improving the results is to optimize the slag sampling method to favor more homogenous samples from the converter and the ladle. The technique's repeatability for the main elements and their oxides, CaO, SiO<sub>2</sub> and Fe<sub>total</sub> were 0.6, 1.5 and 0.7%, respectively.

The use of LIBS across an open path of 10 m to analyze stainless steel samples in high temperature conditions had been reported by Garcia *et al.* (Garcia *et al.*, 2004). Despite the good properties of stainless steel, at high temperature it can lose its protecting oxide layer and accumulate superficial oxidation called scaling. LIBS represents a simple non-contact method to generate information about the sample in the area affected by the laser. In this work, a Nd:YAG laser beam was expanded to about 70 mm in diameter and then focused with a lens system. Light from the plasma was collected from up to 10 m distance with a Galilean telescope and focused on the entrance slit of a small Czerny-Turner spectrometer with an ICCD detector. Stainless steel samples were placed in the geometrical center of an oven whose door was opened for a short time for rapid measurements. The ratios of elements such as chromium to chromium plus iron, observed in a matter of minutes, presented quantitative information about the dynamic growth of the scale layer. Depth of the scale layer was determined by the number of laser pulses required to reach the underlying matrix material. Modeling using kinetics for oxidation of 316L stainless steel indicates a  $t^{1/2}$  dependence of the growth of the scale layer with time. Figure 8.8 shows experimental verification of this trend. The authors concluded that a reasonable start has been made on making this a usable technique. An improvement would allow analyzing the scale composition which could not be done here because it flaked off the sample irregularly.

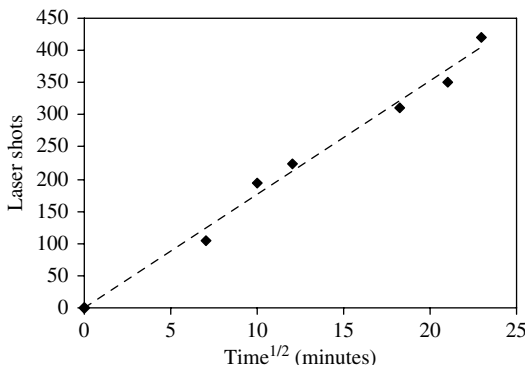


**Figure 8.8** Linear dependence of the number of laser pulses needed to reach the matrix, on the square root of the exposure time at 900°C. The sample was AISI 316L stainless steel. (Adapted from Garcia *et al.*, 2004, with permission from Society for Applied Spectroscopy)

## 8.8 LIBS FOR BIOLOGICAL MATERIALS

Because of terrorist activities, LIBS is being considered for detection and classification of biological aerosols. Hybl *et al.* (Hybl *et al.*, 2003) approached the problem with two objectives: (1) the discrimination potential for aerosol sensing in dense particulates; and (2) identifying biological agents in single particles. For the first they used a broadband, less-tightly focused LIBS system which could not distinguish individual particles for laboratory measurements on an anthrax stimulant *Bacillus subtilis var. niger* (Bg). The laser was a Nd:YAG at 1064 nm, 50 mJ per pulse and 7 ns pulse width. Spectral resolution was provided by two grating spectrometers covering the regions from 200 to 650 nm and 613 to 825 nm. The results were compared with those for common, naturally occurring biological aerosols like pollen and fungal spores, to determine LIBS potential for discriminating biological agents from natural background aerosols. A principal component analysis (PCA) was used to set up a robust set of standards for discriminating between biological material and matrix such as dirt. A three-dimensional color visualization of their results illustrated the capability of PCA in discriminating among several different types of samples: Bg, fungal spores, media and pollen. Many caveats were discussed. The single particle experiments were done with a narrowband, more tightly focused optical system that could spatially resolve individual particles. Their conclusion was that there was sufficient sensitivity to detect Ca, Mg and Na in Bg, but again there were a variety of caveats. Incomplete vaporization or fragmentation of larger particles, particles that only are partially in the plasma, and particles of different sizes are complicating issues. Some of these have been addressed by using cascade impactors to segregate particles of different sizes. They concluded that the technique can result in useful elemental ratios in common biological materials, to discriminate between interferences and biological warfare agents. Its capabilities remain to be tested in a real field environment, however.

Three contributions to the LIBS 2002 Conference (Orlando, FL, USA) addressed different aspects of the analysis of pollens, bacteria, spores, molds and protein (Boyain-Goita *et al.*, 2003; Morel *et al.*, 2003; Samuels *et al.*, 2003). The first of these considered dual analysis by LIBS and Raman. Where LIBS was useful in providing atomic analysis, Raman provided discrimination between biological and mineral samples. The second group analyzed six bacteria and two pollens in pellet form. They concluded that a cumulative intensity ratio was a possibility for a discrimination technique because of its linearity and reproducibility. In the final work, biosamples were loaded onto a porous silver substrate. PCA was used to reduce the data from individual LIBS shots. Their conclusion was that there was adequate information to discriminate between different biomaterials. As always in the realm of analytical techniques, discrimination between similar spectral signatures in a multicomponent environment will be required for the success of any of these approaches. It is likely that simultaneous information from more than one technique would enhance the reliability of the results.

Dixon and Hahn (Dixon and Hahn, 2005) investigated the detection of spores of *Bacillus* as aerosols. A flow system was developed to ensure that only a single particle was in the LIBS spark volume. Detection was based upon observing signals from the Ca(II) lines at 393.4 and 396.9 nm. Also a scheme based on the ratio of calcium to magnesium or sodium was attempted. Their conclusion was that, with their current apparatus and analyses techniques, real time detection of *Bacillus* spores in ambient conditions is not feasible. They noted that the differences between the target and similar particles are rooted in their molecular structure, not in an easily discernible ratio of atomic species. Statistical strategies for improving the LIBS capability for discriminating between benign and toxic agent simulants were also treated by Munson *et al.* (Munson *et al.*, 2005).

## 8.9 NUCLEAR REACTOR APPLICATIONS

An extreme application of LIBS in a hostile environment is the analysis of materials in a nuclear reactor. Three examples from Applied Photonics Ltd will illustrate LIBS capabilities for remote *in-situ* measurements in a location inaccessible to other analytical techniques.

Monitoring materials in a nuclear power plant is one of LIBS most challenging assignments. Whitehouse *et al.* reported on remote material analysis of nuclear power station steam generating tubes by LIBS (Whitehouse *et al.*, 2001). The objective was to determine the copper content in 316H austenitic stainless steel superheater tubing within the pressure vessel of a nuclear power reactor. It was known that high copper concentrations ( $\text{Cu} > 0.4\%$ ) were correlated with low ductility and an increased risk of cracking. Hence the analytical goal was to distinguish three levels of copper content in the joints, low ( $\text{Cu} < 0.06\%$ ), intermediate ( $0.06\% < \text{Cu} < 0.2\%$ ), and high ( $>0.4\%$ ). For safety reasons, a long umbilical fiber optic was required to separate the analytical instrument from the target. The apparatus is shown in Figure 7.18. Figure 8.9 illustrates the convoluted path of the 75 m fiber optic from

the sampling region to the laser equipment. Power density transmitted through the fiber had to be kept low to prevent damage to the fiber, so 5.5 mJ per shot, resulting in  $\sim 1 \text{ GW/cm}^2$  on target was chosen. It was found that a burn-in time of 400 laser pulses was required, after which the next 800 pulses provided reliable data on the samples. Ratios of selected lines of copper and iron were used for the calibration and analysis. Important parameters determined were an estimate of the detection limit (0.036%), precision (3.7%) and accuracy ( $\pm 25\%$ ). A sample of one faulty joint was removed after LIBS analysis, and laboratory analysis confirmed the LIBS result.

In the same vein, other applications followed that original report, as found on the Applied Photonics Ltd web site ([www.appliedphotonics.co.uk](http://www.appliedphotonics.co.uk)). For example, baskets used to catch reprocessed nuclear material were accumulating an unknown waste material. It was determined that the baskets should be changed, but their fate awaited the analysis of the waste product. A laser beam was allowed access to the baskets through a lead glass window in the concrete shielding (Figure 7.7; Plate 13). The LIBS analysis showed that the contaminant material was rich in zirconium and molybdenum, which determined that a low level storage facility would suffice for the baskets.

As underwater spent fuel cooling ponds were being decommissioned, it was necessary to characterize and identify components and material stored in the pond prior to their removal. Doing this under water while the material is submerged offers advantages in safety, speed and overall cost reductions. The unique part of this analysis apparatus was a gas nozzle that cleared the way for a LIBS spark to be formed on submerged solid material, as shown in Figure 8.10. Hence the LIBS analysis could proceed in a gas rather than a liquid medium. The probe was usable

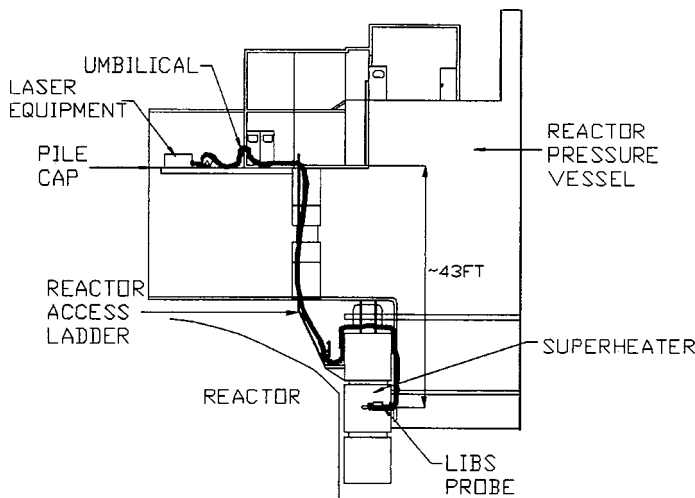


**Figure 8.9** Sectional view of the Advanced Gas Cooled Reactor vessel showing the umbilical fiber optic. (Reproduced from Whitehouse *et al.*, 2001, with permission from Elsevier)



**Figure 8.10** A 75 mm diameter aluminum disk submerged in water being analyzed by a LIBS instrument. Gas emerging from the nozzle clears the path for a LIBS spark to be formed on the surface. (Source: Applied Photonics website, Applications Note 004, 2005, with permission from Applied Photonics Ltd)

at depths up to 10 m and a gap of 2 mm at the end of the probe was generated by the gas pressure. A variety of materials could be identified quickly because of their unique spectral signatures.

## 8.10 LIBS FOR SPACE APPLICATIONS

One of the more exotic and exciting recent applications of LIBS is for instrumentation on space missions to planet surfaces. Although widespread interest in the use of LIBS for space applications is recent, consideration of the use of a laser for space missions dates back to the 1980s. In 1986 the Max Planck Institute commissioned a German firm to conduct a study of instrumentation for a flyby asteroid mission (Vertes *et al.*, 1993). A multi-instrument analysis package

concept (FRAS or ‘Facility for Remote Analysis of Small Bodies’) was developed. A laser would be used to remotely interrogate the target surface. Instruments were to include: time-of-flight laser ionization mass spectrometry, secondary ion mass spectrometry, laser-induced fluorescence, and UV spectrometry along with remote Raman spectrometry and surface profile measurements. Although laser plasma spectroscopy was a well-established method in the scientific literature and commercial laboratory instruments developed, it was not included as an instrument. LIBS may have been considered but not implemented for some reason.

Two Mars-bound Soviet space craft, Phobos 1 and 2, launched in 1989 carried laser-based instruments for chemical analysis. The instruments, named LIMA-D, involved firing laser pulses at the Martian moon Phobos from a 30 m distance during a flyby (Sagdeev *et al.*, 1985). The laser was to evaporate an area of 1–2 mm in diameter to a depth of 0.002 mm and the chemical composition of the resulting gas cloud traveling away from Phobos was to be analyzed by a mass spectrometer. Element masses between hydrogen and lead would be determined. Unfortunately, a combination of equipment failures and ground control problems precluded successful use of the LIMA-D instruments on both spacecraft.

Current technological developments in lasers, spectrographs and detectors have made the use of LIBS for space exploration feasible. These developments, in addition to its many advantages compared with past and current methods of elemental analysis deployed on space craft, have brought LIBS to the forefront. These prior methods are XRF on the Viking (Clark *et al.*, 1977) and Venera (Hunten *et al.*, 1983) missions and alpha-proton x-ray spectrometry (APXS) on the Pathfinder (Economou, 2001) and Mars exploration rovers (MER) (Rieder *et al.*, 2003). LIBS promises to greatly increase the scientific return from new missions by providing extensive data relating to planetary geology, one main goal of space exploration. Planetary geology is important because it can answer questions dealing with (1) the physical and chemical evolution of the solar system, (2) what the early solar system was like, and (3) compare processes that occurred on other bodies with geologic processes on Earth. Also, a geologic analysis can tell us something of a planet’s history such as whether earlier conditions were favorable for life (e.g. indications of past water).

Advantages of LIBS that make the method particularly attractive for space applications include:

- rapid elemental analysis (one measurement per pulse);
- stand-off or remote analysis at tens of meters;
- small analysis area of  $\leq 1$  mm, even at distance (Figures 8.11 and 8.12);
- detect elements in natural matrix without sample preparation;
- ability to detect all elements (high and low atomic number);
- low detection limits for many elements (element specific, 2–1000 ppm);
- compact, lightweight, and able to operate in severe environments;
- eliminate ambiguous results from current instruments (e.g. IR);
- remove dusts and weathering layers with pre-analysis ablation pulses;
- easily combined with other spectroscopic methods (e.g. Raman and LIF).

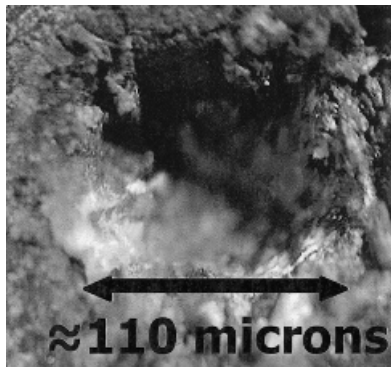


**Figure 8.11** Ablation crater formed on basalt at 3 m distance. Depths ablated per pulse ranged between 0.5 and 1  $\mu\text{m}$

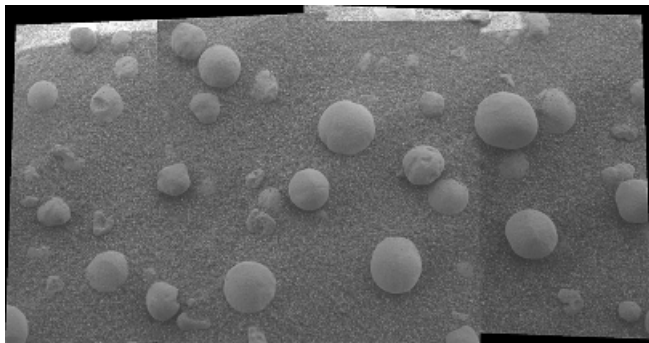


**Figure 8.12** Extreme close-up of round, blueberry-shaped formations in the Martian soil near an outcrop at Meridiani Planum. The image is one of the highest resolution images ever taken by the microscopic imager deployed on the Opportunity rover. Image is 3 cm across (with permission from NASA)

Perhaps the most important advantage of LIBS is stand-off analysis and point detection. These allow the interrogation of interesting geological features that may not be accessible to either an *in-situ* detector (APXS) or sample retrieval arm (XRF). Examples of interesting geological features discovered by the MER Opportunity rover that would benefit from a LIBS analysis are shown in Figure 8.13(a) and (b). The layers shown (about 1 cm thick) could be directly accessed by the laser plasma formed at a distance. A laser plasma formed on a cliff bank on Earth is shown in Figure 8.13(c). The point sampling capability of LIBS demonstrated in Figure 8.11 could be used to interrogate small samples such as the ‘berries’ captured by the Opportunity microscopic imager (Figure 8.12).

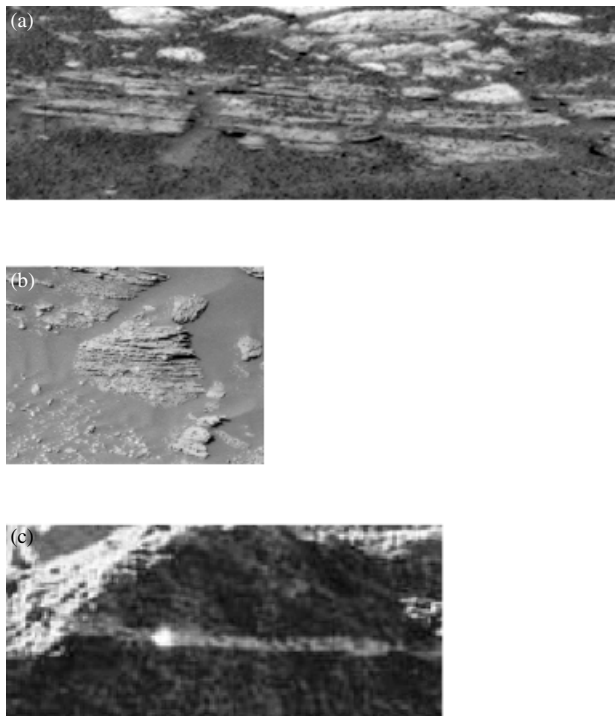


**Figure 8.13** (a), (b) Images (courtesy of NASA/JPL/Cornell) taken by the Opportunity rover at the landing site (Meridiani Planum). (c) Laser plasma formed on a cliff face at 24 m distance in air on Earth. The horizontal strip in (c) is the result of moving the laser beam to interrogate different locations.

Stand-off and rapid analysis capabilities of LIBS will greatly increase the number of samples that can be analyzed during the limited mission lifetime. For comparison, a very small number of samples were analyzed on the Surveyor missions 5, 6 and 7 (2, 1 and 3 samples, respectively) (NASA, 1969). Over an operational period of 322 days, the Soviet Lunokhod rover conducted 25 soil analyses and traveled 10 540 m. In 1 month of operation, the Sojourner rover of the Pathfinder mission returned 10 chemical analyses of Martian soils and rocks (Golombek *et al.*, 1997) from a 100 m<sup>2</sup> area. For LIBS, it is anticipated that a measurement of 75 laser shots can be carried out every 2 min with the time between different targets projected to be 5 min, determined by the time to optically acquire and focus the targeting system. Based on these projections, a LIBS stand-off method of analysis will greatly increase the scientific return from future missions.

Several studies have addressed the feasibility of LIBS for space exploration. The results of some of these are summarized in Table 8.2. Currently, preliminary tests have demonstrated some capabilities of LIBS for analysis at close-up and stand-off distances and for atmospheric pressures and compositions simulating Mars, Venus

**Table 8.2** Studies of LIBS for space exploration applications

---

Demonstration of LIBS analysis of a cliff bank in air at 24 m using lab equipment outdoors.
Discussion of requirements for a flyable LIBS system (Blacic <i>et al.</i> , 1992)
Remote analysis of an Apollo 11 rock simulant at 10.5 m using lab components. Demonstration that stand-off LIBS has sufficient sensitivity to monitor the elements Si, Ti, Al, Fe, Mg, Mn, Ca, Na, K, P, Cr at concentrations in the rock simulant (Cremers <i>et al.</i> , 1995)
Detailed study of stand-off LIBS (up to 19 m) using moderate pulse energy (80 mJ) with samples in 7 Torr CO <sub>2</sub> . Preliminary evaluation of analytical capabilities. Demonstration of stand-off LIBS at 19 m using a micro-laser (Knight <i>et al.</i> , 2000)
Preliminary field evaluation of a compact LIBS system (2–3 m) operated on a NASA rover, qualitative analysis capabilities such as rock identification, and comparison with IR spectroscopy (Wiens <i>et al.</i> , 2002)
Study and optimization of experimental factors affecting plasma emission under Mars atmospheric pressure and composition conditions at 1 m distance (Brennetot <i>et al.</i> , 2003)
Study of plasma emission characteristics and determination of optimal experimental parameters for samples interrogated in air and in a simulated Mars atmosphere (0.225 m) (Colao <i>et al.</i> , 2004a)
Under Mars atmospheric conditions, a comparison was made between analysis results obtained by CF-LIBS and SEM-EDX for close distances (0.15 m) (Colao <i>et al.</i> , 2004b)
Evaluation of stand-off LIBS for analysis of water ice and ice/soil mixtures at 4 and 6.5 m under Mars atmospheric conditions (Arp <i>et al.</i> , 2004a)
Study of the S and Cl detection at stand-off distances (3–12 m) in a Mars atmosphere (Sallé <i>et al.</i> , 2004)
Demonstration (~1 m) of LIBS at 90 atm pressure for application to a Venus mission. Strong effect of pressure on some element emissions observed (Arp <i>et al.</i> , 2004b)
Study of the use of the vacuum ultraviolet (VUV) for <i>in-situ</i> monitoring of elements in geological samples in a Mars atmosphere. The residual 7 Torr CO <sub>2</sub> gas will prohibit detection of VUV lines at stand-off distances (Radziemski <i>et al.</i> , 2005)
Study of the effect of atmospheric pressure on the <i>in-situ</i> analysis of soil and clay samples and the effect of pressure on some matrix effects (Sallé <i>et al.</i> , 2005b)
Comparison of LIBS capabilities at atmospheric, Mars and low pressures (simulating the Moon, asteroids) for <i>in-situ</i> and stand-off analysis (5.3 m). Emission intensities at low pressure are strongly reduced (Harris <i>et al.</i> , 2004)

---

and the Moon. Corresponding pressures are Mars (7 Torr CO<sub>2</sub>), Venus (90 atm CO<sub>2</sub>) and the Moon ( $\sim 10^{-9}$  Torr). Figure 8.14 shows how the emissions from four elements depend on pressure for targets of Mars, the Moon and other airless bodies. The behavior shown here can be understood as the result of the pressure dependence of competing processes on collisional excitation of species in the plasma and ablation of the target (Knight *et al.*, 2000). The data indicate that signals are actually enhanced under Mars conditions (7 Torr) compared with the other pressures. For pressures below about 0.001 Torr no changes in element signals were observed with further pressure decreases down to 0.00002 Torr (lowest pressure monitored in Figure 8.14). Therefore, it is believed that measurements made at pressures below 0.001 Torr should simulate an airless body such as the Moon very well in terms of LIBS excitation. LIBS signals are significantly reduced at the lower pressures limiting the range of stand-off measurements (Harris *et al.*, 2004).

Another target of interest is Venus characterized by pressures on the order of 90 atm and temperatures of 725°C. Photographs of the Venus surface taken by Venera

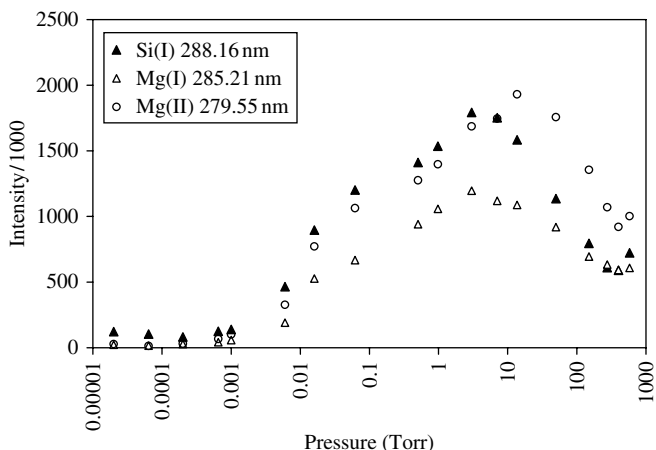


**Figure 8.14** Element signals as a function of pressure determined at the *in-situ* analysis distance of 7 cm (Harris *et al.*, 2004)

14 (Figure 8.15) show a transparent, though thick, atmosphere through which a laser beam may be propagated. The use of LIBS at high temperatures has not been shown to be a problem with molten glass and metals being analyzed. There are some data relating to LIBS analysis at high pressures on the order of 30 atm (Noda *et al.*, 2002). More recent work has shown that measurements providing useful LIBS spectra can be carried out at higher pressures (Arp *et al.*, 2004b). Figure 8.16 shows basalt spectra obtained at 90 and at 0.77 atm for comparison for a sample distance of 1 m. At room temperature, CO<sub>2</sub> liquefies at pressures above about 58 atm and so nitrogen gas was used instead. Lines of some major elements in the sample exhibit strong self-absorption whereas other lines do not appear affected by the pressure. This indicates that analytical lines will have to be carefully selected but that at



**Figure 8.15** The Venusian surface as recorded by Venera 14. (Courtesy of NASA and NSSDC)

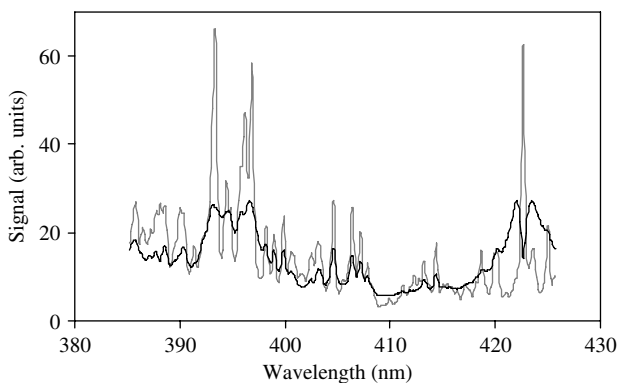


**Figure 8.16** Spectra of basalt rock at 0.77 atm (grey line) and 90 atm (black line). The recorded signals were strong and were reduced by 10 000 for plotting here. (Modified from Arp *et al.*, 2004b, with permission from Elsevier)

least qualitative analysis should be possible. The hostile environment on Venus will require that the LIBS system be shielded from the high surface temperatures and pressures. This will necessitate that the instrument be confined to the interior of the insulated lander with remote analysis provided through a window. Although the spectra of Figure 8.16 were obtained at only 1 m distance, the strength of the signals show that stand-off analysis of many meters should be feasible.

Some representative LIBS limits of detection for stand-off analysis of soil samples maintained in a 7 Torr CO<sub>2</sub> atmosphere are presented in Table 8.3. In general, LIBS has sufficient sensitivity to monitor the majority of elements of interest to geologists at useful concentrations. On the other hand, some elements such as Cl and Br may be present at levels below current LIBS detection limits (e.g. Cl ~ 1.2% and Br ~ 20–1000 ppm at certain locations on Mars established by the MER). Observation of lines below 200 nm may improve that situation.

Another advantage of LIBS is that it is readily combined with other laser and nonlaser-based spectroscopic methods that use essentially the same instrumentation and have remote analysis capability. The combination of LIBS/Raman is currently

**Table 8.3** Stand-off LIBS detection limits for elements in soils and soil simulants (100 mJ/pulse; 19 m; 7 Torr CO<sub>2</sub>) (Knight *et al.*, 2000)

Element	LOD (ppm)	Element	LOD (ppm)
Ba	21	Ni	224
Cr	39	Pb	95
Cu	43	Sn	84
Hg	647	Sr	1.9
Li	20		

LOD, limit of detection.

being investigated. A LIBS system can readily be converted into a Raman system by the addition of two minor components. This is shown in Figure 8.17. By inserting a doubling crystal in the laser beam path to generate 532 nm second harmonic light and a narrowband filter to block the scattered second harmonic light from the sample, Raman measurements can be provided using the same detection system. The use of Raman at stand-off distances has been demonstrated (Sharma *et al.*, 2003). Using a compact LIBS sampling head and inserting a small KD\*P crystal in the beam path, Raman spectra have been recorded at several meters.

While laboratory work has shown the general capabilities of LIBS for future space missions, work has begun on demonstrating that compact LIBS instrumentation can provide useful analytical results. A micro-laser has been used to record useful LIBS spectra at 19 m with the soil sample maintained in a 7 Torr CO<sub>2</sub> atmosphere. In addition compact spectrographs are being evaluated for use on such missions. Mass, size and power requirements are stringent requirements for space applications necessitating the development of high performance systems.

Preliminary field tests of a LIBS instrument have been carried out using commercial off the shelf components (Wiens *et al.*, 2002). The compact system consisted of a sampling head (~0.5 kg) housing the laser and adjustable focusing and light collection optics (Figure 8.18a). The detection system employed a small

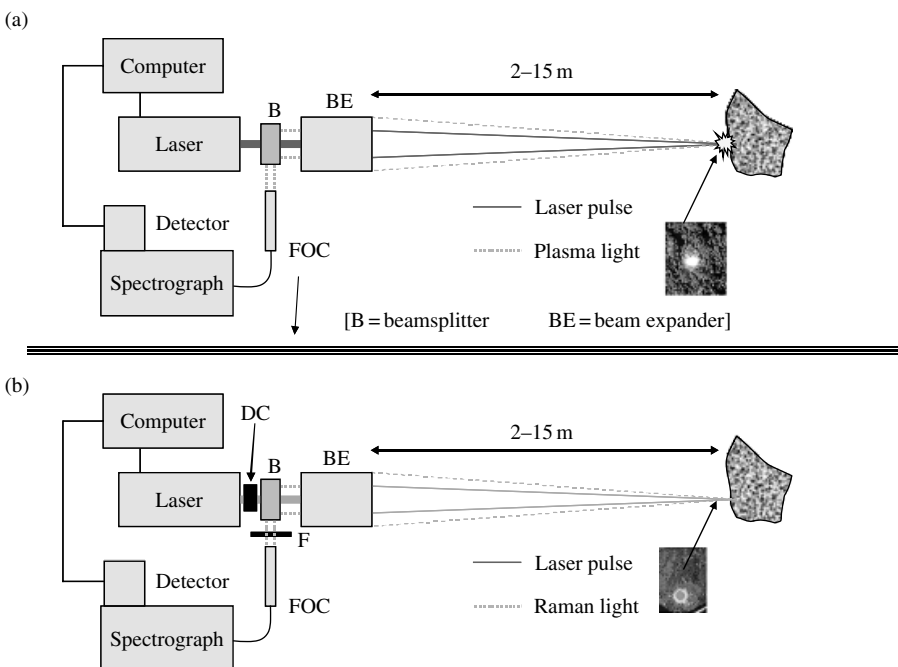


**Figure 8.17** A LIBS system (a) is readily converted to a Raman system (b) by the addition of a doubling crystal (DC) and filter (F) to block scattered laser light.

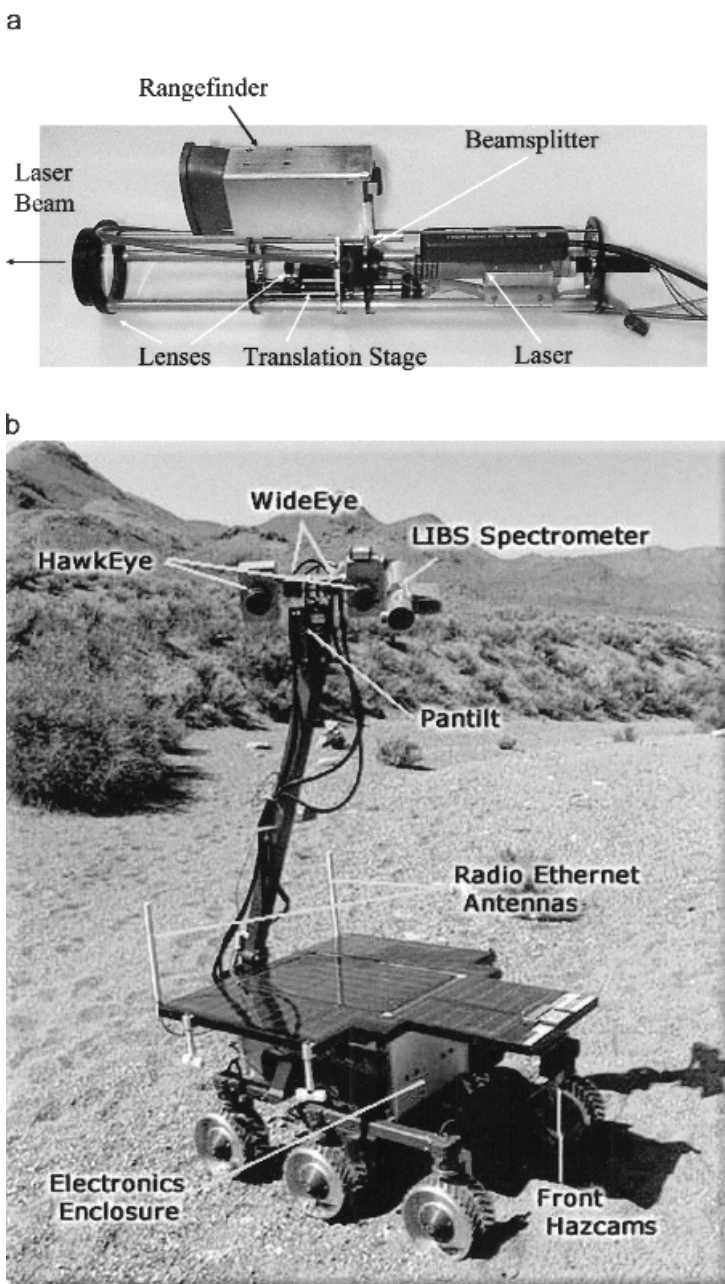


**Figure 8.18** (a) LIBS sampling head mounted on mast of test rover. (b) LIBS system integrated on test rover. Spectrograph and detector were positioned in the body of the rover

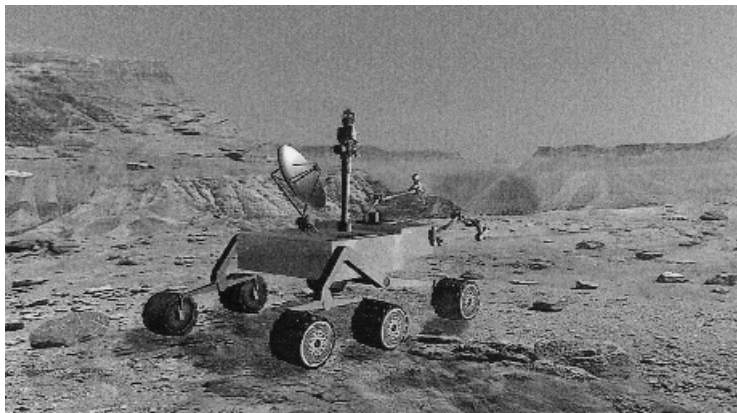


**Figure 8.19** LIBS instrument shown on board the MSL rover for the planned 2009 mission. (Rover artwork courtesy of NASA/JPL)

grating spectrograph and ICCD detector. The sampling head and LIBS system were mounted on a rover during a field test in 2000 (Figure 8.18b).

As a result of work by an international team which included studies of LIBS capabilities for Mars analysis (Table 8.2) and engineering work on development of a flyable laser, optical system, and spectrograph, a design for a LIBS instrument has been selected as an instrument on the 2009 Mars Science Laboratory (MSL) rover. The LIBS analyzer and micro-imager combination (named ChemCam) is projected to provide elemental analysis data at a range from 2 to 12 m from the rover. As in the field test instrument (Figure 8.18b), the laser and optical system will be mounted on the mast, ~1 m above ground. Electrical and fiber optic cables will provide information and control links between the spectrographs laser power supply. An artist's conception of LIBS operating on the MSL rover is shown in Figure 8.19. Current specifications indicate this rover will be the largest ever landed on Mars (900 kg mass). The rover is planned to traverse a 6 km path on the Martian surface over the projected >1 year mission lifetime.

## REFERENCES

- Aguilera, J.A., J. Bengoechea and C. Aragón (2003). Curves of growth of spectral lines emitted by a laser-induced plasma: influence of the temporal evolution and spatial inhomogeneity of the plasma. *Spectrochim. Acta Part B* 58: 221–237.
- Aguilera, J.A. and C. Aragón (2004). Characterization of a laser-induced plasma by spatially resolved spectroscopy of neutral atom and ion emissions. Comparison of local and spatially integrated measurements. *Spectrochim. Acta Part B* 59: 1861–1876.
- Arp, Z.A., D.A. Cremers, R.C. Wiens, D.M. Wayne, B. Sallé and S. Maurice (2004a). Analysis of water ice and water/ice soil mixtures using laser-induced breakdown spectroscopy: application to Mars polar exploration. *Appl. Spectrosc.* 58: 897–909.

- Arp, Z.A., D.A. Cremers, R.D. Harris, D.M. Oschwald, G.R. Parker and D.M. Wayne (2004b). Feasibility of generating a useful laser-induced breakdown spectroscopy plasma on rocks at high pressure: preliminary study for a Venus mission. *Spectrochim. Acta Part B* 59: 987–999.
- Bette, H., R. Noll, G. Müller, H.-W. Jansen, C. Nazikkol and H. Mittelstädt (2005). High-speed scanning LIBS at 1000 Hz with single pulse evaluation for the detection of inclusions in steel. *J. Laser Appl.* 17: 183–190.
- Bindhu, C.V., S.S. Harilal, M.S. Tillack, F. Najmabadi and A.C. Gaeris (2004). Energy absorption and propagation in laser created sparks. *Appl. Spectrosc.* 58: 719–726.
- Blacic, J.D., D.R. Pettit and D.A. Cremers (1992). Laser-induced breakdown spectroscopy for remote elemental analysis of planetary surfaces. *Proceedings of the International Symposium on Spectral Sensing Research*, Maui, HI.
- Bogaerts, A., Z. Chen, R. Gijbels and A. Vertes (2003). Laser ablation for analytical sampling: what can we learn from modeling? *Spectrochim. Acta Part B* 58: 1867–1893.
- Boyain-Goita, A.R., D.C.S. Beddows, B.C. Griffiths and H.H. Telle (2003). Single-pollen analysis by laser-induced breakdown spectroscopy and Raman microscopy. *Appl. Opt.* 42: 6119–6132.
- Brennetot, R., J.L. Lacour, E. Vors, A. Rivoallan, D. Vailhen and S. Maurice (2003). Mars analysis by laser-induced breakdown spectroscopy (MALIS): influence of Mars atmosphere on plasma emission and study of factors influencing plasma emission with the use of Doehlert designs. *Appl. Spectrosc.* 57: 744–752.
- Bulajic, D., M. Corsi, G. Cristoforetti, S. Legnaioli, V. Palleschi, A. Salvetti and E. Tognoni (2002). A procedure for correcting self-absorption in calibration free-laser induced breakdown spectroscopy. *Spectrochim. Acta Part B* 57: 339–353.
- Ciucci, A., M. Corsi, V. Palleschi, S. Rastelli, A. Salvetti and E. Tognoni (1999). New procedure for quantitative elemental analysis by laser-induced plasma spectroscopy. *Appl. Spectrosc.* 53: 960–964.
- Clark III, B.C. A.K. Baird, H.J. Rose Jr, P. Toulmin III, R.P. Christian, W.C. Kelliher, A.J. Castro, C.D. Rowe, K. Keil and G.R. Huss (1977). The Viking X ray fluorescence experiment: analytical methods and early results. *J. Geophys. Res.* 82: 4577–4594.
- Colao, F., R. Fantoni, V. Lazic and A. Paolini (2004a). LIBS application for analyses of Martian crust analogues: search for the optimal experimental parameters in air and CO<sub>2</sub> atmosphere. *Appl. Phys. A* 79: 143–152.
- Colao, F., R. Fantoni, V. Lazic, A. Paolini, G.G. Ori, L. Marinangeli and A. Baliva (2004b). Investigation of LIBS feasibility for *in situ* planetary exploration: an analysis on Martian rock analogues. *Planet. Space Sci.* 52: 117–123.
- Corsi, M., G. Cristoforetti, M. Hidalgo, D. Iriarte, S. Legnaioli, V. Palleschi, A. Salvetti and E. Tognoni (2003). Temporal and spatial evolution of a laser-induced plasma from a steel target. *Appl. Spectrosc.* 57: 715–721.
- Cremers, D.A., M.J. Ferris, C.Y. Han, J.D. Blacic and D.R. Pettit (1995). Remote elemental analysis using laser-induced breakdown spectroscopy. *Proc. SPIE* 2385: 28.
- Cristoforetti, G., S. Legnaioli, V. Palleschi, A. Salvetti and E. Tognoni (2004). Influence of ambient gas pressure on laser-induced breakdown spectroscopy technique in the parallel double-pulse configuration. *Spectrochim. Acta Part B* 59: 1907–1917.
- Dixon, P.D. and D.W. Hahn (2005). Feasibility of detection and identification of individual bioaerosols using laser-induced breakdown spectroscopy. *Anal. Chem.* 77: 631–638.
- Economou, T. (2001). Chemical analyses of Martian soil and rocks obtained by the Pathfinder alpha proton x-ray spectrometer. *Radiat. Phys. Chem.* 61: 191–197.
- Garcia, P.L., J.M. Vadillo and J.J. Laserna (2004). Real-time monitoring of high-temperature corrosion in stainless steels by open-path laser-induced plasma spectrometry. *Appl. Spectrosc.* 58: 1347–1352.
- Gautier, C., P. Fichet, D. Menut, J.-L. Lacour, D. L’Hermite and J. Dubessy (2005). Quantification of the intensity enhancements for the double-pulse laser-induced breakdown spectroscopy in the orthogonal beam geometry. *Spectrochim. Acta Part B* 60: 265–276.

- Golombek, M.P., R.A. Cook, T. Economou, W.M. Folkner, A.F.C. Haldemann, P.H. Kallemyer, J.M. Knudsen, R.M. Manning, H.J. Moore, T.J. Parker, R. Rieder, J.T. Schofield, P.H. Smith and R.M. Vaughan (1997). Overview of the Mars Pathfinder Mission and assessment of landing site predictions. *Science* 278: 1743–1748.
- Gornushkin, I.B., K. Ampsonah-Manager, B.W. Smith, N. Omenetto and J.D. Winefordner (2004a). Microchip laser-induced breakdown spectroscopy: a preliminary feasibility investigation. *Appl. Spectrosc.* 58: 762–769.
- Gornushkin, I.B., N. Omenetto, B.W. Smith and J.D. Winefordner (2004b). High-resolution two-grating spectrometer for dual wavelength spectral imaging. *Appl. Spectrosc.* 58: 1341–1346.
- Gornushkin, I.B., A.Ya. Kazakov, N. Omenetto, B.W. Smith and J.D. Winefordner (2005). Experimental variation of a radiative model of laser-induced plasma expanding into a vacuum. *Spectrochim. Acta Part B* 60: 215–230.
- Harris, R.D., D.A. Cremers, K. Benelli and C. Khoo (2004). Unpublished data.
- Hunten, D.M., L. Colin, T.M. Donahue and V.I. Moroz (Eds) (1983) *Venus*, The University of Arizona Press, Tucson: 45–68.
- Hybl, J.D., G.A. Lithgow and S.G. Buckley (2003). Laser-induced breakdown spectroscopy detection and classification of biological aerosols. *Appl. Spectrosc.* 57: 1207–1215.
- Knight, A.K., N.L. Scherbarth, D.A. Cremers and M.J. Ferris (2000). Characterization of laser-induced breakdown spectroscopy (LIBS) for application to space exploration. *Appl. Spectrosc.* 54: 331–340.
- Kraushaar, M., R. Noll and H.-U. Schmitz (2003). Slag analysis with laser-induced breakdown spectrometry. *Appl. Spectrosc.* 57: 1282–1287.
- Mateo, M.P., J.M. Vadillo and J.J. Laserna (2001). Irradiance-dependent depth profiling of layered materials using laser-induced plasma spectrometry. *J. Anal. At. Spectrom.* 16: 1317–1321.
- Mateo, M.P., L.M. Cabalín and J.J. Laserna (2003). Automated line-focused laser ablation for mapping of inclusions in stainless steel. *Appl. Spectrosc.* 57: 1461–1467.
- Morel, S., N. Leone, P. Adam and J. Amouroux (2003). Detection of bacteria by time-resolved laser-induced breakdown spectroscopy. *Appl. Opt.* 42: 6185–6191.
- Munson, C.A., F.C. De Lucia Jr, T. Piehler, K.L. McNesby and A.W. Mizolek (2005). Investigation of statistics strategies for improving the discriminating power of laser-induced breakdown spectroscopy for chemical and biological warfare agent simulants. *Spectrochim. Acta Part B* 60: 1217–1224.
- NASA (1969). Surveyor program results, NASA SP-184, Scientific and Technical Division, Office of Technology Utilization, NASA, Washington, DC.
- Noda, M., Y. Deguchi, S. Iwasaki and N. Yoshikawa (2002). Detection of carbon content in a high-temperature and high-pressure environment using laser-induced breakdown spectroscopy. *Spectrochim. Acta Part B* 57: 701–709.
- Radziemski, L.J., D.A. Cremers, K. Benelli, C. Khoo and R.D. Harris (2005). Use of the vacuum ultraviolet spectral region for laser-induced breakdown spectroscopy-based Martian geology and exploration. *Spectrochim. Acta Part B* 60: 237–248.
- Rieder, R., R. Gellert, J. Bruckner, G. Klingelhofer, G. Dreibus, A. Yen and S.W. Squyers (2003). The new Athena alpha particle X-ray spectrometer for the Mars Exploration Rovers. *J. Geophys. Res.* B108 (E12): 8066.
- Rodolfa, K.T. and D.A. Cremers (2004). Capabilities of surface composition analysis using a long LIBS spark. *Appl. Spectrosc.* 58: 367–375.
- Sagdeev, R.Z., G.G. Managadze, I.Yu. Shutyaev, K. Szego and P.P. Timofeev (1985). Methods of remote surface chemical analysis for asteroid missions. *Adv. Space Res.* 5: 111–120.
- Sallé, B., J.-L. Lacour, E. Vors, P. Fichet, S. Maurice, D.A. Cremers and R.C. Wiens (2004). Laser-induced breakdown spectroscopy for Mars surface analysis: capabilities at stand-off distances and detection of chlorine and sulfur elements. *Spectrochim. Acta Part B* 59: 1413–1422.

- Sallé, B., P. Mauchien, L.-J. Lacour, A. Maurice and R.C. Wiens (2005a). Laser-induced breakdown spectroscopy: a new method for stand-off quantitative analysis of samples on Mars. *Lunar and Planetary Science XXXVI*, abstract 1693.
- Sallé, B., D.A. Cremers, S. Maurice and R.C. Wiens (2005b). Laser-induced breakdown spectroscopy for space exploration applications: influence of the ambient pressure on the calibration curves prepared from soil and clay samples. *Spectrochim. Acta Part B* 60: 479–490.
- Samuels, A.C., F.C. DeLucia Jr, K.L. McNesby and A.W. Mizolek (2003). Laser-induced breakdown spectroscopy of bacterial spores, molds, pollens and protein: initial studies of discrimination potential. *Appl. Opt.* 42: 6205–6209.
- Semerok, A. and C. Dutouquet (2004). Ultrashort double pulse laser ablation of metals. *Thin Solid Films* 453–454: 501–505.
- Sharma, S.K., P.G. Lucey, M. Ghosh, H.W. Hubble and K.A. Horton (2003). Stand-off Raman spectroscopic detection of minerals on planetary surfaces. *Spectrochim. Acta Part A* 59: 2391–2407.
- Vadillo, J.M. and J.J. Laserna (2004). Laser-induced plasma spectrometry: truly a surface analytical tool. *Spectrochim. Acta Part B* 59: 147–161.
- Vertes, A., R. Gijbels and F. Adams (Eds) (1993). *Laser Ionization Mass Analysis*, John Wiley & Sons, Ltd, New York: 529–532.
- Whitehouse, A.I., J. Young, I.M. Botheroyd, S. Lawson, C.P. Evans and J. Wright (2001). Remote material analysis of nuclear power station steam generator tubes by laser-induced breakdown spectroscopy. *Spectrochim. Acta Part B* 56: 821–830.
- Wiens, R.C., R.E. Arvidson, D.A. Cremers, M.J. Ferris, J.D. Blacic and F.P. Seelos IV (2002). Combined remote mineralogical and elemental identification from rovers: field and laboratory tests using reflectance and laser-induced breakdown spectroscopy. *J. Geophys. Res. (Planets)* 107 (E11): FIDO 3-1–3-14.
- Yamamoto, K.Y., D.A. Cremers, L.E. Foster, M.P. Davies and R.D. Harris (2005). Laser-induced breakdown spectroscopy analysis of solids using a long-pulse (150 ns) Q-switched Nd:YAG laser. *Appl. Spectrosc.* 59: 1082–1097.
- Zel'dovich, Ya.B. and Yu.P. Raizer (2002). *Physics of Shock waves and High-temperature Hydrodynamic Phenomena*, eds W.D. Hayes and R.F. Probstein, Dover, Mineola, NY.

---

# 9 The Future of LIBS

---

## 9.1 INTRODUCTION

The laser spark as a curious phenomenon, a ‘graduate student parlor trick,’ and subject of off and on research, has been around since shortly after the invention of the laser in 1960. The name LIBS appeared first in 1981 in connection with serious interest at Los Alamos in the development of laser spark spectroscopy for a variety of applications. Thus LIBS as a true analytical technique, is about 25 years old. Complex technologies, like the laser, can take 30–40 years to mature into techniques that support a variety of applications (Radziemski, 2002). The increase in attention being given to LIBS is manifest in the increasing numbers of papers, patents and international groups working on it. Some have termed it a future ‘super star’ analytical technique (Winefordner *et al.*, 2004). What is needed to advance the technique? What is possible? Where is LIBS going as a technology?

## 9.2 EXPANDING THE UNDERSTANDING AND CAPABILITY OF THE LIBS PROCESS

Understanding the processes by which LIBS plasmas are created and develop leads to control, reproducibility, increased analytical capability and acceptance. Some of the improvements made over recent years are:

*Optics related:*

- Lens-to-surface distance control, especially useful for an eroding surface, and irregular surfaces encountered in the field, such as metal and plastic scrap sorting.
- Collimation of the laser beam so that it has a substantial Rayleigh range, reducing the effect of surface roughness.
- Fiber optics to carry the laser beam close to a target and retrieve the emitted light.
- Development of very compact, low f-number echelle spectrographs to provide complete spectral coverage in a small package.

In the future we may see aspheric optics for shaped focusing, fibers with higher damage thresholds, and newer hollow fibers.

*Laser and technique related:*

- Separation of the ablating process from the excitation process, that is double-pulse LIBS.
- Use of different laser pulse widths, primarily from femtosecond to hundreds of nanoseconds.
- Using UV wavelengths in bond-breaking.
- Use of high frequency, low energy per pulse lasers for an increased rate of spatial or depth sampling.

Several laser advances could affect LIBS. Microchip lasers with higher power could be used individually, or in arrays depending on the applications. Arrays of microlasers could lead to new surface scanning techniques, or generating plasmas only at their overlap. Field deployable, robust, inexpensive femtosecond lasers would facilitate LIBS use in cases where the avoidance of plasma shielding was an important factor. The use of femtosecond lasers for long range propagation without focusing optics is just now being investigated (Rohwetter *et al.*, 2005) and holds promise for applications at distances out to a kilometer. Also it has been observed that raising the temperature of a surface can increase the subsequent ablation rate. It would be interesting to use a laser pre-heating pulse plus the ablation pulse to see how far this can be pushed. For surfaces that absorb at  $10\mu\text{m}$ , a combination of CO<sub>2</sub> and Nd:YAG lasers may provide interesting results.

*Modeling the plasma process:*

- Modeling the expansion of the plasma into a vacuum has led to the observation that the plasma is not homogeneous in temperatures and densities at different points in its lifetime.

Most LIBS applications occur in air or in a controlled atmosphere. Sophisticated models that are designed to include plasma expansion into a variety of atmospheres at a range of pressures will be very helpful in advancing the understanding of the interaction of the plasma with the ambient environment. These will have to consider chemistry as well as shock physics, and may shed light on the origin of some observed matrix effects.

*Other:*

- Better understanding of the effect of the ambient atmosphere, its nature and pressure. For example, work in Mars type atmosphere shows that the plasma has a maximum in brightness in the 5–15 Torr range.
- Development of calibration-free techniques based on plasma properties.

### 9.3 WIDENING THE UNIVERSE OF LIBS APPLICATIONS

For many years the laser was a solution searching for a problem, because the laser was a discontinuous rather than a continuous innovation. It had to generate its own applications. This was the situation with LIBS in the 1970s and 1980s. Now there is no lack of ingenuity from both LIBS researchers and technologists in devising new applications for LIBS. From the planets, to carbon in terrestrial soils, to the depths of the oceans, there are thoughts about how its analytical capabilities might enhance and cast light on a variety of theories, from global climate change to planetary evolution. Here are some evolving capabilities that are opening the door to further innovations.

Surface scanning by LIBS is finding more and more applications. There are two ways to scan surfaces: point by point with a small spark formed by spherical optics or line by line with a spark formed by cylindrical optics. The use of the latter technique is growing, for surface scanning of steel, or examining surfaces for contamination. Going over the same area repeatedly adds a third dimension to the technique, and can result in profiling the depths of inclusions that reside on or very near to the surface. Because only micrometers of depth are ablated per shot at most, the technique at this point is still limited to the top fraction of a millimeter of a surface.

Combining LIBS with other techniques to interrogate molecules can bring different types of analytical information to bear synergistically and make this application practical. LIBS is inherently a way of linking spectral signatures from atoms to species concentrations. Although some progress has been made in correlating LIBS signals with molecules, the direct connection will always be tenuous. On the other hand, combining it with techniques that have molecular identification capability could provide added benefits. The most likely emerging combination, discussed in Chapter 8, is LIBS plus Raman (Sharma *et al.*, 2003; Thompson *et al.*, 2005). With a simple change of a component or two, a LIBS interrogation can turn into a Raman measurement. The combination of data will be powerful. Likewise LIBS and fluorescence has possibilities because of the prevalence of molecular fluorescence. Advanced data reduction and display techniques may be employed to provide more reliable signatures of potentially dangerous biological aerosols.

Remote environmental sensing with LIBS may get an assist from NASA's Mars exploration. Much effort is going into the development of remote LIBS and imaging for the ChemCam project to be mounted on the Mars Science Laboratory (2009) rover. A possible spin off is a miniature terrestrial rover, smaller than the Teramobile (Wille *et al.*, 2002), for detection of hazardous materials in spills, evaluation of potentially contaminated ground (such as New Orleans after Katrina), detection assignments connected with security of military personnel, the detection of improvised explosive devices, and homeland security applications.

A US Department of Energy report (US Department of Energy, 2004) cites the installation of LIBS at a full-scale commercial aluminum operation. The LIBS probe

provides *in-situ*, real-time measurement of melt constituents and temperature with a system costing between US\$65 000 and US\$250 000 depending on the application. The probe enables manufacturers to eliminate furnace idle time due to off-line measurements and reduces product rejections due to variations in melt composition.

New spectral regions can lead to useful signatures. Regions in which LIBS spectra have not yet been investigated in detail include the IR beyond 900 nm and the VUV below 100 nm, down to the x-ray region.

## 9.4 FACTORS THAT WILL SPEED THE COMMERCIALIZATION OF LIBS

The potential manufacturers of LIBS instruments are faced with the problem of many applications, with a few units needed for each. To keep costs down, easily assembled modules are called for. These may include separate modules for the laser and propagation optics, spectrometer/detector, light-capturing optics, electronics and sampling head. Some Micro-Electrical-Mechanical-Systems (MEMS) integration may be possible. Training a technical staff is an important issue. Laser safety is a must both during technique and apparatus development and in everyday use for applications. (See Appendix A for details.)

### 9.4.1 LIBS STANDARDIZATION AND QUANTIFICATION

For several years now, a group of six laboratories has been preparing a round-robin test of LIBS results on identical samples, using data taken separately at each location. The effort is led by M. Sabsabi, and the goal is to present evidence to the analytical community of the reproducibility and accuracy of LIBS results. This validation of the quantification that LIBS can provide is an important step in placing this technique on an equal footing with other, more developed methods. An early meeting of this group agreed that the following issues were important:

- ionic to atomic line intensity ratio measurements as sensitive measures of reproducibility;
- sampling approach and optimization;
- practical resolution measurements;
- scale of limit of detection;
- drift diagnostics.

### 9.4.2 ROUTINE LIBS USE IN INDUSTRIAL APPLICATIONS

Accepted use will stimulate the positive reputation of LIBS in the industrial community. Much recent research has resulted in concepts, designs, or prototypes for

instruments that could be developed. Some of these have been discussed in previous chapters of this book, such as the open-path LIBS analysis system developed by Palanco and Laserna (Palanco and Laserna, 2004) and described in Chapter 7, and the deployed nuclear reactor materials interrogation system of Whitehouse *et al.* (Whitehouse *et al.*, 2001), treated in Chapter 8.

A recent article by Noll *et al.* (Noll *et al.*, 2005) discusses the operating performance of inspection machines used in industrial settings. The particular application is called Laser Identification of Fittings and Tubes (LIFT). More than 1.5 million products have been inspected in the past 5 years to verify the materials used and prevent materials errors from occurring.

In 2001 the Industrial Materials Institute (IMI) of the National Research Council of Canada (NRC) installed a LIBS system at an industrial plant for continuously monitoring the composition of a liquid process stream. This sensor has flawlessly operated 24 h per day, 7 days per week, for over 2 years, at a rate of one measurement per minute, and has completely replaced previous analytical practice.

Based on promising early work on pharmaceutical analysis (St-Onge *et al.*, 2002), some in collaboration with Merck Frosst Canada & Co., Pharma Laser Inc. was founded in 1997 and is now offering a commercial LIBS instrument, which has been sold to pharmaceutical companies in Canada and the United States. This fully automated instrument has been designed to support pharmaceutical research and development and, more importantly, to be used on the production floor for the unattended at-line analysis of up to 26 tablet samples/analysis, a full sample set taking only on the order of 15 min to analyze. Currently the instrument is principally used in a research and development environment for formulation development and process optimization.

#### 9.4.3 AVAILABILITY OF COMPONENTS AND SYSTEMS

Potential LIBS users need to be aware of some commercial venues for obtaining LIBS apparatus or systems, and ways of obtaining assistance in deploying LIBS. Below we list some companies, addresses where given, web sites active in late 2005, and a short description of products, without endorsing any company's products. These are companies that are connected with LIBS more specifically. There are many others that supply lasers, timing electronics, and other components that one can find on the web or through buyers guides. A useful method for new users to find up to date information is to use web search engines with key words like 'LIBS apparatus' or 'LIBS applications.' Also a search of the web sites of LIBS conferences can reveal relevant company information, such as for the LIBS 2005 meeting ([www.ilt.fraunhofer.de/emslibs2005/](http://www.ilt.fraunhofer.de/emslibs2005/)):

*Acton Research Corporation*, 15 Discovery Way, Acton, MA 01720, USA; [acton-research.com](http://acton-research.com) (spectroscopic equipment).

*Andor Corp.* USA; [andor.com](http://andor.com) (CCD and ICCD detectors and Spectrographs).

*Applied Photonics Limited*, Unit 8, Carleton Business Park, Carleton New Road, Skipton, North Yorkshire BD23 2DE, UK; appliedphotonics.co.uk (LIBS applications and instrumentation).

*Catalina Scientific Corp.*, 1870 West Prince Road, Suite 21, Tucson, AZ 85705, USA; catalinasci.com (echelle spectrometers and software).

*Energy Research Corporation*, 2571-A Arthur Kill Rd, Staten Island, NY 10309, USA; er-co.com (LIBS applications for environmental analysis).

*Fraunhofer Institute for Laser Technology (ILT)*, Steinbachstr. 15, 52074 Aachen, Germany; ilt.fraunhofer.de (industrial applications of LIBS).

*Industrial Materials Institute (IMI)* of the National Research Council of Canada (NRC), Boucherville, Québec, CA; imi.cnrc-nrc.gc.ca (LIBS applications).

*Foster & Freeman USA Inc.*, 46030 Manekin Plaza, Suite 170, Sterling, VA 20166, USA; fosterfreeman.co.uk/products/evidence/ecco/ecco.html (forensic LIBS instrument).

*Kigre Inc.*, 100 Marshland Road, Hilton Head, SC 29926, USA; kigre.com (portable LIBS instrument).

*LLA Instruments GmbH*, Germany; lla.de (LIBS instruments).

*PharmaLaser*, 75 boul. De Mortagne, Boucherville, Québec, J4B 6Y4 CA; pharmalaser.com (pharmaceutical application).

*Ocean Optics Inc.*, 830 Douglas Ave., Dunedin, FL 34698, USA; oceanoptics.com (LIBS system, spectroscopy components).

*Rhea Corporation*, 4001 Kennett Pike, Suite 134-452, Wilmington, DE 19807, USA; rheacorp.com (LIBS hardware and software).

*Roper Scientific*, USA; roperscientific.com (detectors such as CCD and ICCD).

*Solid Optics Inc.*, 365 Valle del Sol Road, Los Alamos, NM 87544-3563, USA; solidoptics.com (LIBS support).

*StellarNet Inc.*, 14390 Carlson Circle, Tampa, FL 33626, USA; stellarnet-inc.com (LIBS software).

## 9.5 CONCLUSION

So where is LIBS in the nonlinear progression from science to mature technology? A good idea has been recognized and this evolving technique is being advanced in more and more laboratories throughout the world. Real-world applications expose difficult technical problems such as those associated with analytical issues (sample inhomogeneity, calibration, precision, accuracy, interferences), instrumental ruggedness, sample access, and ease of data capture and analysis. Components are readily available, and some complete instruments are being sold commercially. There the issues of cost/benefit ratios, capability against competing technologies, and reliability come to the fore. To parallel the development of the laser, one can imagine smaller, lighter instruments, each dedicated to a limited set of problems. Newer optical components could simplify that part of the system. Compact, inexpensive diode lasers may reduce the cost and increase the flexibility of approaches. Figure 9.1 shows what some LIBS instruments might look like in the future.

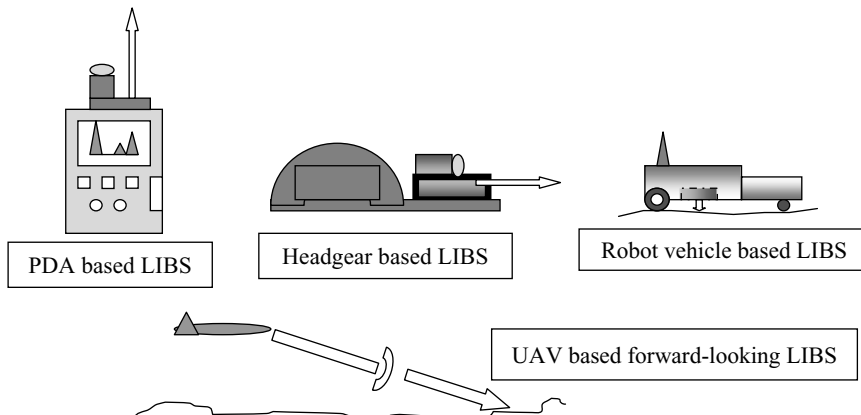


**Figure 9.1** Different future embodiments of LIBS technology. How many more can we imagine?

## REFERENCES

- Noll, R., I. Mönch, O. Klein and A. Lamott (2005). Concept and operating performance of inspection machines for industrial use based on laser-induced breakdown spectroscopy measurements. *Spectrochim. Acta Part B* 60: 1070–1075.
- Palanco, S. and J. Laserna (2004). Remote sensing instrument for solid samples based on open-path atomic emission spectrometry. *Rev. Sci. Instrum.* 75: 2068–2074.
- Radziemski, L.J. (2002). From LASER to LIBS, the path of technology development. *Spectrochim. Acta Part B* 57: 1109–1114.
- Rohwetter, Ph., K. Stelmaszczyk, L. Wöste, R. Ackermann, G. Méjean, E. Salmon, J. Kasparian, J. Yu and J.-P. Wolf (2005). Filament-induced remote surface ablation for long range laser-induced breakdown spectroscopy operation. *Spectrochim. Acta Part B* 60: 1025–1033.
- Sharma, S.K., P.G. Lucey, M. Ghosh, H.W. Hubble and K.A. Horton (2003). Stand-off Raman spectroscopic detection of minerals on planetary surfaces. *Spectrochim. Acta Part A* 59: 2391–2407.
- St-Onge, L., E. Kwong, M. Sabsabi and E.B. Vadas (2002). Quantitative analysis of pharmaceutical products by laser-induced breakdown spectroscopy. *Spectrochim. Acta Part B* 57: 1131–1140.
- Thompson, J., R. Wiens, S. Sharma, P. Lucey and A. Misra (2005). Combined remote LIBS and Raman spectroscopy measurements. *Lunar and Planetary Science Conference XXXVI*, submission 1517.
- US Department of Energy (2004). In-situ, real-time measurement of melt constituents. CPS#980, Office of Energy Efficiency and Renewable Energy.
- Whitehouse, A.I., J. Young, I.M. Botheroyd, S. Lawson, C.P. Evans and J. Wright (2001). Remote material analysis of nuclear power station steam generator tubes by laser-induced breakdown spectroscopy. *Spectrochim. Acta Part B* 56: 821–830.
- Wille, H., M. Rodriguez, J. Kasparian, D. Mondelain, J. Yu, A. Mysyrowicz, R. Sauerbrey, J.P. Wolf and L. Wöste (2002). Teramobile: a mobile femtosecond-terawatt laser and detection system. *Eur. Phys. J. AP* 20: 183–190.
- Winefordner, J.D., I.B. Gornushkin, T. Correll, E. Gibb, B.W. Smith and N. Omenetto (2004). Comparing several atomic spectrometric methods to the super stars: special emphasis on laser induced breakdown spectrometry, LIBS, a future super star. *J. Anal. At. Spectrom.* 19: 1061–1083.

---

## APPENDICES

---

---

# A Safety Considerations in LIBS

---

## A.1 SAFETY PLANS

The components used in a LIBS measurement system are typically commercially designed and are generally safe if used properly. The laboratory represents a controlled environment in which experimental conditions can be controlled and safety measures more easily implemented than in the field. Because LIBS is being deployed in the field, under conditions and in locations and with materials that cannot be anticipated here, each situation must be evaluated by those involved in the experiment or application. During the many years we have worked with LIBS the working environments have ranged from a coal gasification system, the Mojave Desert in summer with  $\sim 43^{\circ}\text{C}$  temperatures in the shade, Yucca Mountain in tunneling operations, procedures, and steel making operation. Each location and LIBS measurement had unique safety requirements. To adequately take into account these operating hazards, it is recommended that a safety plan, standard operating procedure, or hazard control plan be prepared that is reviewed by personnel trained in each of the hazards associated with the operation. Examples include, for example, the laser safety officer, occupational health professional, and industrial safety officer. Often it will be advisable that any operations involving chemicals be reviewed by a chemist who may point out hazards not foreseen by the other professionals. Here we present a brief overview of some more common safety related issues that must be considered and in many cases addressed (Table A.1).

## A.2 LASER SAFETY

Commercial laser systems are well developed, reliable and safe instruments that must meet certain government regulations. The voltages and currents used in many lasers are hazardous and potentially lethal. Personnel are protected from high voltages and electric shock by interlocks and grounded metal shielding. Interlocks are sometimes defeated so that maintenance and alignment operations can be carried out and extreme care must be taken during these times to assure safe operations. Lasers used for LIBS measurements are generally Class IV with the laser light posing an ocular and skin hazard. Because LIBS is increasingly being used in the field and

**Table A.1** Some possible hazards associated with LIBS experiments

Source	Hazard	Information sources
Laser light	Ocular and/or skin damage	ANSI Z136.1 (2000); institution laser safety officer; Laser Institute of America; laser operator's manual (ANSI, 2000)
High voltages (e.g. laser power supplies)	Potentially lethal voltages	Laser operator's manual; institution electrical safety officer; consult with laser manufacturer prior to work on electrical system; arrange work by manufacturer technician skilled in the system (NFPA, 2005)
Handling and storage of materials used with LIBS	Toxic, corrosive, may interact with other materials	MSDS (material safety data sheets, available from the web)
Laser produced aerosols	Inhalation hazard (Be, As, Cr compounds, Tl, silica dusts, etc.)	MSDS; institution industrial hygienist; maximum permissible exposure limits listed by OSHA and ACGIH (ACGIH, 2005a,b)
Laser produced ignition	Explosive mixtures (e.g. H <sub>2</sub> and O <sub>2</sub> ; aerosolized solvents, liquid solvents)	MSDS; institution safety officer; chemical experts; (Davletshina and Cheremisinoff, 1998)

for remote open path analysis over distances of several meters, special care must be taken in designing and conducting LIBS measurements. Common sense and safety regulations such as ANSI Z136.1 (ANSI, 2000) provide accepted rules and regulations for safe laser use and these should be consulted in all cases. In addition, it should be noted that eye protection will depend on the laser wavelength. For example, eye protection suitable for 1064 nm will not be adequate at the harmonic wavelengths such as 532 nm. The Laser Institute of America in Orlando, Florida, has information regarding laser safety, safety training, and materials and devices to minimize exposure to laser radiation.

### A.3 GENERATION OF AEROSOLS

The laser pulse directed at a solid or liquid can generate particulate matter, which although representing a small mass per laser pulse, may accumulate after many shots to toxic levels. For example, the action of a single 100 mJ laser pulse on beryllium metals can liberate 10 ng of material. After 1 min of sparking a sample (10 Hz), very possible during a LIBS measurement or even setting up a LIBS experiment, the amount of beryllium aerosolized can be on the order of 6 µg. If it is recognized that the maximum permissible exposure to airborne beryllium particles is 2 µg/m<sup>3</sup> (8 h work day), it is clear that a situation exists in which regulated safe levels of beryllium may be readily exceeded. The maximum permissible level for beryllium

over a 30 min exposure period is  $25 \mu\text{g}/\text{m}^3$ . Beryllium, although recognized as highly toxic under these conditions, is more or less toxic than other materials that may be used in LIBS measurements. Therefore, it is clear that extreme caution must be used when designing and performing LIBS measurements.

#### A.4 LASER PULSE INDUCED IGNITION

The laser pulses used for LIBS generate a hot plasma that typically contains a small amount of energy that does not represent a strong ignition source for most flammable materials. The amount of heating will be minimal except for high repetition rate lasers (e.g. acousto-optically Q-switched laser at several kHz producing several tens of watts). Most materials when irradiated by these laser pulses will be visually damaged but the damage will generally be minimal. It is obvious in certain operations that the LIBS should not be deployed under usual working conditions. An example is the stand-off analysis of an exposed surface in an underground mine in which flammable gases (e.g. methane) may be present. Another example is the dust laden atmosphere within a grain elevator. These applications must be reviewed critically as the occurrence of an explosion could lead to catastrophic results. It may not always be easy to identify such potentially hazardous situations. For example, cellulose acetate filters when irradiated by a laser beam as shown in Figures 1.5 and 3.9 are not significantly damaged by the action of the laser pulse. Only a small portion of the filter surface is ablated by the laser pulse. The same filter, however, if struck by the laser pulse on edge can be made instantly flammable, with the results resembling flash paper.

#### REFERENCES

- ANSI (2000). ANSI Z136.1 (2000) Standard: Safe Use of Lasers, American National Standards Institute, Washington, DC.
- ACGIH (2005a). Guide to Occupational Exposure Values, 2005, ACGIH, Cincinnati, OH.
- ACGIH (2005b). 2005 TLVs and BEIs, ACGIH, Cincinnati, OH.
- Davletshina, T.A. and N.P. Cheremisinoff (1998). *Fire and Explosion Hazards Handbook of Industrial Chemicals*, William Andrew Publishing/Noyes, New York, NY.
- NFPA (2005). National Electrical Code 2005, Edition (NFPA 70), National Fire Protection Association, Quincy, MA.

## B Recommended Methods for Commencing LIBS Research on a Variety of Samples

**Table B.1** Recommended methods for commencing LIBS research on a variety of samples

LIBS applications	Rec. laser and $\lambda$	Parameters							
		Laser energy (mJ)	Pulse length (ns)	Rep. rate (Hz)	Focusing; focal lengths (cm)	Line focus	Time gating	Stabilize LTSD	Spectrometer
Solid sampling									
Surface analysis of metals (Bette <i>et al.</i> , 2005)	Nd:YAG 1064 or 532 nm	50–700	5–10	10	5–50	useful for surface distribution of elements	usually	no	echelle or grating VUV through IR
Art history (Burgo <i>et al.</i> , 2001)	Nd:YAG 355 nm	2	3–10	single shot	5	no	yes	no	ICCD, IPDA, PMT
Nuclear reactor materials (Whitehouse <i>et al.</i> , 2001)	Nd:YAG 1064 nm	50 mJ reduced to 5 mJ at fiber	6	20	long fiber optic with telescope	no	yes	yes	grating UV through IR
Soils and rocks (Harris <i>et al.</i> , 2004)	Nd:YAG 1064 or 532 nm	20–150	5–10	10	10–25	useful for surface distribution of elements	usually	could be useful to counter erosion	echelle or grating VUV through IR
Liquid sampling (Cremers <i>et al.</i> , 1984; Pichahchy <i>et al.</i> , 1997)	Nd:YAG 1064 or 532 nm	20–150	5–10	10	20–50 closer risks splashing	no	usually	no	intensified CCD, linear array or photomultipliers
Gas sampling, aerosols and bioaerosols (Sturm and Noll, 2003; Dixon and Hahn, 2005; Hohreiter and Hahn, 2005)	Nd:YAG 1064 or 532 nm	50–200	5–10	10	5–50 mm	no	usually	no	ICCD

**Table B.1** (Continued)

LIBS applications	Analysis software	System cost (US\$)	Weight (kg)	Assembly time after parts in hand (months)	Parameters		
					Single or double pulse	Calibration procedure	Qual. or quant. analysis
Solid sampling Surface analysis of metals (Bette <i>et al.</i> , 2005)	usually comes with CCD detector	50–100	68	2	single	calibration curves	ambient air or other gas
Art history (Burgio <i>et al.</i> , 2001)	usually comes with CCD detector	50–100	68	2	single	qual.	ambient air or other gas
Nuclear reactor materials (Whitehouse <i>et al.</i> , 2001)	usually comes with detector	400	91	12	single	calibration curves	ambient air open
Soils and rocks (Harris <i>et al.</i> , 2004)	usually comes with CCD detector	50–100	68	2	single	calibration curves	ambient air or other gas
Liquid sampling (Cremers <i>et al.</i> , 1984; Fichahchy <i>et al.</i> , 1997)	usually comes with CCD detector	50–100	68	2	double	calibration curves	open to air, but liquid confined to flow tube
Gas sampling, aerosols and bioaerosols (Sturm and Noll, 2003; Dixon and Hahn, 2005; Hohreiter and Hahn, 2005)	usually comes with CCD detector	50–100	68	2	single	calibration curves	ambient air or other gas

qual., qualitative; quant., quantitative.

**REFERENCES**

- Bette, H., R. Noll, G. Müller, H.-W. Jansen, C. Nazikkol and H. Mittelstädt (2005). High-speed scanning LIBS at 1000 Hz with single pulse evaluation for the detection of inclusions in steel. *J. Laser Appl.* 17: 183–190.
- Burgio, L., K. Melessanaki, M. Doulgeridis, R.J.H. Clark and D. Anglos (2001). Pigment identification in paintings employing laser induced breakdown spectroscopy and Raman microscopy. *Spectrochim. Acta Part B* 56: 905–913.
- Cremers, D.A., L.J. Radziemski and T.R. Loree (1984). Spectrochemical analysis of liquids using the laser spark. *Appl. Spectrosc.* 38: 721–726.
- Dixon, P.B. and D.W. Hahn (2005). Feasibility of detection and identification of individual bioaerosols using laser-induced breakdown spectroscopy. *Anal. Chem.* 77: 631–638.
- Harris, R.D., D.A. Cremers, M.H. Ebinger and B.K. Bluhm (2004). Determination of nitrogen in sand using laser-induced breakdown spectroscopy. *Appl. Spectrosc.* 58: 770–775.
- Hohreiter, H. and D.W. Hahn (2005). Calibration effects for laser-induced breakdown spectroscopy of gaseous sample streams: analyte response of gas-phase species versus solid-phase species. *Anal. Chem.* 77: 1118–1124.
- Pichahchy, A.E., D.A. Cremers and M.J. Ferris (1997). Detection of metals underwater using laser-induced breakdown spectroscopy. *Spectrochim. Acta Part B* 52: 25–39.
- Sturm, V. and R. Noll (2003). Laser-induced breakdown spectroscopy of gas mixtures of air, CO<sub>2</sub>, N<sub>2</sub>, and C<sub>3</sub>H<sub>8</sub> for simultaneous measurement of C, H, O, and N. *Appl. Opt.* 42: 6221–6225.
- Whitehouse, A.I., J. Young, I.M. Botheroyd, S. Lawson, C.P. Evans and J. Wright (2001). Remote material analysis of nuclear power station steam generator tubes by laser-induced breakdown spectroscopy. *Spectrochim. Acta Part B* 56: 821–830.

---

## C Representative LIBS Detection Limits

---

### C.1 DETECTION LIMITS FROM THE LITERATURE

The LOD values listed in Tables C.1–C.3 are from the literature. These values refer to a specific matrix and some additional information that may be of interest is also listed. The literature reference is given along with the wavelength(s) used for detection with the wavelength values taken directly from the source. The original literature source should be consulted to determine the particular experimental parameters under which each LOD was determined and for additional information. The detection limits for an element in a certain matrix determined by different laboratories may be significantly different due to the use of different measurement parameters.

**Table C.1** Representative detection limits for elements in selected matrices: gases and liquids

Element	Gas/aerosol in gas (ppm unless other unit specified)	Liquid (ppm unless other unit specified)
	LOD (matrix) [ref.] $\lambda$ in nm	LOD (matrix) [ref.] $\lambda$ in nm
Ag		0.43 (water) [Schmidt and Goode, 2002] 328.1
Al		20 (water) [Cremers <i>et al.</i> , 1984] 396.15 5.2 (droplet) [Archontaki and Crouch, 1988] 396.15
As	0.5 (aerosol) [Radziemski <i>et al.</i> , 1983] 228.8 600 $\mu\text{g}/\text{acm}^a$ (gas effluent) [Zhang <i>et al.</i> , 1999] 278.02 400 $\mu\text{g}/\text{dscm}^b$ (gas effluent) [Buckley <i>et al.</i> , 2000] 286.0 400 $\mu\text{g}/\text{m}^3$ (aerosol) [Fisher <i>et al.</i> , 2001] 228.81	5 (liq. evp. graphite <sup>c</sup> ) [Van der Wal <i>et al.</i> , 1999] 274.5, 278.02, 286.04 1200 (water) [Cremers <i>et al.</i> , 1984] 249.68/249.77 80 (water using RSP) [Cremers <i>et al.</i> , 1984] 249.68/249.77 0.054 (electrodep., CO <sub>2</sub> laser <sup>c</sup> ) [Pardede <i>et al.</i> , 2001] 249.7
B		6.8 (water) [Knopp <i>et al.</i> , 1996] 455.4 4.9 (Ba <sup>2+</sup> , water) [Bundschuh <i>et al.</i> , 2001] 455.4 0.007 (water) [Lo and Cheung, 2002] 455.4 0.13 (water) [Schmidt and Goode, 2002] 493.4 12 and 66 (ice/10% soil) [Atp <i>et al.</i> , 2004] 455.5 10 (water) [Cremers <i>et al.</i> , 1984] 313.04/313.11
Be	0.0006 (aerosol) [Radziemski <i>et al.</i> , 1983] 313.1 <0.1 $\mu\text{g}/\text{acm}$ (gas effluent) [Zhang <i>et al.</i> , 1999] 313.04 1 $\mu\text{g}/\text{acm}$ (gas effluent) [Zhang <i>et al.</i> , 1999] 234.8 2 $\mu\text{g}/\text{dscm}$ (gas effluent) [Buckley <i>et al.</i> , 2000] 313.0 40 $\mu\text{g}/\text{m}^3$ (aerosol) [Fisher <i>et al.</i> , 2001] 234.86 10 $\mu\text{g}/\text{m}^3$ (aerosol) [Fisher <i>et al.</i> , 2001] 313.1	
Ca	2.9 ng (particle in COD <sup>c</sup> ) [Cremers <i>et al.</i> , 1985] 393.37 ~3 fg (N <sub>2</sub> gas) [Hahn and Lunden, 2000] 393.66, 396.85	0.8 (water) [Cremers <i>et al.</i> , 1984] 393.37 0.4 (droplet) [Archontaki and Crouch, 1988] 393.37

	0.5 fg (particle in air) [Carranza <i>et al.</i> , 2001] 393.37, 396.85 30 fg (aerosol) [Hybl <i>et al.</i> , 2003] 422.67	0.13 (water) [Knopp <i>et al.</i> , 1996] 422.7 0.01 (liq. evp. graphite <sup>c</sup> ) [Van der Wal <i>et al.</i> , 1999] 393.37, 396.85
Cd	0.019 (aerosol in air) [Essien <i>et al.</i> , 1988] 228.8 39 µg/acm (gas effluent) [Zhang <i>et al.</i> , 1999] 228.8 120 µg/acm (gas effluent) [Zhang <i>et al.</i> , 1999] 326.11 5 µg/dscm (gas effluent) [Buckley <i>et al.</i> , 2000] 228.8 60 µg/m <sup>3</sup> (aerosol) [Fisher <i>et al.</i> , 2001] 226.50 120 µg/m <sup>3</sup> (aerosol) [Fisher <i>et al.</i> , 2001] 228.80	500 (water) [Knopp <i>et al.</i> , 1996] 361.2 0.1 (liq. evp. graphite <sup>c</sup> ) [Van der Wal <i>et al.</i> , 1999] 226.5, 228.5 1 (liq. evp. graphite <sup>c</sup> ) [Van der Wal <i>et al.</i> , 1999] 214.44 0.21 (water) [Schmidt and Goode, 2002] 361.1
Cl	8 (freon in air) [Cremers and Radziemski, 1983] 837.6 0.16 (air) [Haisch <i>et al.</i> , 1996] 1435.8 90 (air) [Dudragne <i>et al.</i> , 1998] 837.594	>0.1 (liq. evp. graphite <sup>c</sup> ) [Van der Wal <i>et al.</i> , 1999] 238–242, 340–348, 349–353
Co	3.5 ng (particle in COD <sup>c</sup> ) [Cremers <i>et al.</i> , 1985] 425.44	0.1 (water) [Arca <i>et al.</i> , 1997] 283.563
Cr	6 µg/acm (gas effluent) [Zhang <i>et al.</i> , 1999] 425.44 400 ng/dscm air [Martin and Cheng, 2000] 425.5 5 µg/dscm (gas effluent) [Buckley <i>et al.</i> , 2000] 283.6 30 µg/m <sup>3</sup> (aerosol) [Fisher <i>et al.</i> , 2001] 425.44 40 µg/m <sup>3</sup> (aerosol) [Fisher <i>et al.</i> , 2001] 428.97	0.1 (liq. evp. graphite <sup>c</sup> ) [Van der Wal <i>et al.</i> , 1999] 266–268, 274–279, 283–288 200 (water) [Samek <i>et al.</i> , 2000] 520.45 310 (under water, purge gas) [Beddoes <i>et al.</i> , 2002] 427.28 0.13 (water) [Schmidt and Goode, 2002] 520.9 0.4 (water) [Yueh <i>et al.</i> , 2002] 425.4 1 (water) [Cremers <i>et al.</i> , 1984] 852.11

Table C.1 (Continued)

Element	Gas/aerosol in gas (ppm unless other unit specified) LOD (matrix) [ref.] $\lambda$ in nm	Liquid (ppm unless other unit specified) LOD (matrix) [ref.] $\lambda$ in nm
Cu	0.87 ng (particle in COD <sup>e</sup> ) [Cremers <i>et al.</i> , 1985] 324.75 5 (water) [Sanek <i>et al.</i> , 2000] 324.75	0.01 (liq. evp. graphite <sup>c</sup> ) [Van der Wal <i>et al.</i> , 1999] 324.75, 327.4
	0.017 (electrodep., CO <sub>2</sub> laser <sup>d</sup> ) [Pardedé <i>et al.</i> , 2001] 327.4	
	0.0042 (water) [Schmidt and Goode, 2002] 510.6	
	0.0095 (water) [Schmidt and Goode, 2002] 324.7	
Eu	5.0 (Eu <sup>3+</sup> , water) [Bundschuh <i>et al.</i> , 2001] 459.4, 462.7, 466.1 0.03 (Eu <sub>2</sub> O <sub>3</sub> , water) [Bundschuh <i>et al.</i> , 2001] 459.4, 462.7, 466.1	
	3.3 × 10 <sup>-5</sup> mol/l (Eu <sup>+3</sup> , water) [Yun <i>et al.</i> , 2001] 459.4, 462.7, 466.1	
	2.0 × 10 <sup>-7</sup> mol/l (Eu <sub>2</sub> O <sub>3</sub> , water) [Yun <i>et al.</i> , 2001] 459.4, 462.7, 466.1	
F	38 (freon in air) [Cremers and Radziemski, 1983] 685.6 20 (air) [Dudragne <i>et al.</i> , 1998] 685.64 40 (C <sub>2</sub> F <sub>5</sub> H in air) [Williamson <i>et al.</i> , 1998] 685.6	0.01 (liq. evp. graphite <sup>c</sup> ) [Van der Wal <i>et al.</i> , 1999] 238–241, 260–263, 273–276 0.05 (electrodep., CO <sub>2</sub> laser <sup>d</sup> ) [Pardedé <i>et al.</i> , 2001] 358.1
Fe		
Hg	0.5 (aerosol) [Radziemski <i>et al.</i> , 1983] 253.6 0.005 (vapor) [Lazzari <i>et al.</i> , 1994] 253.65 680 µg/acm (gas effluent) [Zhang <i>et al.</i> , 1999] 253.65 80 µg/dscm (gas effluent) [Buckley <i>et al.</i> , 2000] 253.7 230 µg/m <sup>3</sup> (aerosol) [Fisher <i>et al.</i> , 2001] 253.65	10 (liq. evp. graphite <sup>c</sup> ) [Van der Wal <i>et al.</i> , 1999] 253.65 2.0 (water) [Schmidt and Goode, 2002] 435.8
K		1.2 (water) [Cremers <i>et al.</i> , 1984] 766.49 4 (water) [Sanek <i>et al.</i> , 2000] 766.49 1.2 (0.5 pg) (water) [Huang <i>et al.</i> , 2002] 766
Li	1.5 ng (particle in COD <sup>e</sup> ) [Cremers <i>et al.</i> , 1985] 670.78/670.79	0.006 (water) [Cremers <i>et al.</i> , 1984] 670.78 0.3 (droplet) [Archontaki and Crouch, 1988] 670.78 0.013 (water) [Knopp <i>et al.</i> , 1996] 670.8

Mg	$\sim 3 \text{ fg}$ ( $\text{N}_2$ gas) [Hahn and Lunder, 2000] 279.55, 280.2, 285.21 1.2 fg (particle in air) [Caranza <i>et al.</i> , 2001] 279.55, 280.27, 285.21 20 fg (aerosol) [Hybl <i>et al.</i> , 2003] 285.2	0.009 (water) [Samek <i>et al.</i> , 2000] 670.774 0.05 (electrodep., $\text{CO}_2$ laser <sup>c</sup> ) [Paredes <i>et al.</i> , 2001] 670.7 6 and 3 (ice/10% soil) [App <i>et al.</i> , 2004] 670.8
Mn		100 (water) [Cremers <i>et al.</i> , 1984] 279.55 1.9 (droplet) [Archontaki and Crouch, 1988] 279.55 0.01 (liq. evp. graphite <sup>c</sup> ) [Van der Wal <i>et al.</i> , 1999] 279.55, 280.27 3 (water) [Samek <i>et al.</i> , 2000] 285.21 1 (water) [Charifi and Harith, 2002] 279.55 1.2 (water, mixed) [Charifi and Harith, 2002] 279.55 0.1 (water) [Yueh <i>et al.</i> , 2002] 279.55 7.2 (droplet) [Archontaki and Crouch, 1988] 257.61 10 (water) [Samek <i>et al.</i> , 2000] 403.08 32.5 (water) [Beddoes <i>et al.</i> , 2002] 403.08 0.7 (under water, purge gas) [Yueh <i>et al.</i> , 2002] 403.076 1.5 and 101 (ice/10% soil) [App <i>et al.</i> , 2004] 403.0403.3/403.4
Na	0.006 (aerosol) [Radziemski <i>et al.</i> , 1983] 588.9 5.2 mg (particle in COD <sup>c</sup> ) [Cremers <i>et al.</i> , 1985] 589.00 3.3 mg (particle in air) [Caranza <i>et al.</i> , 2001] 589.00, 589.59 100 fg (aerosol) [Hybl <i>et al.</i> , 2003] 589.0	0.014 (water) [Cremers <i>et al.</i> , 1984] 589.00 2.2 (droplet) [Archontaki and Crouch, 1988] 589.00 0.0075 (water) [Knopp <i>et al.</i> , 1996] 589.3 0.08 (water) [Samek <i>et al.</i> , 2000] 588.99 2 (water ice, $\text{CO}_2$ laser) [Caceres <i>et al.</i> , 2001] 588.99 0.63 (0.3 pg) water) [Huang <i>et al.</i> , 2002] 589 2 (water) [Charifi and Harith, 2002] 588.99 2.5 (water, mixed) [Charifi and Harith, 2002] 588.99 0.0004 (water) [Lo and Cheung, 2002] 589.0 1 (water) [Huang and Harith, 2004] 589
Ni		36.4 (water, 1064 nm) [Berman and Wolf, 1998] 341.48, 352.45, 361.94 18 (water, 355 nm) [Berman and Wolf, 1998] 341.48, 352.45, 361.94 0.01 (liq. evp. graphite <sup>c</sup> ) [Van der Wal <i>et al.</i> , 1999] 221–223, 229–231 0.31 (water) [Schmidt and Goode, 2002] 353.0
P	1.2 (aerosol) [Radziemski <i>et al.</i> , 1983] 253.3	

**Table C.1** (Continued)

Element	Gas/aerosol in gas (ppm unless other unit specified) LOD (matrix) [ref.] $\lambda$ in nm	Liquid (ppm unless other unit specified) LOD (matrix) [ref.] $\lambda$ in nm
Pb	0.21 (aerosol in air) [Essien <i>et al.</i> , 1988] 405.8 1.55 $\mu\text{g}/\text{m}^3$ (aerosol in air) [Neuhäuser <i>et al.</i> , 1997] 405.8 68 $\mu\text{g}/\text{acm}$ (gas effluent) [Zhang <i>et al.</i> , 1999] 405.78 20 $\mu\text{g}/\text{dscm}$ (gas effluent) [Buckley <i>et al.</i> , 2000] 220.4 190 $\mu\text{g}/\text{m}^3$ (aerosol) [Fisher <i>et al.</i> , 2001] 405.78	12.5 (water) [Knopp <i>et al.</i> , 1996] 405.8 2 (liq. evp. graphite <sup>c</sup> ) [Van der Wal <i>et al.</i> , 1999] 261.37, 261.42, 280.2, 283.31 10 (liq. evp. graphite <sup>c</sup> ) [Van der Wal <i>et al.</i> , 1999] 405.78, 406.21 40 (water) [Samek <i>et al.</i> , 2000] 405.78 13.1 ( $\text{Pb}^{2+}$ , water) [Bundschuh <i>et al.</i> , 2001] 405.7 0.025 (electrodep., $\text{CO}_2$ laser <sup>d</sup> ) [Pardede <i>et al.</i> , 2001] 405.7 0.3 (water) [Lo and Cheung, 2002] 405.8 1.1 (water) [Schmidt and Goode, 2002] 405.8 8 (water) [Yueh <i>et al.</i> , 2002] 346.046 0.2 (water) [Cremers <i>et al.</i> , 1984] 780.03
Re		
Rb		
S	1500 (air) [Dudragne <i>et al.</i> , 1998] 921.29	0.01 (liq. evp. graphite <sup>c</sup> ) [Van der Wal <i>et al.</i> , 1999] 288.16, 251-253
Sb	120 $\mu\text{g}/\text{acm}$ [Zhang <i>et al.</i> , 1999] 259.81	455 (under water, purge gas) [Beddoes <i>et al.</i> , 2002] 288.16
Si		1 and 2 (ice/10% soil) [Atp <i>et al.</i> , 2004] 460.7
Sr		25 (water) [Samek <i>et al.</i> , 2000] 429.71
Tc		0.1 (liq. evp. graphite <sup>c</sup> ) [Van der Wal <i>et al.</i> , 1999] 323.4, 334-339
Ti		111 and 520 (ice/10% soil) [Atp <i>et al.</i> , 2004] 398.2
U		100 (4 M nitric acid/aqueous) [Wachter and Cremers, 1987] 409.02
Zn	0.24 (aerosol in air) [Essien <i>et al.</i> , 1988] 481.1	450 (water) [Samek <i>et al.</i> , 2000] 409.02 11 (liq. evp. graphite <sup>c</sup> ) [Van der Wal <i>et al.</i> , 1999] 330.26, 330.29, 334.5, 334.56 0.85 (water) [Schmidt and Goode, 2002] 472.2

RSP, repetitive spark pair.  
<sup>a</sup> acm, actual cubic meters.

<sup>b</sup> dscm, dry standard cubic meters.  
<sup>c</sup> Liquid evaporated on graphite, dried, and then analyzed using LIBS.

<sup>d</sup> Element electro-deposited and then analyzed on electrode using LIBS and a  $\text{CO}_2$  laser.  
<sup>e</sup> Particles ablated from element-containing compound into COD (continuous optical discharge).

**Table C.2** Representative detection limits for elements in selected matrices: surfaces and solids

Element	Surface (ng/cm <sup>2</sup> unless other unit specified) LOD (matrix) [ref.] $\lambda$ in nm	Solid (ppm unless other unit specified) LOD (matrix) [ref.] $\lambda$ in nm
Ag	(liq. on filter) [Appendix C.2]	200 (UO <sub>2</sub> pellet) [Fichet <i>et al.</i> , 1999] 328.0683 60 (PuO <sub>2</sub> pellet) [Fichet <i>et al.</i> , 1999] 328.0683
Al	(liq. on filter) [Appendix C.2]	130 (Al <sub>2</sub> O <sub>3</sub> in Fe ore) [Grant <i>et al.</i> , 1991] 396.2 54, 30 (glass, air 1 and 5 Torr) [Kurniawan <i>et al.</i> , 1995] 396.1 16 (zinc alloy) [St-Onge <i>et al.</i> , 1997] 308.22 9 (zinc alloy) [St-Onge <i>et al.</i> , 1997] 309.27 1–10 (aluminum, echelle) [Bauer <i>et al.</i> , 1998] not found 1 (plant material) [Sun <i>et al.</i> , 1999] 308.2 200 (UO <sub>2</sub> pellet) [Fichet <i>et al.</i> , 1999] 396.1527 60 (lignite) [Wallis <i>et al.</i> , 2000] 309.27/309.29 2 (starch-based flour) [Cho <i>et al.</i> , 2001] 396.153 18, 3 (wood) [Uhli <i>et al.</i> , 2001] 394.403 90 (low-ash lignite) [Chadwick and Body, 2002] not found 7 (steel in Ar) [Sturm <i>et al.</i> , 2004] 396.2 1.8–5.7% (soil, 7 Torr CO <sub>2</sub> ) [Sallé <i>et al.</i> , 2005] 396.14
As	440 (aerosol on filter) [Neuhäuser <i>et al.</i> , 1999] 235.0 910 (quartz filter) [Panne <i>et al.</i> , 2001] 235.0	15, 2.7 (wood) [Uhli <i>et al.</i> , 2001] 234.984 3.3 (soil) [Lazic <i>et al.</i> , 2001] 235.0 0.044 (soil, 7 Torr CO <sub>2</sub> ) [Radzienski <i>et al.</i> , 2004] 189.0
Au	(liq. on filter) [Appendix C.2]	30, 40 (glass, air 1 and 5 Torr) [Kurniawan <i>et al.</i> , 1995] 345.1
B	(liq. on filter) [Appendix C.2]	65 (UO <sub>2</sub> pellet) [Fichet <i>et al.</i> , 1999] 249.7733 1.5, 0.3 (wood) [Uhli <i>et al.</i> , 2001] 249.7733
Ba	18 (solution on Al) [Rodolfa and Cremers, 2004] 413.1 18 (liq. on Al <sup>b</sup> ) [Yamamoto <i>et al.</i> , 2005] 455.40 13 pg (liq. on Al <sup>b</sup> ) [Yamamoto <i>et al.</i> , 2005] 455.40 4.4–8 (particles on Al <sup>b</sup> ) [Yamamoto <i>et al.</i> , 2005] 455.40 3.1–5.6 pg (particles on Al <sup>b</sup> ) [Yamamoto <i>et al.</i> , 2005] 455.40 (liq. on filter) [Appendix C.2]	180, 99 (glass, air 1 and 5 Torr) [Kurniawan <i>et al.</i> , 1995] 553.5 42 (soil) [Eppler <i>et al.</i> , 1996] 455.4 265 (soil) [Yamamoto <i>et al.</i> , 1996] 455.4 76 (sand) [Eppler <i>et al.</i> , 1996] 455.4 600 (UO <sub>2</sub> pellet) [Fichet <i>et al.</i> , 1999] 455.4042 100 (PuO <sub>2</sub> pellet) [Fichet <i>et al.</i> , 1999] 455.4042 3, 21 (synthetic silicate in 5 Torr CO <sub>2</sub> ) [Knight <i>et al.</i> , 2000] 455.40 30–170 (soil, 7 Torr CO <sub>2</sub> ) [Sallé <i>et al.</i> , 2005] 455.39

Table C.2 (Continued)

Element	Surface (ng/cm <sup>2</sup> unless other unit specified) LOD (matrix) [ref.] $\lambda$ in nm	Solid (ppm unless other unit specified) LOD (matrix) [ref.] $\lambda$ in nm
Be	0.45 (0.5–5 µm particles on filter) [Cremers and Radziemski, 1985] 31.3/0.2/31.3/10.7 (liq. on filter) [Appendix C.2]	9.3 (soil) [Yamamoto <i>et al.</i> , 1996] 313.0/313.1 0.4–1.2 (soil) [Multari <i>et al.</i> , 1996] 313.0/313.1 350 (UO <sub>2</sub> pellet) [Fichet <i>et al.</i> , 1999] 306.7/716 0.0028 mole fraction (org. solid in air) [Tran <i>et al.</i> , 2001] 827.2 0.00029 mole fraction (org. solid in He) [Tran <i>et al.</i> , 2001] 827.2 15.000 and 11.000 (ABS polymer) [Stepputat and Noll, 2003] 827.24 0.05% (thermoplast) [Radivojevic <i>et al.</i> , 2004b] 131.0 3.75% (thermoplast) [Radivojevic <i>et al.</i> , 2004b] 826.5 1.1% (thermoplast) [Radivojevic <i>et al.</i> , 2004b] 833.5 5.9% (soil, 0.25 Torr CO <sub>2</sub> ) [Radziemski <i>et al.</i> , 2004] 154.1 5.6% (soil, 0.25 Torr CO <sub>2</sub> ) [Radziemski <i>et al.</i> , 2004] 163.3 30 (CaO in Fe ore) [Grant <i>et al.</i> , 1991] 431.86 85, 85 (glass, air 1 and 5 Torr) [Kurinawan <i>et al.</i> , 1995] 422.6 1–10 (aluminum, etched) [Bauer <i>et al.</i> , 1998] not found 1 (plant material) [Sun <i>et al.</i> , 1999] 428.3 60 (lignite) [Wallis <i>et al.</i> , 2000] 396.85 60 (low-ash lignite) [Chadwick and Body, 2002] not given 850–2200 (soil, 7 Torr CO <sub>2</sub> ) [Salké <i>et al.</i> , 2005] 393.36 65 (steel) [Aguilera <i>et al.</i> , 1992] 193.09 80 (steel) [Aragón <i>et al.</i> , 1999] 193.09 7 (steel) [Sturm <i>et al.</i> , 2000] 193.09 87 (steel) [Khater <i>et al.</i> , 2000] 97.7 300 (soil) [Cremers <i>et al.</i> , 2001] 247.8 3 (steel in air) [Noll <i>et al.</i> , 2001] 193.1 5 (steel) [Hemmerlin <i>et al.</i> , 2001] 133.571 1.2 (steel) [Khater <i>et al.</i> , 2002] 97.7 0.24% (soil, 7 Torr CO <sub>2</sub> ) [Radziemski <i>et al.</i> , 2004] 247.8 0.32% (soil, 7 Torr CO <sub>2</sub> ) [Radziemski <i>et al.</i> , 2004] 193.1
Br		
Bi		
Ca		
C		

Cd	400 (aerosol on filter) [Neuhäuser <i>et al.</i> , 1999] 228.8 400 (quartz filter) [Panne <i>et al.</i> , 2001] 228.8 (liq. on filter) [Appendix C.2]	0.51% (soil, 7 Torr CO <sub>2</sub> ) [Radziemski <i>et al.</i> , 2004] 165.7 7 (steel in Ar) [Sturm <i>et al.</i> , 2004] 193.1 7 (steel) [Radivojevic <i>et al.</i> , 2004a] 193.091 30 (soil) [Wisbrun <i>et al.</i> , 1994] PCR using multiple lines 19–306 (soil cone penetrometer) [Theriault <i>et al.</i> , 1998] 508.58 8 (starch-based flour) [Cho <i>et al.</i> , 2001] 226.502 1.6, 0.5 (wood) [Uhl <i>et al.</i> , 2001] 226.502/228.802 6 (soil) [Lazic <i>et al.</i> , 2001] 228.8 19, 11 (ABS polymer) [Stepputat and Noll, 2003] 228.80 96 (ABS polymer, on-line analyzer) [Stepputat and Noll, 2003] 228.80 0.011 mole fraction (org. solid in air) [Tran <i>et al.</i> , 2001] 837.6 0.00088 mole fraction (org. solid in He) [Tran <i>et al.</i> , 2001] 837.6 7.5% (soil, 0.25 Torr CO <sub>2</sub> ) [Radziemski <i>et al.</i> , 2004] 133.6 1880 (NaCl in pressed sample in He) [Asimellis <i>et al.</i> , 2005] 837.59
Cl		10 (soil) [Wisbrun <i>et al.</i> , 1994] PCR using multiple lines 40 (iron) [Paksy <i>et al.</i> , 1996] 425.4 8–69 (soil) [Mutari <i>et al.</i> , 1996] 425.44 5.8–52 (soil) [Mutari <i>et al.</i> , 1996] 427.48 367 (steel under water; RSP) [Pichahchy <i>et al.</i> , 1997] 425.44 5.2–31.3 (soil cone penetrometer) [Theriault <i>et al.</i> , 1998] 1425.43 1–10 (aluminum, echelle) [Bauer <i>et al.</i> , 1998] not found 6 (steel) [Aragón <i>et al.</i> , 1999] 267.72 70 (UO <sub>2</sub> pellet) [Fichet <i>et al.</i> , 1999] 520.8436 35 (PuO <sub>2</sub> pellet) [Fichet <i>et al.</i> , 1999] 520.8436 7 (steel) [Sturm <i>et al.</i> , 2000] 267.72 88, 39 (synthetic silicate in 5 Torr CO <sub>2</sub> ) [Knight <i>et al.</i> , 2000] 267.71 1 (starch-based flour) [Cho <i>et al.</i> , 2001] 425.435 <1 (wood) [Uhl <i>et al.</i> , 2001] 283.563 2.5 (soil) [Lazic <i>et al.</i> , 2001] 425.4
Co	100 (aerosol on filter) [Neuhäuser <i>et al.</i> , 1999] 238.4 100 (quartz filter) [Panne <i>et al.</i> , 2001] 238.4 (liq. on filter) [Appendix C.2]	
Cr	40 (aerosol on filter) [Neuhäuser <i>et al.</i> , 1999] 267.7 40 (quartz filter) [Panne <i>et al.</i> , 2001] 267.7 4.3 (liq. on Al <sup>b</sup> ) [Yamamoto <i>et al.</i> , 2005] 425.44 3 pg (liq. on Al <sup>b</sup> ) [Yamamoto <i>et al.</i> , 2005] 425.44 4.4–8.1 (particles on Al <sup>b</sup> ) [Yamamoto <i>et al.</i> , 2005] 425.44 3.1–5.7 pg (particles on Al <sup>b</sup> ) [Yamamoto <i>et al.</i> , 2005] 425.44 (liq. on filter) [Appendix C.2]	

Table C.2 (Continued)

Element	Surface (ng/cm <sup>2</sup> unless other unit specified) LOD (matrix) [ref.] $\lambda$ in nm	Solid (ppm unless other unit specified) LOD (matrix) [ref.] $\lambda$ in nm
Cu	19 (aerosol on filter) [Neuhäuser <i>et al.</i> , 1999] 324.8 10 (quartz filter) [Panne <i>et al.</i> , 2001] 324.8 (liq. on filter) [Appendix C.2]	3 (Al alloy, FO LIBS) [Rai <i>et al.</i> , 2001] 359.349 3 (Al alloy) [Rai <i>et al.</i> , 2001] 359.349 30 (soil) [Capitelli <i>et al.</i> , 2002] 520.6, 520.8 204, 256 (Al <sup>IV</sup> ) [Rieger <i>et al.</i> , 2002] 425.4 2, 4 (ABS polymer) [Stepputat and Noll, 2003] 425.43 73 (ABS polymer, on-line analyzer) [Stepputat and Noll, 2003] 425.43 7 (steel in Ar) [Sturm <i>et al.</i> , 2004] 267.7 2100 (slag) [López-Moreno <i>et al.</i> , 2004] 520.45, 520.60, 520.84 11 (Al alloy) [Sallé <i>et al.</i> , 2004] 357.869 1190 (molten steel) [Palanco <i>et al.</i> , 2004] not stated, 370–400 nm region 100, 30 (steel, microchip laser) [López-Moreno <i>et al.</i> , 2005] 425 44–64 (steel <sup>b</sup> ) [Yamamoto <i>et al.</i> , 2005] 425.44 20 (soil) [Wibshun <i>et al.</i> , 1994] PCR using multiple lines 10 (Al alloy) [Sababi and Cielo, 1995] 327.4 4.8–15 (soil) [Multari <i>et al.</i> , 1996] 324.75 4.5–11 (soil) [Multari <i>et al.</i> , 1996] 327.40 544 (zinc alloy) [St-Onge <i>et al.</i> , 1997] 282.44 520 (steel under water; RSP) [Pichahchy <i>et al.</i> , 1997] 324.75 1–10 (aluminum, echelle) [Bauer <i>et al.</i> , 1998] not found 1 (plant material) [Sun <i>et al.</i> , 1999] 324.8 150 (UO <sub>2</sub> pellet) [Fichet <i>et al.</i> , 1999] 324.7540 90 (PuO <sub>2</sub> pellet) [Fichet <i>et al.</i> , 1999] 324.7540 38, 43 (synthetic silicate in 5 Torr CO <sub>2</sub> ) [Knight <i>et al.</i> , 2000] 327.39 1 (starch-based flour) [Cho <i>et al.</i> , 2001] 324.754 1.8, 0.3 (wood) [Uhli <i>et al.</i> , 2001] 324.754 3.3 (soil) [Lazic <i>et al.</i> , 2001] 324.8 56 (Al alloy, FO LIBS) [Rai <i>et al.</i> , 2001] 324.7 160 (Al alloy) [Rai <i>et al.</i> , 2001] 324.7 360 (stainless steel) [Whitehouse <i>et al.</i> , 2001] 324.75, 327.40 30 (soil) [Capitelli <i>et al.</i> , 2002] 327.4

Dy	42, 61 (Al <sup>a</sup> ) [Rieger <i>et al.</i> , 2002] 324.8
Er	12 (Al <sup>a</sup> ) [Rieger <i>et al.</i> , 2002] 324.8
Eu	22 (Al <sup>a</sup> ) [Rieger <i>et al.</i> , 2002] 324.8
F	7 (steel in Ar) [Sturm <i>et al.</i> , 2004] 324.8 2 (Al, RSS) [Gauthier <i>et al.</i> , 2004] 327.4 3 (Al, RSP) [Gauthier <i>et al.</i> , 2004] 327.4 23.8 (Al) [Ismail <i>et al.</i> , 2004] 324 6.3 (steel) [Ismail <i>et al.</i> , 2004] 324
Fe	100 ng (femtosecond laser, 25 m) [Rohwetter <i>et al.</i> , 2004] 521.82 163–353 (steel <sup>b</sup> ) [Yamanoto <i>et al.</i> , 2005] 324.75 0.40, 0.36 (aluminum alloy, microchip laser) [Freedman <i>et al.</i> , 2005] 324.7537 10 (NaCl) [Ishizuka, 1973] 353.17 30 (NaCl) [Ishizuka, 1973] 349.91 5 (NaCl) [Ishizuka, 1973] 381.97
	0.016 mole fraction (org. solid in air) [Tran <i>et al.</i> , 2001] 685.6 0.0010 mole fraction (org. solid in He) [Tran <i>et al.</i> , 2001] 712.8 300 (NF in pressed sample in He) [Asimellis <i>et al.</i> , 2005] 685.60
	22 (zinc alloy) [St-Onge <i>et al.</i> , 1997] 302.06 1–10 (aluminum, echelle) [Bauer <i>et al.</i> , 1998] not found 1 (plant material) [Sun <i>et al.</i> , 1999] 404.6 400 (UO <sub>2</sub> pellet) [Fichet <i>et al.</i> , 1999] 248.3271 90 (lignite) [Wallis <i>et al.</i> , 2000] 238.20 30 (Al alloy, FO LIBS) [Rai <i>et al.</i> , 2001] 344.0606 15 (Al alloy) [Rai <i>et al.</i> , 2001] 344.0606 500 (soil) [Capitelli <i>et al.</i> , 2002] 404.6, 406.4, 407.2 100 (low-ash lignite) [Chadwick and Body, 2002] not found 447.628 (Al <sup>a</sup> ) [Rieger <i>et al.</i> , 2002] 438.4 1900 (slag) [López-Moreno <i>et al.</i> , 2004] 489.2 6 (Al, RSS) [Gauthier <i>et al.</i> , 2004] 259.9 3 (Al, RSP) [Gauthier <i>et al.</i> , 2004] 259.9 3–7.5% (soil, 7 Torr CO <sub>2</sub> ) [Sallé <i>et al.</i> , 2005] 404.58 0.32, 0.14 (aluminum alloy, microchip laser) [Freedman <i>et al.</i> , 2005] 373.3317, 373.4864, 373.7131

**Table C.2** (Continued)

Element	Surface (ng/cm <sup>2</sup> unless other unit specified) LOD (matrix) [ref.] λ in nm	Solid (ppm unless other unit specified) LOD (matrix) [ref.] λ in nm
Ga	(liq. on filter) [Appendix C.2]	240 (UO <sub>2</sub> pellet) [Fichet <i>et al.</i> , 1999] 417.2056 80 (PuO <sub>2</sub> pellet) [Fichet <i>et al.</i> , 1999] 417.2056 200 (NaCl) [Ishizuka, 1973] 367.12
Gd		10 (zircaloy in He at 15 Torr) [Idris <i>et al.</i> , 2004] 656.2
H		300, 647 (synthetic silicate in 5 Torr CO <sub>2</sub> ) [Knight <i>et al.</i> , 2000] 435.83
Hg		19, 4.6 (wood) [Uhl <i>et al.</i> , 2001] 253.65/435.835 84 (soil) [Lazic <i>et al.</i> , 2001] 253.7
Ho		16, 24 (ABS polymer) [Stepputat and Noll, 2003] 253.65 60 (ABS polymer, on-line analyzer) [Stepputat and Noll, 2003] 253.65
In	(liq. on filter) [Appendix C.2]	10 (NaCl) [Ishizuka, 1973] 345.60
		160 (UO <sub>2</sub> pellet) [Fichet <i>et al.</i> , 1999] 451.1323 150 (PuO <sub>2</sub> pellet) [Fichet <i>et al.</i> , 1999] 451.1323
K		190, 240 (glass, air 1 and 5 Torr) [Kurniawan <i>et al.</i> , 1995] 766.5 3 (starch-based flour) [Choi <i>et al.</i> , 2001] 766.490 3.5, 0.7 (wood) [Uhl <i>et al.</i> , 2001] 766.491 2000–38 000 (soil, 7 Torr CO <sub>2</sub> ) [Sallé <i>et al.</i> , 2005] 766.49
La	(liq. on filter) [Appendix C.2]	10 (NaCl) [Ishizuka, 1973] 394.91
Li	(liq. on filter) [Appendix C.2]	10, 14 (glass, air 1 and 5 Torr) [Kurniawan <i>et al.</i> , 1995] 670.7 35 (UO <sub>2</sub> pellet) [Fichet <i>et al.</i> , 1999] 610.3642 40 (PuO <sub>2</sub> pellet) [Fichet <i>et al.</i> , 1999] 610.3642
		2.5 and 20 (synthetic silicate in 5 Torr CO <sub>2</sub> ) [Knight <i>et al.</i> , 2000] 670.77/670.79 10–20 (soil, 7 Torr CO <sub>2</sub> ) [Sallé <i>et al.</i> , 2005] 670.78
Lu		20 (NaCl) [Ishizuka, 1973] 291.14
Mg	(liq. on filter) [Appendix C.2]	230 (MgO in Fe ore) [Grant <i>et al.</i> , 1991] 518.4 0.5 (Al alloy) [Sababi and Cielo, 1995] 285.2 130, 28 (glass, air 1 and 5 Torr) [Kurniawan <i>et al.</i> , 1995] 383.8

	1–10 (aluminum, echelle) [Bauer <i>et al.</i> , 1998] not found
	1 (plant material) [Sun <i>et al.</i> , 1999] 278.0
	70 ( $\text{UO}_2$ pellet) [Fichet <i>et al.</i> , 1999] 285.2129
	200 (lignite) [Wallis <i>et al.</i> , 2000] 285.21
	0.4 (starch-based flour) [Cho <i>et al.</i> , 2001] 279.553
	<1 (wood) [Uhl <i>et al.</i> , 2001] 279.553
	7 (Al alloy, FO LIBS) [Rai <i>et al.</i> , 2001] 383.829
	6 (Al alloy) [Rai <i>et al.</i> , 2001] 383.829
	90 (low-ash lignite) [Chadwick and Body, 2002] not given
	1.8–64 ( $\text{Al}^{19}$ ) [Rieger <i>et al.</i> , 2002] 285.2
	20–32 ( $\text{Al}^{19}$ ) [Rieger <i>et al.</i> , 2002] 279.6
	0.5 (Al, RSS) [Gautier <i>et al.</i> , 2004] 280.3
	0.2 (Al, RSP) [Gautier <i>et al.</i> , 2004] 280.3
	28.2 (Al) [Ismail <i>et al.</i> , 2004] 285
	76.8 (steel) [Ismail <i>et al.</i> , 2004] 285
	7 (Al alloy) [Sallé <i>et al.</i> , 2004] 285.213
	160–450 (soil, 7 Tor $\text{CO}_2$ ) [Sallé <i>et al.</i> , 2005] 280.27
	0.26, 0.11 (aluminum alloy, microchip laser) [Freedman <i>et al.</i> , 2005] 382.9355,
	383.2299, 383.2304, 383.8292, 383.8295
Mn	30 (aerosol on filter) [Neuhäuser <i>et al.</i> , 1999] 259.4
	30 (quartz filter) [Panne <i>et al.</i> , 2001] 259.4
	22 (liq. on $\text{Al}^{19}$ ) [Yamamoto <i>et al.</i> , 2005]
	403.08/403.31/403.45
	16 pg (liq. on $\text{Al}^{19}$ ) [Yamamoto <i>et al.</i> , 2005]
	403.08/403.31/403.45
	23–51 (particles on $\text{Al}^{19}$ ) [Yamamoto <i>et al.</i> , 2005]
	403.08/403.31/403.45
	16–58 pg (particles on $\text{Al}^{19}$ ) [Yamamoto <i>et al.</i> , 2005]
	403.08/403.31/403.45
	(liq. on filter) [Appendix C.2]
	1 (plant material) [Sun <i>et al.</i> , 1999] 403.1
	60 ( $\text{UO}_2$ pellet) [Fichet <i>et al.</i> , 1999] 403.45
	1200 (steel under water; RSP) [Pichalchy <i>et al.</i> , 1997]
	403.08/403.31/403.45/403.57
	1–10 (aluminum, echelle) [Bauer <i>et al.</i> , 1998] not found
	1 (starch-based flour) [Cho <i>et al.</i> , 2001] 257.610
	90 (Al alloy, FO LIBS) [Rai <i>et al.</i> , 2001] 404.136
	10 (Al alloy) [Rai <i>et al.</i> , 2001] 404.136
	113 (steel alloy, 1064 nm laser) [Bassiotis <i>et al.</i> , 2001] 482.352
	235 (steel alloy, 355 nm laser) [Bassiotis <i>et al.</i> , 2001] 482.352

**Table C.2** (Continued)

	Element	Surface (ng/cm <sup>2</sup> unless other unit specified) LOD (matrix) [ref.] $\lambda$ in nm	Solid (ppm unless other unit specified) LOD (matrix) [ref.] $\lambda$ in nm
			100 (soil) [Capitelli <i>et al.</i> , 2002] 475.4, 472.7, 478.3, 482.3
		35, 36 (Al <sup>a</sup> ) [Rieger <i>et al.</i> , 2002]	279.5
		67, 78 (Al <sup>a</sup> ) [Rieger <i>et al.</i> , 2002]	403.1
		51, 72 (Al <sup>a</sup> ) [Rieger <i>et al.</i> , 2002]	294.9
		7 (steel in Ar) [Sturm <i>et al.</i> , 2004]	293.3
		8 (Al, RSP) [Gautier <i>et al.</i> , 2004]	294.9
		3 (Al, RSP) [Gautier <i>et al.</i> , 2004]	294.9
		15.3 (Al) [Ismail <i>et al.</i> , 2004]	403
		5.0 (steel) [Ismail <i>et al.</i> , 2004]	403
		30, 40 (steel, microchip laser) [López-Moreno <i>et al.</i> , 2005]	403.1
		211–454 (steel) [Yamamoto <i>et al.</i> , 2005]	403.08/403.31/403.45
		300–450 (soil, 7 Torr CO <sub>2</sub> ) [Sallé <i>et al.</i> , 2005]	403.08
		0.11, 0.05 (aluminum alloy, microchip laser) [Freedman <i>et al.</i> , 2005]	403.07/53,
		403.3062, 403.4483	
	Mo	11 (solution on Al) [Rodolfa and Cremers, 2004]	407.0
		426–1730 (stainless steel, diff. surface finishes) [Cabalín <i>et al.</i> , 1999]	550.6
		7 (steel in Ar) [Sturm <i>et al.</i> , 2004]	281.6
		80, 90 (steel, microchip laser) [López-Moreno <i>et al.</i> , 2005]	384.4
		14, 18 (glass, air 1 and 5 Torr) [Kurniawan <i>et al.</i> , 1995]	589.0
		70 (lignite) [Wallis <i>et al.</i> , 2000]	589.0/589.59
		<1 (wood) [Uhl <i>et al.</i> , 2001]	588.99/5330.232
		30 (low-ash lignite) [Chadwick and Boddy, 2002]	not found
		70–600 (soil, 7 Torr CO <sub>2</sub> ) [Sallé <i>et al.</i> , 2005]	588.97
		15–25 (steel) [Hemmerlin <i>et al.</i> , 2001]	149.262
		500 (NaCl) [Ishizuka, 1973]	430.36
	N	20 (soil) [Wisbrun <i>et al.</i> , 1994]	PCR using multiple lines
	Nd	20 (soil) [Aguilera <i>et al.</i> , 1998]	377.6
	Ni	64 (steel) [Aguilera <i>et al.</i> , 1998]	not found
		1–10 (aluminum, echelle) [Bauer <i>et al.</i> , 1998]	
		50 (steel) [Aragón <i>et al.</i> , 1999]	231.60
		6 (steel) [Sturm <i>et al.</i> , 2000]	231.60
		12, 224 (synthetic silicate in 5 Torr CO <sub>2</sub> ) [Knight <i>et al.</i> , 2000]	352.45

Pb	35 000 (on copper and sulfur) [Franzke <i>et al.</i> , 1992] 401.99, 405.78, 406.21, 416.81 <10 ppm (on copper) [Franzke <i>et al.</i> , 1992] 401.99, 405.78, 406.21, 416.81 460 (aerosol on filter) [Neuhäuser <i>et al.</i> , 1999] 405.8 60 (quartz filter) [Panne <i>et al.</i> , 2001] 405.8 (iq, on filter) [Appendix C.2]
Pr	(iq, on filter) [Appendix C.2]
Rb	(iq, on filter) [Capitelli <i>et al.</i> , 2002]

**Table C.2** (Continued)

Element	Surface (ng/cm <sup>2</sup> unless other unit specified) LOD (matrix) [ref.] $\lambda$ in nm	Solid (ppm unless other unit specified) LOD (matrix) [ref.] $\lambda$ in nm
S		
Sb	280 (aerosol on filter) [Neuhäuser <i>et al.</i> , 1999] 259.8 550 (quartz filter) [Panne <i>et al.</i> , 2001] 259.8 (liq. on filter) [Appendix C.2]	70 (steel) [Gonzalez <i>et al.</i> , 1995] 180.7/182.0 8 (steel) [Sturm <i>et al.</i> , 2000] 180.73 11 (steel) in air [Noll <i>et al.</i> , 2001] 180.7 4.5 (steel) [Hemmerlin <i>et al.</i> , 2001] 180.73 1.03% (soil, 7 Torr CO <sub>2</sub> ) [Radziemski <i>et al.</i> , 2004] 180.7 1.77% (soil, 7 Torr CO <sub>2</sub> ) [Radziemski <i>et al.</i> , 2004] 182.6 0.11% (soil, 7 Torr CO <sub>2</sub> ) [Radziemski <i>et al.</i> , 2004] 545.4 7 (steel in Ar) [Sturm <i>et al.</i> , 2004] 180.7 73 (steel) [Radivojevic <i>et al.</i> , 2004a] 182.034
Sc		50, 17 (ABS polymer) [Stepputat and Noll, 2003] 259.80
Si		80 (ABS polymer, on-line analyzer) [Stepputat and Noll, 2003] 259.80 2 (NaCl) [Ishizuka, 1973] 361.38 1500 (SiO in Fe ore) [Grant <i>et al.</i> , 1991] 390.55 14 (Al alloy) [Sabasti and Cielo, 1995] 251.6 600 (iron) [Paksy <i>et al.</i> , 1996] 288.158 600 (Al) [Paksy <i>et al.</i> , 1996] 288.158 1190 (steel under water: RSP) [Pichahshey <i>et al.</i> , 1997] 288.16 1–10 (aluminum, echeille) [Bauer <i>et al.</i> , 1998] not found 80 (steel) [Aragón <i>et al.</i> , 1999] 288.16 11 (steel) [Sturm <i>et al.</i> , 2000] 288.16 200 (lignite) [Wallis <i>et al.</i> , 2000] 288.16 5.3, 1.0 (wood) [Uhli <i>et al.</i> , 2001] 288.158 400 (low-ash lignite) [Chadwick and Body, 2002] not found 141, 155 (Al <sup>10</sup> ) [Rieger <i>et al.</i> , 2002] 288.2 283.9 (Al) [Ismail <i>et al.</i> , 2004] 288 6.6 (steel) [Ismail <i>et al.</i> , 2004] 288 74 (Al alloy) [Sallé <i>et al.</i> , 2004] 288.158 200 (steel, microchip laser) [López-Moreno <i>et al.</i> , 2005] 288.16 235–319 (steel <sup>b</sup> ) [Yamamoto <i>et al.</i> , 2005] 288.16 9–45% (soil, 7 Torr CO <sub>2</sub> ) [Sallé <i>et al.</i> , 2005] 288.18 1.87, 0.14 (aluminum alloy, microchip laser) [Freedman <i>et al.</i> , 2005] 288.1578

Sm	40 (NaCl) [Ishizuka, 1973] 356.83
Sn	50 (aerosol on filter) [Neuhäuser <i>et al.</i> , 1999] 284.0 50 (quartz filter) [Panne <i>et al.</i> , 2001] 284.0
Sr	8.8 (solution on Al) [Rodolfa and Cremers, 2004] 407.8 3.5 (liq. on Al <sup>b</sup> ) [Yamamoto <i>et al.</i> , 2005] 403.08/403.31/403.45 2.5 pg (liq. on Al <sup>b</sup> ) [Yamamoto <i>et al.</i> , 2005] 403.08/403.31/403.45 1.7–3.1 (particles on Al <sup>b</sup> ) [Yamamoto <i>et al.</i> , 2005] 403.08/403.31/403.45 1.2–3.6 pg (particles on Al <sup>b</sup> ) [Yamamoto <i>et al.</i> , 2005] 403.08/403.31/403.45 (liq. on filter) [Appendix C.2]
Tb	60 (NaCl) [Ishizuka, 1973] 384.88
Th	(liq. on filter) [Appendix C.2]
Ti	111 (solution on Al) [Rodolfa and Cremers, 2004] 398.2 (liq. on filter) [Appendix C.2]
Tl	40 (filter) [Arnold and Cremers, 1995] 535.05 100 (aerosol on filter) [Neuhäuser <i>et al.</i> , 1999] 276.8 130 (quartz filter) [Panne <i>et al.</i> , 2001] 276.8
Tm	30 (NaCl) [Ishizuka, 1973] 388.31
U	1000 (soil) [Cremers and Ferris, 1996] 409.02
V	90 (aerosol on filter) [Neuhäuser <i>et al.</i> , 1999] 292.5 60 (quartz filter) [Panne <i>et al.</i> , 2001] 292.5 (liq. on filter) [Appendix C.2]

33 (zinc alloy) [Sr-Onge *et al.*, 1997] 284.00  
54 (zinc alloy) [St-Onge *et al.*, 1997] 286.33  
34 (zinc alloy) [Sr-Onge *et al.*, 1997] 303.41  
26, 84 (synthetic silicate in 5 Torr CO<sub>2</sub>) [Knight *et al.*, 2000] 303.41  
8.2, 2.2 (wood) [Uhl *et al.*, 2001] 286.333

42 (soil) [Yamamoto *et al.*, 1996] 407.77  
3.–75 (soil) [Multari *et al.*, 1996] 407.77  
5.2–40 (soil) [Multari *et al.*, 1996] 405.78  
1–10 (aluminum, echelle) [Bauer *et al.*, 1998] not found  
130 (UO<sub>2</sub> pellet) [Fichet *et al.*, 1999] 407.7714  
90 (PuO<sub>2</sub> pellet) [Fichet *et al.*, 1999] 407.7714  
1.2, 1.9 (synthetic silicate in 5 Torr CO<sub>2</sub>) [Knight *et al.*, 2000] 407.77  
0.3 (starch-based flour) [Cho *et al.*, 2001] 421.552  
30–40 (soil, 7 Torr CO<sub>2</sub>) [Sallé *et al.*, 2005] 407.78

230 (TiO<sub>2</sub> in Fe ore) [Grant *et al.*, 1991] 498.17  
410, 350 (glass, air at 1 and 5 Torr) [Kurniawan *et al.*, 1995] 365.3  
1–10 (aluminum, echelle) [Bauer *et al.*, 1998] not found  
48 (soil) [Lazic *et al.*, 2001] 351.9  
4 (Al, RSS) [Gautier *et al.*, 2004] 323.5  
3 (Al, RSP) [Gautier *et al.*, 2004] 323.5  
1000–2400 (soil, 7 Torr CO<sub>2</sub>) [Sallé *et al.*, 2005] 398.92  
100 (UO<sub>2</sub> pellet) [Fichet *et al.*, 1999] 535.0460

**Table C.2** (Continued)

Element	Surface (ng/cm <sup>2</sup> unless other unit specified) LOD (matrix) [ref.] $\lambda$ in nm	Solid (ppm unless other unit specified) LOD (matrix) [ref.] $\lambda$ in nm
Y	(liq. on filter) [Appendix C.2]	2 (NaCl) [Ishizuka, 1973] 371.03 2 (NaCl) [Ishizuka, 1973] 369.42
Yb		160, 130 (glass, air 1 and 5 Torr) [Kurniawan <i>et al.</i> , 1995] 481.0
Zn	(liq. on filter) [Appendix C.2]	1–10 (aluminum, echelle) [Bauer <i>et al.</i> , 1998] not found 1 (plant material) [Sun <i>et al.</i> , 1999] 2 [3.930 (soil)] 98 (soil) [Lazic <i>et al.</i> , 2001] 334.5 38 (Al alloy, FO LIBS) [Rai <i>et al.</i> , 2001] 330.259 0.29 (Al alloy) [Rai <i>et al.</i> , 2001] 330.259 30 (soil) [Capelli <i>et al.</i> , 2002] 472.2 281, 380 (Al <sup>b</sup> ) [Rieger <i>et al.</i> , 2002] 334.5 1.36, 0.10 (aluminum alloy, microchip laser) [Freedman <i>et al.</i> , 2005] 334.5015 290, 190 (glass, air 1 and 5 Torr) [Kurniawan <i>et al.</i> , 1995] 360.1
Zr	(liq. on filter) [Appendix C.2]	

PCR, principal component analysis.

FO LIBS, fiber optic LIBS.

<sup>a</sup> LOD depended on concentration of element in the sample and the laser energy.<sup>b</sup> Using acousto-optic Q-switched laser (150 ns pulse width).

## C.2 UNIFORM DETECTION LIMITS

These detection limits were determined using 100 mJ laser pulses from a Q-switched Nd:YAG laser incident on 37 mm diameter filter paper (Whatman 42). Elements were provided by atomic absorption standard (AAS) solutions deposited on the filter over an area of approximately 1 cm<sup>2</sup>. The lens focal length was 100 mm. Each measurement consisted of averaging the spectra from 100 laser plasmas. During each measurement, the filter was translated under the laser pulses. Each measurement was repeated six times and the results averaged to provide an element signal at a specific concentration on the filter. Detection limits were determined using LOD = 3sm as described in Section 4.5, where m is the slope of the calibration curve at the lower concentrations of solutions on the filter. In those cases in which the element line was ratioed to an adjacent line as an internal standard, this line is listed in parentheses along with the element name (Table C.4) (Cremers and Radziemski, 2003). Note that some detection limits may be higher than expected in view of the emission line strength. This could be due to self-absorption or other effects related to high concentrations of the element on the filter.

**Table C.3** Other detection limits

Material	Conditions
Naphthalene	20 ng on surface [Portnov <i>et al.</i> , 2003] via C <sub>2</sub> , CN emission
Halon-14	490 ppm in nitrogen/Ar [Lancaster <i>et al.</i> , 1999] via F(I) emission at 685.6 nm
Halon-1301	750 ppm in nitrogen/Ar [Lancaster <i>et al.</i> , 1999] via F(I) emission at 685.6 nm
FM-200	170 ppm in nitrogen/Ar [Lancaster <i>et al.</i> , 1999] via F(I) emission at 685.6 nm
HFC-134a	530 ppm in nitrogen/Ar [Lancaster <i>et al.</i> , 1999] via F(I) emission at 685.6 nm

**Table C.4** Detection limits obtained from AAS solutions deposited on a filter [Ratio lines: 393.4 and 396.9 nm Ca(II) and 247.8 nm C(I)]

Element (ratio line)	$\lambda$ (nm)	$\mu\text{g}/\text{cm}^2$	Element (ratio line)	$\lambda$ (nm)	$\mu\text{g}/\text{cm}^2$
Aluminum	308.2	8	Bismuth (393.4)	289.7	47
	309.2	34		293.8	62
	394.4	16		302.4	33
	396.1	21		306.7	15
	413.0	165		472.2	644
Barium (393.4)	455.4	84	Boron	249.6 <sup>a</sup>	412
	493.4	86	Cadmium	441.5	2313
	553.5	45		508.5	228
	614.1	59	Chromium (393.4)	357.8	77
	649.6	226		359.3	124
	705.9	110		529.8	40
	728.0	207		534.5	298
Beryllium (393.4)	234.8	657		540.9	23
	265.0 <sup>a</sup>	212	Cobalt (393.4)	340.5	164
	313.0 <sup>a</sup>	100		345.3	53
	332.1	73		350.2	125

**Table C.4** (Continued)

Element (ratio line)	$\lambda$ (nm)	$\mu\text{g}/\text{cm}^2$	Element (ratio line)	$\lambda$ (nm)	$\mu\text{g}/\text{cm}^2$
Copper (393.4)	399.5	242	Scandium (393.4)	335.3	126
	412.1	71		337.2	122
	324.7	48		467.0	81
	327.3	419		474.3	82
	353.0	1181		507.0	101
Gallium (393.4)	515.3	301	Silicon (393.4)	523.9	157
	294.4 <sup>a</sup>	107		535.6	102
	403.2	62		567.1	56
	417.2	45		621.0	114
Gold Indium (393.4)	267.5	384	Silver (393.4)	251.6	172
	303.9	245		288.1	50
	325.6	43		568.8	14
	410.1	38		624.3	55
Iron (396.9)	451.1	39	Strontium (393.4)	328	78
	275.0	279		338.3	95
	302.0	121		520.9	71
	344.0	195		546.5	32
	373.4	258		346.4	44
	430.7	335		407.7	59
	438.3	50		421.5	87
	440.4	162		460.7	86
	526.9 <sup>a</sup>	222		707.0	14
	532.8 <sup>a</sup>	419		411.6	54
Lanthanum (393.4)	333.7	80	Thorium	438.1	184
	375.9	112		439.1	96
	398.8	40		308.8	117
Lead	280.1	116	Titanium (393.4)	323.4	51
	283.3	223		334.9	98
	287.3	83		336.1	321
	357.2	42		365.3	87
	363.9	45		368.5	90
	368.3	51		375.9	61
	373.9	33		439.5	64
	460.2 <sup>a</sup>	45		499.1	130
Lithium (393.4)	497.1 <sup>a</sup>	96	Vanadium (393.4)	289.3	132
	670.7 <sup>a</sup>	374		292.4	80
	812.6 <sup>a</sup>	114		309.3	56
	279.5	64		318.3 <sup>a</sup>	52
Magnesium (393.4)	285.2	86	Yttrium (393.4)	327.6	144
	383.2	142		370.3	316
	517.3	78		411.1	47
	518.3	85		437.9	18
	294.9	177		446.0	40
Manganese (247.8)	356.9	420		459.4	56
	482.3	126		488.1	101
	310.1	1005		572.7	52
	341.4	222		624.3	50
Nickel (393.4)	344.6	353		430.9	35
	361.9	43		442.2	76
	247.2	65		452.7	65
	780.0	9		464.3	89

	490.0	38		334.5 <sup>a</sup>	112
	508.7	49		468.0	204
	520.0	68		472.2	149
	546.6	29		481.0	85
	552.7	93	Zirconium (393.4)	327.3	200
YO	597.2	33		339.1	228
YO	613.2	24		349.6	93
YO	616.5	59		357.2	135
Zinc (393.4)	213.8	340		407.2	193
	330.2 <sup>a</sup>	181			

<sup>a</sup>Unresolved lines.

## REFERENCES

- Aguilera, J.A., C. Aragón and J. Campos (1992). Determination of carbon content in steel using laser-induced breakdown spectroscopy. *Appl. Spectrosc.* 46: 1382–1387.
- Aguilera, J.A., C. Aragón and F. Penalba (1998). Plasma shielding effect in laser ablation of metallic samples and its influence on LIBS analysis. *Appl. Surf. Sci.* 127–129: 309–314.
- Aragón, C., J.A. Aguilera and F. Penalba (1999). Improvements in quantitative analysis of steel composition by laser-induced breakdown spectroscopy at atmospheric pressure. *Appl. Spectrosc.* 53: 1259–1267.
- Arca, G., A. Ciucci, V. Palleschi, S. Rastelli and E. Tognoni (1997). Trace element analysis in water by the laser-induced breakdown spectroscopy technique. *Appl. Spectrosc.* 51: 1102–1105.
- Archontaki, H.A. and S.R. Crouch (1988). Evaluation of an isolated droplet sample introduction system for laser-induced breakdown spectroscopy. *Appl. Spectrosc.* 42: 741–746.
- Arnold, S.D. and D.A. Cremers (1995). Rapid determination of metal particles on air sampling filters using laser-induced breakdown spectroscopy. *Am. Ind. Hyg. Assoc J.* 56: 1180–1186.
- Arp, Z.A., D.A. Cremers, R.C. Wiens, D.M. Wayne, B. Sallé and S. Maurice (2004). Analysis of water ice and water/ice soil mixtures using laser-induced breakdown spectroscopy: application to Mars polar exploration. *Appl. Spectrosc.* 58: 897–909.
- Asimellis, G., S. Hamilton, A. Giannoudakos and M. Kompitsas (2005). Controlled inert gas environment for enhanced chlorine and fluorine detection in the visible and near-infrared by laser-induced breakdown spectroscopy. *Spectrochim. Acta Part B* 60: 1132–1139.
- Assion, A., M. Wollenhaupt, L. Haag, F. Mayorov, C. Sarpe-Tudoran, M. Winter, U. Kutschera and T. Baumert (2003). Femtosecond laser-induced-breakdown spectrometry for Ca<sup>2+</sup> analysis of biological samples with high spatial resolution. *Appl. Phys. B* 77: 391–397.
- Bassiotis, I., A. Diamantopoulou, A. Giannoudakos, F. Roubani-Kalantzopoulou and M. Kompitsas (2001). Effects of experimental parameters in quantitative analysis of steel alloy by laser-induced breakdown spectroscopy. *Spectrochim. Acta Part B* 56: 671–683.
- Bauer, H.E., F. Leis and K. Niemax (1998). Laser induced breakdown spectrometry with an echelle spectrometer and intensified charge coupled device detection. *Spectrochim. Acta Part B* 53: 1815–1825.
- Beddows, D.C.S., O. Samek, M. Liska and H.H. Telle (2002). Single-pulse laser-induced breakdown spectroscopy of samples submerged in water using a single fibre light delivery system. *Spectrochim. Acta Part B* 57: 1461–1471.
- Berman, L.M. and P.J. Wolf (1998). Laser-induced breakdown spectroscopy of liquids: Aqueous solutions of nickel and chlorinated hydrocarbons. *Appl. Spectrosc.* 52: 438–443.

- Buckley, S.G., H.A. Johnsen, K.R. Hencken and D.W. Hahn (2000). Implementation of laser-induced breakdown spectroscopy as a continuous emissions monitor for toxic metals. *Waste Manage.* 20: 455–462.
- Bundschuh, T., J.I. Yun and R. Knopp (2001). Determination of size, concentration and elemental composition of colloids with laser-induced breakdown detection/spectroscopy (LIBD/S). *Fresenius J. Anal. Chem.* 371: 1063–1069.
- Cabalín, L.M., D. Romero, J.M. Baena and J.J. Laserna (1999). Effect of surface topography in the characterization of stainless steel using laser-induced breakdown spectrometry. *Surf. Interface Anal.* 27: 805–810.
- Caceres, J.O., J.T. Lopez, H.H. Telle and A.G. Urena (2001). Quantitative analysis of trace metal ions in ice using laser-induced breakdown spectroscopy. *Spectrochim. Acta Part B* 56: 831–838.
- Capitelli, F., F. Colao, M.R. Provenzano, R. Fantoni, G. Brunetti and N. Senesi (2002). Determination of heavy metals in soils by laser induced breakdown spectroscopy. *Geoderma* 106: 45–62.
- Carranza, J.E., B.T. Fisher, G.D. Yoder and D.W. Hahn (2001). On-line analysis of ambient air aerosols using laser-induced breakdown spectroscopy. *Spectrochim. Acta Part B* 56: 851–864.
- Chadwick, B.L. and D. Body (2002). Development and commercial evaluation of laser-induced breakdown spectroscopy chemical analysis technology in the coal power generation industry. *Appl. Spectrosc.* 56: 70–74.
- Charfi, B. and M.A. Harith (2002). Panoramic laser-induced breakdown spectrometry of water. *Spectrochim. Acta Part B* 57: 1141–1153.
- Cho, H.-H., Y.-J. Kim, Y.-S. Jo, K. Kitagawa, N. Arai and Y.-I. Lee (2001). Application of laser-induced breakdown spectroscopy for direct determination of trace elements in starch-based flours. *J. Anal. At. Spectrom.* 16: 622–627.
- Cremers, D.A. and L.J. Radziemski (1983). Detection of fluorine and chlorine in air by laser-induced breakdown spectroscopy. *Anal. Chem.* 55: 1252–1256.
- Cremers, D.A. and L.J. Radziemski (1985). Direct detection of beryllium on filters using the laser spark. *Appl. Spectrosc.* 39: 57–63.
- Cremers, D.A. and M.J. Ferris (1996). Unpublished results.
- Cremers, D.A. and L.J. Radziemski (2003). Unpublished results.
- Cremers, D.A., L.J. Radziemski and T.R. Loree (1984). Spectrochemical analysis of liquids using the laser spark. *Appl. Spectrosc.* 38: 721–729.
- Cremers, D.A., F.L. Archuleta and R.J. Martinez (1985). Evaluation of the continuous optical discharge for spectrochemical analysis. *Spectrochim. Acta Part B* 40: 665–679.
- Cremers, D.A., M.H. Ebinger, D.D. Breshears, P.J. Unkefer, S.A. Kammerdiener, M.J. Ferris, K.M. Catlett and J.R. Brown (2001). Measuring total soil carbon with laser-induced breakdown spectroscopy (LIBS). *J. Environ. Qual.* 30: 2002–2206.
- De Giacomo, A., M. Dell'aglio and O. De Pascale (2004). Single pulse-laser induced breakdown spectroscopy in aqueous solution. *Appl. Phys. A* 79: 1035–1038.
- Dudragne, L., Ph. Adam and J. Amouroux (1998). Time-resolved laser-induced breakdown spectroscopy: application for qualitative and quantitative detection of fluorine, chlorine, sulfur, and carbon in air. *Appl. Spectrosc.* 52: 1321–1327.
- Eppler, A.S., D.A. Cremers, D.D. Hickmott and A.C. Koskelo (1996). Matrix effects in the detection of Pb and Ba in soils using laser-induced breakdown spectroscopy. *Appl. Spectrosc.* 50: 1175–1181.
- Essien, M., L.J. Radziemski and J. Sneddon (1988). Detection of cadmium, lead, zinc in aerosols by laser-induced breakdown spectrometry. *J. Anal. At. Spectrom.* 3: 985–988.
- Fichet, P., P. Mauchien and C. Moulin (1999). Determination of impurities in uranium and plutonium dioxides by laser-induced breakdown spectroscopy. *Appl. Spectrosc.* 53: 1111–1117.

- Fisher, B.T., H.A. Johnsen, S.G. Buckley and D.W. Hahn (2001). Temporal gating for the optimization of laser-induced breakdown spectroscopy detection and analysis of toxic metals. *Appl. Spectrosc.* 55: 1312–1319.
- Franzke, D., H. Klos and A. Wokaun (1992). Element identification on the surface of inorganic solids by excimer laser-induced emission spectroscopy. *Appl. Spectrosc.* 46: 587–592.
- Freedman, A., F.J. Iannarilli and J.C. Wormhoudt (2005). Aluminum alloy analysis using microchip-laser induced breakdown spectroscopy. *Spectrochim. Acta Part B* 60: 1076–1082.
- Gautier, C., P. Fichet, D. Menuta, J.-L. Lacour, D. L’Hermite and J. Dubessy (2004). Study of the double-pulse setup with an orthogonal beam geometry for laser-induced breakdown spectroscopy. *Spectrochim. Acta Part B* 59: 975–986.
- Gonzalez, A., M. Ortiz and J. Campos (1995). Determination of sulfur content in steel by laser-produced plasma atomic emission spectroscopy. *Appl. Spectrosc.* 49: 1632–1635.
- Grant, K., G.L. Paul and J.A. O'Neill (1991). Quantitative elemental analysis of iron ore by laser-induced breakdown spectroscopy. *Appl. Spectrosc.* 45: 701–705.
- Hahn, D.W. and M.M. Lunden (2000). Detection and analysis of aerosol particles by laser-induced breakdown spectroscopy. *Aerosol Sci. Technol.* 33: 30–48.
- Haisch, C., R. Niessner, O.I. Matveev, U. Panne and N. Omenetto (1996). Element-specific determination of chlorine in gases by laser-induced-breakdown-spectroscopy (LIBS). *Fresenius J. Anal. Chem.* 356: 21–26.
- Hemmerlin, M., R. Meilland, H. Falk, P. Wintzens and L. Paukeri (2001). Application of vacuum ultraviolet laser-induced breakdown spectrometry for steel analysis—comparison with spark-optical emissions spectrometry figures of merit. *Spectrochim. Acta Part B* 56: 661–669.
- Huang, J.-S., C.-B. Ke, L.S. Huang and K.C. Lin (2002). The correlation between ion production and emission intensity in the laser-induced breakdown spectroscopy of liquid droplets. *Spectrochim. Acta Part B* 57: 35–48.
- Huang, J.-S., C.-B. Ke and K.-C. Lin (2004). Matrix effect on emission/current correlated analysis in laser-induced breakdown spectroscopy of liquid droplets. *Spectrochim. Acta Part B* 59: 321–326.
- Hybl, J.D., G.A. Lithgow and S.G. Buckley (2003). Laser-induced breakdown spectroscopy detection and classification of biological aerosols. *Appl. Spectrosc.* 57: 1207–1215.
- Idris, N., H. Kurniawan, T.J. Lie, M. Parded, H. Suyanto, R. Hedwig, T. Kobayashi, K. Kagawa and T. Maruyama (2004). Characteristics of hydrogen emission in laser plasma induced by focusing fundamental Q-sw YAG laser on solid samples. *Japan. J. Appl. Phys.* 43: 4221–4228.
- Ishizuka, T. (1973). Laser emission spectrography of rare earth elements. *Anal. Chem.* 45: 538–541.
- Ismail, M.A., H. Imam, A. Elhassan, W.T. Youniss and M.A. Harith (2004). LIBS limit of detection and plasma parameters of some elements in two different metallic matrices. *J. Anal. At. Spectrom.* 19: 489–494.
- Janzen, C., R. Fleige, R. Noll, H. Schwenke, W. Lahmann, J. Knoth, P. Beaven, E. Jantzen, A. Oest and P. Koke (2005). Analysis of small droplets with a new detector for liquid chromatography based on laser-induced breakdown spectroscopy. *Spectrochim. Acta Part B* 60: 993–1001.
- Khater, M.A., P. van Kampen, J.T. Costello, J.-P. Mosnier and E.T. Kennedy (2000). Time-integrated laser-induced plasma spectroscopy in the vacuum ultraviolet for the quantitative elemental characterization of steel alloys. *J. Phys. D: Appl. Phys.* 33: 2252–2262.
- Khater, M.A., J.T. Costello and E.T. Kennedy (2002). Optimization of the emission characteristics of laser-produced steel plasmas in the vacuum ultraviolet: significant improvements in carbon detection limits. *Appl. Spectrosc.* 56: 970–983.

- Knight, A.K., N.L. Scherbarth, D.A. Cremers and M.J. Ferris (2000). Characterization of laser-induced breakdown spectroscopy (LIBS) for application to space exploration. *Appl. Spectrosc.* 54: 331–340.
- Knopp, R., F.J. Scherbaum and J.I. Kim (1996). Laser induced breakdown spectrometry (LIBS) as an analytical tool for the detection of metal ions in aqueous solution. *Fresenius J. Anal. Chem.* 355: 16–20.
- Kurniawan, H., S. Nakajima, J.E. Batubara, M. Marpaung, M. Okamoto and K. Kagawa (1995). Laser-induced wave plasma in glass and its application to elemental analysis. *Appl. Spectrosc.* 49: 1067–1072.
- Lancaster, E.D., K.L. McNesby, R.G. Daniel and A.W. Mizolek (1999). Spectroscopic analysis of fire suppressants and refrigerants by laser-induced breakdown spectroscopy. *Appl. Opt.* 38: 1476–1480.
- Lazic, V., R. Barbini, F. Colao, R. Fantoni and A. Palucci (2001). *Spectrochim. Acta Part B* 56: 807–820.
- Lazzari, C., M. De Rosa, S. Rastelli, A. Ciucci, V. Palleschi and A. Salvetti (1994). Detection of mercury in air by time-resolved laser-induced breakdown spectroscopy technique. *Laser Part. Beams* 12: 525–530.
- Lo, K.M. and N.H. Cheung (2002). ArF laser-induced plasma spectroscopy for part-per-billion analysis of metal ions in aqueous solutions. *Appl. Spectrosc.* 56: 682–688.
- López-Moreno, C., S. Palanco and J.J. Laserna (2004). Remote laser-induced plasma spectrometry for elemental analysis of samples of environmental interest. *J. Anal. At. Spectrom.* 19: 1479–1484.
- López-Moreno, C., K. Ampionsah-Manager, B.W. Smith, I.B. Gornushkin, N. Omenetto, S. Palanco, J.J. Laserna and J.D. Winefordner (2005). Quantitative analysis of low-alloy steel by microchip laser induced breakdown spectroscopy. *J. Anal. At. Spectrom.* 20: 552–556.
- Lucena, P., L.M. Cabalín, E. Pardo, F. Martín, L.J. Alemany and J.J. Laserna (1998). Laser induced breakdown spectrometry of vanadium in titania supported silica catalysts. *Talanta* 47: 143–151.
- Martin, M. and M.-D. Cheng (2000). Detection of chromium aerosol using time-resolved laser-induced plasma spectroscopy. *Appl. Spectrosc.* 54: 1279–1285.
- Multari, R.A., L.E. Foster, D.A. Cremers and M.J. Ferris (1996). Effect of sampling geometry on elemental emissions in laser-induced breakdown spectroscopy. *Appl. Spectrosc.* 50: 1483–1499.
- Neuhäuser, R.E., U. Panne, R. Niessner, G.A. Petrucci, P. Cavalli and N. Omenetto (1997). On-line and in-situ detection of lead aerosols by plasma-spectroscopy and laser-excited atomic fluorescence spectroscopy. *Anal. Chim. Acta* 346: 37–48.
- Neuhäuser, R.E., U. Panne and R. Niessner (1999). Laser-induced plasma spectroscopy (LIPS): a versatile tool for monitoring heavy metal aerosols. *Anal. Chim. Acta* 392: 47–54.
- Noll, R., H. Bette, A. Brysch, M. Kraushaar, I. Monch, L. Peter and V. Sturm (2001). Laser-induced breakdown spectrometry – applications for production control and quality assurance in the steel industry. *Spectrochim. Acta Part B* 56: 637–649.
- Pakhomov, A.V., W. Nichols and J. Borysow (1996). Laser-induced breakdown spectroscopy for detection of lead in concrete. *Appl. Spectrosc.* 50: 880–884.
- Paksy, L., B. Német, A. Lengyel, L. Kozma and J. Czekkel (1996). Production control of metal alloys by laser spectroscopy of the molten metals. Part 1. Preliminary investigations. *Spectrochim. Acta Part B* 51: 279–290.
- Palanco, S., S. Conesa and J.J. Laserna (2004). Analytical control of liquid steel in an induction melting furnace using a remote laser induced plasma spectrometer. *J. Anal. At. Spectrom.* 19: 462–467.
- Panne, U., R.E. Neuhäuser, M. Theisen, H. Fink and R. Niessner (2001). Analysis of heavy metal aerosols on filters by laser-induced plasma spectroscopy. *Spectrochim. Acta Part B* 56: 839–850.

- Pardede, M., H. Kurniawan, M.O. Tjia, K. Ikezawa, T. Maruyama and K. Kagawa (2001). Spectrochemical analysis of metal elements electrodeposited from water samples by laser-induced shock wave plasma spectroscopy. *Appl. Spectrosc.* 55: 1229–1236.
- Pichahchy, A.E., D.A. Cremers and M.J. Ferris (1997). Detection of metals underwater using laser-induced breakdown spectroscopy. *Spectrochim. Acta Part B* 52: 25–39.
- Portnov, A., S. Rosenwaks and I. Bar (2003). Emission following laser-induced breakdown spectroscopy of organic compounds in ambient air. *Appl. Opt.* 42: 2835–2842.
- Radivojevic, I., C. Haisch, R. Niessner, S. Florek, H. Becker-Ross and U. Panne (2004a). Microanalysis by laser-induced plasma spectroscopy in the vacuum ultraviolet. *Anal. Chem.* 76: 1648–1658.
- Radivojevic, I., R. Niessner, C. Haisch, S. Florek, H. Becker-Ross and U. Panne (2004b). Detection of bromine in thermoplasts from consumer electronics by laser-induced plasma spectroscopy. *Spectrochim. Acta Part B* 59: 335–343.
- Radziemski, L.J., T.R. Loree, D.A. Cremers and N.M. Hoffman (1983). Time-resolved laser-induced breakdown spectrometry of aerosols. *Anal. Chem.* 55: 1246–1252.
- Radziemski, L.J., D.A. Cremers, K. Benelli, C. Khoo and R.D. Harris (2004). Use of the vacuum ultraviolet spectral region for LIBS-based Martian geology and exploration. *Spectrochim. Acta Part B* 60: 237–248.
- Rai, A.K., H. Zhang, F.Y. Yueh, J.P. Singh and A. Weisburg (2001). Parametric study of a fiber-optic laser-induced breakdown spectroscopy probe for analysis of aluminum alloys. *Spectrochim. Acta Part B* 56: 2371–2383.
- Rieger, G.W., M. Taschuk, Y.Y. Tsui and R. Fedosejevs (2002). Laser-induced breakdown spectroscopy for microanalysis using submillijoule UV laser pulses. *Appl. Spectrosc.* 56: 689–698.
- Rodolfa, K.T. and D.A. Cremers (2004). Capabilities of surface composition analysis using a long laser-induced breakdown spectroscopy spark. *Appl. Spectrosc.* 58: 367–375.
- Rohwetter, Ph., J. Yu, G. Méjean, K. Stelmaszczyk, E. Salmon, J. Kasparian, J.-P. Wolf and L. Wöste (2004). Remote LIBS with ultrashort pulses: characteristics in the picosecond and femtosecond regime. *J. Anal. At. Spectrom.*, 19: 437–444.
- Sabsabi, M. and P. Cielo (1995). Quantitative analysis of aluminum alloys by laser-induced breakdown spectroscopy and plasma characterization. *Appl. Spectrosc.* 49: 499–507.
- Sallé, B., J.-L. Lacour, E. Vors, P. Fichet, S. Maurice, D.A. Cremers and R.C. Wiens (2004). Laser-induced breakdown spectroscopy for Mars surface analysis: capabilities at stand-off distances and detection of chlorine and sulfur elements. *Spectrochim. Acta Part B* 59: 1413–1422.
- Sallé, B., D.A. Cremers, S. Maurice, R.C. Wiens and P. Fichet (2005). Evaluation of a compact spectrograph for in-situ and stand-off laser-induced breakdown spectroscopy analyses of geological samples on Mars missions. *Spectrochim. Acta Part B* 60: 805–815.
- Samek, O., D.C.S. Beddows, J. Kaiser, S.V. Kukhlevsky, M. Liska, H.H. Telle and J. Young (2000). Application of laser-induced breakdown spectroscopy to in situ analysis of liquid samples. *Opt. Eng.* 39: 2248–2262.
- Schmidt, N.E. and S.R. Goode (2002). Analysis of aqueous solutions by laser-induced breakdown spectroscopy of ion exchange membranes. *Appl. Spectrosc.* 56: 370–374.
- Stepputat, M. and R. Noll (2003). On-line detection of heavy metals and brominated flame retardants in technical polymers with laser-induced breakdown spectrometry. *Appl. Opt.* 42: 6210–6220.
- St-Onge, L., M. Sabsabi and P. Cielo (1997). Quantitative analysis of additives in solid zinc alloys by laser-induced plasma spectrometry. *J. Anal. At. Spectrom.* 12: 997–1004.
- Sturm, V., L. Peter and R. Noll (2000). Steel analysis with laser-induced breakdown spectrometry in the vacuum ultraviolet. *Appl. Spectrosc.* 54: 1275–1278.
- Sturm, V., J. Vrenegor, R. Noll and M. Hemmerlin (2004). Bulk analysis of steel samples with surface scale layers by enhanced laser ablation and LIBS analysis of C, P, S, Al, Cr, Cu, Mn and Mo. *J. Anal. At. Spectrom.* 19: 451–456.

- Sun, Q., M. Tran, B.W. Smith and J.D. Winefordner (1999). Direct determination of P, Al, Ca, Cu, Mn, Zn, Mg and Fe in plant materials by laser-induced plasma spectroscopy. *Can. J. Anal. Sci. Spectrosc.* 44: 164–170.
- Theriault, G.A., S. Bodensteiner and S.H. Lieberman (1998). A real-time fiber-optic probe for the in-situ delineation of metals in soils. *Field Anal. Chem. Technol.* 2: 117–125.
- Tran, M., Q. Sun, B.W. Smith and J.D. Winefordner (2001). Determination of F, Cl, and Br in solid organic compounds by laser-induced plasma spectroscopy. *Appl. Spectrosc.* 55: 739–744.
- Uhl, A., K. Loebe and L. Kreuchwig (2001). Fast analysis of wood preservers using laser induced breakdown spectroscopy. *Spectrochim. Acta Part B* 56: 795–806.
- Van der Wal, R.L., T.M. Ticich, J.R. West and P.A. Householder (1999). Trace metal detection by laser-induced breakdown spectroscopy. *Appl. Spectrosc.* 53: 1226–1236.
- Wachter, J.R. and D.A. Cremers (1987). Determination of uranium in solution using laser-induced breakdown spectroscopy. *Appl. Spectrosc.* 41: 1042–1048.
- Wallis, F.J., B.L. Chadwick and R.J.S. Morrison (2000). Analysis of lignite using laser-induced breakdown spectroscopy. *Appl. Spectrosc.* 54: 1231–1235.
- Whitehouse, A.I., J. Young, I.M. Botheroyd, S. Lawson, C.P. Evans and J. Wright (2001). Remote material analysis of nuclear power station steam generator tubes by laser-induced breakdown spectroscopy. *Spectrochim. Acta Part B* 56: 821–830.
- Williamson, C.K., R.G. Daniel, K.L. McNesby and A.W. Mizolek (1998). Laser-induced breakdown spectroscopy for real-time detection of halon alternative agents. *Anal. Chem.* 70: 1186–1191.
- Wisbrun, R., I. Schechter, R. Niessner and K.L. Kompa (1994). Detector for trace elemental analysis of solid environmental samples by laser plasma spectroscopy. *Anal. Chem.* 66: 2964–2975.
- Yamamoto, K.Y., D.A. Cremers, L.E. Foster and M.J. Ferris (1996). Detection of metals in the environment using a portable laser-induced breakdown spectroscopy instrument. *Appl. Spectrosc.* 50: 222–233.
- Yamamoto, K.Y., D.A. Cremers, L.E. Foster, M.P. Davies and R.D. Harris (2005). Laser-induced breakdown spectroscopy analysis of solids using a long pulse (150 ns) Q-switched Nd:YAG laser. *Appl. Spectrosc.* 59: 1082–1097.
- Yaroshchyk, P., R.J.S. Morrison and B.L. Chadwick (2004). Dual beam spectrometer using laser-induced breakdown spectroscopy. *Rev. Sci. Instrum.* 75: 5050–5052.
- Yueh, F.-Y., R.C. Sharma, J.P. Singh, H. Zhang and W.A. Spencer (2002). Evaluation of the potential of laser-induced breakdown spectroscopy for detection of trace element in liquid. *J. Air Waste Manage. Assoc.* 52: 1307–1315.
- Yun, J.I., T. Bundschuh, V. Neck and J.I. Kim (2001). Selective determination of europium (III) oxide and hydroxide colloids in aqueous solution by laser-induced breakdown spectroscopy. *Appl. Spectrosc.* 55: 273–278.
- Zhang, H., F.Y. Yueh and J.P. Singh (1999). Laser-induced breakdown spectroscopy as a multi-metal continuous-emission monitor. *Appl. Opt.* 38: 1459–1466.

---

## D Major LIBS References

---

### ***Books and book chapters on LIBS, laser-induced plasmas, and plasma physics and spectroscopy***

- Adrain, R.S. (1982). Some industrial uses of laser induced plasmas. Ch. 7 in *Industrial Applications of Lasers*, ed. H. Koebner, Wiley, New York: 135–176.
- Cremers, D.A. and L.J. Radziemski (1987). Laser plasmas for chemical analysis. Ch. 5 in *Laser Spectroscopy and its Application*, eds L.J. Radziemski, R.W. Solarz and J.A. Paisner, Marcel Dekker, New York: 351–415.
- Cremers, D.A. and A.E. Pichahchy (1998). Laser-induced breakdown spectroscopy. In *Encyclopedia of Environmental Analysis and Remediation*, ed. R.A. Myers, John Wiley & Sons, Ltd, New York.
- Cremers, D.A. and A.K. Knight (2000). Laser-induced breakdown spectroscopy. In *Encyclopedia of Analytical Chemistry*, ed. R.A. Meyers, John Wiley & Sons, Ltd, Chichester: 9595–9613.
- Griem, H.R. (1964). *Plasma Spectroscopy*, McGraw-Hill, New York.
- Griem, H.R. (1974). *Spectral Line Broadening by Plasmas*, Academic Press, New York.
- Griem, H.R. (1997). *Principles of Plasma Spectroscopy*, Cambridge University Press, New York.
- Kim, Y.W. (1989). Fundamentals of analysis of solids by laser-produced plasmas. Ch. 8 in *Laser-induced Plasmas and Applications*, eds L.J. Radziemski and D.A. Cremers, Marcel Dekker, New York.
- Lee, Y.-I., K. Song and J. Sneddon (1997). Laser induced plasmas for analytical atomic spectroscopy. Ch. 5 in *Lasers in Analytical Atomic Spectroscopy*, eds J. Sneddon, T.L. Thiem and Y.-I. Lee, VCH, New York: 197–235.
- Lochte-Holtgreven, W. (1968). *Plasma Diagnostics*, Wiley, New York.
- Miziolek, A., V. Palleschi and I. Schechter (Eds) (2006). *Laser Induced Breakdown Spectroscopy*, Cambridge University Press, Cambridge.
- Moenke-Blankenburg, L. (1989). *Laser Micro Analysis*, John Wiley & Sons, Ltd, New York.
- Raizer, Y.P. (1977). *Laser-induced Discharge Phenomena*, Consultants Bureau, New York.
- Radziemski, L.J. and D.A. Cremers (Eds) (1989). *Laser-induced Plasmas and Applications*, Marcel Dekker, New York.
- Radziemski, L.J. and D.A. Cremers (1989). Spectrochemical analysis using laser plasma excitation. Ch. 7 in *Laser-induced Plasmas and Applications*, eds L.J. Radziemski and D.A. Cremers, Marcel Dekker, New York.
- Root, R.G. (1989). Modeling of post-breakdown phenomena. Ch. 2 in *Laser-induced Plasmas and Applications*, eds L.J. Radziemski and D.A. Cremers, Marcel Dekker, New York.
- Singh, J.P. and S.N. Thakur (Eds) (2006). *Laser-induced Breakdown Spectroscopy*, Elsevier Science BV, Amsterdam.

- Weyl, G.M. (1989). Physics of laser-induced breakdown. Ch. 1 in *Laser-induced Plasmas and Applications*, eds L.J. Radziemski and D.A. Cremers, Marcel Dekker, New York.
- Zel'dovich, Ya.B. and Yu.P. Raizer (2002). *Physics of Shock Waves and High-temperature Hydrodynamic Phenomena*, Dover Publications, Mineola, NY.

### Conferences

- LIBS 2000 (Pisa, Italy)
- Corsi, M., V. Palleschi and E. Tognoni (Eds) (2001). Special issue, 1st international conference on laser induced plasma spectroscopy. *Spectrochim. Acta Part B* 50: 565–1034.
- LIBS 2002 (Orlando, FL, USA)
- Hahn, D.W., A.W. Mizolek and V. Palleschi (Eds) (2003). Special issue on LIBS 2002. *Appl. Optics* 42: 5933–6225.
- LIBS 2004 (Malaga, Spain)
- Laserna, J.J. (2005). Third international conference on laser induced plasma spectroscopy and applications. *Spectrochim. Acta Part B* 60: 877–878.
- EMSLIBS 2001 (Cairo, Egypt)
- Harith, M.A., V. Palleschi and L.J. Radziemski (Eds) (2002). Special issue on 1st Euro-Mediterranean symposium and laser-induced breakdown spectrometry. *Spectrochim. Acta Part B* 57: 1107–1249.
- EMSLIBS 2003 (Crete, Greece)
- Anglos, D. and M.A. Harith (2004). Special issue on 2nd Euro-Mediterranean symposium and laser-induced breakdown spectrometry. *J. Anal. At. Spectrom.* 19: 419–504.
- EMSLIBS 2005 (Aachen, Germany)

### Articles (in order of year published, most recent last)

- Loree, T.R and L.J. Radziemski (1981). Laser-induced breakdown spectroscopy: time-integrated applications. *Plasma Chem. Plasma Process.* 1: 271–280.
- Radziemski, L.J. and T.R. Loree (1981). Laser-induced breakdown spectroscopy: time-resolved spectrochemical applications. *Plasma Chem. Plasma Process.* 1: 281–293.
- Radziemski, L.J. (1994). Review of selected analytical applications of laser plasmas and laser ablation, 1987–1994. *Microchem. J.* 50: 218–234.
- Rusak, D.A., B.C. Castle, B.W. Smith and J.D. Winefordner (1997). Fundamentals and applications of laser-induced breakdown spectroscopy. *Crit. Rev. Anal. Chem.* 27: 257–290.
- Song, K., Y.-I. Lee and J. Sneddon (1997). Applications of laser-induced breakdown spectrometry (LIBS). *Appl. Spectrosc. Rev.* 32: 183–235.
- Rusak, D.A., B.C. Castle, B.W. Smith and J.D. Winefordner (1998). Recent trends and the future of laser-induced breakdown spectroscopy. *Trends Anal. Chem.* 17: 453–461.
- Hahn, D.W. and M.M. Lunden (2000). Detection and analysis of aerosol particles by laser-induced breakdown spectroscopy. *Aerosol Sci. Technol.* 33: 30–48.
- Knight, A.K., N.L. Scherbarth, D.A. Cremers and M.J. Ferris (2000). Characterization of laser-induced breakdown spectroscopy (LIBS) for application to space exploration. *Appl. Spectrosc.* 54: 331–340.
- Radziemski, L.J. (2002). From LASER to LIBS, the path of technology development. *Spectrochim. Acta Part B* 57: 1109–1114.
- Tognoni, E., V. Palleschi, M. Corsi and G. Christoforetti (2002). Quantitative micro-analysis by laser-induced breakdown spectroscopy: a review of the experimental approaches. *Spectrochim. Acta Part B* 57: 1115–1130.
- Vadillo, J.M. and J.J. Laserna (2004). Laser-induced plasma spectrometry: truly a surface analytical tool. *Spectrochim. Acta Part B* 59: 147–161.

- Winefordner, J.D., I.B. Gornishkin, T. Correll, E. Gibb, B.W. Smith and N. Omenetto (2004). Comparing several atomic spectrometric methods to the super stars: special emphasis on laser induced breakdown spectrometry, LIBS, a future super star. *J. Anal. At. Spectrom.* 19: 1061–1083.
- Lee, W.-B., J. Wu, Y.-I. Lee and J. Sneddon (2004). Recent applications of laser-induced breakdown spectrometry: a review of material approaches. *Appl. Spectrosc. Rev.* 39: 27–97.

*Articles (in alphabetical order for last name of first author)*

- Hahn, D.W. and M.M. Lunden (2000). Detection and analysis of aerosol particles by laser-induced breakdown spectroscopy. *Aerosol Sci. Technol.* 33: 30–48.
- Knight, A.K., N.L. Scherbarth, D.A. Cremers and M.J. Ferris (2000). Characterization of laser-induced breakdown spectroscopy (LIBS) for application to space exploration. *Appl. Spectrosc.* 54: 331–340.
- Lee, W.-B., J. Wu, Y.-I. Lee and J. Sneddon (2004). Recent applications of laser-induced breakdown spectrometry: a review of material approaches. *Appl. Spectrosc. Rev.* 39: 27–97.
- Loree, T.R and L.J. Radziemski (1981). Laser-induced breakdown spectroscopy: time-integrated applications. *Plasma Chem. Plasma Proc.* 1: 271–280.
- Radziemski, L.J. and T.R. Loree (1981). Laser-induced breakdown spectroscopy: time-resolved spectrochemical applications. *Plasma Chem. Plasma Proc.* 1: 281–293.
- Radziemski, L.J. (1994). Review of selected analytical applications of laser plasmas and laser ablation, 1987–1994. *Microchem. J.* 50: 218–234.
- Radziemski, L.J. (2002). From LASER to LIBS, the path of technology development. *Spectrochim. Acta Part B* 57: 1109–1114.
- Rusak, D.A., B.C. Castle, B.W. Smith and J.D. Winefordner (1997). Fundamentals and applications of laser-induced breakdown spectroscopy. *Crit. Rev. Anal. Chem.* 27(4): 257–290.
- Rusak, D.A., B.C. Castle, B.W. Smith and J.D. Winefordner (1998). Recent trends and the future of laser-induced breakdown spectroscopy. *Trends Anal. Chem.* 17: 453–461.
- Song, K., Y.-I. Lee and J. Sneddon (1997). Applications of laser-induced breakdown spectrometry (LIBS). *Appl. Spectrosc. Rev.* 32: 183–235.
- Tognoni, E., V. Palleschi, M. Corsi and G. Christoforetti (2002). Quantitative micro-analysis by laser-induced breakdown spectroscopy: a review of the experimental approaches. *Spectrochim. Acta Part B* 57: 1115–1130.
- Vadillo, J.M. and J.J. Laserna (2004). Laser-induced plasma spectrometry: truly a surface analytical tool. *Spectrochim. Acta B* 59: 147–161.
- Winefordner, J.D., I.B. Gornishkin, T. Correll, E. Gibb, B.W. Smith and N. Omenetto (2004). Comparing several atomic spectrometric methods to the super stars: special emphasis on laser induced breakdown spectrometry, LIBS, a future super star. *J. Anal. At. Spectrom.* 19: 1061–1083.

---

# Index

---

Note: Page numbers in *italics* indicate figures and those in **bold** indicate tables.

- Absorption depths 198  
Accuracy 115–116, 164, *165*  
Acousto-optic tunable filters (AOTF) 71,  
  **71**, 73–74, 75  
Acousto-optically switched Nd:YAG  
  lasers 204  
Aerosols 9  
  analysis of biological 211  
  breakdown 40  
  generation of 238–239  
AlO emissions, monitoring oxide removal  
  using *130, 132, 133*  
Aluminum  
  AlO spectrum from laser plasma formed  
    on oxidized Al metal 127  
  experimental arrangement for surface  
    cleaning of 126–127  
  LIBS at commercial Al operation  
    229–230  
mass ablated as a function of LTSD for  
  spherical and cylindrical lenses  
    *144, 145*  
monitoring oxide removal using AlO  
  emissions *130, 132, 133*  
monitoring oxide removal using O(I)  
  emissions 127–130  
rate of oxide removal 130–132  
spectra from Al metals with different  
  degrees of surface contamination  
    *134, 135*  
spectra recorded from an anodized Al  
  metal plate *128, 129*  
spectra recorded from an unanodized Al  
  metal plate *127, 128*  
surface condition after cleaning *133*
- Analysis  
  contaminants of nuclear fuel  
    reprocessing plants 182  
  industrial environment samples 181  
  material sorting and type of  
    134–136  
    underwater *192, 213, 214*  
Analytical figures-of-merit (FOM)  
  99–116, 164–168  
Antarctic sediments, LIBS results  
  *165, 167*  
Anti-reflection coatings, on lenses 64  
AOTF (Acousto-optic tunable filters) 71,  
  **71**, 73–74, 75  
Apparatus, LIBS 2, 3, 53–97, 126–127,  
  *156, 157, 173–174*  
Array detectors, shutters 84–88  
Art analysis 13  
Asbestos  
  comparison of spectra of building  
    materials and *124, 124*  
  material identification 122  
  spectra of cement, ceiling tile  
    and *123*  
Atom counting 124–125  
Atomic optical emission spectrochemistry  
  (OES) 1–2  
Avalanche photodiodes 83
- Backpack LIBS instruments *137, 139*  
Ba(II) signals, dependence on  
  compound form in solid matrix  
    *154, 155*  
Bandpass filters 71–73  
Barium, concentrations in soil 141

- Basalt  
 calibration curves for Ba and Si using samples of 137, 139  
 composition differences between samples 137  
 identification of the strong line in spectrum 121  
 LIBS spectrum of 33, 34  
 overlapped spectra of samples 137, 138  
 spectra at 90 and 0.77 atm 219, 220  
 spectrum from rock sample 100, 101, 102, 119, 121
- Beam diffraction, smallest spot size 175–176
- BeCu particles, LIBS analysis of different sized 151
- Beryllium processing plant 140
- Beryllium solutions, LIBS spectra 99, 100
- Beryllium, aerosolization of 238–239
- Biological materials, LIBS for 211–212
- Boltzmann temperature determination 31, 33, 34, 35, 36, 199
- Breakdown  
 in gases 36–38  
 in solids, aerosols and liquids 39–41
- Breakdown thresholds 40–41  
 for various lasers and gases 37, 38  
 in molecular oxygen and nitrogen 37
- Bremsstrahlung process 23, 197
- Broadening  
 collision 26  
 Doppler 25–26  
 natural 27  
 pressure 69  
 Stark 26, 69  
 time dependent 109
- Calibration  
 detection systems 88–92  
 wavelength 88–90, 91
- Calibration curves 107–113, 147  
 of Ca(II) in soil and clay samples 148–149  
 definition 114  
 dependence of slope on pressure 112, 113  
 as a function of laser energy 112
- LiCl solution impurity detection 162, 163  
 nonlinear and linear 110–111
- Calibration-free LIBS (CF-LIBS) 12, 164, 201–203
- Calibration sample, definition 114
- Calibration standards 113–114
- Carbon, internal standardization in detection of C in soil 152–153
- CCD, *see* Charged coupled device (CCD)
- Certified reference material, definition 114
- CFCs (chlorofluorocarbons), atom counting 124–125
- Charged coupled device (CCD) 83, 85, 86, 87, 88
- Chemical matrix effects 153–155
- Chirped pulses 183–184, 186
- Chromatic aberrations, lens 62, 63, 178
- Clay, calibration curve of Ca(II) 148–149
- Collinear laser beams 48, 49, 61, 62
- Collinear laser pulses, laser microablation and plasma reheating 209
- Collinear pulse configuration 61
- Collision broadening 26
- Color filters 71
- Compact lasers 56, 57, 94
- Compact LIBS instruments 137, 139, 221
- Compact probe fiber optic LIBS 94, 95, 137, 139, 172
- Continuous optical discharges (COD) 8, 39
- Conventional electrode spark 1, 2, 172
- Conventional remote LIBS 173  
 using femtosecond laser pulses 182–184
- Conventional remote open path LIBS 173–182  
 analysis results 179–182  
 apparatus 173–174  
 cliff bank interrogation demonstration 174, 180  
 laser pulse focusing 174–178
- Cr solutions, LIBS spectra 99, 100
- Cu(I), calculated profiles at 324.7 nm as function of species density 202

- Cylindrical optics 63, 64  
Czerny-Turner spectrograph 74, 76, 77, 79
- Depth resolution 205  
Detection limits 115, 164  
bibliography for 117  
for impurities in LiCl solutions 158, 163  
representative 245–270  
uniform 263–265
- Detection system calibrations 88–92  
spectral response calibration 90–92  
wavelength calibration 88–90, 91
- Detectors 83–88
- Diagnostic techniques 25
- Diameters of laser pulses 64
- Diode lasers 13, 58
- Directionality, laser pulse 60
- Donut mode laser pulses 63, 64
- Doppler broadening 25–26
- Doppler widths 27, 28, 29
- Double pulse LIBS 47–49, 61–62  
geometric arrangements 48, 49, 61, 62  
reheating experiments 208, 209  
studies and applications 208–209
- Echelle grating 80
- Echelle spectrographs 80–83  
comparison of two 83  
diagram 81  
example of spectra 82
- Echelleograms 81, 82
- Edge filters 72, 80
- Electrode spark 1, 2, 172
- Electron densities, determination from spectral line widths 27–30
- Electron temperature, convergence of 31
- Elements  
identification of 119–122  
ionization stage of 120  
ionization stage of, labels 101  
signals as function of pressure 218, 219
- Emission lines  
comparison of peak heights and areas 104, 105  
determining area of 103–104
- determining intensity of 102–103  
as function of LTSD 146  
observation of multiple 121  
ratioed intensities as a function of LTSD 147  
topics to consider when identifying 119–121
- Errors in accuracy 115–116
- Femtosecond laser pulses, conventional  
remote LIBS using 182–184
- Femtosecond lasers 39, 40, 58, 171, 173, 182–187
- Fiber optic cables (FOCs) 65–69  
cladding materials 66  
core diameters 66  
custom configurations 68  
fused silica 65, 66  
laser pulse delivery 68, 69  
laser pulses injected into 94, 95, 189–193, 194  
spectral transmissions 66, 67
- Fiber optic coupled LIBS  
for analysis of nuclear reactor components 194  
literature relating to 193
- Fiber optic LIBS 172, 187–194
- Fiber optics 171  
applications of 192–194  
for laser pulse delivery 189–192  
for light collection 68, 187–189
- Figures-of-merit 99–116, 164–168
- Filamentation 184
- Filaments  
images produced in air 185, 186  
images produced on a target 187
- Filters  
edge 80  
single line 89  
spectral 71–73
- Flashlamp-pumped Nd:YAG lasers 54–57
- Flyby asteroid mission, LIBS for 214
- FOC, *see* Fiber optic cables (FOCs)
- Focal lengths 64  
relationship between beam diameter and 175, 176
- Free-electron bremsstrahlung 197

- Galilean telescopes 190, 191  
Gases  
  analysis of 179  
  breakdown in 36–38  
  post-breakdown phenomena in 39  
Gate pulses, timing between laser pulse and 93–94  
Gaussian profiles 26  
Geiger photodiodes 83  
Geological samples, LIBS remote analysis of 180  
Graphite, LIBS spectrum 101  
Grating spectrographs, dispersion of 78  
  
Harmonic generation 60, 61  
Hazards, associated with LIBS experiments 238  
Hg calibration spectrum 89  
High speed scanning LIBS 207  
History of LIBS  
  1960–1980 6–9  
  1980–1990 9–11  
  1990–2000 11–15  
Hydrogen  
  Doppler and Stark widths of 28, 29  
  Stark broadening of H(I) 104  
  
Incinerators, on-line continuous monitoring of emissions from 166, 167  
Inductively coupled plasma (ICP) 1, 2  
Industrial environment samples, analysis of 181  
Injection, seeded Nd:YAG lasers 57  
Intensified CCD (ICCD) 83, 88  
Internal standardization 110–111, 152–153  
Ionization, multiphoton 36  
Irradiance (intensity) 59  
  
K9 rover 11, 12  
Kerr effect 184, 185  
  
Laser ablation 43–47  
Laser beams 48, 49  
Laser detonation wave (LDW) 43  
Laser Identification of Fittings and Tubes (LIFT) 231  
  
Laser-induced breakdown 36–43  
  in gases 36–38  
post-breakdown phenomena in gases 39  
post-breakdown phenomena on solid surfaces 41–43  
solids, aerosols and liquids 39–41  
Laser-induced breakdown spectroscopy (LIBS) 2–6  
  1960–1980 history 6–9  
  1980–1990 history 9–11  
  1990–2000 history 11–15  
  ablation crater 216  
  accuracy of 164, 165  
  active areas of investigation (2000–2002) 15–16  
  advantages for space applications 215  
  apparatus 2, 3, 53–97  
  applications 229–230  
  at commercial aluminum operation 229–230  
  backpack instruments 137, 139  
  for biological materials 211–212  
  combining with other analytical techniques 229  
  comparison of SEM-EDX and 165, 166  
  components and systems availability 231–232  
  continuous monitoring of composition of liquid process stream 231  
  deployment methods 94–96  
  detection limits 245–270  
  development milestones 6  
  factors to speed commercialization of 230–232  
  field tests 221–223  
  fundamental research 197–201  
  future of 227–233  
  high resolution spectrum 69–70  
  improvements made in recent years 227–228  
  instrument with sampling head mounted on mast of test rover 222, 223  
  major references 271–273  
  measurement basics 99–105  
  multiple pulses 47–49, 61–62, 208, 209  
  papers per year (1966–2005) 15  
  patents per year (1979–2002) 16

- recommended methods for commencing LIBS research on a variety of samples **241–242**
- remote analysis applications 11, 179–182, 192–193, **194**
- routine use in industrial applications 230–231
- space applications 214–223
- spectra 3–4, 5
- standardization and quantification 230
- time-resolved detection 93–94
- in underwater analysis 213, **214**
- useful operating range 177, **178**
- Laser-induced breakdown spectroscopy (LIBS) plasma 23–49
- double or multiple pulse LIBS 47–49
- fundamentals 23–36
- inhomogeneities 198
- laser ablation 43–47
- laser-induced breakdown 36–43
- temporal history 23, 24
- temporal history when two laser pulses are used 47, 48
- Laser-induced plasma spectroscopy (LIPS), *see* Laser-induced breakdown spectroscopy (LIBS)
- Laser-induced Plasmas and Applications* (Radziemski and Cremers) 11
- Laser microablation and plasma reheating, with collinear laser pulses 209
- Laser optical emission spectrochemistry (OES) 1–2
- Laser plasmas
- generation on soil 190
  - homogeneity of 199
  - information from 69
- Laser pulse transport, factors influencing fiber damage for **192**
- Laser pulses
- diameters 64
  - directionality 60
  - donut mode 63, 64
  - fibers for delivery 189–192
  - FOC delivering 68, 69
  - focusing 62, 63, 174–178
  - induced ignition 239
- microablation and plasma reheating with collinear 209
- required to reach matrix 210, **211**
- timing between gate pulse and 93–94
- Laser safety 237–238
- Laser spark spectroscopy (LSS), *see* Laser-induced breakdown spectroscopy (LIBS)
- Laser sparks 1, 2, 197
- spectra of Al surface contaminated by Tl-containing solution 149, **150**
- Laser-supported combustion (LSC) waves 42
- Laser-supported detonation (LSD) waves 42
- Laser-supported radiation (LSR) waves 42
- Lasers 54–62
- acousto-optically switched
  - Nd:YAG 204
  - advances 203–204
  - breakdown thresholds 37, **38**
  - compact 57, 94
  - diode 13, 58
  - femtosecond 39, **40**, 58, 182–184
  - flashlamp-pumped Nd:YAG 54–55, 56
  - fundamentals of 54–55
  - generation of additional wavelengths 60–61
  - injection seeded Nd:YAG 57
  - interactions with different pulse lengths on solid surfaces 44, 45
  - microchip 58, 203–204
  - monochromaticity 60
  - nanosecond 183
  - Nd:YAG 54–57, 181, 204
  - picosecond 183
  - properties important for LIBS 59–60
  - Q-switched 55
  - spatial quality 59
  - specifications for LIBS 55, **56**
  - surface cleaning 125, **126**
  - types of 55–58
- Lens systems 62, 64
- Lens-to-sample distance (LTSD) 143, **145**
- Lens types 65
- Lenses 63–65
- chromatic aberrations 62, 63, 178
  - materials 64

- LIBS, *see* Laser-induced breakdown spectroscopy (LIBS)
- LiCl solutions
- analytical lines of impurities 157, **158**
  - apparatus for LIBS measurements 156, **157**
  - calibration curves 157, 162
  - calibration curves for the impurities Ca, Mg and Si 162
  - calibration curves for the impurities Cr, Ni and C 163
  - calibration curves for the impurities K, Na and Fe 163
  - detection limits 158, 164
  - impurity detection 155–165
    - experimental procedure 157–158
    - measurement precision 157–158, 161–163
    - results 158–165
    - results discussion 163–164
  - objective of study 155–156
  - preparation of 156–157
  - spectrum of Cr 158, **161**
  - spectrum of Mg(I) line 158, **159**
  - spectrum of Ni 158, **160**
- LIDAR (light detection and ranging) 172
- Light collection, with a fiber optic 187
- Limit of detection 115, 158, 163, **164**, 245–270
- Line filters 71, 73
- Line profiles, spectral lines and 25–27
- Line (long) sparks 9, 10, 63, 64, 126
- Linear dispersion 78
- Linear dynamic range 107
- Lines, determining area of 103–104
- LIPS, *see* Laser-induced breakdown spectroscopy (LIBS)
- Liquids
- breakdown thresholds 40–41
  - generating plasmas in 8
  - remote analysis 179
- Lithium solutions, detection of impurities in 155–165
- Lithium, Doppler and Stark widths of **28**, 29
- Local thermodynamic equilibrium (LTE) 31, 32
- Long wave pass edge filters 71
- Lorentz profiles 26
- LSS, *see* Laser-induced breakdown spectroscopy (LIBS)
- LTSD, *see* Lens-to-sample distance (LTSD)
- Lunokhod rover 217
- Mars
- analysis of Phobos 215
  - image of berry shaped formations 216
  - LIBS studies **218**
- Mars Science Laboratory rover (MSL) 222, 223, 229
- Marx bank pulse generators 61
- Materials
- identification 119, 122–125
  - sorting 133–137
- Matrix effects 153–155
- Measurement repeatability 105
- MER Opportunity rover, geological features discovered by 216, **217**
- Mercury calibration spectrum 89
- Metals, effect of plasma shielding on ablation rate of pure **45**, **46**
- Microablation and plasma reheating, with collinear laser pulses 209
- Microchannel plates (MCPs) 87
- Microchip lasers 58, 203–204
- Mineral melt, stand-off analysis of major elements in 180
- Mirror systems 62, 63
- Mn, matrix effect example 153–154
- Molten steel, analysis of 182
- Monochromaticity, lasers 60
- MSL rover 222, 223, 229
- Multiphoton ionization 36
- Multiple pulse LIBS 47–49
- Nanosecond pulses, interaction with a copper target in vacuum 201
- Narrow bandpass filters 73
- Natural line widths 27
- Nd:YAG lasers 54–57, 181, 183, 204
- Negative chirped pulses 183
- Notch filters 71
- Nuclear fuel reprocessing plants, analysis of contaminants 182
- Nuclear reactors, LIBS applications 212–214

- O(I) emissions  
intensity after removal of anodized area surrounding ablation region 128–130, *131*  
intensity versus shot number for an anodized Al metal plate 128, *130*  
intensity versus shot number for an anodized Al metal plate after removal of anodized region surrounding ablation region 128–130, *131*  
intensity versus shot number for an unanodized Al metal plate 128, *129*  
monitoring oxide removal using 127–130  
recorded from laser plasma formed on oxidized Al metal *127*
- On-line continuous monitoring, emissions from incinerators 166, *167*
- Open path LIBS 171–172, 173, *181*
- Open path transportable LIBS 182
- Optical emission spectroscopy (OES) 1–2
- Optical systems 62–69  
fiber optic cables 65–69  
focusing and light collection 62–63  
lenses 63–65
- Orthogonal laser beams 48, *49*
- Orthogonal pulse configuration 61
- Oxide, removal rate from Al 130–132
- Particle size and incomplete vaporization 151
- Paschen-Runge polychromator 75, 77
- Pb(I) signals, dependence on compound form in solid matrix 154, *155*
- Pencil lamps 89
- Photodetectors 84
- Photodiode array (PDA) **83, 84, 85, 86, 87**
- Photomultiplier tubes (PMTs) 83, 84
- Picosecond lasers 183
- Plasma emissions, apparatus used to monitor 126
- Plasma formation *185*
- Plasma light  
collecting 178–179  
focusing onto a spectrograph slit 188  
plasma position change and observed signal 188, *189*
- Plasma models 199
- Plasma propagation, speed towards  
laser beam for air and argon  
sparks 198
- Plasma temperature  
as function of LTSD 144, *146*  
parameters and energy levels for two-line determination of 33, *33*  
Saha method of determining 34, *35*
- Plasmas 23  
ablation of material into 46, *47*  
continuous laser-induced 39  
formation on a plane surface 41, *42*  
modeling into a vacuum 228  
opacity 30  
radiation processes 24, *25*  
size variation of 42, *44*  
spectral lines and line profiles 25–27  
temperature and thermodynamic equilibrium 31–36
- Portable soil analyzer *139*
- Positive chirped pulses 183
- Post-breakdown phenomena  
in gases 39  
on solid surfaces 41–43
- Precision 105–107, 161–164
- Pressure broadening 69
- Process monitoring 125–133
- Pulse generators, Marx bank 61
- Pulses 183  
collinear configuration 61  
interaction of nanosecond pulses  
with a copper target in vacuum 201
- Q-switched lasers 55
- Qualitative LIBS analysis 119–141  
asbestos, cement and ceiling tile 122, *123*  
element identification 119–122  
examples **120**  
experimental conditions 120  
knowledge of the sample 119  
material identification 122–125  
material sorting 133–137  
process monitoring 125–133  
site screening 137–141

- Quantitative LIBS analysis 143–169  
     chemical matrix effects 153–155  
     factors affecting 143, 144, 145, 151  
     figures-of-merit 164–168  
     internal standardization 110–111,  
         152–153  
     Li solution impurities detection  
         155–165  
     particle size 151  
     sampling considerations 147–150  
     sampling geometry 143–147  
     Quasi-static Holtzmark theory 27
- Raman, combination of LIBS and  
     220–221, 229
- Random errors 116
- Rayleigh range 176, 177
- Reciprocal linear dispersion 78
- Recombination process (free–bound) 23
- Reference material, definition 114
- Refractive index, dependence on  
     wavelength 62
- Remote analysis by femtosecond pulse  
     produced filamentation 184–185
- Remote LIBS  
     collecting the plasma light 178–179  
     using femtosecond pulses 186–187
- Remote LIBS measurements 171–196  
     conventional open path LIBS  
         173–182  
     fiber optic 187–194  
     stand-off LIBS using femtosecond pulses  
         182–187
- Replicate measurements 106
- Representative LIBS detection limits  
     245–270  
     in gases and liquids 246–250  
     in other materials 263  
     in surfaces and solids 251–262
- Response curves 90, 92
- Rhyolite rock surface, inhomogeneities on  
     149, 150
- Rock  
     ablation 121, 122  
     comparison of bulk rock, basalt and  
         dolomite spectra 122, 124  
     identification of type of 122, 124
- Safety considerations in LIBS 237–239
- Saha (Saha–Eggert) equation 34
- Saha (Saha–Eggert) plots, temperatures  
     obtained from 35, 36, 199
- Saha (Saha–Eggert), method of determining  
     plasma temperature 34, 35
- Sampling geometry, effects of 143–147
- Scratch and dig 65
- Sediment samples, concentration of major  
     elements in 154
- Self-absorption 30, 109, 110
- SEM-EDX, comparison of LIBS and  
     165, 166
- Sensitivity 108  
     loss at high concentrations 109
- Shutters, array detectors 87
- Single lens system, minimum spot size 175
- Single line filters 89
- Site screening, using LIBS 137–141
- Slag samples, multi-elemental  
     analysis 210
- Soil  
     barium concentration in 141  
     calibration of Ca(II) in 148–149  
     generation of laser plasmas on 190
- Soil analysis 137–141  
     calibration standards 113  
     use of internal standards 152–153
- Sojourner rover of Pathfinder mission 217
- Solids  
     analysis of 179, 180  
     breakdown 39–41  
     surface post-breakdown phenomena  
         41–43
- Space applications, LIBS 214–223
- Sparks  
     conventional electrode 1, 2  
     laser created 197  
     line 126  
     long 9, 10, 63, 64
- Spectral filters 71–73
- Spectral interferences 108–109
- Spectral lamps 89
- Spectral line widths, determining electron  
     densities from 27–30
- Spectral lines and line profiles 25–27, 202
- Spectral resolution 69–83  
     devices 70–83

- Spectral response calibration 90–92  
Spectrochemical LIDAR instruments 179  
Spectrographs 74–80  
compact 79  
Czerny-Turner 74, 76, 77, 79  
designs 74  
dispersion of grating 78  
Echelle 80–83  
examples of spectra recorded by 74, 76  
spectrum from compact 79  
Spectrometers  
advances in 203–204  
dual-grating high-resolution 204  
Spherical aberration, smallest spot size 175  
Spherical optics 63  
Spores, detection of 212  
Stainless steel  
analysis of 181  
LIBS analysis across an open path 210  
mapping of inclusions 206–207  
*see also* Steel  
Stand-off analysis 180, 182  
of soil samples 220  
using femtosecond pulses 182–187  
Standard reference materials 164, 165  
Standard, definition **114**  
Standardization, internal 152–153  
Stark broadening 26, 69  
Stark widths 27–29, **28**, 30  
Steel  
analysis of molten 182  
high speed scanning for inclusion detection 207  
LIBS analysis applications 210–211  
monitoring spatial and temporal evolution 198–199, 200  
*see also* Stainless steel  
Surface analysis 205–208  
Surface cleaning 125, 126  
Surface condition in material sorting 134  
Surface deposits, determination of underlying bulk composition 149  
Surface detection 121  
Surfaces  
scanning by LIBS 229  
scanning with elongated sparks 205, 206  
spatial distributions 205, 206  
Systematic errors 116  
TABLASER 9  
Target distances, methods of measuring **177**  
Telescopes, Galilean 190, **191**  
Temperature and thermodynamic equilibrium of plasmas 31–36  
Teramobile 185–186  
Thermodynamic equilibrium, tests for existence of 32  
Ti, line intensity 102, 103  
Time-resolved detection, timing between laser pulse and gate pulse 93–94  
Titanium, gated spectra 5  
Transparent materials, breakdown in 40  
Transportable LIBS instruments 137, **139**  
soil analysis 194  
Tunable filters 73  
Underwater analysis 213, **214**  
using fiber optics 192  
Uniform detection limits 263–265  
Vaporization, minimum power density required to produce 43  
Venus, surface of 218–219  
Voigt profiles 26, 202  
Water, breakdown thresholds 40, **41**  
Wavelength calibration 88–90, 91  
Wavelength coupling 58–59  
Wavelength tables  
compendiums 100  
relative intensities of lines from 120  
Workplace monitoring 137